University of Alberta

Microfluidics for Use in Capillary Electrochromatography and Multiplexed Protein Analysis

by

Dolores Martinez 

A thesis submitted to the Faculty of Graduate Studies and Research
in partial fulfillment of the requirements for the degree of

Doctor of Philosophy

Department of Chemistry

Edmonton, Alberta
Fall 2007

Your file Votre référence
ISBN: 978-0-494-33024-1
Our file Notre référence
ISBN: 978-0-494-33024-1

ABSTRACT

Two microfluidics devices for chemical analyses are fabricated and tested. In the first, bead-based strong cation exchange capillary electrochromatography (SCX CEC) of a series of poly-lysines is described, using laser-induced fluorescence detection. Conditions for efficient analyte separation are tested. The effect of buffer ionic strength and separation voltage on plate height (H) numbers is studied. Under optimal conditions, efficiencies equal to 196,000 plates/meter for dilysine, 400,000 plates/meter for trilysine and 238,000 plates/meter for tetralysine are obtained. A two-column CEC microsystem, using strong cation exchange followed by reverse-phase columns, is discussed: its use for two-column sequential analysis of a mixture of dyes and dilysine under laser-induced fluorescence detection is described. The second microfluidics device consists of a hybrid silicon-glass system for single- and multi-channel protein analysis by pressure-driven electrospray ionization mass spectrometry (ESI MS). Microchannels are defined in a glass substrate; these are connected to silicon beds through a thin (< 20 μm) or thick (> 600 μm) polydimethylsiloxane (PDMS) layer. The silicon beds are octadecylsilyl-derivatized and therefore act as solid phase extraction (SPE) beds. For efficient elution of analytes off the silicon SPE beds in the multichannel device, uniform bed-to-bed porosity is shown to be a critical factor. Because the silicon SPE beds are micromachined to be porous using well-known lithographic techniques, all are uniform and of equal porosity. Microdevice fabrication is discussed including glass, silicon and PDMS processing. A novel PDMS processing technique utilizing reactive ion etching (RIE) is described. Single channel microdevices are used for on-chip protein sorption and on-bed trypsin digestion for cytochrome c, myoglobin and bovine serum albumin. In

the multichannel microdevices built using the thin PDMS approach, defects in the PDMS layer prevent sequential elution off the silicon SPE beds. Laser-induced fluorescence microscopy shows sequential elution off the silicon SPE beds in the multichannel microdevice built using the thick PDMS. However, cytochrome c analysis under ESI MS detection showed that baseline-resolved peak elution is not possible due to the large dead volume introduced by the thick PDMS layer. Theoretical bandbroadening analysis describes conditions for resolved cytochrome c peak analysis by pressure-driven ESI MS.

ACKNOWLEDGEMENTS

I would like to thank all who have contributed to this work:
My thesis supervisor, D. Jed Harrison, the personnel at the
University of Alberta's Nanofab and group members.

To the good friends I have made while in Edmonton, thank you
for keeping me sane and entertained.

For helping me out both inside and outside of the lab, many
thanks to Abebaw Jemere, Justine Taylor and Kowlasar Misir.

Finalement, merci aux membres de ma famille pour tout le
soutient qu'ils m'ont apporté.

TABLE OF CONTENTS

LIST OF TABLES

LIST OF FIGURES

LIST OF ABBREVIATIONS

ACN _____ acetonitrile
BSA _____ bovine serum albumin
BOE _____ buffered oxide etch
C18 _____ octadecylsilyl
CCD _____ charged couple device
CD _____ critical dimension
CE _____ capillary electrophoresis
C.L. _____ confidence limit
2D-GE _____ two-dimensional gel electrophoresis
EOF _____ electroosmotic flow
ESI _____ electrospray ionization
FITC _____ fluorescein isothiocyanate
HMDS _____ hexamethyldisilazane
ICP _____ inductively coupled plasma
IC _____ integrated circuit
i.d. _____ internal diameter
IEF _____ isoelectric focusing
IMAC _____ immobilized metal affinity chromatography
LC _____ liquid chromatography
LIF _____ laser-induced fluorescence
MC _____ missed cleavage
MALDI _____ matrix-assisted laser desorption ionization
MeOH _____ methanol
MEKC _____ micellar electrokinetic chromatography
MS _____ mass spectrometer
MET-OX _____ methionine oxidized
M.W. _____ molecular weight
N.A. _____ numerical aperture
o.d. _____ outer diameter

ODS _____ octadecylsilyl

OTE _____ octadecyltriethoxysilane

PDMS _____ polydimethylsiloxane

PMT _____ photomultiplier tube

PR _____ photoresist

RF _____ radio frequency

RP _____ reverse-phase

RSD _____ relative standard deviation

RIE _____ reactive ion etching

SDS-PAGE _____ sodium dodecyl sulfate polyacrylamide gel electrophoresis

SPE _____ solid phase extraction

SCX _____ strong cation exchange

SEM _____ scanning electron microscope

TIC _____ total ion chromatogram

UV _____ ultraviolet

WCX _____ weak cation exchange

LIST OF SYMBOLS

GENERAL

Å	10^{-10}
n	10^{-9}
μ	10^{-6}
m	10^{-3}
k	10^{3}
g	gram
m	meter
M	molar
s	second
W	watts
V	volts
a.f.u.	arbitrary fluorescence unit
m/z	mass-to-charge
c.p.s.	counts per seconds
a.m.u.	atomic mass unit

MICROFABRICATION

B_{min}	minimal line width
λ	wavelength
Z	photoresist thickness
S	distance
R	rate
r	radius
t	time

ELECTROPHORESIS

δ	double layer thickness
d	diameter

ζ _____ zeta potential

μ _____ electrophoretic mobility

V _____ velocity

E _____ electric field

ε_o _____ permittivity of vacuum

ε_r _____ dielectric constant

η _____ viscosity

q _____ charge

r _____ radius

SEPARATION EFFICIENCY _____

σ^2 _____ variance

σ _____ standard deviation

L _____ length

H _____ plate height

t_{corr} _____ corrected elution time

μ _____ velocity

A _____ eddy diffusion

B/μ _____ longitudinal diffusion

μC_s _____ mass transfer in the solid phase

μC_m _____ mass transfer in the mobile phase

λ _____ packing constant

d_p _____ particle diameter

γ _____ packing constant

D_m _____ diffusion coefficient in the mobile phase

d_f _____ film thickness

D_s _____ diffusion coefficient in the solid phase

k' _____ capacity factor

α _____ selectivity

N _____ theoretical plates

n _____ peak capacity

R_s _____ resolution

W _____ width of the peak

CATION EXCHANGE CHROMATOGRAPHY _____

R _____ resin

K _____ equilibrium constant

k _____ distribution coefficient

C_s _____ concentration of analyte in the solid phase

C_m _____ concentration of analyte in the mobile phase

BANDBROADENING ANALYSIS _____

D _____ diffusion coefficient

A _____ cross-sectional area

L _____ length

F _____ flow rate

V _____ volume

w _____ width

d _____ depth

CHAPTER 1 INTRODUCTION TO MICROFLUIDICS IN PROTEOMICS AND SEPARATION SCIENCE

1.1.INTRODUCTION

Microfluidics, the study of fluid flow in micrometer-scale channels, has attracted much research in the past 15 years. The concept is illustrated in Figure 1.1, where work published in 1992 on the first microfluidic platform for capillary electrophoresis analysis is presented[1, 7, 11]. The device consists of two glass wafers thermally bonded together. The lower wafer contains 10 μm deep channels micromachined using photolithographic techniques (channel 1: 1 mm wide, channels 2 and 3: 30 μm wide). The upper wafer has drilled holes which act as reservoirs and are used to access the microchannels. Channels 1 and 3 are filled with buffer solution, channel 2 with sample (a mixture of two dyes, fluorescein and calcein). By applying a voltage between channels 2 and 3 for 30 s, the dye mixture is driven towards the channel intersection. The voltage is then applied across channels 1 and 3; the dye mixture is injected into channel 3 and separated by capillary electrophoresis.

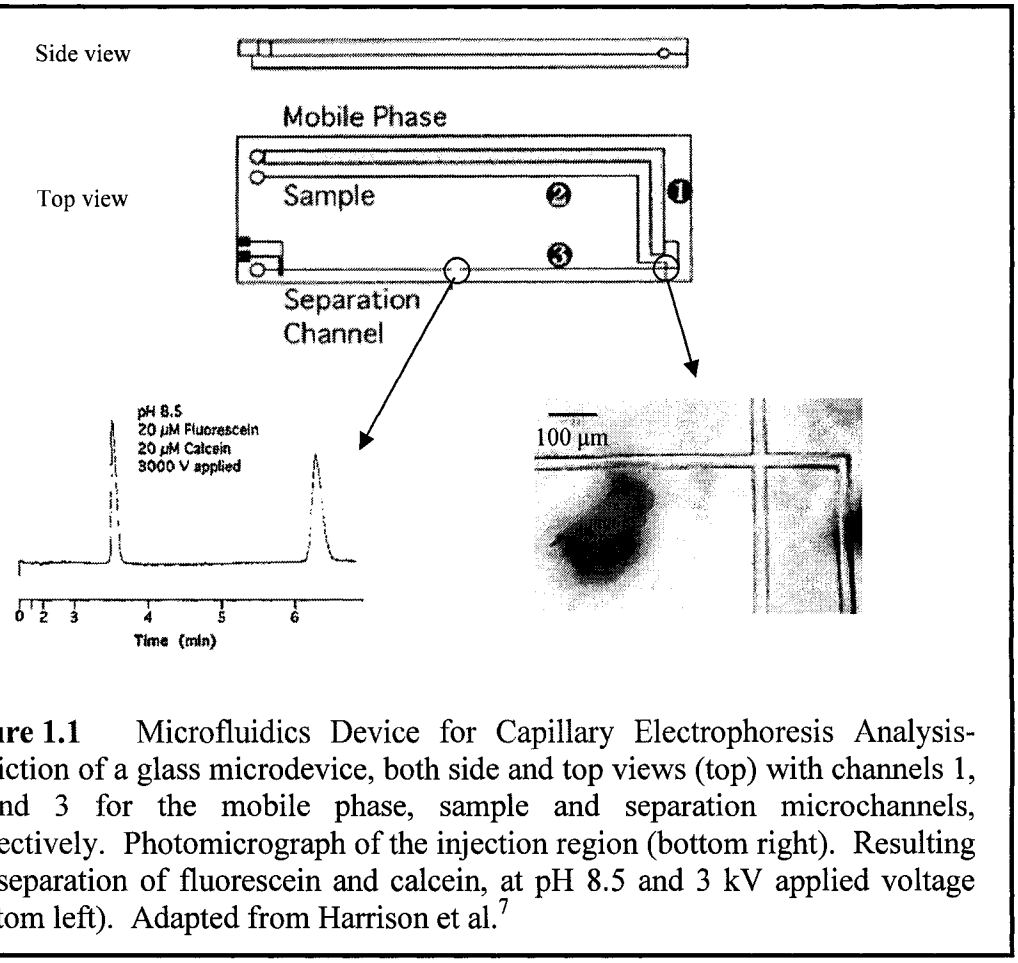

Figure 1.1 Microfluidics Device for Capillary Electrophoresis Analysis- Depiction of a glass microdevice, both side and top views (top) with channels 1, 2 and 3 for the mobile phase, sample and separation microchannels, respectively. Photomicrograph of the injection region (bottom right). Resulting CE separation of fluorescein and calcein, at pH 8.5 and 3 kV applied voltage (bottom left). Adapted from Harrison et al.[7]

The first miniaturized device for chemical analysis was introduced in 1979 by Terry et al. in the form of a gas chromatograph on a silicon substrate[12]. Interest in the miniaturization concept was revived in 1990 after a decade hiatus, when Manz et al. published a manuscript describing the benefits to be gained through chemical analysis in microchannels[13]. From Manz, benefits could be gained through the integration of sample pretreatment, analysis and detection on a single miniaturized platform. Miniaturization would result in higher separation efficiencies, rapid analysis times, lower sample and reagent consumption and the possibility of multiplexing numerous analyses with little efficiency loss. When considering the demands placed on analytical techniques for use in the medical field, the scientific community would stand to benefit from new miniaturized technologies.

While rapid analysis times and low sample and reagent consumption has been achieved on microdevices, multiplexing and use for complex sample analysis are issues that have yet to be solved. These problems have led to a wide array of microdevice designs and have pushed the research forward.

In this thesis, two microfluidics platforms were built and tested for analysis of peptides and proteins. The first, described in Chapter 2, consists of a glass microdevice for one- and two-bed capillary electrochromatography (CEC) of peptides with laser-induced fluorescence detection. Strong cation exchange beads (SCX) were packed in a previously-described[8, 14] microfluidic device: the efficiency of the resulting separation for positively-charged peptides was studied. In the two-bed microdevice, the first bed was packed with SCX beads, the second, with octadecylsilyl (ODS) beads. The resulting separation is discussed. The second microdevice is a hybrid glass-silicon platform for electrospray ionization (ESI) mass spectrometric (MS) analysis of proteins: microchannels were fabricated in glass substrates and connected to silicon beds via a machined polydimethylsiloxane (PDMS) layer. The silicon beds were micromachined using photolithographic techniques and inductively coupled plasma reactive ion etching (ICP RIE), and further derivatized with an ODS phase to act as solid phase extraction (SPE) beds. Several approaches were tested for efficient glass-to-silicon coupling: two approaches were eventually retained. First, coupling through a thin (< 20 μm) PDMS layer, machined using reactive ion etching (RIE); second, coupling through a thick (> 600

μm) PDMS machined by punching the layer with a sharpened 100 μm i.d. puncher. Chapter 3 details the fabrication procedures, including silicon, glass and PDMS processing: in Chapter 4, the performance of two microdevices (with thick and thin PDMS) is discussed.

The following discussion first deals with microprocessing techniques relevant to fabrication of the silicon-glass device used for ESI MS protein analysis. Also discussed are other approaches used in the microfluidics community to tackle the problem of protein analysis (broadly termed proteomics). Finally, the principles behind CEC as well as microfluidics devices for on-chip CEC analysis are described.

1.2.MICROFABRICATION

Photolithographic processes producing well-defined, micrometer-scale structures were introduced by the semiconductor industry for use in integrated circuit fabrication. ATT Bell Labs developed the first transistor in 1947. Efforts to interconnect 2 to 100 transistors on one unit resulted in the integrated circuits (IC), co-invented by Noyce and Kilby. Today, technologies capable of producing submicrometer structures allow over 5 million components to be integrated into one wafer. The basic lithographic techniques used in IC production are used for processing microfluidics devices.

At the initial stage of a lithographic process, photoresist is spin-coated onto a substrate. A positive photoresist consists of a polymer which is removable by a base upon exposure to UV light. A mask is used to selectively expose the photoresist; exposed areas can then be further processed with the remaining photoresist acting as a protection layer. For a photolithographic process, the minimum theoretical feature size is:

$$B_{min} = 1.5\,[\,\lambda\,(S + Z/2\,)]^{1/2} \qquad (1.1)$$

where B_{min} is the minimum line width, λ is the wavelength of exposing light, Z is the photoresist thickness and S, the distance between the mask and the photoresist during exposure. Typically, λ is 365 nm and Z is 1.2 μm. Assuming perfect contact between the mask and substrate (i.e. S at 0 μm), the theoretical limit is 0.7 μm. Note that smaller features can be obtained using alternative lithographic techniques, such as Deep UV and e-beam lithography. For more information about both techniques, the reader is directed to Wolf's book on microchip manufacturing[15].

Typical substrates for microfluidics applications include glass and elastomers, such as polydimethylsiloxane (PDMS). For glass chips, UV-exposed areas define the channels used for fluid flow; those are etched after exposure using a strong acid solution. For PDMS chips, the processed substrate is silicon. The negative image of the final chip design is etched into the silicon wafer; PDMS is then poured onto the wafer and cured.

The final on-chip feature size will be dependant on etching type. Dry plasma etching processes can result in anisotropic etching, with features having aspect ratios of 30/1 or greater. For isotropic wet etching, the ratio is about 1/1.

1.2.1. SUBSTRATE ETCHING

Both glass and silicon can be etched in hydrofluoric acid-containing solutions. For glass:

$$SiO_{2(s)} + 6HF_{(l)} \rightarrow H_2SiF_{6(aq)} + 2H_2O_{(l)} \qquad (1.2)$$

The product is water soluble resulting in an etched glass substrate. For silicon, the etching solution contains HNO_3: nitric acid first reacts with silicon and the resulting silicon dioxide is etched by reaction with HF. Reaction 1.2 is diffusion-limited, proceeding at the same rate, R, in all directions: an isotropic etch results in a flat bottom part and curved edges of radius r. The profile is shown in Figure 1.2, for an etch time t. The isotropic etch thus limits the possible feature size on a glass substrate: two exposed, congruent areas need to be more than 20 micrometers apart for a 10 micrometer etch to be possible.

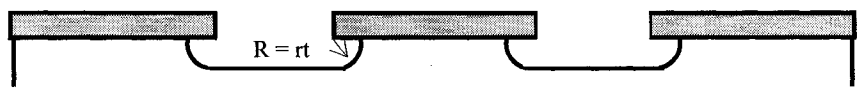

Figure 1.2 Isotropic Wet Etch Profile- Depiction of an isotropic etch proceeding at rate R in all directions. For etch time t, a curved edge of radius r results.

For a substrate to be etchable using dry plasma etching techniques, the product of the reaction between the exposed substrate and the processing gas must be volatile:

etching under plasma conditions can result in anisotropic etches. For example, silicon and quartz can be etched anisotropically using a plasma. In glass substrates, non-volatile reaction products result due to the presence of impurities, such as aluminum and iron, in the glass matrix: anisotropic dry etching of most glasses is therefore not developed.

A plasma is a partially ionized gas made of up ions, electrons, radicals and neutral species. For example, under CF_4 gas flow, different species will be present in the plasma chamber:

$$e^- + CF_4 \rightarrow CF_3^+ + F^\cdot + 2e^- \quad (1.3)$$

$$e^- + CF_4 \rightarrow CF_3^\cdot + F^\cdot + e^- \quad (1.4)$$

Ions and radicals formed will play a role in substrate etching. Under C_4F_8 gas flow, a Teflon-like "polymer" is formed on the substrate: this product is used in the Bosch etching process, explained on the next page.

The resulting profile for a plasma etching process will be anisotropic or isotropic depending on the type of reaction mechanism between the substrate and the process gas. In the first mechanism, radicals formed in the plasma will spontaneously react with the substrate's exposed surface and form a volatile by-product. For example, by using SF_6 process gas to etch silicon, $SiF_{4(g)}$ is produced, resulting in an isotropic profile, as shown in Figure 1.3a. The second mechanism is a two-step process, whereby a process gas radical first interacts with the surface, followed by release of the surface/radical pair by bombardment of process gas ions. Radicals approach the substrate from all directions, but since ions only strike the surface vertically, the result is an anisotropic etch, as shown in Figures 1.3b. Only silicon dioxide and Teflon-like polymers formed in the plasma can be etched using this mechanism.

Three different types of plasma etchers are available: barrel etcher, reactive ion etcher (RIE) and inductively coupled plasma RIE (ICP RIE). The last two will be discussed here. RIE produces both ions and radicals and, depending on the gas and substrate type, can etch according to the first or second mechanism. The main issue with this etcher is the slow etching rate due to the low ion and radical density. The RIE is, however, very versatile and can be used for processes that would contaminate the ICP RIE system.

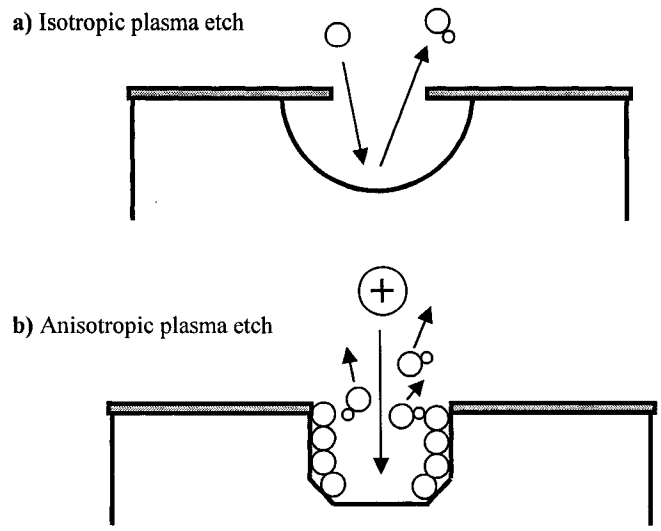

Figure 1.3 Dry Plasma Etching Mechanisms- Depiction of plasma etching mechanism resulting in a) isotropic and b) anisotropic etches. In a) radicals strike the substrate in all directions, producing volatile by-product. In b) radicals are adsorbed on the surface; ions striking the surface perpendicularly will produce volatile by-products.

By producing gas species using an ICP, a much higher gas species density is obtained. The concentration of ions and electrons is 100 times higher than in a reactive ion etcher; that of radicals, 10 times higher. The result for ICP RIE systems is a high etch rate and the possibility of deep etches (up to 500 μm).

Silicon can be etched anisotropically in an ICP RIE system using techniques involving sidewall inhibitors. Only two such techniques will be discussed here. For more information about the others, the reader is directed to Wolf's book[15]. In the first technique, cryogenic silicon etch, the process gas is a mixture of SF_6 and oxygen. The silicon therefore etches by the first mechanism; this should result in an isotropic etch. However, with the presence of oxygen species in the chamber, the byproduct of the silicon etching produces a polymer, SiO_xF_y. By keeping the substrate at -150 °C, the polymer deposits on the etched sidewall. As mentioned previously, such polymers only etch when striked vertically by ions. The sidewall inhibitor therefore protects the etched sidewall from further processing, producing an anisotropic profile. Figure 1.4a presents the SEM of a substrate etched using this technique, taken from the literature[1]. This

a) Cryogenic ICP RIE etch result

b) Bosch ICP RIE etch result

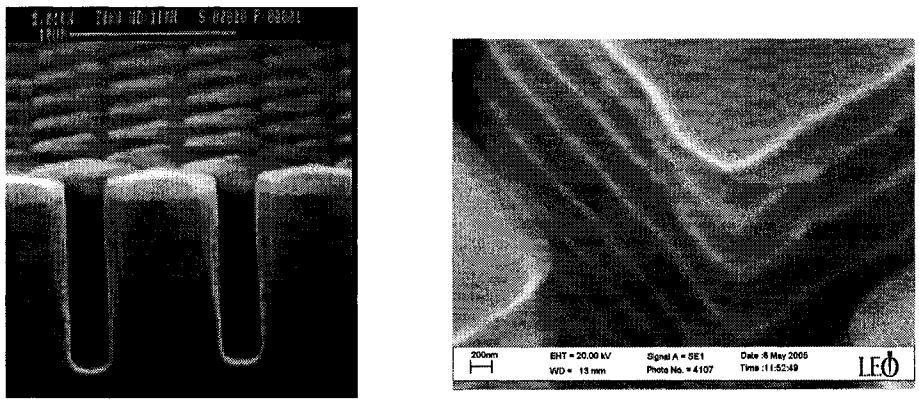

Figure 1.4 Silicon Etching Results- SEM image of a) cryogenic and b) Bosch ICP RIE etch. The cryogenic etch results in smooth side-walls, whereas the Bosch process results in stepped side-walls. Adapted from a) He et al.[1], with permission from authors.

technique produces smooth sidewalls but is, however, difficult to optimize for specific wafer features.

A technique that is easily transferable from one wafer feature to another is the Bosch process. Here again sidewall inhibitors are in use, however the etching/polymer deposition steps are decoupled. First, silicon is etched under SF_6 flow; second, polymer is deposited under C_4F_8 flow. The cycle is repeated until the target depth is reached. The overall profile for this process is anisotropic with stepped sidewall (step height varies but is usually around 0.5 μm). The SEM of a silicon substrate, presented in Chapter 3 of this thesis and etched using the Bosch technique, is shown in Figure 1.4b.

1.3.ANALYTICAL SEPARATIONS-ELECTROPHORESIS

The electric field created when a voltage is applied to a solution will move ionic species differentially according to their size-to-charge ratio. This is the main principle behind electrophoresis. In the nineteen thirties, Tiselius extracted the first principles of electrophoresis from his study of protein solutions' behavior under electric fields[16]. High efficiency separations were achieved by Jorgenson in the nineteen eighties, when he conducted electrophoretic separations in silica microcapillaries having 75 μm internal diameter[17]. In the early nineties, the concept was applied in microfluidics format by Manz et al.[7, 13, 18]

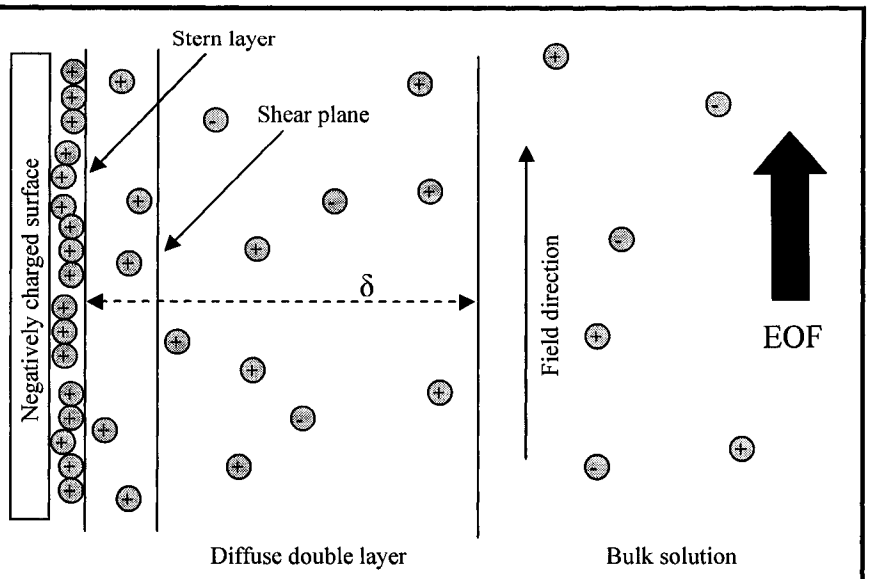

Figure 1.5 Electroosmotic Flow Definition

Capillary electrophoresis involves two concepts: bulk solution flow and differential movement of ionic species.

In Figure 1.5, a silica microcapillary is filled with buffer solution. The walls of the capillary are negatively charged, due to deprotonation of silanol groups in contact with the solution. To maintain charge balance, non-hydrated counterions (cations) in solution migrate to the wall of the capillary: these form the static Stern layer. Hydrated counterions form the next layer, also static, followed by the diffuse double layer. Both negatively- and positively-charge hydrated ions are present in the diffuse double layer, with an excess of positively-charged ions. A potential develops between the wall and the solution; the potential at the plane of shear is called the zeta potential, ζ, and decreases exponentially with distance from the plane. Upon application of a voltage, hydrated counterions at the plane of shear will move towards the negative electrode and, through viscous drag, a bulk flow towards the cathode, termed electroosmotic flow (EOF), is obtained. A main feature of EOF is that its flow profile is flat in microcapillaries (for diameters smaller than 200 μm), contributing to high separation efficiencies. Also shown in Figure 1.5 is the double layer thickness, δ, which denotes the length between the Stern layer and the point in the bulk solution where the zeta potential is 0.37 times that of the

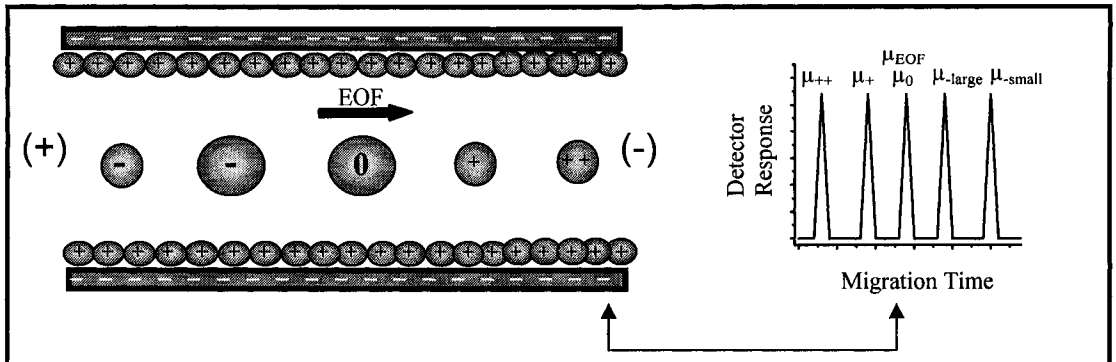

Figure 1.6 Capillary Electrophoresis- In a capillary (left) and the resulting electrochromatogram (right).

potential at the plane of shear. For example, for a 1 mM NaCl solution in water, Knox[19] calculated a δ value of 10 nm.

Superimposed on this EOF is the movement of individual ionic species in solution. Under applied voltage, positively-charged analytes will move towards the cathode, neutral analytes will move with the EOF and negatively-charged analytes will move towards the anode. The velocity of this movement depends on the amount of charge on the analyte and on its size, as shown in Figure 1.6.

Species velocity (V) during a capillary electrophoresis experiment is directly dependent on applied electric field (E):

$$V = \mu E \qquad (1.6)$$

where μ is the electrophoretic mobility. Electrophoretic mobility for the EOF is defined by:

$$\mu_{eof} = \varepsilon_o \varepsilon_r \zeta / \eta \quad (1.7)$$

where ε_o, ε_r and η are the permittivity of vacuum, dielectric constant and viscosity of the solution, respectively. For the analyte, electrophoretic mobility is:

$$\mu_e = q / 6\pi\eta r \quad (1.8)$$

where q is the ion charge and r, its radius. Adding equations 1.7 and 1.8 gives the overall mobility of an analyte, μ_a. EOF control is therefore important in CE-based separations. From equation 1.7, factors influencing μ_{eof} include: electrolyte pH and ionic strength (through ζ term), addition of organic modifier in buffer (through ε_r and η terms) and analyte adsorption on the capillary walls (through ζ term).

1.3.1. CAPILLARY ELECTROCHROMATOGRAPHY

Pretorius et al.[20] initially proposed voltage-driven separations in packed columns used for liquid chromatography (LC); the hybrid LC/CE technique was made technically feasible with the introduction of capillary electrophoresis by Jorgenson[17]. The theoretical studies of Knox and Grant on the subject established the technique in the late nineteen eigthies[19, 21]. The use of packing material in electrokinetically-driven separations, a technique called capillary electrochromatography (CEC), would expand the use of CE to include, for example, separation of neutral analytes. Also, compared to liquid chromatography (LC), CEC shows a higher inherent efficiency, making it an attractive alternative to LC. Finally, because no pressure drop would occur at the bed, smaller bead diameter could be used than those in LC, resulting in higher separation efficiencies.

As mentioned earlier, the bulk flow profile during a CE experiment is flat due to the uniformity of the charge distribution along the capillary wall. On the other hand, liquid chromatography shows a parabolic profile: friction between the pump-driven buffer and the column wall leads to a pressure drop along the column and results in a parabolic flow. This has an implication on separation efficiency. The plate height (H) is an indicator of efficiency in separation science: the smaller the plate height, the smaller the elution peak width resulting in a more efficient separation. Technically, H defines the amount of diffusion per unit length along a separation column, σ^2 / L. A simplification of the total plate height equation for a LC separation is:

$$H = H_{eddy} + H_{ld} + (H_S + H_M) \qquad (1.9)$$

or

$$H = A + B / \mu + (C_S + C_M)\,\mu \qquad (1.10)$$

Each parameter is defined in Table 1.1. H_{eddy} (A), also called Eddy diffusion, arises from the parabolic flow profile during LC separation. Individual analyte particles will move through the column at different velocities depending on the path taken, resulting in band broadening. H_{ld} (B/μ), called longitudinal diffusion, stems from the random movement of individual components about the center of the moving peak. H_S (μC_S) and H_M (μC_M) are the resistance to mass transfer in the solid and mobile phase, respectively. These two terms arise from the finite rate of transfer of the analyte in and out of the stationary and mobile phases.

Parameter	Definition
$A = 2\lambda d_p$	λ : constant, dependent on packing quality d_p : packing particle diameter
$B = 2\gamma D_M$	γ : constant, dependent on packing quality D_M: analyte mobile phase diffusion coefficient
$C_M = f_M(k')d_p^2 / D_M$	$f_S(k')$: function of retention factor
$C_S = f_S(k')d_f^2 / D_S$	d_f : packing particle film thickness D_S: analyte solid phase diffusion coefficient $f_M(k')$: function of retention factor

Table 1.1 Plate Height Parameters

In a CEC experiment, the flat flow profile implies uniform velocity in all flow paths taken through the column; the Eddy diffusion term is therefore minimized. Figure 1.7, taken from a publication by Dittman et al.[3] illustrates this point.

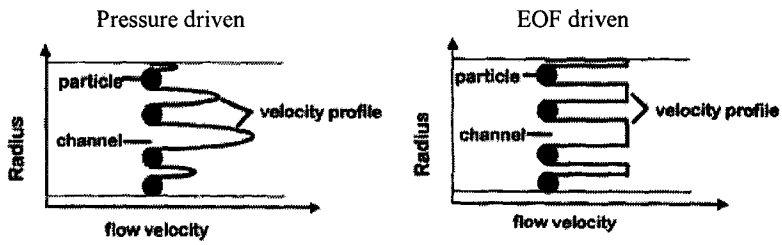

Figure 1.7 LC versus CEC Flow Profile- For a capillary filled with particles, the flat flow profile in voltage-driven separations (right), compared to pressure-driven systems (left), result in equal velocity along the capillary, minimizing Eddy diffusion. Adapted from Dittman et al.[3], with permission from Elsevier.

Plotting overall plate height versus linear velocity results in a van Deemter plot, a useful diagnostic tool used in separation science to pinpoint the source of band broadening. A theoretical van Deemter plot for a column under LC versus CEC flow was produced by Dittman et al.[3] The theoretical column had 5 μm diameter particles. The results, presented in Figure 1.8, clearly show the advantage of the CEC-based separation.

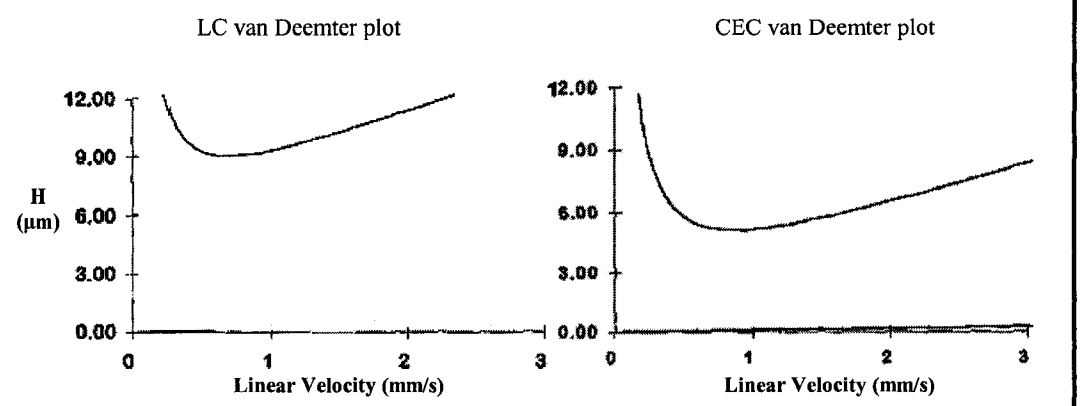

Figure 1.8 LC versus CEC van Deemter Plot- Theoretical plot showing the lower plate height resulting in capillary electrochromatography (right) compared to liquid chromatography separations (left). Adapted from Dittman et al.[3], with permission from Elsevier.

The higher efficiency translates into higher resolving power and peak capacities. Resolution is defined in equation 1.10:

$$R_S = \frac{1}{4} [k' / (1+k')] [(\alpha-1) / \alpha] N^{1/2} \qquad (1.10)$$

$$N = L / H \qquad (1.11)$$

where k' is the capacity factor, α is the selectivity, N, the number of theoretical plates and L, the column length. Peak capacity, i.e. the number of resolvable peaks for a separation, is:

$$n = L / W \qquad (1.12)$$

where L is the length of the separation channel and W, the average width of the eluting peak (4σ or full width at half maximum). The peak capacity is also proportional to $N^{1/2}$. Therefore, the decrease in plate height results in an increased resolution and peak capacity for CEC-based separations.

1.3.2. EOF IN CEC

As shown in Figure 1.8, the best efficiency for a column is obtained at a set linear velocity; control of electroosmotic flow is therefore an important component of CEC separations. In section 1.3, factors influencing μ_{eof} in CE were enumerated. In CEC, the presence of packing material will also affect EOF velocity. For a column packed with uncharged particles, Overbeek[22] predicted a decrease in average EOF velocity

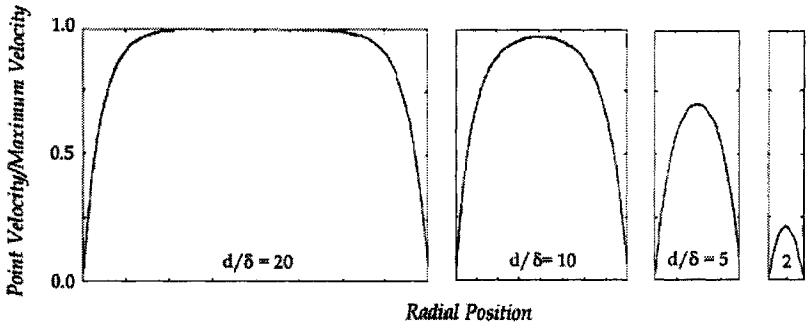

Figure 1.9 Theoretical EOF Profile- Smaller d/δ values result in a reduction of EOF velocity. Adapted from Li et al.[2], with permission from authors.

proportional to the ratio of particle diameter-to-capillary radius due to the resistance from the packed section. For charged particles, however, the surface develops an electrical double layer and the particles can support electroosmotic flow, maintaining EOF velocity through the packed region. If the double layer of two nearby, charged surfaces overlaps, the electroosmotic flow becomes distorted, resulting in a quasi-parabolic profile. Figure 1.9 presents a theoretical plot of EOF velocity versus d/δ, the ratio of diameter-to-double layer thickness, taken from Li et al.[2]: as the capillary diameter decreases, the double layers overlap, leading to a decrease in EOF velocity. At the extreme, no flow will be produced. The question then arises about the flow profile in the interstitial space, since a reduction in flow velocity between charged particles would have an affect on separation efficiency. The interstitial space for packed columns is about ¼ of the particle diameter; for 3 or 5 μm particles usually used in CEC, this space is larger than the double layer thickness. The EOF profile is sustained in the interstitial space and can therefore be described as before, in Figure 1.7. The double layer overlap can, however, affect pore flow. Li et al.[2] tested different pore sizes for CEC on reversed-phase columns and found a net effect on plate height, as shown in Figure 1.10, taken from their publication. From the plots of plate height versus linear velocity at different pore sizes, an increase in H was observed at smaller pore sizes: no significant change in efficiency was observed for 10, 30 and 50 nm, indicating that no perfusive flow existed. A clear effect on efficiency was seen for 100 and 400 nm pore sizes: through-pore flow was allowed, leading to a

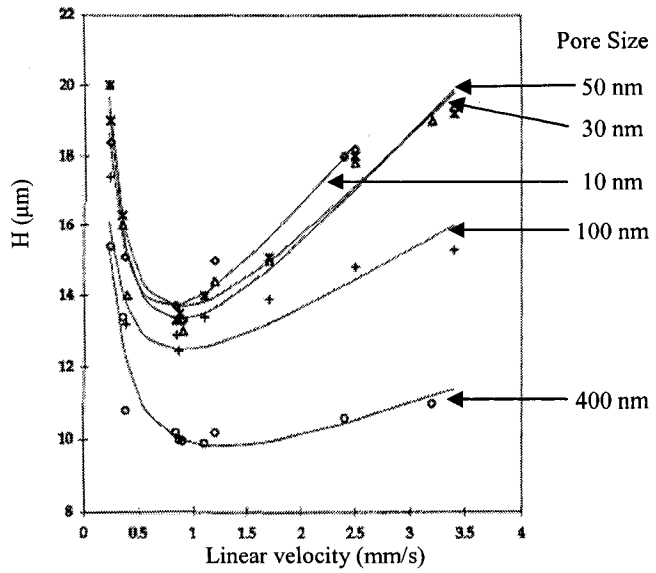

Figure 1.10 Effect of EOF Profile on Plate Height- Higher plate heights are observed for CEC in small pore size. Adapted from Li et al.[2], with permission from authors.

decrease in effective particle diameter size and therefore to a decrease in Eddy diffusion. Perfusive flow also decreased diffusion due to slow analyte transfer to and from the stagnant mobile phase in the pores. The 400 nm pore size maximized efficiency because a larger fraction of pores were wide enough to support EOF compared to the 100 nm size.

1.3.3. CEC IN MICROFLUIDICS

On-chip capillary electrochromatography has been implemented using three different techniques: open-channel, packed-bed and monolithic column CEC. In the first technique, a stationary phase is attached to the channel walls. In packed-channel CEC, part of the chip is packed with commercially-available chromatographic beads. Monolithic column CEC includes both microchips with lithographically-defined columns and polymer-based monoliths.

The first on-chip CEC system, published by Jacobson et al., used the open-channel technique: the glass microchip channels were derivatized with octadecylsilyl (C18) for reversed-phase CEC of three neutral dyes[23]. Improvements in stationary phase coating and chip design led to studies of more complicated samples, including β-casein

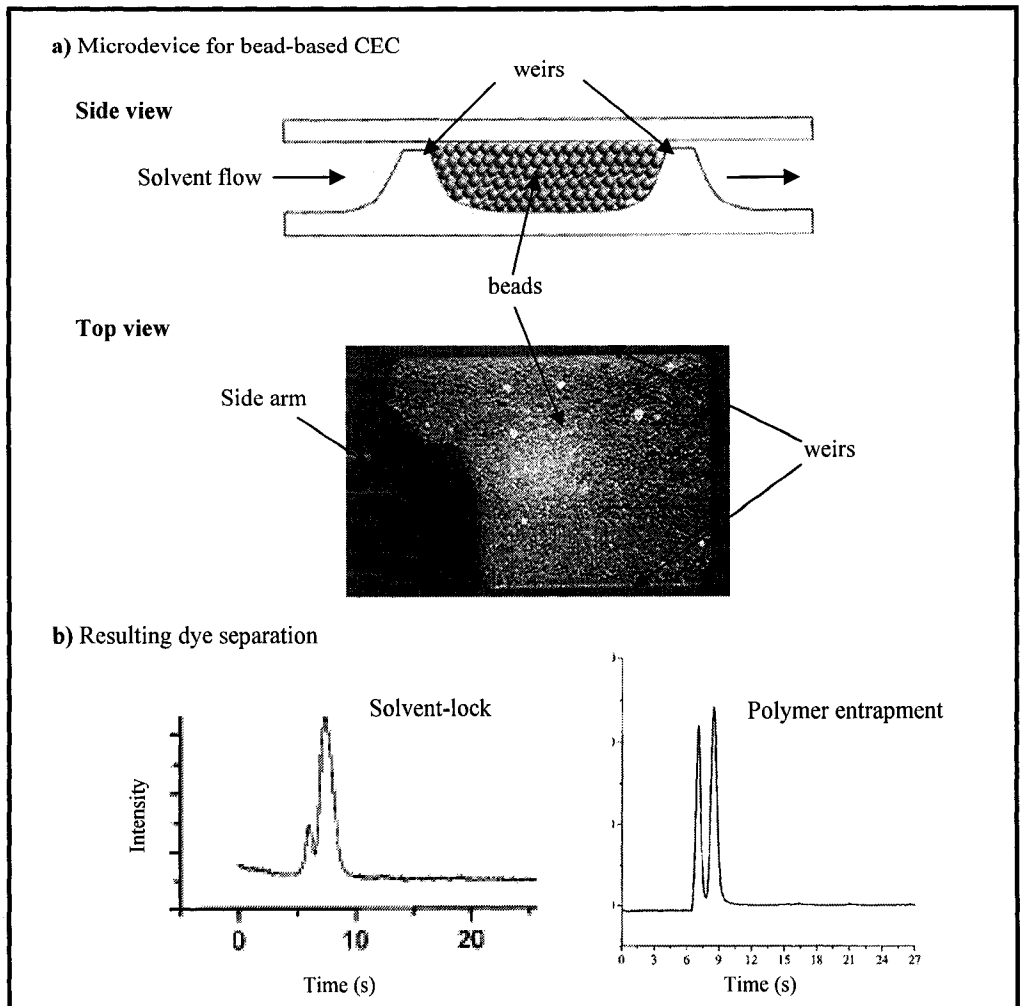

Figure 1.11 Microfluidics Device for Packed Bed CEC- a) Design and picture of the bed section of a microdevice for RP CEC; b) resulting separation of two dyes for solvent-lock system (bottom left) and polymer entrapment (bottom right) techniques. Adapted from Oleschuk et al.[4] and Jemere et al.[8]

tryptic digest, DNA fragments and polycyclic aromatic hydrocarbons (PAHs). The effect of channel coating on EOF velocity was also studied; for a C18 stationary phase on glass channels, a decrease by 10-25% was observed. An interesting example was published by Xu et al. using a polyester microchip: the authors chose a reagent to act as a stationary phase (here, 10-undecen-1-ol) and copolymerized it with the bulk material to form the microchip[24, 25]. This then allowed the surface chemistry to be built-in the chip without extra derivatization procedure.

Because the stationary phase is only present at the walls, a small channel diameter must be used in open-channel CEC for sufficient analyte/stationary phase interaction, leading to channel plugging. Also, the small amount of stationary phase available drastically limits the sample load. The use of beads alleviates these problems. Oleschuck et al.[4] introduced a bead packing technique on glass microchip, presented in Figure 1.11a. The device consists of 10 μm deep channels with two 1 μm deep weirs. The 1.5 μm diameter reverse-phase beads are packed through a side-arm and retained within the 200 μm length column by the two weirs. Bead-packing proceeded using a combination of voltage and negative pressure flow. The 1 μm gap between the weir and cover plate allow for fluid flow along the separation channel. To keep the beads from migrating back into the side-arm upon application of voltage, a "solvent-lock" mechanism was used: after bead-packing in acetonitrile, the side-arm was filled with an aqueous buffer, preventing bead backflow by inducing bead aggregation. Two dyes, BODIPY (0 charge) and fluorescein (-1 charge), were separated in under 20 seconds with the BODIPY eluting last, as expected for reverse-phase CEC. Jemere et al.[8] used polymer entrapment to prevent bead backflow: after packing, a monomer solution was flowed into the side-arm up to, but not into, the bed and polymerized by UV exposure. This led to higher bed efficiency and peak resolution, as shown in Figure 1.11b, for the separation of BODIPY and acridine orange (both 0 charge, BODIPY eluted first). However, the small column length of this device did not allow for high peak capacities; longer columns were prepared for reverse-phase CEC on 1, 2 and 5 mm length beds[14]. Three fluorescent dyes were successfully separated in the 1 and 2 mm columns. Difficulties packing the 5 mm channel led to large voids in the column and no separation was possible at this bed length. Chapter 2 describes the use of such a system for strong cation exchange (SCX) capillary electrochromatography separation of peptides on a 2 mm length column.

Other packed-bed microfluidics systems were built using different bead confinement methods. Ro et al. fabricated PDMS microchips with built-in frits for reverse-phase CEC of two coumarin dyes[26]. However, due to the poor EOF behavior of PDMS surfaces, poor efficiencies were obtained. Ceriotti et al. used microchannels with tapered ends (70 μm width column tapered to 16 μm) for entrapment on a hybrid glass-

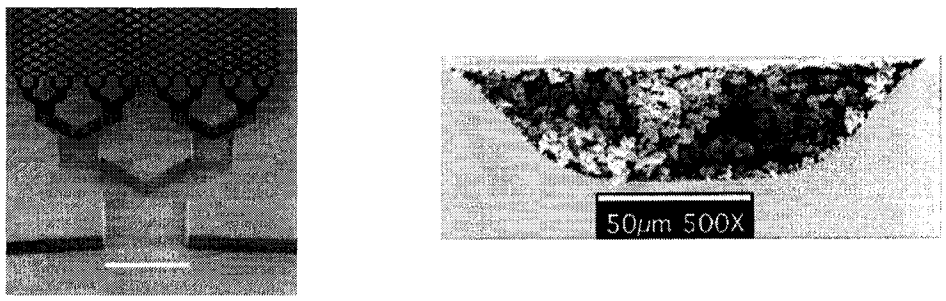

Figure 1.12 Monolithic Columns for On-Chip CEC- Microfabricated monolith on a) quartz substrate and b) in-situ polymerized monoliths. Adapted from a) He et al.[1] and b) Throckmorton et al.[10], with permission from authors.

PDMS microchip device[27]. The device could separate four fluorescently-labeled amino acids within 50 seconds.

Difficulties in packing long columns on-chip lead to low separation efficiencies and peak capacities. Monoliths, either built-in or derivatized in-situ, have the advantage of having long-range homogeneity. The Regnier group constructed a lithographically-defined column on quartz for reverse-phase CEC of a dye and fluorescently labeled ovalbumin digest[1, 28]. The device, shown in Figure 1.12a, consisted of a 4.5 cm long column with 5 μm square posts 1.5 μm apart, etched down 10 μm using cryogenic ICP RIE, coated with a C18 stationary phase. The quartz microdevice being costly, PDMS devices were used for further experiments probing surface derivatization methodology and post geometries[29-31].

In-situ derivatization of polymer monoliths has become the method of choice for on-chip CEC. Fabricating a monolithic column in microchannels is simple: a solution composed of a monomer, cross-linker, porogenic solvent and UV radical initiator is flushed into the microchip. The area where the bed is to be fabricated is UV-irradiated, with the rest of the device masked. After exposure, excess solution is washed away; the SEM of the cross-section of a glass device microchannel containing such polymer monolith is shown Figure 1.12b. The basic method is simple, however tailoring the bed chemistry and particle dimension reproducibly is difficult. Many studies have been published for on-chip CEC using polymer monoliths, only a few will be mentioned here.

For more information, the reader is directed to Pumera's review on the subject[11] and Hilder's review of monolith fabrication for conventional CEC applications[32].

The first on chip photoinitiated polymer monolith for CEC applications was published by Ngola et al.[33] In their work, they conducted an extensive study of the influence of monomer chemistry on the reverse-phase CEC behavior in silica capillaries for the separation of benzene derivatives and further demonstrated on-chip CEC separation of three fluorescently-labeled polycyclic aromatic hydrocarbons on quartz microdevices. Lazar et al. used the polymer monolith method for on-chip CEC of a digested protein with electrospray ionization (ESI) mass spectrometric (MS) detection[34]. No PDMS-based CEC publications have been found using polymer monoliths. It was found that polymerization in native PDMS microdevices results in a nonporous gel; two possible explanations were given to explain this. First, the PDMS is permeable to oxygen, a radical polymerization quencher. Second, the PDMS surface adsorbs the monomer solution and a gel results. Bedair et al. did produce a polymer monolith on a PDMS chip for use as an ESI emitter[35].

1.3.4. STRONG CATION EXCHANGE CEC

In ion exchange chromatography, the packing material contains fixed charged sites; analytes having opposite charges interact with the column and separate according to charge. For a cation exchange material R^- interacting with an analyte B^+ or C^{+2} :

$$(R^-A^+)_R + B^+ \leftrightarrow (R^-B^+)_R + A^+ \qquad (1.13)$$

$$2(R^-A^+)_R + C^{+2} \leftrightarrow (R_2^-C^{+2})_R + 2A^+ \qquad (1.14)$$

where A^+ is a counter-ion from the buffer solution. $(R^-A^+)_R$, $(R^-B^+)_R$ and $(R_2^-C^{+2})_R$ indicate A^+, B^+ and C^{+2} in the cation exchange resin R. Typical cation exchangers include sulfonated resins (strong cation exchanger, SCX) and resins containing carboxylate groups (weak cation exchanger, WCX). The equilibrium constants for equation 1.13 and 1.14 are:

$$K_{AtoB} = [R^-B^+]_R [A^+] / [R^-A^+]_R [B^+] \qquad (1.15)$$

$$K_{AtoC} = [R_2^-C^{+2}]_R [A^+]^2 / [R^-A^+]_R^2 [C^{+2}] \qquad (1.16)$$

The degree of interaction between an analyte and the packing material is defined by k, the distribution coefficient:

$$k = C_S / C_M \qquad (1.17)$$

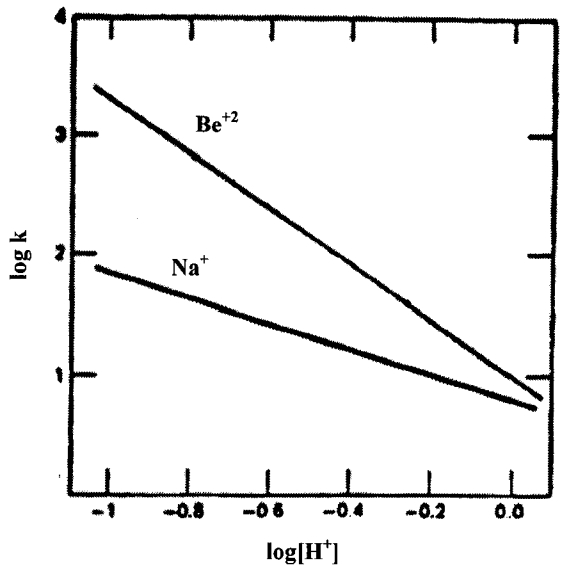

Figure 1.13 Effect of Charge on Elution in LC SCX- For a singly-charged analyte (Na^+), the log of the distribution coefficient, k, is proportional to the log of the concentration of eluent, $[H^+]$. For doubly-charged analyte (Be^{+2}), it is proportional to $2\log[H^+]$.

where C_S and C_M are the concentration of analyte in the stationary and mobile phases, respectively. Two analytes with different k values lead to different retention on the column, i.e. to separation. The distribution coefficient for analytes B^+ and C^{+2} in terms of their equilibrium constant:

$$k_B = [R^-B^+]_R / [B^+] = K_{AtoB} [R^-A^+]_R / [A^+] \quad (1.18)$$

$$k_C = [R_2^-C^{+2}]_R / [C^{+2}] = K_{AtoC} [R^-A^+]_R^2 / [A^+]^2 \quad (1.19)$$

Under trace conditions, i.e. $[A^+] >> [B^+]$ and $[A^+] >> [C^{+2}]$:

$$\log k_B \alpha -\log[A^+] \quad (1.20)$$

$$\log k_C \alpha -2\log[A^+] \quad (1.21)$$

The effect of eluent concentration (in this case H^+) on the distribution coefficient of two analytes (Be^{+2} and Na^+) is shown in Figure 1.13. The elution of a compound will therefore be affected by the analyte charge and counter-ion concentration in the mobile phase.

For EOF-driven cation exchange separations, the relationship is not as straightforward. Analyte charge will affect both residence time on the column and

electrophoretic mobility, μ_e; mobile phase counter-ion concentration will affect both interaction with the ion-exchange bed and EOF mobility, μ_{eof}. Also, the negative charges on the packing material allow EOF to develop on the separation bed. This is true at all pH for a strong cation exchanger like SO_3^-, for a weak cation exchanger like COOH, the pH of the solution will affect on-bed EOF.

A demonstration of SCX CEC has been shown on-chip by Ericson et al. using polymer monolith. The column was primarily reverse-phase (RP); SO_3^- groups were used in the polymer matrix to maintain EOF on the bed. The experiments involved a monolith made of isopropyl groups (C_3) and a small percentage of sulfonic acid groups for reverse-phase separation of alkylphenones in a quartz chip at pH 2.5[36]. At this pH, no EOF would be present in a CE separation; however, with the presence of sulfonate groups throughout the columns, a CEC separation was possible. The authors also used the device under true SCX CEC conditions: two positively-charged antidepressant drugs were separated in 10 minutes. The separation was driven by a combination of ion-exchange chromatography and difference in electrophoretic mobility. Several demonstrations of SCX CEC have been shown in conventional silica capillaries, for more the reader is directed to a review on CEC of peptides and proteins by Bandilla et al.[37]

1.3.5. LASER-INDUCED FLUORESCENCE DETECTION

Detection systems for on-chip CEC include UV, mass spectrometry (MS) and laser-induced fluorescence (LIF)[11]. Compared to UV and MS detection, LIF provides low detection limits and is easily coupled to the chip system. The main drawback of the technique is the need to derivatize the analytes with a fluorophore. This leads to differentially-labeled samples and multiply-derivatized analytes, which changes the CEC behavior. Some analytes, such as proteins containing aromatic amino acids, show native fluorescence; however, Misir[38] showed that the native laser-induced fluorescence detection scheme results in high detection limits.

The detection system for on-chip LIF detection is shown in Figure 1.14; the following discussion is with respect to the detection system used for the chip SCX CEC study presented in chapter 2. The microdevice (A) sits on top of an inverted microscope. A laser beam (C, Argon ion laser, 488 nm) enters the microscope, hits a dichroic mirror (D) which directs and focuses it on the chip microchannel (A). An analyte derivatized

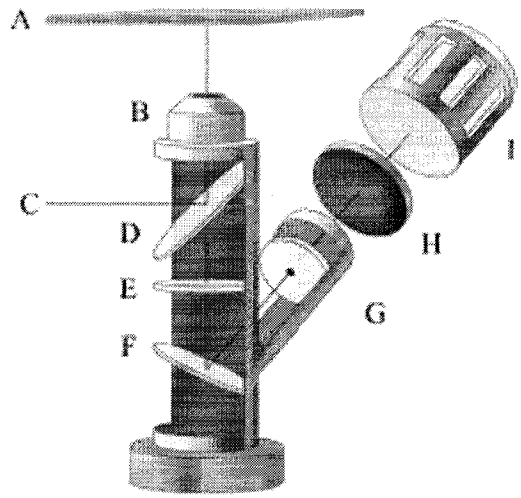

Figure 1.14 LIF Detection- A- microdevice, B- objective, C- argon ion laser, D- dichroic mirror, E- tube lens, F- mirror, G- pinhole, H- emission filter, I- photomultiplier tube.

with fluorescein (FITC, excitation at 494 nm, emission at 518 nm) will fluoresce; the resulting fluorescence is collected through the high numerical aperture objective (B, 40x, 0.6 N.A.), focused by the tube lens (E) and redirected by a mirror (F) to form an image at the pinhole (G, 400 μm). The image is filtered by an emission filter (H) and collected by the photomultiplier tube (I). Both the dichroic mirror and emission filter are used to filter out fluorescence from the laser beam, reducing background noise. The dichroic reflects light at 488 nm and transmits at 518 nm, while the emission filter transmits between 510-540 nm. Two other factors make this system highly efficient: the high N.A. objective allows for small detection volumes to be detected with high efficiencies and the pinhole at the image plane selects which slice of the microchannel volume will be detected, rejecting scattered or reflected light from the microchannel walls. This confocal epifluorescent detection scheme reduces background noise and improves detection limits to the femtomolar range[39].

1.4.PROTEOMICS

Proteomics is concerned with the identification and quantification of all proteins, their functionality, interactions, location and modifications in the healthy and diseased state. The sheer number of proteins found in, for example, a human tissue (over 10,000)

and the large dynamic range they cover (over 10 orders of magnitude) make for a daunting task. The conventional (and to date most successful) analytical approach to complex protein sample analysis is two-dimensional gel electrophoresis (2D-GE) coupled to mass spectrometry.

2D-GE involves two orthogonal separations: isoelectric focusing (IEF) followed by sodium dodecyl sulfate polyacrylamide gel electrophoresis (SDS-PAGE). In the first dimension, a voltage is applied across a polyacrylamide gel containing ampholite molecules. Ampholites being zwitterions, i.e. contain both acidic and basic moieties, a pH gradient is established along the polyacrylamide gel. A charged protein mixture sitting at one end of the gel will migrate upon applying an electric field, as discussed in section 1.3. A specific protein will stop its movement when entering the pH region in the gel where its net charge is zero, i.e. when section pH equals protein pI. Protein separation is usually obtained in 1-2 hours. In the second dimension, the polyacrylamide gel contains SDS, which results in all proteins having similar charge. The gel is a sieving matrix: when a voltage is applied, the larger proteins will move slower than the smaller ones, and a size-dependant separation is obtained. The second separation takes between 6 to 24 hours. Staining is used for visualization of the protein spots: different stains are available, for example silver stain can achieve detection limits down to 10^{-10} M. An example of 2D-GE from a sample of plasma proteins, taken from the EXPASY databank (//ca.expasy.org/ch2d/), is shown in Figure 1.15a (only the acidic proteins are shown). A review of the technique is available[40].

For protein identification, the spots are individually excised, enzyme-digested, purified, concentrated and analyzed by a mass spectrometric method, either electrospray ionization (ESI) or Matrix-Assisted Laser Desorption Ionization (MALDI). Enzyme digestion results in the protein's unique peptide map; trypsin is a commonly used enzyme for protein digestion due to its high cleaving specificity. The peptides detected during MS analysis are entered in a computer database (for example, Swiss-Prot); the protein corresponding to the peptide MS fingerprint can then be identified. Although widely used, this multi-step approach to protein analysis has several shortfalls including: time-consuming (and therefore expensive) analysis, difficulties in automating the 2D-GE step,

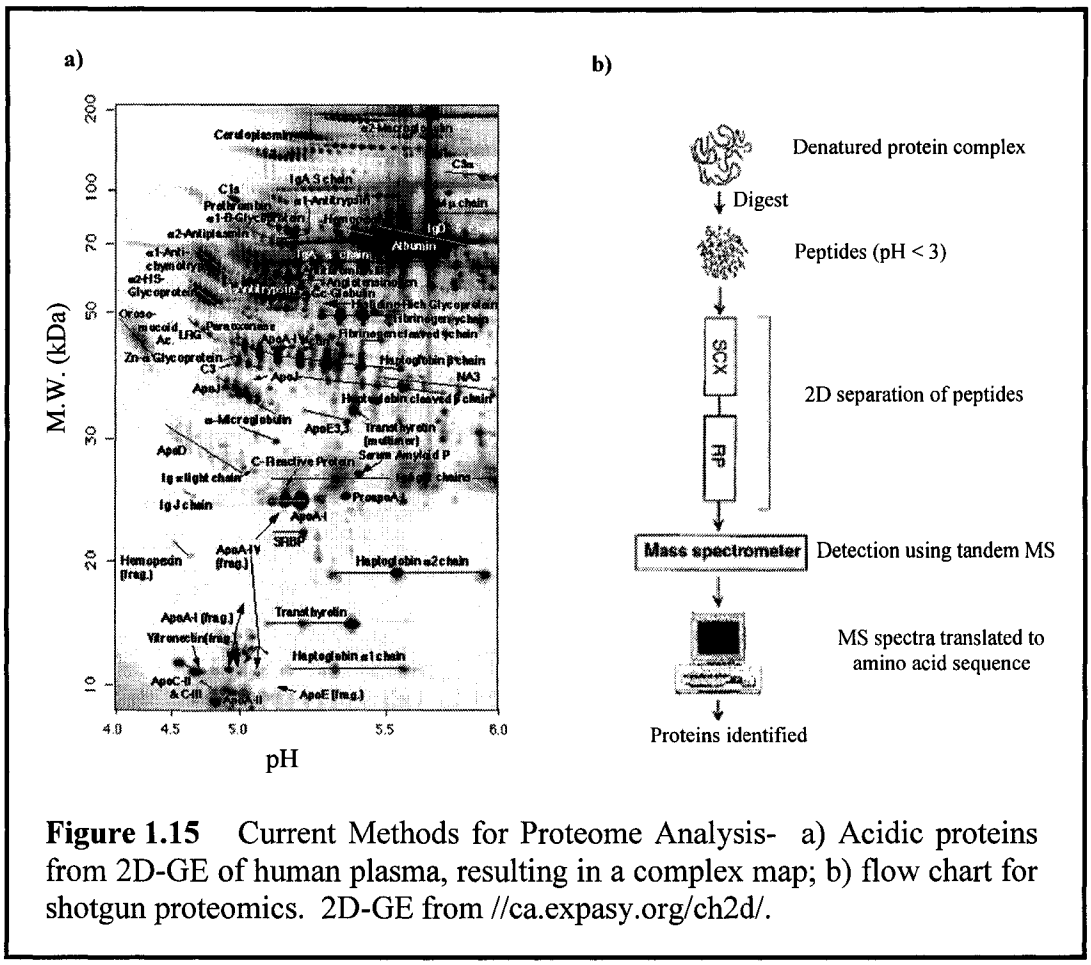

Figure 1.15 Current Methods for Proteome Analysis- a) Acidic proteins from 2D-GE of human plasma, resulting in a complex map; b) flow chart for shotgun proteomics. 2D-GE from //ca.expasy.org/ch2d/.

detection of mainly the most abundant proteins in the gel, and the difficulty in obtaining proteins at extreme molecular weight and pH values from the 2D-GE[40].

A method pioneered by the Yates group[41-43], called shotgun proteomics, avoids the 2D-GE step. First, the complete sample is digested. This is followed by peptides purification and concentration. The peptides are then run though a two-column LC system (SCX followed by RP) and analyzed by MS. Figure 1.15b presents a schematic of the technique[43]. Although the time-consuming 2D-GE step is not used in this approach, eluting peptides must be analyzed using a combination of tandem MS and complex protein database searches (called SEQUEST). Also, several pre-LC purification steps are needed, leading again to long analysis times. Still, the method was successfully used by Yates to detect and identify 1,484 proteins from yeast[43]. Developments in microfluidics for proteome analysis aim to circumvent problems related to both described approaches.

1.4.1. MICROFLUIDICS IN PROTEOMICS

Several reports have described the use of microdevices for proteome analysis; a complete review is out of the scope of this thesis and several reviews are available[44-47]. The article by Friere and Wheeler[47] on the advances made and challenges faced by the microfluidics community in producing what they call a "proteome-on-a-chip" outlines four critical areas for on-chip proteomics research, namely 1) chemical processing (for example, enzyme digestion), 2) sample preconcentration and cleanup, 3) separation and 4) MS interface fabrication. Discussed here is the third aspect, separations, focusing on two-dimensional separations and chip-to-MS systems.

1.4.1.1. ON-CHIP TWO-DIMENSIONAL SEPARATIONS

For microfluidics to be widely applicable in proteome analysis, high peak capacity methods for protein or peptides separation must be devised. A standard 2D gel can detect between 1,000 and 3,000 proteins[48]; up to 9,000 proteins have been detected in larger gel formats[49]. Microfludics applications must at least equal if not surpass this benchmark. Methods for on-chip high peak capacity separations have been attempted in two forms mirroring the two approaches discussed before: shotgun and 2D-GE separations.

The Ramsey group has published studies on two-dimensional systems, coupling open-channel CEC[50] or micellar electrokinetic chromatography (MEKC)[51, 52] in the first dimension to CE in the second. The MEKC-CE analysis of the fluorescently-labeled tryptic digest of a protein produced peak capacities for the system of 4,200[52]. Considering that the high peak capacity observed in 2D-GE is due to the high resolutions achieved in the first IEF dimension, approaches have been studied to couple on-chip IEF with a second separation. Whiteside's approach used two physically isolated PDMS chips: the first consisted of a single channel for in-gel IEF and the second, an array of 11 channels for CE separation. After IEF separation, the two chips were brought in contact and the CE separation ran[53]. In Han's microdevice, the two dimensions were physically isolated by a microfuidic valve system in PDMS[54]. An approach combining IEF and SDS gel electrophoresis was presented for the multidimensional detection of *E. coli* cell lysate: an IEF channel overlaid on an array of 10 to 32 parallel channels in polycarbonate chips was used[55, 56]. Herr et al. developed a simple T-junction geometry for solution-phase IEF-CE[57]. The IEF was conducted in the first channel and fractions intermittently

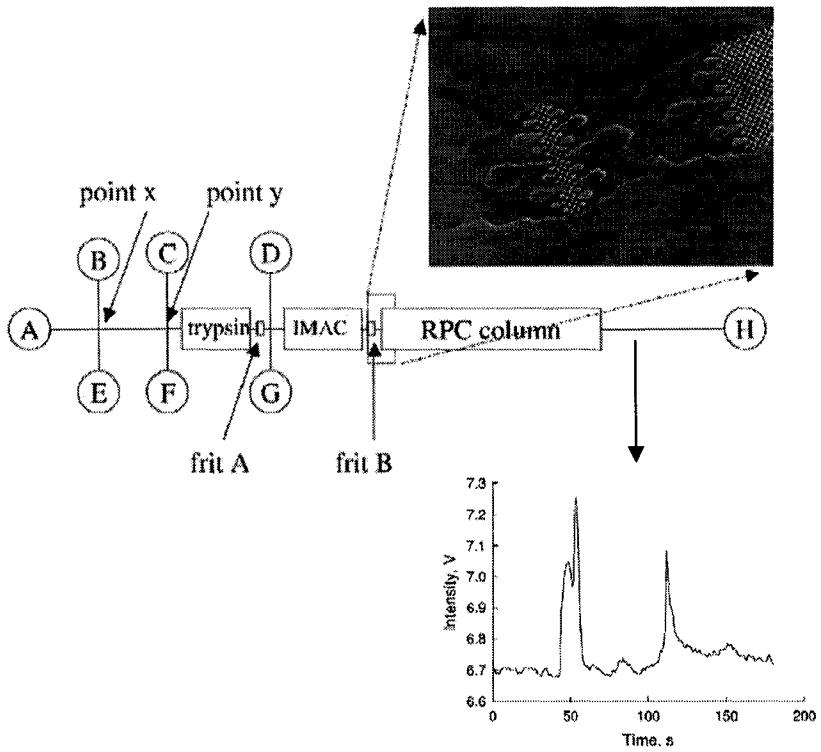

Figure 1.16 Multicolumn Microdevice for Protein Processing- Depiction (top) and SEM (top right) of the microdevice with the resulting fluorescence detection of BSA (bottom) after digestion through the trypsin bed, affinity trapping and CEC through the microfabricated reverse-phase column. Adapted from Slentz et al.[5], with permission with permission from authors.

injected in the second channel for CE in the second dimension, giving an estimated peak capacity of 1,300. While impressive, the main issue with the systems presented is that all used fluorescence detection; no direct MS coupling would be possible.

The Regnier group presented a multicolumn device for protein processing based on their micromachined bed system discussed in section 1.3.3. (see Figure 1.12a)[5]. The system is shown in Figure 1.16. The microdevice is made in PDMS, frits A and B are used to trap the trypsin-derivatized beads and copper(II)-immobilized metal affinity chromatographic (IMAC) beads, respectively. The reverse-phase column (RPC) was micromachined, as shown in the SEM image. Fluorescently-labeled BSA was then driven electrophoretically through the trypsin bed for enzyme digestion; through the IMAC bed for affinity trapping of histidine-containing peptides and; through the RPC

bed for CEC of the trapped peptides. The resulting fluorescence electrochromatograph is shown.

1.4.1.2. CHIP-TO-MS SYSTEMS

Coupling of conventional separation methods with mass spectrometric analysis has proven to be the most successful approach for protein identification of a complex sample. It then follows that microfluidics-to-MS coupling could prove to be a viable method for complex protein sample analysis: all sample treatment would be automated on-chip, followed mass spectrometric identification. Although methods involving MALDI MS detection have been described[58-68], microfluidics-to-MALDI MS coupling is laborious. Several ESI MS couplings have been described: spraying directly from the microdevice channel[35, 69-74], spaying from a tapered capillary tip[75-81] and spraying from micromachined tips[82-90]. A review is available[91]. In the following discussion, one example of MALDI MS will be described; the rest will focus on ESI MS methods.

Ekstrom et al. introduced a silicon-based microdevice for MALDI MS analysis in 2001[92]. The device consisted of 32 parallel silicon microchannels coated with trypsin; the microstructures led to a micromachined silicon opening used for piezo-actuated MALDI plate spotting. A protein would be flowed through the silicon microdevice, where it would be digested, and be directly spotted onto a MALDI plate for further MS analysis. This research led to their introduction in 2006 of silicon-based nanovials for use as MALDI plates[93].

A mass spectrometer will detect ions in the gas phase: in ESI MS, a liquid sample is vaporized by applying a voltage between the conductive tube delivering the sample and the MS entrance. The ESI process will be stable, and continuous MS detection will therefore be possible, for a range of flow rates and tube diameters. The MS flow rate range, nl/min to μl/min, is compatible with microfluidics flow rates: their coupling was inevitable. The first microdevice-to-MS coupling was published by Xu et al. in 1997[70] by direct spraying from the exposed edge of the microchannel. However, wetting at the edge reduced ESI efficiency and overall performance. By inserting a gold-coated, tapered microcapillary tip at the exposed edge, detection limits were improved to the low attomole range for peptide detection in glass[76] and PDMS[77] microdevices. Several microsystems were devised for multiplexed analyte detection using ESI MS[79, 94-96].

Zhang et al. interfaced a microdevice with a 96-well plate for automated sample introduction[79]. The microdevice was fitted with an emitter for ESI MS detection. The sample from one well was automatically loaded into the microdevice and CE-MS was conducted; the microtiter plate then moved position, another well sample was introduced into the microdevice for CE-MS, etc. for all wells position. Liu et al. presented the use of a microdevice fitted with multiple ESI emitters for pressure-driven multiplexed detection of peptides[95]. Another multiplexed microfluidic system was published by Figeys et al.[94]; multiple channels were etched in a microdevice, all meeting at one outlet. The outlet was fitted with a microcapillary emitter: applying a voltage sequentially from one channel to the next, CE-MS was conducted on BSA and myoglobin tryptic digests (digestion conducted off-chip). Finally, Tan et al. developed an array of eight microchannels, each containing a UV-initiated polymer monolith for on-chip solid phase extraction of peptides[96]. The microdevice was fitted with eight microcapillary tips for ESI MS. While effective ESI emitters, tapered capillary tips have one major drawback: coupling to a microdevice is time consuming. As mentioned before, several strategies for micofabricating ESI tips have been proposed. An interesting example comes from Agilent Technologies which has marketed a plastic microdevice for peptide analysis. The microsystem is composed of three on-chip components: a sample enrichment loop, bead-based liquid chromatography column and ESI emitter[84, 97-100].

On-chip protein digestion was first demonstrated by Xue et al.[101]: a solution of trypsin and mellitin were mixed in the microdevice's entrance reservoir and infused for ESI MS detection. Wang et al.[9] improved the digestion efficiency by incorporating trypsin beads in glass microchannels, as shown in Figure 1.17. The device was fitted with a pulled microcapillary tip and used for on-chip BSA digestion, followed by CE-ESI MS of the resulting peptide fragments. Further development led to a two-bed microfluidic system: trypsin digestion beads were used for on-chip digestion followed by reverse-phase beads for solid phase extraction (SPE) of the eluting peptides. CE-MS was then conducted in high organic buffer solution for peptide elution off the SPE bed[102].

Taylor proposed a multiplexed microdevice for protein analysis based on Wang's two-bed system[6]. The platform is shown in Figure 1.18. The microdevice's entry point is coupled to a microcapillary and the exit, to a pulled microcapillary for on-line MS

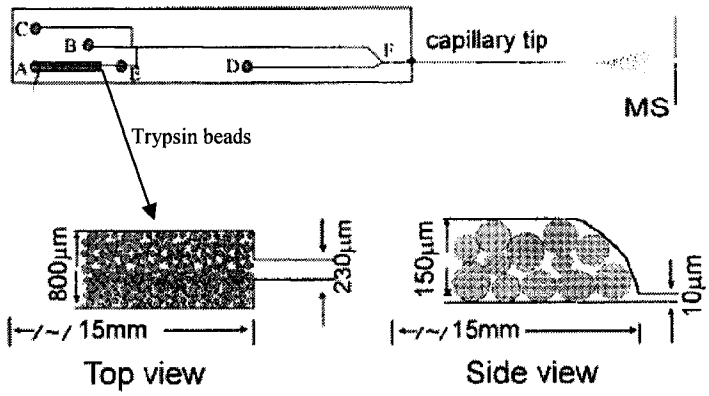

Figure 1.17 On-Chip Digestion/CE/ESI MS System- Depiction of the microdevice (top) with both top and side-view of the trypsin bed region (bottom). Adapted from Wang et al.[9]

detection. The glass chip contains 20 microchannels: each contains the two beds mentioned above, the first for trypsin digestion and second for solid phase extraction. SPE-to-MS microchannel length increases by 0.5 cm from channel-to-channel (called Delay Lines in Figure 1.18). Each microchannel is fitted with an electrode inserted through a septum, as shown in the inset. A protein mixture introduced into the capillary is first separated by isoelectric focusing followed by sequential grounding of the electrodes to drive each protein fraction into one of the 20 channels on the fluidic device. A syringe pump is then used to drive the fractions through the trypsin-immobilized beds, where proteins are digested; the SPE beds trap the resulting peptides. Upon elution from the SPE beds using high organic content buffer, peptides travel down the microchannel towards the mass spectrometer for the final mass-to-charge analysis. As the SPE-to-MS length increases by 0.5 cm from channel-to-channel, peptides eluting from the shortest microchannel will be detected first by the MS, followed by the second shortest channel, etc. up to the 20^{th} channel. This delay line allows sequential MS analysis of peptides fractions, each corresponding to an IEF-fractionated protein.

In designing this platform, it was assumed that the resistance in each microchannel would be a function of SPE-to-MS length, and sequential elution would result. However, resistance is controlled by the trypsin-immobilized and SPE beds. Due

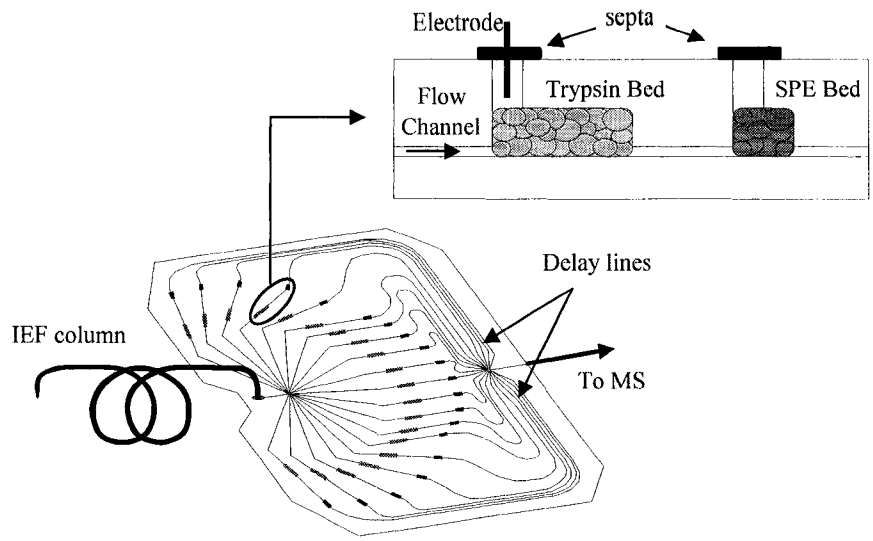

Figure 1.18 Microfluidics Platform for Multiplexed Protein Analysis- The complete platform (bottom) and side-view of one of the 20 microchannel (top) is depicted. After initial capillary IEF, sequential grounding of the electrode drives protein fractions into separate channels. Following trypsin digestion and SPE of resulting peptides, peptides are released. Delay lines allow for discrete fractions, each corresponding to a fractionated protein, to be analyzed by pressure-driven ESI MS. Adapted from Taylor et al.[6]

to non-uniform bead packing, bed-to-bed resistance varied, leading to chaotic peptide elution off the microdevice.

1.5.SCOPE OF THE THESIS

The following thesis presents two microfluidics platforms for peptide and protein analysis. The first, discussed in Chapter 2, is a capillary electrochromatography microdevice for peptide analysis. Conditions for efficient separation and plate height analysis of a bead-based microfluidic device for strong cation exchange CEC of test peptides is studied under LIF detection. The performance of a two-bed CEC (first bed: SCX, second bed: RP) is also discussed. The second platform tackles the chaotic elution behavior studied by Taylor which was described in the last section. To overcome the problem, a hybrid glass-silicon microdevice was built and tested for chip-ESI MS protein analysis. Microchannels were etched in glass substrates and connected to micromachined silicon beds through a PDMS layer. Because the silicon beds are micromachined using well-known photolithographic techniques, all beds will be uniform and of equal

resistance leading to sequential elution to the ESI MS. Both single and multi channel devices were built: protein sorption and on-chip digestion were tested on the single channel device, while sequential elution was tested in the multichannel device. In Chapter 3, the microdevice fabrication is described, including silicon and glass processing, as well as the different approaches tested to efficiently connect the silicon and glass substrates. Of these, two were retained: connection through a thick (> 600 μm) PDMS and through a thin (< 20 μm) PDMS layer. For connection through a thin PDMS layer, we developed a novel PDMS machining procedure. The performance of the two resulting microdevices for single channel protein sorption and on-chip digestion, as well as sequential elution off the multichannel device, is presented in Chapter 4.

1.6.REFERENCES

(1) HE, B.; TAIT, N.; REGNIER, F. *ANALYTICAL CHEMISTRY* **1998**, *70*, 3790-3797.

(2) LI, D.; REMCHO, V. T. *JOURNAL OF MICROCOLUMN SEPARATION* **1997**, *9*, 389-397.

(3) DITTMAN, M. M.; ROZING, G. P. *JOURNAL OF CHROMATOGRAPHY A* **1996**, *744*, 63-74.

(4) OLESCHUK, R. D.; SHULTZ-LOCKYEAR, L. L.; NING, Y.; HARRISON, D. J. *ANALYTICAL CHEMISTRY* **2000**, *72*, 585-590.

(5) SLENTZ, B. E.; PENNER, N. A.; REGNIER, F. *JOURNAL OF CHROMATOGRAPHY A* **2003**, *984*, 97-107.

(6) TAYLOR, J., UNIVERSITY OF ALBERTA, EDMONTON, 2004.

(7) HARRISON, D. J.; MANZ, A.; FAN, Z.; LUDI, H.; WIDMER, H. M. *ANALYTICAL CHEMISTRY* **1992**, *64*, 1926-1932.

(8) JEMERE, A. B.; OLESCHUK, R. D.; OUCHEN, F.; FAJUYIGBE, F.; HARRISON, D. J. *ELECTROPHORESIS* **2002**, *23*, 3537-3544.

(9) WANG, C.; OLESCHUK, R.; OUCHEN, F.; LI, J. J.; THIBAULT, P.; HARRISON, D. J. *RAPID COMMUNICATIONS IN MASS SPECTROMETRY* **2000**, *14*, 1377-1383.

(10) THROCKMORTON, D. J.; SHEPODD, T. J.; SINGH, A. K. *ANALYTICAL CHEMISTRY* **2002**, *74*, 784-789.

(11) PUMERA, M. *TALANTA* **2005**, *66*, 1048-1062.

(12) TERRY, S. C.; JERMAN, J. H.; ANGELL, J. B. *IEEE TRANS. ELECTRON DEVICES* **1979**, *26*, 1880-1886.

(13) MANZ, A.; GRABER, N.; WIDMER, H. M. *SENSORS AND ACTUATORS* **1990**, *B1*, 244-248.

(14) JEMERE, A. B.; OLESCHUK, R. D.; HARRISON, D. J. *ELECTROPHORESIS* **2003**, *24*, 3018-3025.

(15) WOLF, S. *MICROCHIP MANUFACTURING*; LATTICE PRESS: CALIFORNIA, 2004.

(16) TISELIUS, A. *TRANS. FARADAY SOCIETY* **1937**, *33*, 524.

(17) JORGENSON, J. W.; LUCAS, K. D. *JOURNAL OF CHROMATOGRAPHY* **1981**, *218*, 209-216.

(18) MANZ, A.; HARRISON, D. J.; VERPOORTE, E. M. J.; FETTINGER, J. C.; PAULUS, A.; LUDI, H.; WIDMER, H. M. *JOURNAL OF CHROMATOGRAPHY* **1992**, *593*, 253-258.

(19) KNOX, J. H.; GRANT, I. H. *CHROMATOGRAPHIA* **1987**, *24*, 135-143.

(20) PRETORIUS, V.; HOPKINS, B. J.; SCHIEKE, J. D. *JOURNAL OF CHROMATOGRAPHY A* **1974**, *99*, 23.

(21) KNOX, J. H.; GRANT, I. H. *CHROMATOGRAPHIA* **1991**, *32*, 317-327.

(22) RATHORE, A. S.; HORVATH, C. S. *JOURNAL OF CHROMATOGRAPHY A* **1997**, *781*, 185-195.

(23) JACOBSON, S. C.; HERGENRODER, R.; KOUTNY, L. B.; RAMSEY, J. M. *ANALYTICAL CHEMISTRY* **1994**, *66*, 2369-2373.

(24) XU, W.; UCHIYAMA, K.; SHIMOSAKA, T.; HOBO, T. *JOURNAL OF CHROMATOGRAPHY A* **2001**, *907*, 279-289.

(25) XU, W.; UCHIYAMA, K.; HOBO, T. *CHROMATOGRAPHIA* **2002**, *23*, 131-138.

(26) RO, K. W.; CHANG, W.-J.; KIM, H.; KOO, Y.-M.; HAHN, J. H. *ELECTROPHORESIS* **2003**, *24*, 3253-3259.

(27) CERIOTTI, L.; ROOIJ, N.; VERPOORTE, E. M. J. *ANALYTICAL CHEMISTRY* **2002**, *74*, 639-647.

(28) HE, B.; JI, J.; REGNIER, F. *JOURNAL OF CHROMATOGRAPHY A* **1999**, *853*, 257-262.

(29) SLENTZ, B. E.; PENNER, N. A.; REGNIER, F. *JOURNAL OF CHROMATOGRAPHY A* **2002**, *948*, 225-233.

(30) SLENTZ, B. E.; PENNER, N. A.; LUGOWSKA, E.; REGNIER, F. *ELECTROPHORESIS* **2001**, *22*, 3736-3743.

(31) SLENTZ, B. E.; PENNER, N. A.; REGNIER, F. *JOURNAL OF SEPARATION SCIENCE* **2002**, *25*, 1011-1018.

(32) HILDER, E. F.; SVEC, F.; FRECHET, J. M. J. *ELECTROPHORESIS* **2002**, *23*, 3934.

(33) NGOLA, S. M.; FINTSCHENKO, Y.; CHOI, W. Y.; SHEPODD, T. J. *ANALYTICAL CHEMISTRY* **2001**, *73*, 849-856.

(34) LAZAR, I. M.; LI, L.; YANG, Y.; KARGER, B. L. *ELECTROPHORESIS* **2003**, *24*, 3655-3662.

(35) BEDAIR, M. F.; OLESCHUK, R. D. *ANALYTICAL CHEMISTRY* **2006**, *78*, 1130-1138.

(36) ERICSON, C.; HOLM, J.; ERICSON, T.; HJERTEN, S. *ANALYTICAL CHEMISTRY* **2000**, *72*, 81-87.

(37) BANDILLA, D.; SKINNER, C. D. *JOURNAL OF CHROMATOGRAPHY A* **2004**, *1044*, 113-129.

(38) MISIR, K., UNIVERSITY OF ALBERTA, EDMONTON, 2005.

(39) OCVIRK, G.; TANG, T.; HARRISON, D. J. *ANALYST* **1998**, *123*, 1429-1434.

(40) RABILLOUD, T. *PROTEOMICS* **2002**, *2*, 3-10.

(41) ENG, J. K.; MCCORMACK, A. L.; YATES, J. R. *JOURNAL OF THE AMERICAN SOCIETY FOR MASS SPECTROMETRY* **1994**, *5*, 976-989.

(42) WASHBURN, M. P.; WOLTERS, D.; YATES, J. R. *NATURE BIOTECHNOLOGY* **2001**, *19*, 242-247.

(43) LINK, A. J.; ENG, J. K.; SCHIELTZ, D. M.; CARMACK, E.; MIZE, G. J.; MORRIS, D. R.; GARVIC, B. M.; YATES, J. R. *NATURE BIOTECHNOLOGY* **1999**, *17*, 676-689.

(44) FIGEYS, D.; PINTO, D. *ELECTROPHORESIS* **2001**, *22*, 208.

(45) LION, N.; REYMOND, F.; GIRAULT, H. H.; ROSSIER, J. *CURRENT OPINION BIOTECHNOLOGY* **2004**, *15*, 31-37.

(46) LION, N.; ROHNER, T. C.; DAYON, L.; ARNAUD, I. L.; DAMOC, E.; YOUHNOVSKI, N.; WU, Z.-Y.; ROUSSEL, C.; JOSSERAND, J.; JENSEN, H.; ROSSIER, J. S.; PRZYBYLSKI, M.; GIRAULT, H. H. *ELECTROPHORESIS* **2003**, *24*, 3533-3562.

(47) FRIERE, S. L. S.; WHEELER, A. R. *LAB ON A CHIP* **2006**, *6*, 1415-1423.

(48) HOVING, S.; VOSHOL, H.; OOSTRUM, J. *ELECTROPHORESIS* **2000**, *21*, 2617-2621.

(49) KLOSE, J. *METHODS IN MOLECULAR BIOLOGY* **1999**, *112*, 147-172.

(50) GOTTSCHLICH, N.; JACOBSON, S. C.; CULBERTSON, C. T.; RAMSEY, J. M. *ANALYTICAL CHEMISTRY* **2001**, *73*, 2669-2674.

(51) ROCKLIN, R. D.; RAMSEY, R. S.; RAMSEY, J. M. *ANALYTICAL CHEMISTRY* **2000**, *72*, 5244-5249.

(52) RAMSEY, J. D.; JACOBSON, S. C.; CULBERTSON, C. T.; RAMSEY, J. M. *ANALYTICAL CHEMISTRY* **2003**, *75*.

(53) CHEN, X.; WU, H.; MAO, C.; WHITESIDES, G. M. *ANALYTICAL CHEMISTRY* **2002**, *74*, 1772-1778.

(54) WANG, Y.; CHOI, M. H.; HAN, J. *ANALYTICAL CHEMISTRY* **2004**, *76*, 4426-4431.

(55) LI, Y.; BUCH, J. S.; ROSENBERGER, F.; DEVOE, D. L.; LEE, C. S. *ANALYTICAL CHEMISTRY* **2004**, *76*, 742-748.

(56) BUCH, J. S.; LIU, J.; YANG, S.; TSAO, C.-W.; SONG, T.; SIVANESAN, P.; PHALNIKAR, K.; LEE, C. S.; DEVOE, D. L., TOKYO 2006; 1579-1581.

(57) HERR, A. E.; MOLHO, J. I.; DROUVALAKIS, K. A.; MIKKELSEN, J. C.; UTZ, P. J.; SANTIAGO, J. G.; KENNY, T. W. *ANALYTICAL CHEMISTRY* **2003**, *75*, 1180-1187.

(58) RO, K. W.; LIU, J.; KNAPP, D. *JOURNAL OF CHROMATOGRAPHY A* **2006**, *1111*, 40-47.

(59) BRIVIO, M.; FOKKENS, R. H.; VERBOOM, W.; REINHOUDT, D. N.; TAS, N. R.; GOEDBLOED, M.; VAN DEN BERG, A. *ANALYTICAL CHEMISTRY* **2002**, *74*, 3972-3976.

(60) GUSTAFSSON, M.; HIRSCHBERG, D.; PALMBERG, C.; JORNVALL, H.; BERGMAN, T. *ANALYTICAL CHEMISTRY* **2004**, *76*, 345-350.

(61) LITTLE, D. P.; CORNISH, T. J.; O'DONNELL, M. J.; BRAUN, A.; COTTER, R. J.; KOSTER, H. **1997**.

(62) GUNDRY, R. L.; EDWARD, R.; KOLE, T. P.; SUTTON, C.; COTTER, R. J. *ANALYTICAL CHEMISTRY* **2005**, *77*, 6609-6617.

(63) WHEELER, A. R.; MOON, H.; BIRD, C. A.; LOO, R. R. O.; KIM, C. J.; LOO, J. A.; GARRELL, R. L. *ANALYTICAL CHEMISTRY* **2005**, *77*, 534-540.

(64) WHEELER, A. R.; MOON, H.; KIM, C. J.; LOO, J. A.; GARRELL, R. L. *ANALYTICAL CHEMISTRY* **2004**, *76*, 4833-4838.

(65) EKSTROM, S.; ERICSSON, D.; ONNERFJORD, P.; BENGTSSON, M.; NILSSON, J.; MARKO-VARGA, G.; LAURELL, T. *ANALYTICAL CHEMISTRY* **2001**, *73*, 214-219.

(66) WANG, Y. X.; ZHOU, Y.; BALGLEY, B. M.; COOPER, J. W.; LEE, C. S.; DEVOE, D. L. *ELECTROPHORESIS* **2005**, *26*, 3631-3640.

(67) MUSYIMI, H. K.; GUY, J.; NARCISSE, D. A.; SOPER, S. A.; MURRAY, K. K. *ELECTROPHORESIS* **2005**, *26*, 4703-4710.

(68) MOON, H.; WHEELER, A. R.; GARRELL, R. L.; LOO, J. A.; KIM, C. J. *LAB ON A CHIP* **2006**, *6*, 1213-1219.

(69) LION, N.; GELLON, J. O.; JENSEN, H.; GIRAULT, H. H. *JOURNAL OF CHROMATOGRAPHY A* **2003**, *1003*, 11-19.

(70) XUE, Q. F.; FORET, F.; DUNAYEVSKIY, Y. M.; ZAVRACKY, P. M.; MCGRUER, N. E.; KARGER, B. L. *ANALYTICAL CHEMISTRY* **1997**, *69*, 426-430.

(71) RAMSEY, R. S.; RAMSEY, J. M. *ANALYTICAL CHEMISTRY* **1997**, *69*, 2617-2617.

(72) LION, N.; GOBRY, V.; JENSEN, H.; ROSSIER, J. S.; GIRAULT, H. *ELECTROPHORESIS* **2002**, *23*, 3583-3588.

(73) WANG, Y. X.; COOPER, J. W.; LEE, C. S.; DEVOE, D. L. *LAB ON A CHIP* **2004**, *4*, 363-367.

(74) KOERNER, T.; OLESCHUK, R. D. *RAPID COMMUNICATIONS IN MASS SPECTROMETRY* **2005**, *19*, 3279-3286.

(75) LI, J. J.; LERICHE, T.; TREMBLAY, T. L.; WANG, C.; BONNEIL, E.; HARRISON, D. J.; THIBAULT, P. *MOLECULAR & CELLULAR PROTEOMICS* **2002**, *1*, 157-168.

(76) LAZAR, I. M.; RAMSEY, R. S.; SUNDBERG, S.; RAMSEY, J. M. *ANALYTICAL CHEMISTRY* **1999**, *71*, 3627-3631.

(77) CHAN, J. H.; TIMPERMAN, A. T.; QIN, D.; AEBERSOLD, R. *ANALYTICAL CHEMISTRY* **1999**, *71*, 4437-4444.

(78) PINTO, D. M.; NING, Y. B.; FIGEYS, D. *ELECTROPHORESIS* **2000**, *21*, 181-190.

(79) ZHANG, B. L.; FORET, F.; KARGER, B. L. *ANALYTICAL CHEMISTRY* **2001**, *73*, 2675-2681.

(80) CHEN, S. H.; SUNG, W. C.; LEE, G. B.; LIN, Z. Y.; CHEN, P. W.; LIAO, P. C. *ELECTROPHORESIS* **2001**, *22*, 3972-3977.

(81) DENG, Y. Z.; HENION, J.; LI, J. J.; THIBAULT, P.; WANG, C.; HARRISON, D. J. *ANALYTICAL CHEMISTRY* **2001**, *73*, 639-646.

(82) DAHLIN, A. P.; BERGSTROM, S. K.; ANDREN, P. E.; MARKIDES, K. E.; BERGQUIST, J. *ANALYTICAL CHEMISTRY* **2005**, *77*, 5356-5363.

(83) XIE, J.; MIAO, Y. N.; SHIH, J.; TAI, Y. C.; LEE, T. D. *ANALYTICAL CHEMISTRY* **2005**, *77*, 6947-6953.

(84) YIN, N. F.; KILLEEN, K.; BRENNEN, R.; SOBEK, D.; WERLICH, M.; VAN DE GOOR, T. V. *ANALYTICAL CHEMISTRY* **2005**, *77*, 527-533.

(85) SCHULTZ, G. A.; CORSO, T. N.; PROSSER, S. J.; ZHANG, S. *ANALYTICAL CHEMISTRY* **2000**, *72*, 4058-4063.

(86) KAMEOKA, J.; ORTH, R.; ILIC, B.; CZAPLEWSKI, D.; WACHS, T.; CRAIGHEAD, H. G. *ANALYTICAL CHEMISTRY* **2002**, *74*, 5897-5901.

(87) XIE, J.; MIAO, Y. N.; SHIH, J.; HE, Q.; LIU, J.; TAI, Y. C.; LEE, T. D. *ANALYTICAL CHEMISTRY* **2004**, *76*, 3756-3763.

(88) SVEDBERG, M.; VESZELEI, M.; AXELSSON, J.; VANGBO, M.; NIKOLAJEFF, F. *LAB ON A CHIP* **2004**, *4*, 322-327.

(89) SCHILLING, M.; NIGGE, W.; RUDZINSKI, A.; NEYER, A.; HERGENRODER, R. *LAB ON A CHIP* **2004**, *4*, 220-224.

(90) LICKLIDER, L.; WANG, X. Q.; DESAI, A.; TAI, Y. C.; LEE, T. D. *ANALYTICAL CHEMISTRY* **2000**, *72*, 367-375.

(91) SUNG, W. C.; MAKAMBA, H.; CHEN, S. H. *ELECTROPHORESIS* **2005**, *26*, 1783-1791.

(92) EKSTROM, S.; ONNERFJORD, P.; NILSSON, J.; BENGTSSON, M.; LAURELL, T.; MARKO-VARGA, G. *ANALYTICAL CHEMISTRY* **2000**, *72*, 286-293.

(93) FINNSKOG, D.; JARAS, K.; RESSINE, A.; MALM, J.; MARKO-VARGA, G.; LILJA, H.; LAURELL, T. *ELECTROPHORESIS* **2006**, *27*, 1093-1103.

(94) FIGEYS, D.; GYGI, S. P.; MCKINNON, G.; AEBERSOLD, R. *ANALYTICAL CHEMISTRY* **1998**, *70*, 3728-3734.

(95) LIU, H. H.; FELTEN, C.; XUE, Q. F.; ZHANG, B. L.; JEDRZEJEWSKI, P.; KARGER, B. L.; FORET, F. *ANALYTICAL CHEMISTRY* **2000**, *72*, 3303-3310.

(96) TAN, A. M.; BENETTON, S.; HENION, J. D. *ANALYTICAL CHEMISTRY* **2003**, *75*, 5504-5511.

(97) GHITUN, M.; BONNEIL, E.; FORTIER, M. H.; YIN, H. F.; KILLEEN, K.; THIBAULT, P. *JOURNAL OF SEPARATION SCIENCE* **2006**, *29*, 1539-1549.

(98) FORTIER, M. H.; BONNEIL, E.; GOODLEY, P.; THIBAULT, P. *ANALYTICAL CHEMISTRY* **2005**, *77*, 1631-1640.

(99) HARDOUIN, J.; DUCHATEAU, M.; JOUBERT-CARON, R.; CARON, M. *RAPID COMMUNICATIONS IN MASS SPECTROMETRY* **2006**, *20*, 3236-3244.

(100) CANELLE, L.; BOUSQUET, J.; PIONNEAU, C.; HARDOUIN, J.; CHOQUET-KASTYLEVSKY, G.; JOUBERT-CARON, R.; CARON, M. *ELECTROPHORESIS* **2006**, *27*, 1609-1616.

(101) XUE, Q. F.; DUNAYEVSKIY, Y. M.; FORET, F.; KARGER, B. L. *RAPID COMMUNICATIONS IN MASS SPECTROMETRY* **1997**, *11*, 1253-1256.

(102) WANG, C., UNIVERSITY OF ALBERTA, EDMONTON, 2001.

CHAPTER 2 ON-CHIP CAPILLARY ELECTROCHROMATOGRAPHY

2.1.INTRODUCTION

Analysis by capillary electrochromatography (CEC) offers the possibility of high separation efficiency, and therefore high column peak capacity, due to the lower bandbroadening during the separation process. Compared to liquid chromatography, the flat electroosmotic flow (EOF) profile produced in CEC reduces bandbroadening from Eddy diffusion, reducing plate height (H) numbers. Several microdevice approaches have been described for on-chip CEC, using open-channel[1-3], bead entrapment[4-8], micromachined monoliths[9-13] or in-situ polymer growth[14-16] techniques. Our laboratory developed a bead entrapment technique for reverse-phase (ODS) separation of a mixture of dyes[4-6]. The microdevice consisted of 10 μm deep microchannels containing two 1 μm deep weirs in the separation region. The region between the weirs, 1 or 2 mm apart, were packed with commercially-available ODS beads having 1.5 μm diameter. The weirs therefore contained ODS beads within the bed region while allowing fluid flow in the separation microchannel.

Strong cation exchange capillary electrochromatography (SCX CEC) has been demonstrated in several reports using traditional CEC systems[17]. An on-chip CEC microdevice has been reported: it focused on the ability of a polymer-based SCX phase grown into a glass microchannel to support EOF under low pH conditions[18]. The present chapter describes the use of a microdevice for on-chip SCX CEC using the bead entrapment technique described above. Conditions for efficient separation of peptides and further column characterization are described.

On-chip two-dimensional separations based on electrokinetic phenomena have been described[19-27]. For orthogonal separation mechanisms, the total peak capacity (n_t) for a 2D system will be equal to the product of peak capacities in each dimension, $n_{1D}*n_{2D}$. To isolate the first and second dimensions, techniques using both a physical barrier and gated injections were proposed. Section 2.4 presents a microdevice, based on the above-mentioned bead entrapment technique, for two-column CEC (first column: SCX, second column: ODS) with both separations run sequentially; the second dimension must therefore be faster than the first for effective separation of co-eluting peaks in the second dimension.

2.2.EXPERIMENTAL

2.2.1. SOLUTIONS AND REAGENTS

Acetonitrile (ACN, HPLC grade), ethylene dimethacrylate (EDMA), 2,2'-azo-bis(isobutyronitrile) (AIBN), DMSO, Tween 20, rhodamine 123, fluorescein isothiocyanate (FITC), arginine, dilysine, trilysine and tetralysine were purchased from Sigma-Aldrich Chemical Co. (Milwaukee, WI). Acetonitrile was distilled before use. Alexa Fluor and BODIPY were from Molecular Probes. Potassium dihydrogen phosphate was from Fisher Scientific (Ottawa, ON). Reagent grade 1-propanol and 1,4-butanediol were obtained from Caledon Laboratories Ltd. (Georgetown, ON) and Eastman Organic Chemicals (Rochester, NY). Buffers were prepared using ultrapure water prepared with a deionizing system (Millipore Canada, Mississauga, ON) filtered through a nylon syringe filter (0.2 μm pore size, Nalgene, Rochester, NY) prior to use.

Peptide labeling was based on a published protocol[28]. Arginine, dilysine, trilysine and tetralysine solutions, 10 mM, were prepared separately in 200 mM potassium dihydrogen phosphate buffer at pH 7.5, 7.0 and 6.5. FITC (0.0195 g) was dissolved in a mixture of 4.75 ml acetone, 0.25 ml water and 0.05 μl pyridine, for a final FITC concentration of 10 mM. To 500 μl of the peptide solutions, 100 μl FITC solution was added, mixed and left to react at room temperature overnight in the dark.

2.2.2. INSTRUMENTATION

For microdevice capillary electrochromatography experiments, laser-induced fluorescence detection was used. The computer-controlled power supply and relay arrangement has been described previously[29]. In-house written LabVIEW programs (National Instruments, Austin, TX) were used for computer control of the voltages and for data acquisition. The laser-induced confocal epifluorescence detection system used was described in section 1.3.5, here are the operating parameters: 488 nm Ar ion laser (Model 2214-105L, Uniphase, San Jose, CA) operated at 4 mW, 505DRLP dichroic mirror (Omega, Brattleboro, VT), 40x, 0.6 N.A. microscope objective (Planachromat LDN 1.2-A; Carl Zeiss Jena, Jena, Germany), achromat tube lens, f = 200 mm, (Newport, PAC064, Irvine, CA), 400 μm pinhole, 530DF 30 (Omega) emission filter and photo-multiplier tube (PMT) (R1477, Hamamatsu, Bridgewater, NJ). The PMT was biased to 500 V, while the PMT signal was amplified (10^7 gain trans-impedance amplifier), filtered

(active 25 Hz Butterworth filter, house built) and collected on a MacIntosh IIci using a National Instruments NB-MIO16 A/D board at sampling frequency of 40, 100 or 200 Hz.

For capillary electrophoresis experiments, the PACE 5010 commercial CE system (Beckman) was used under laser-induced fluorescence detection. Capillaries were from Polymicro Technologies, 360 μm o.d., 50 μm i.d. and 27 cm in length. All experiments were run in normal polarity mode, i.e. positive inlet voltage and negative outlet voltage.

2.3.SINGLE COLUMN CEC

2.3.1. MICRODEVICE FABRICATION

The microdevice for CEC analysis was fabricated using a two mask approach. Figure 2.1 presents the L-Edit output for the first mask design (grey indicates clear on the glass substrate). In Figure 2.1a the complete microdevice is presented, with R_1, R_2, R_3 and R_4 representing the reservoirs for sample, buffer, sample waste and buffer waste, respectively. R_5 indicates the bead-introduction reservoir. The microchannel width in the separation region was 150 μm and in the bead-introduction channel, 30 μm. Figure 2.1b is an expansion of the circled area from Figure 2.1a, the T injector and 2 mm bed regions are shown. Also shown are the two 40 μm long weirs, both of which are only etched during the second mask process (note that the second mask is shown here as the black weir region). Two design notes: first, the bead introduction channel was attached to the main separation channel at the end of the packed-bed region to minimize sample loss in the side-channel during separation. Second, the T injector was used, as opposed to the double-T injection scheme; the presence of the bed region compresses the injection plug so that the better sample plug definition arrangement provided by the double-T scheme is not needed for high resolution separations.

All microfabrication was done at the University of Alberta Nanofab facility and followed standard procedures published in the literature[30]. A 4 in x 4 in Corning 0211 glass having a 30 nm layer of chrome and 150 nm layer of gold (600 μm thick, Micralyne) was cleaned with acetone and isopropyl alcohol. Photoresist (HPR 504, OCG Microelectronic Materials) was spin-coated unto the Cr/Au 0211 wafer (Solitec, 500 rpm for 10 s, 4,000 rpm for 40 s). The pieces were oven-baked for thirty minutes at 115 °C and left to re-hydrate at room temperature for 15 minutes. The first mask, defining the main channels of the microdevice, and 0211 wafer were loaded onto the mask aligner

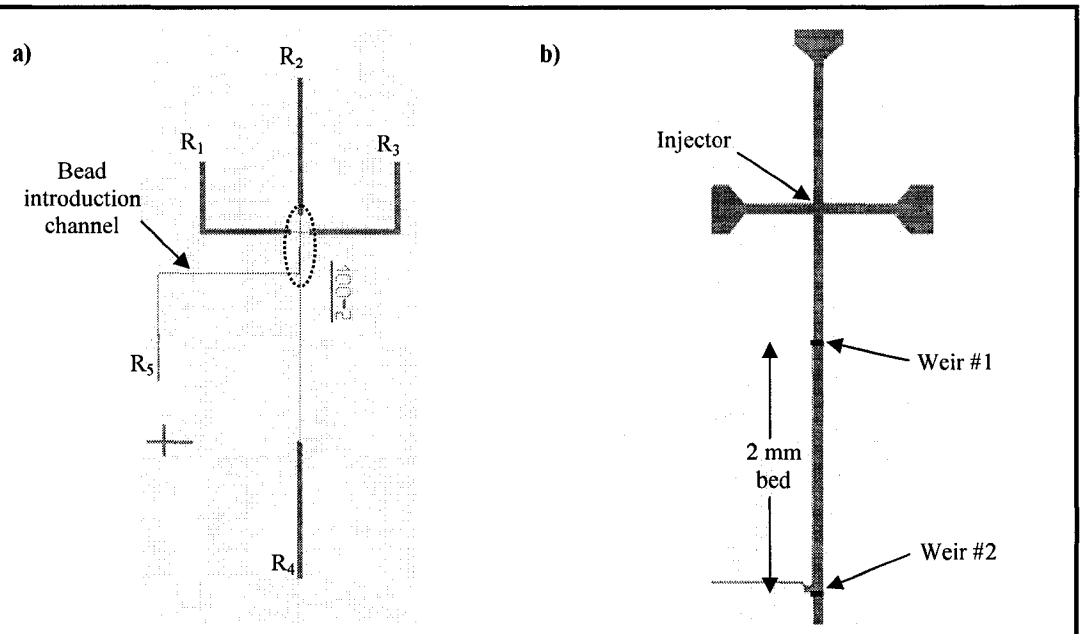

Figure 2.1 Mask Design- L-edit output, with grey representing clear on the mask. a) The microdevice is shown with the 2 mm bed highlighted by a dotted circle; b) a close-up of the bed region is shown. In a) R_1, R_2, R_3, R_4 and R_5 are reservoirs for sample, buffer, sample-waste, buffer-waste and bead introduction, respectively. In b) the two 40 μm long weirs, etched during the second mask process, are depicted.

(ABM Inc.), brought into contact and exposed to UV (λ: 365 nm for 4 seconds). The UV-exposed area of the photoresist was removed by rinsing for 25 seconds with a developer (354 Developer, Electronic Materials L.L.C.). After gold and chrome removal of the exposed areas (Au etching solution: KI:I_2 at 4:1, Cr etching solution: from Fujifilm), the glass wafer was immersed in a glass etching solution (H_2O:HF:HNO_3 , 66:20:14). The target glass depth was 18 μm. The photoresist was then removed using acetone, and the second mask process was begun. Photoresist (HPR 504, OCG Microelectronic Materials) was spin-coated unto the etched wafer (Solitec, 500 rpm for 10 s, 4,000 rpm for 40 s). The pieces were oven-baked for 30 minutes at 115 °C and left to re-hydrate at room temperature for 15 minutes. The second mask, defining the 40 μm weir region, and etched 0211 wafer were loaded onto the mask aligner (ABM Inc.), aligned, brought into contact and exposed to UV (λ: 365 nm for 4 seconds). The UV-exposed area of the photoresist was removed by rinsing for 25 seconds with a developer (354 Developer, Electronic Materials L.L.C.). After gold and chrome removal of the

exposed areas (Au etching solution: KI:I_2 at 4:1, Cr etching solution: from Fujifilm), the glass wafer was immersed in a glass etching solution (H_2O:HF:HNO_3 , 66:20:14). The target glass depth was 2 μm. To prepare the wafer for bonding to the upper glass wafer, excess photoresist was removed with acetone and the wafer given a piranha (H_2SO_4 : H_2O_2 at 3:1) wash. Remaining gold and chrome were removed using the gold and chrome etchants.

Access reservoirs R_1 to R_5 were drilled on the upper glass wafer using 2 mm diameter drill bit (Lee Valley): a 4 in x 4 in Corning 0211 glass (600 μm thick, Precision Glass and Optics) was mounted on a thick support glass wafer using Crystalbond (#509, Aremco Products Inc.). After drilling (Model 7010, Servo Products Company), the 600 μm glass was removed from the support wafer by heating on a hot plate, which softens the Crystalbond, and immersed in an acetone bath (20 minutes twice) for partial removal of the Crystalbond.

For bonding of the microchannel-containing glass to the upper drilled wafer, both were immersed in a piranha solution for 20 minutes. After thorough rinsing with water, both wafers were separately dried, mounted on a ring holder and loaded into a high pressure washer (Micro Automation 2066, settings: 5 rinse cycles, 10 dry cycles). The two were then aligned and brought into contact. After this initial cold bonding process, the two wafers were irreversibly bonded in a thermal bonding oven (settings: room temperature to 440 °C at 10 °C/min hold 30 min, 440 °C to 473 °C at 2 °C/min hold 30 min, 473 °C to 592 °C at 2 °C/min hold 6 hours, 592 °C to 473 °C at 4 °C/min hold 30 min). After thermal bonding, cut pipette tips were glued onto the microdevice at R_1 to R_5 to act as reservoirs.

After conditioning the device with, successively, 0.1M NaOH and deionized water, a ~3 μg/ml bead slurry in 1:1 MeOH : water solution was introduced into the bead introduction reservoir. The beads (5 μm diameter and 80 Å pore size) were obtained from a guard column of PhenoSphere strong cation exchange material (SCX, from Phenomenex, Torrance, CA). Bead packing proceeded using both electrokinetic and negative pressure forces. Figure 2.2 presents pictures taken during the packing process (the microdevice was placed on the inverted microscope detection system and a CCD camera (SONY) was placed at the image plane). The pictures show a sequence of four

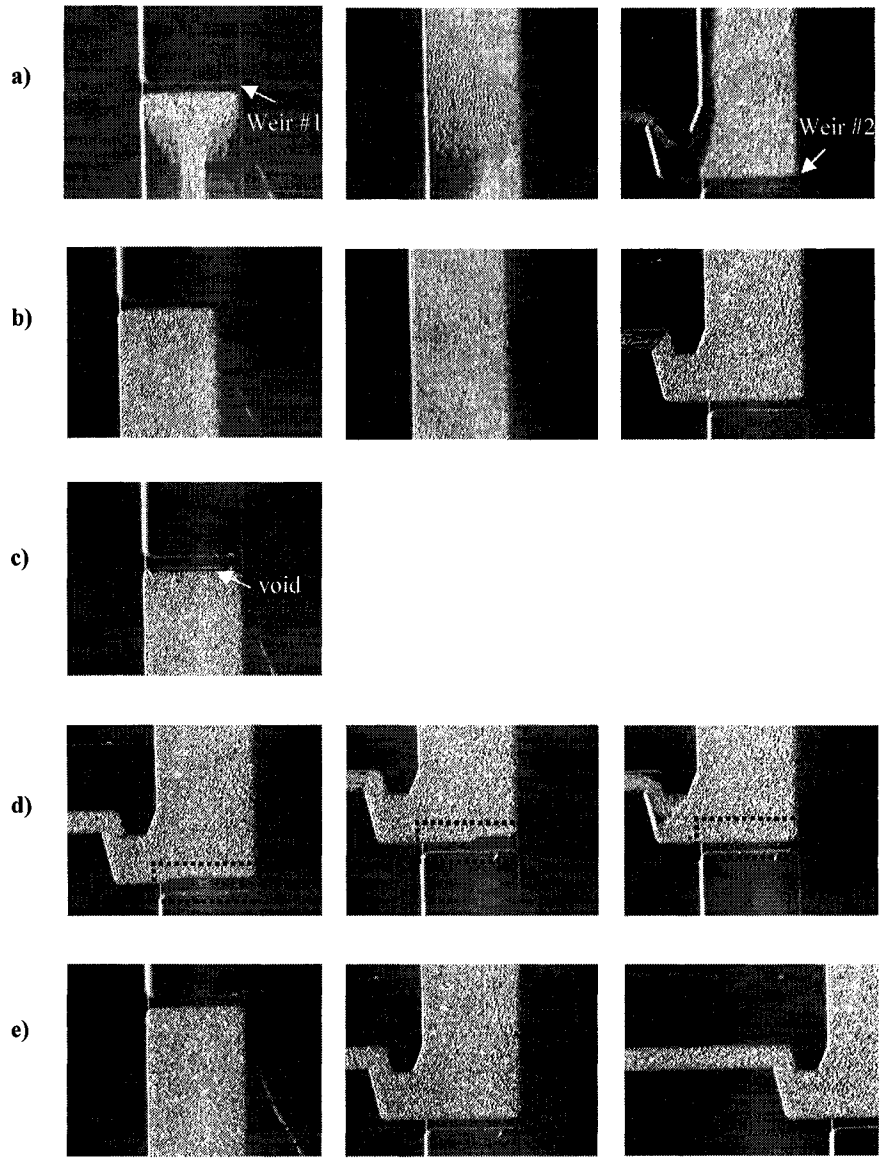

Figure 2.2 Column Packing Sequence- a) Initial electrokinetic packing resulted in a poorly packed bed; b) applying negative pressure at R_2 filled the main voids but c) not completely; d) applying a voltage ramp, from 0 V to 650 V, between R_5 and R_3 while maintaining negative pressure at R_2 filled the void; e) the sequence resulted in a well-packed 2 mm column.

events, from a) to d). Figure 2.2e presents the resulting packed microcolumn. Note that the two weirs are visible on the pictures. The packing process starts at a) with R_5 being grounded and R_3 at -300 V. The three pictures show the head, middle and end of the

column region as the packing progresses. Through electrokinetic forces, the 5 μm beads are driven towards the head of the column. Both weirs being etched only 2 μm deep, the beads (5 μm diameter) are trapped at the head of the column, as shown in the first picture of Figure 2.2a. Electrokinetic forces produce loosely packed beds; the resulting columns are prone to void formation as shown in the second and third pictures of sequence 2.2a. In the second sequence 2.2b, negative pressure (~0.5 bar) is applied using a vacuum line to R_2 while keeping the applied voltage on R_5 and R_3. From the three pictures of the event (head, middle and end of the column) this seemingly results in a uniformly packed bed. However, as shown in sequence 2.2c, applying negative pressure to R_4 shifts the bed and reveals a void at the head of the column. In the last event (2.2d) negative pressure is returned to R_2, shifting the bed upwards: the void created at weir #2 is highlighted by a dotted box. To fill this gap, R_5 is grounded and the voltage applied to R4 is shifted from 0 V (first picture), to - 450 V (second picture) to - 650 V (last picture). As seen in the pictures, this voltage ramp pushes the beads from the bead introduction channel into the column, filling the void at weir #2. In pictures of Figure 2.2d, the column head and end is shown, as well as part of the bead introduction channels: all are well-packed.

Once packed, the beads were entrapped using the polymer plug technique described previously[5, 6]. A monomeric solution was drawn into the bead introduction channel and flow was stopped before the solution reached the separation bed. The monomer was then polymerized by placing the chip under UV light (Hg lamp, λ = 365 nm) for about 5 minutes. The monomeric solution consisted of a mixture of 200 μL EDMA and 2 wt% AIBN per weight of EDMA in 800 μL of a ternary solvent mixture (10 wt% H_2O, 40 wt% 1,4-butanediol and 50 wt% 1-propanol). The solution was purged under nitrogen for 15 minutes before use.

2.3.2. MICRODEVICE OPERATION

Before use, the microdevice was conditioned for 10 minutes with deionized water and 20 minutes with the mobile phase. All samples were diluted in the mobile phase. The detector was positioned in the center of the microchannel either upstream or downstream of the column, with the weir just out of the field of view. The voltage configuration for on-chip studies is described next; it describes most studies unless otherwise stated.

Reservoirs R_2, R_3 and R_4 were filled with the running buffer solution, while R_1 contained the analyte (diluted to the mentioned concentration in the running buffer). Note that all buffer solutions contained 0.005% Tween 20. For analyte injection, R_1 was grounded and R_3 was kept at – 0.5 kV with R_2 and R_4 left floating. After 10 seconds, separation in the main channel proceeded by applying a voltage across R_2 and R_4 (with R_2 grounded and R_4 at a negative voltage value, as mentioned in the results section). To avoid sample leakage from the side channels, a low negative voltage was applied to R_1 and R_3 during separation (set at ¼ of the voltage applied on the main separation channel).

2.3.3. RESULTS

2.3.3.1. INITIAL STUDIES

The commercial beads used in this study were SO_3^- terminated: analyte separation on the column therefore proceeded by cation exchange, whereby positively-charged analytes would sorb onto the negatively-charged bed and be displaced by counter-ions in the buffer solution according to the analyte's charge number (see section 1.3.4. for liquid chromatography-based thermodynamic equations). The stationary phase, because of its negative charge down to pH 3, supports electroosmotic flow; an on-chip capillary electrochromatographic experiment using strong cation exchange stationary phases has been presented in the literature using low buffer pH for sorption of cationic species[18]. In this example, however, the capillary was completely filled with a polymer monolith and EOF was therefore supported throughout the separation channel. In conventional systems, SCX CEC is run while applying pressure at the inlet and outlet reservoirs during separation[31]. In the microdevice format presented here, only the two millimeter bed is packed, with the injector portion being open; also, no pressure was applied during the separation process. This then presents an injection problem in low pH buffers: EOF in the upper section of the microdevice is lower than in the packed section, creating an EOF mismatch that could disturb the injection procedure.

To test the effect of EOF mismatch, the injection behavior of two dyes, BODIPY and Alexa Fluor 488, was studied. Both dyes were 50 nM in the separation buffer. The fluorescence of BODIPY is near its maximum efficiency at pH 7 whereas Alexa Fluor 488 fluorescence is nearly pH independent, from pH 4 to 10. Buffer conditions for BODIPY: 40% acetonitrile / 60% ammonium acetate, 25 mM, pH 7; buffer conditions for

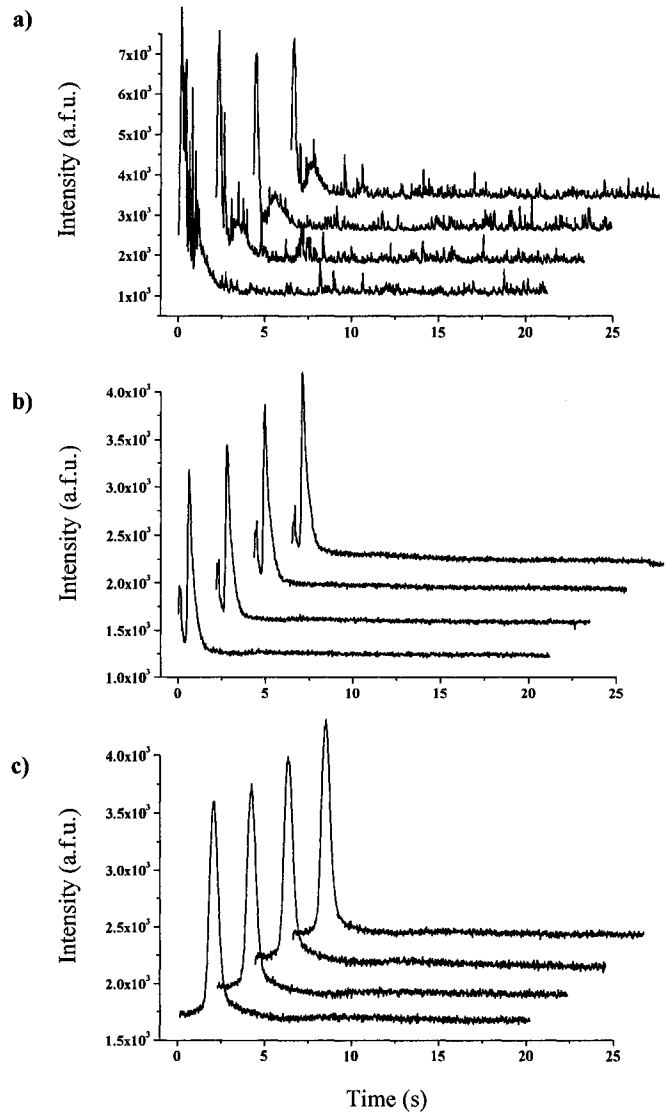

Figure 2.3 Injection Behavior- Four consecutive injections for a) 50 nM Alexa Fluor in pH 5.0 buffer, b) 50 nM Alexa Fluor in pH 6.0 buffer and c) 50 nM BODIPY in pH 7.0 buffer. Parameters: injection: 5 s at 500 V, separation: 1 kV with -250 V pushback. Detection before the first weir.

Alexa Fluor: 40% acetonitrile / 60% phosphate, 25 mM, pH 4, 5 and 6. The detector was located at the head of the column after the injector cross and fluorescence was monitored after a 5 s injection at 0.5 kV. Separation conditions: 1 kV separation, - 250 V pushback. Figure 2.3 presents the results for a) Alexa Fluor at pH 5, b) Alexa Fluor at pH 6 and c) BODIPY at pH 7. No signal was obtained for Alexa Fluor at pH 4. The traces shown are

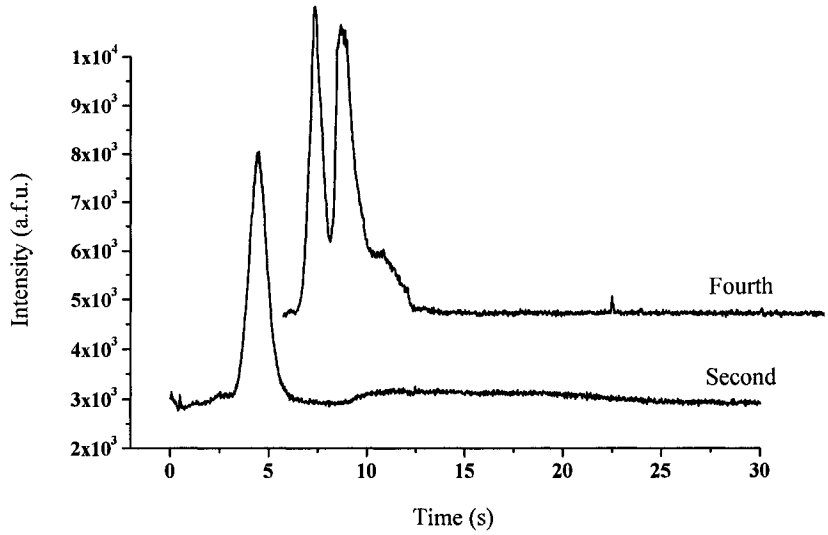

Figure 2.4 Rhodamine 123 in Ammonium Acetate Buffer- Detection, after the column, for the first and fourth injection. Parameters: 50% NH_4OAc, pH 7 / 50% acetonitrile, injection: 10 s at 500 V, separation: 2 kV with -400 V pushback.

for 4 consecutive injections and are presented in stacked form. From these, a stable injection was obtained at pH 6 and 7 where both the microchannel walls and packed bed portion are negatively charged. EOF is clearly supported throughout the separation channel and stable injection is possible. A chaotic, unstable injection was obtained at pH 5 (Figure 2.3 a): the number of deprotonated silanol groups on the microchannel walls at this pH value is reduced, reducing the EOF in the injector portion of the microdevice and creating a mismatch between EOF in the microchannel versus in the packed bed. This then does not allow for reproducible injections. As mentioned above, no signal was obtained at pH 4. The detector was then located at the middle of the injector cross to monitor dye intensity during the 5 s injection from the sample to sample-waste reservoirs: the intensity increased, indicating that the dye did make its way into the injector cross region at pH 4. This result indicated that the low EOF obtained at pH 4 was too weak to overcome the backpressure created by the packed bed region so that no dye entered the separation region under separation voltage.

The choice of separation buffer affected separations. At pH 7, rhodamine 123 is a positively charged dye that will interact with the SCX column. On-chip elution of the 10

nM dye was tested in separation buffer. The separation buffer used was 25 mM ammonium acetate in 50% acetonitrile at pH 7. Figure 2.4 presents the resulting electrochromatogram for the second and fourth injection, shown in stacked form. Parameters for injection: 0.5 kV for 10 s and for separation: 2 kV with – 400 V pushback. The dye initially elutes within 5 s. During the fourth elution, two peaks resulted: the first from the elution of non-displaced dye from the previous injections and the second from the fourth injection. It was concluded that the ammonium ion was not efficient at displacing the analyte off the SCX column. Further analyses were done in KH_2PO_4 buffer, potassium being a better displacer than the bulky NH_4^+ cation.

2.3.3.2. COLUMN CHARACTERIZATION

To better characterize the chromatographic behavior of the microdevice under SCX CEC, the lysine series (dilysine, trilysine and tetralysine) was studied. Under optimized labeling conditions, peptides of known overall charge (0 for dilysine, + 1 for trilysine and + 2 for tetralysine) can be obtained and the chromatographic behavior for the SCX column can be probed. Since good injection behavior was easily observed for higher pH buffers, the lysine series was fluorescently labeled with fluorescein and the experiments run at pH 7, where fluorescence emission of the dye is at its maximum.

The reaction mechanism for lysine labeling with fluorescein involves the isothiocyanate group on the FITC reacting with unprotonated amino group on the amino acid. The pK values for the amino groups are 8.9 and 10.5: by adjusting the reaction buffer pH for the labeling reaction, the singly-labeled di-, tri- and tetra-lysine products can be obtained, corresponding to overall peptide charges of 0, + 1 and + 2, respectively. The labeling reaction was described in section 2.2.1.1, the dilysine reaction was set at pH 7.5, at pH 7.0 for trilysine and both 7.0 and 6.5 for tetralysine. The products were analyzed using a traditional capillary electrophoresis instrument with the following parameters: 3 s pressure injection, 10 kV separation voltage, labeled products diluted 10:1 in separation buffer (25 mM KH_2PO_4, pH 7). Before analysis, the capillary was conditioned with 0.1 M NaOH, water and 25 mM KH_2PO_4 pH 7 for 30 minutes, successively. The results are presented in Figure 2.5. Two runs are shown for each labeled compound: one for the resulting product (line) and one for the product spiked with FITC (dot). Figure 2.5 shows results for the following: a) dilysine, b) trilysine, c)

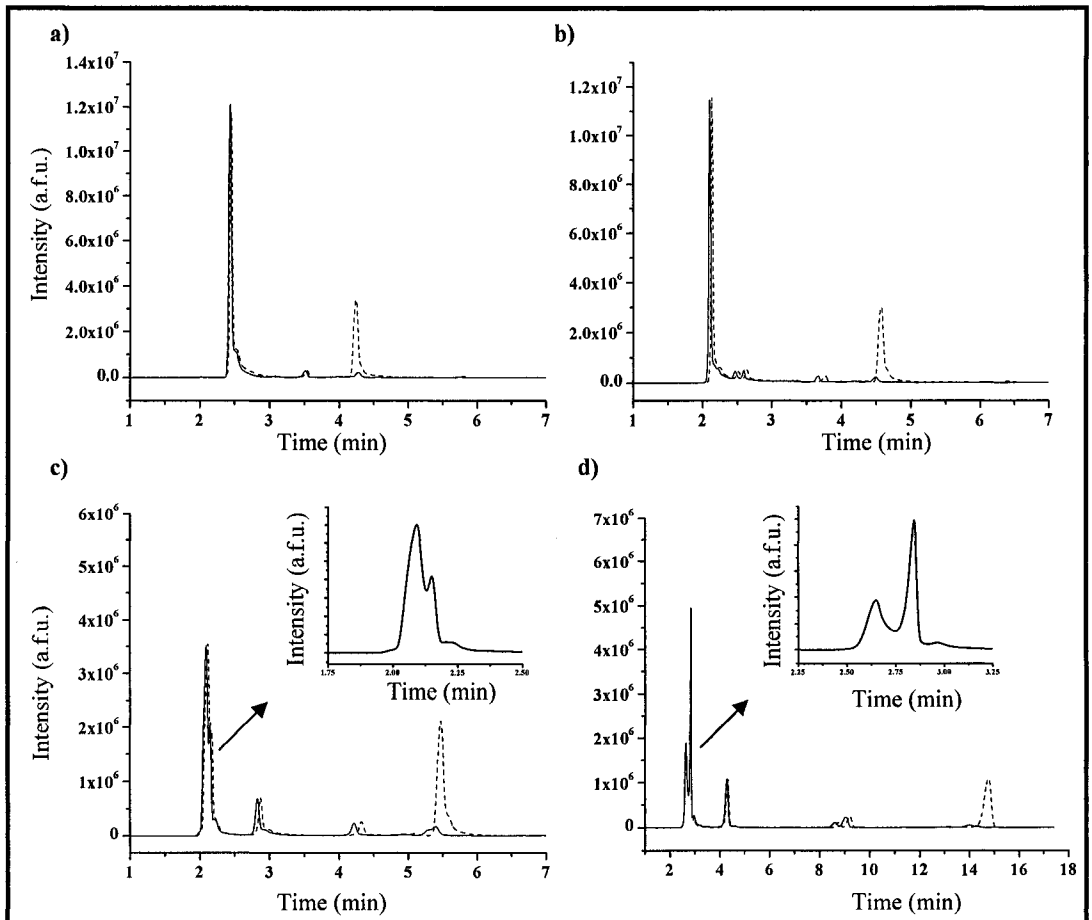

Figure 2.5 Peptides Labeling- Electropherograms, obtained using the Beckman CE system, for labeled products (line) and products spiked with FITC (dotted) for a) dilysine labeled at pH 7.5, b) trilysine labeled at pH 7.0, tetralysine labeled at c) pH 6.5 and d) pH 7.0. Insets: close-up of the peaks.

tetralysine labeled at pH 6.5 and d) tetralysine at pH 7.0. Dylisine and trilysine derivatization resulted in mostly singly labeled product, with some higher-labeled compounds being seen just above the baseline. The tetralysine at pH 6.5 (Figure 2.5 c) and pH 7.0 (Figure 2.5 d) showed multiple, but different, products. The main peaks for both electropherograms are expanded in the inset. At pH 7.0, the main reaction product came from the doubly labeled form of the peptide: the faster eluting peak (+ 2 charge, labeled once) was of lower intensity than the second peak (0 charge, labeled twice). At pH 6.5, from the inset, the singly-labeled reaction product was mainly obtained. By-

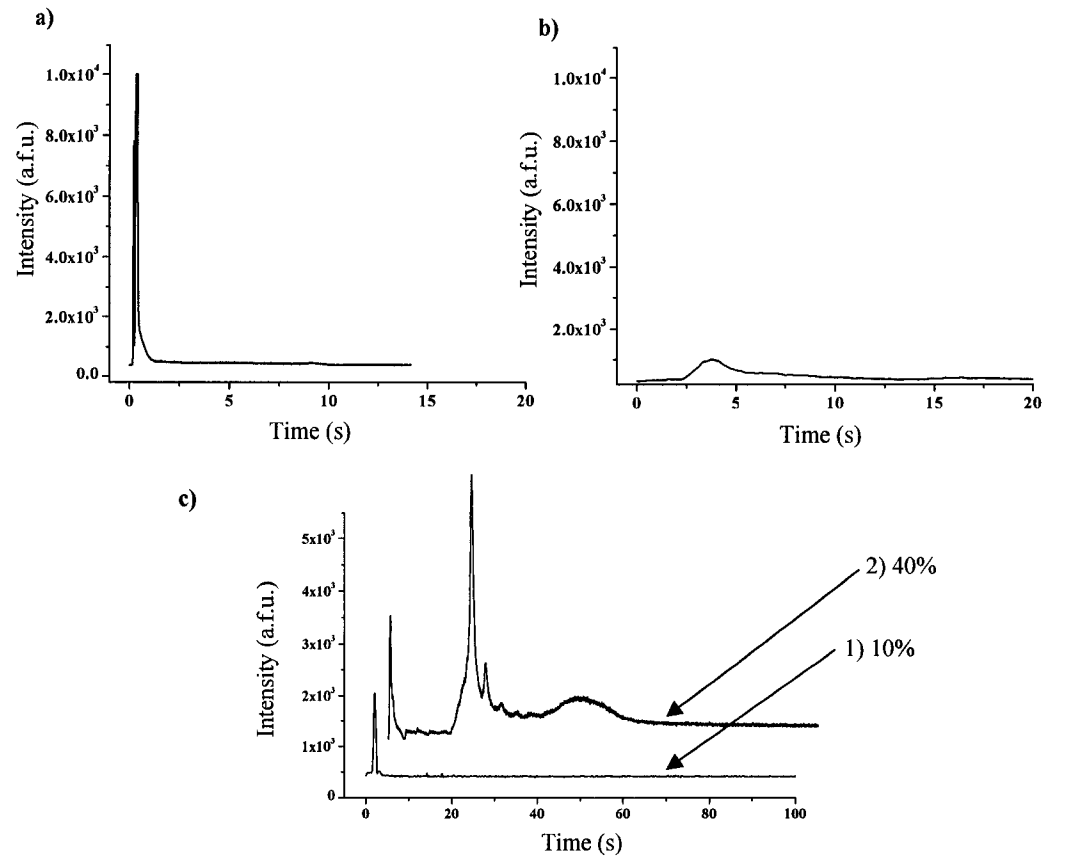

Figure 2.6 Effect of Acetonitrile Percent on Elution- Electrochromatogram in 100% 25 mM KH_2PO_4 buffer, pH 7 for 0.5 μM dilysine with detection a) before and b) after the SCX column; c) resulting elution for a mixture of dilysine (50 nM) and trilysine (50 nM) in 1) 10% acetonitrile / 90% 25 mM KH_2PO_4 buffer, pH 7 and 2) 40% acetonitrile / 60% 25 mM KH_2PO_4 buffer, pH 7. Parameters: Injection: 0.5 kV for 10 s, separation: 1 kV, -250 V pushback.

products from the doubly and triply labeled products can also be seen, corresponding to 0 and –2 charge. The pH 6.5 reaction buffer was subsequently used for tetralysine reaction.

All studies were done in pH 7 buffer containing 0.005% Tween 20. SCX beads used in this study do present some hydrophobic behavior: some acetonitrile must be used in the separation buffer. Initial studies involved dilysine (500 nM in separation buffer) elution using 100% 25 mM KH_2PO_4 buffer. The resulting fluorescence peaks are shown in Figure 2.6 for a) before and b) after column. Parameters: injection at 0.5 kV for 10 s and separation at 1 kV, - 250 V pushback. From these, the injection plug saturated the detector signal before the column (area under the curve: 1,506 a.f.u.(s), note that this underestimated the true injected value since the PMT was saturated), yet only a small

broad peak was eluted (area under the curve: 958 a.f.u.(s)): the analyte is sorbed onto the bed due to hydrophobic interactions with the column. The same was true for a sample solution composed of dilysine and trilysine (50 nM each in elution buffer) for a separation buffer containing 10% acetonitrile: after many injections, examination of the head of the column showed the sample had been sorbed there. Figure 2.6c presents the resulting elution peak for the sample in 1) 10% acetonitrile and 2) 40% acetonitrile (all other parameters as before). The two electrochromatograms are shown in stacked form. It is clear that incomplete elution results in high aqueous conditions. Similarly, higher acetonitrile percent (to 60%) will result in incomplete desorption off the column due to the lower amount of counter-ion present in the separation phase. A 40% acetonitrile percent was therefore used for all studies.

Figure 2.7 shows the resulting electrochromatogram for a) dilysine, b) trilysine and c) tetralysine (50 nM in separation buffer) run independently in 60% 25mM phosphate buffer (pH 7) for a 1 kV separation voltage (- 250 V pushback, injection: 10 s at 0.5 kV). From these, the singly labeled dylisine (0 charge) eluted at 14.3 s, trilysine (+ 1 charge) at 33.7 s and tetralysine, at 48 s. In all traces, the initial peak is for the elution of the unreacted dye, fluorescein. Note that both the trylisine and tetralysine experiments were done on the same microdevice: the fluorescein dye eluted at 2.7 s in both experiments. The tetralysine was run on a different microdevice: the dye eluted at 0.5 s. Peaks at 9.9 s for dilysine, 7.2 s for trilysine and 5.5 s for tetralysine are from the doubly labeled reaction products.

Comparing the results for the on-chip SCX CEC and Beckman CE (Figure 2.5), the elution order was reversed. During a normal polarity capillary electrophoresis experiment, positively charged analytes elute first, followed by neutral and finally negatively charged analytes (see section 1.3 for a more complete discussion on CE): in the Beckman CE experiments, fluorescein eluted after the lysine series. In the SCX CEC experiment, fluorescein eluted first, with the lysine series eluting last: the main mode of operation in the microdevice experiment is therefore cation exchange chromatography. The elution of dilysine (0 charge) at ~ 15 s, trilysine (+ 1 charge) at ~ 35 s and tetralysine (+ 2 charge) at 48 s also pointed to cation exchange as the main mode of separation. In accordance with theory, higher charged peptides eluted last.

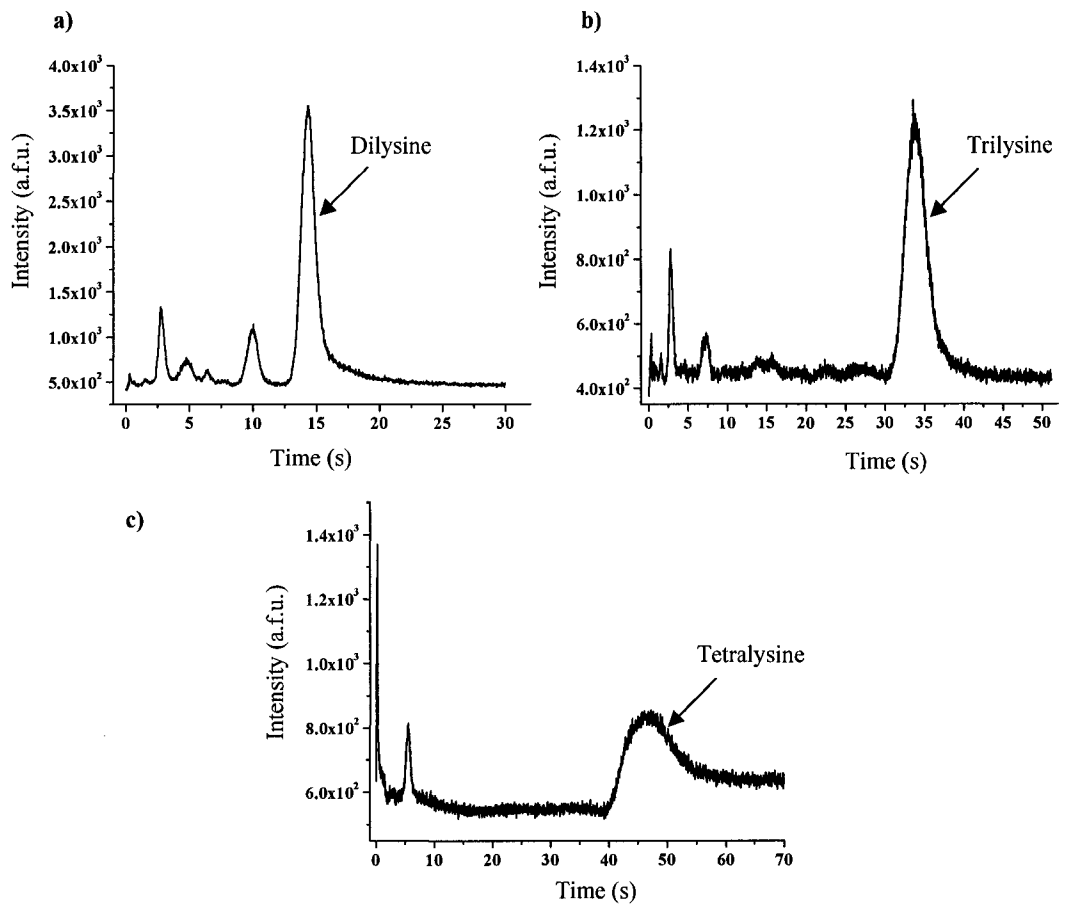

Figure 2.7 Peptide Elution at 25 mM, 1 kV- Elution for a) dilysine (50 nM), b) trilysine (50 nM) and c) tetralysine (50 nM). Buffer: 40% acetonitrile / 60% 25 mM KH_2PO_4, pH 7. Parameters: Injection: 0.5 kV for 10 s, separation: 1 kV, -250 V pushback.

Higher ionic strength values could produce a sharper tetralysine peak. Figure 2.8a presents three traces at different buffer ionic strength. The bottom trace is for the elution of tetralysine in 25 mM buffer at 2 kV (– 450 V pushback, all other parameters as before): the resulting peak is broad at ~ 25 s. Also shown in the middle curve is the elution of trilysine under the same conditions. The final curve shows the electrochromatogram for a 2 kV separation (- 450 pushback) using 50 mM phosphate buffer (all other parameters as before): the effect on peak shape and migration times is evident. From a broad, low-intensity peak, tetralysine becomes sharp with its full width at half maximum decreased drastically under higher ionic strength conditions. The same was true for trilysine. As expected, higher ionic strength buffers work better at displacing

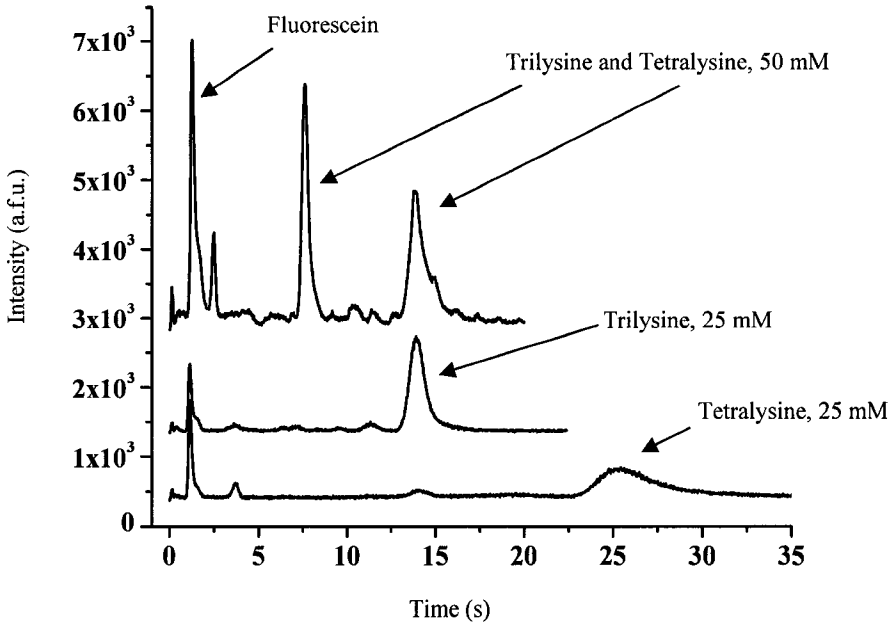

Figure 2.8 Tetralysine and Trilysine Elution at 2 kV- Higher separation efficiencies result in 50 mM buffer for elution of a mixture of trilysine and tetralysine (higher trace) than in lower ionic strength buffer (25 mM, trilysine in the middle trace, tetralysine in the lower trace). Buffers contained 40% acetonitrile. Parameters: injection: 10 s at 0.5 kV, separation: 2 kV with -400 V pushback.

positively charged analytes off a cation exchanger: faster, more efficient elutions result. In CE, higher ionic strength buffers reduce the double layer thickness: the surface potential will drop more rapidly near the capillary walls, resulting in a lower potential at the plane of shear, i.e. in lower EOF values and longer elution times.

Figure 2.9a presents the ionic strength effect on the migration time of the eluted peaks as a function of buffer concentration (error bars: for n = 5, 95% C.L.). All separations were performed at 1 kV with – 250 V pushback (injection: 500 V for 10 s). From the graph, all three analytes are affected by ionic strength conditions: all elute more rapidly in higher ionic strength buffer. The higher charged analyte, tetralysine, was the most affected by the change (slope: -0.92 ± 0.04 s/mM for the first three points), followed by trilysine (slope: -0.46 ± 0. 03 s/mM for the first three points); dilysine, with overall neutral charge, was the least affected (slope: -0.15 ± 0.01 s/mM for the first three points), in accordance with ion exchange chromatographic theory.

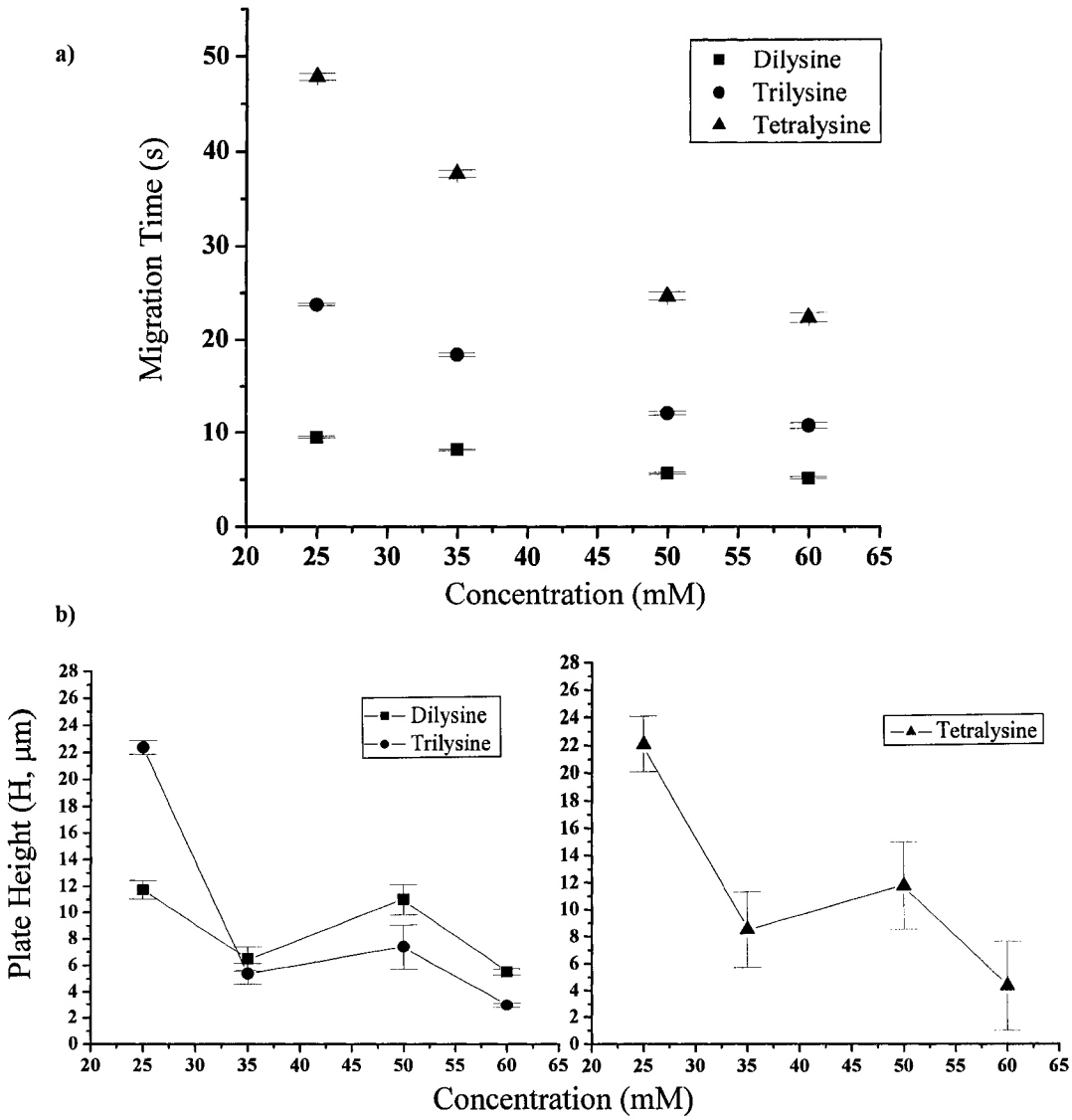

Figure 2.9 Ionic Strength Effect on Migration Times and Efficiency- a) Migration time and b) plate height versus buffer concentration. Parameters: all buffers contained 40% acetonitrile, all sample concentrations were 50 nM. Injection: 500 V for 10 s, separation: 1 kV with –250 V pushback.

Figure 2.9b presents the ionic strength effect on plate height, H (all injection and separation parameters as for Figure 2.9 a). Plate height analysis was discussed in section 1.3.1. Taking into consideration only the separation phenomenon, two sources contribute peak variance along the separation path: first the variance for the peak just before the column and second, the variance contribution for the on-column separation. To calculate column plate height, only the second contribution should be included: variance for the

peak before the column should be subtracted to the total peak variance. The standard deviation for the dilysine peak at three different injection times was: 0.80 s for 5 s injection, 0.76 s for 10 s injection and 0.80 s for 20 s injection. All are equal, which indicated that the injection plug focused at the head of the column, a phenomenon that has been reported previously in SCX and ODS beads[6, 31]: subtracting the variance for the peak at the head of the column would artificially decrease the plate height value. Therefore, total peak variance was used in all H calculations. The total elution time was corrected by the elution time for the peak at the head of the column. Plate height for the 2,000 μm length column is then:

$$H = \frac{2{,}000}{5.54 \left[\frac{t_{corr}}{\sigma\sqrt{8\ln 2}} \right]^2} \qquad (2.1)$$

where H is in micrometers, t_{corr} is the corrected elution time and σ is the standard deviation of the eluted peak. From the graphs, all peptides showed improved efficiencies at higher ionic strengths: faster elutions and sharpened peaks resulted in lower H values for 60 mM versus 25 mM buffer. The separation was inefficient for both trilysine (H = 22.3 ± 0.5 μm) and tetralysine (H = 22 ± 2 μm) at 25 mM: the ionic strength of the separation buffer was too low for efficient elution of cationic species off the anionic bed. The overall neutral analyte, dilysine, was less affected: its plate height value was 11.7 ± 0.7 μm. A reversal in plate efficiencies was seen at 60 mM: trilysine (H = 3.0 ± 0.2 μm) was more efficient then dilysine (H = 5.5 ± 0.2 μm), with the tetralysine plate height value equalled to 4 ± 3 μm. Using the most efficient experimental parameters, the neutral peptide has a higher plate height value than the trilysine, since it only had limited interaction with the ionic phase. An increase in plate height value, outside error intervals, was observed for dilysine at 50 mM buffer concentration: further plate height analysis is shown on the next page.

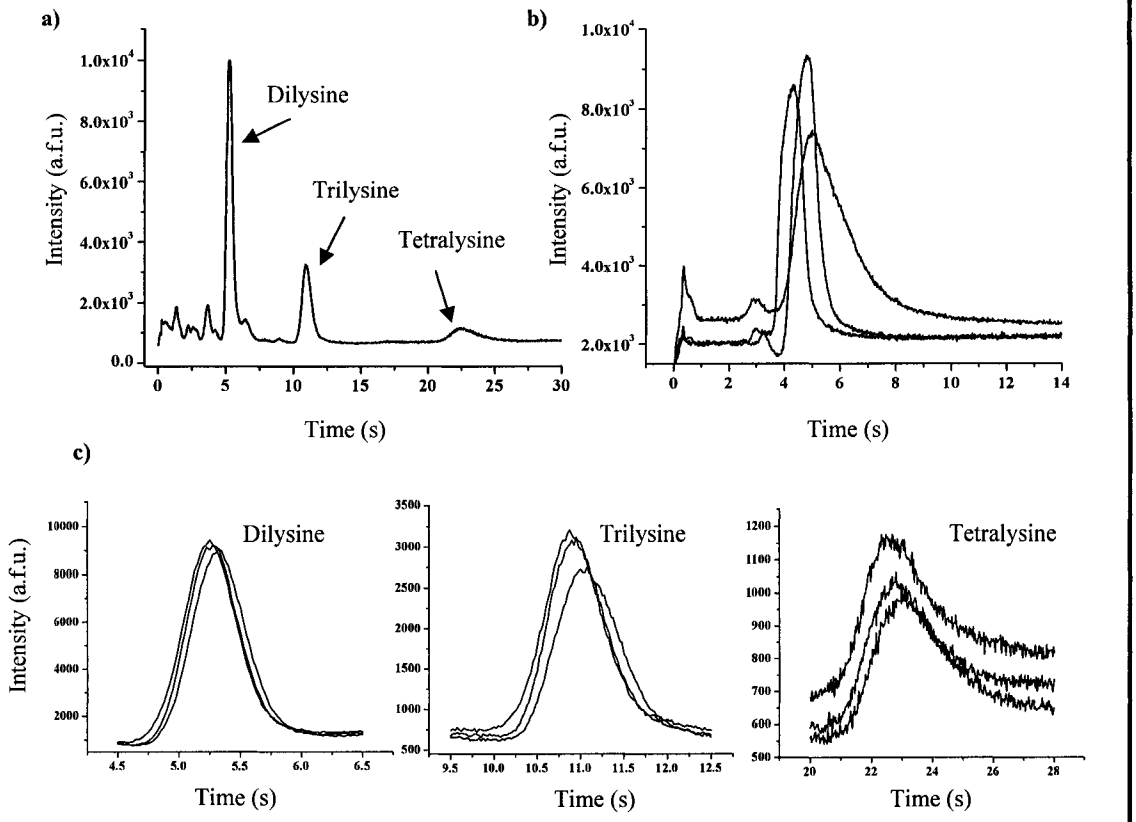

Figure 2.10 Separation with and without Column- a) All three peptides were separated within 25 s on the microdevice containing the SCX bead; b) no separation was possible without the beads; c) elution for three consecutive injections. Conditions: a) buffer: 60% of 60 mM KH_2PO_4, pH 7 in 40% acetonitrile. Injection: 10 s at 500 V, separation: 1 kV with -250 V pushback; b) buffer: 60% of 25 mM KH_2PO_4, pH 7 in 40% acetonitrile. Injection: 5 s at 500 V, separation: 1 kV with -250 V pushback. All peptides at 50 nM concentration.

The resulting electrochromatogram for the separation of the three analytes in the fastest eluting buffer (60 mM) is shown in Figure 2.10a. The separation voltage was set to 1 kV, (- 250 V pushback, 10 s injection at 500 V). The three are separated within 25 seconds, with dilysine eluting at 5.2 s (1.6% RSD for five injections), trilysine at 10.7 s (2.1 % RSD for five injections) and tetralysine at 22.2 s (2.2% RSD for five injections). Throughout this study, tetralysine peaks were less reproducible than the other two: this was attributed to sorption of the positively-charged peptide onto the glass microchannel and negatively-charged bed. Figure 2.10c presents the result for three consecutive runs (all parameters as for Figure 2.10a): both dilysine and trilysine show good reproducibility

(area %RSD: 1.2% for dilysine and 2.1% for trilysine, each for five injections). However, both area %RSD, at 8% for five injections, and peak tailing on the tetralysine peak point to sorption on the glass microchannels and negatively-charged bed. Figure 2.10b shows the resulting electrochromatogram for the three peptides run individually in a microdevice which did not contain packing material: no separation was possible (parameters: 5 s injection at 500 V, separation in 25 mM buffer at 1 kV with – 250 V pushback).

To assess the efficiency of the column, two van Deemter plots were constructed (plate height versus flow velocity), at 50 mM and 60 mM buffer strength. Plate height was defined above. Flow velocity was calculated by dividing the volume between the injector and head of the column by the migration time for the peak at the head of the column. The cross sectional area of the microchannel was 3.2×10^{-9} m^2. For a 2 mm length from injector cross to head of the column, the volume was 6.42 nl. The flow velocity was set by adjusting the separation voltage from 750 V to 1,500 V for the 50 mM analysis, and 650 V to 1,000 V for the 60 mM analysis. Note that the voltage values were set so as to limit the resulting currents during separation (current should not be higher then about 50 μA). All samples were 50 nM in the separation buffer, parameters for injection: 10 s at 500 V. Separation voltage values with associated pushback in brackets (all in volts): for 50 mM: 750 (- 250), 850 (- 300), 950 (- 350), 1,000 (- 375), 1,500 (- 400), for 60 mM: 650 (- 150), 750 (- 200), 850 (-250), 950 (- 300), 1,000 (- 350).

The resulting van Deemter plot is shown in Figure 2.11, a) for 50 mM and b) for 60 mM (error bars: for n = 5, 95% C.L.). At an applied voltage of 750 V, corresponding to 3.6 nl/s in the 60 mM buffer and 7.5 nl/s in the 50 mM buffer, charged peptides have higher efficiencies in the 60 mM buffer (H values: trilysine: 3.7 ± 0.1 μm in 60 mM versus 8.5 ± 0.7 μm in 50 mM; tetralysine: 6.5 ± 0.5 μm in 60 mM versus 11.1 ± 0.4 μm in 50 mM). This suggested, as did Figure 2.9b for the change in plate height as a function of buffer concentration, that the 50 mM buffer does not contain enough counter-ions to properly displace the peptides, and large improvements in plate height numbers ($\Delta H = 4.8 \pm 0.7$ μm for trilysine and $\Delta H = 4.6 \pm 0.6$ μm for tetralysine) were observed for higher buffer ionic strength. For the overall neutral peptide, dilysine, the efficiency was unchanged (dilysine: 7.4 ± 0.5 μm in 60 mM versus 8.2 ± 0.6 μm in 50 mM); because of

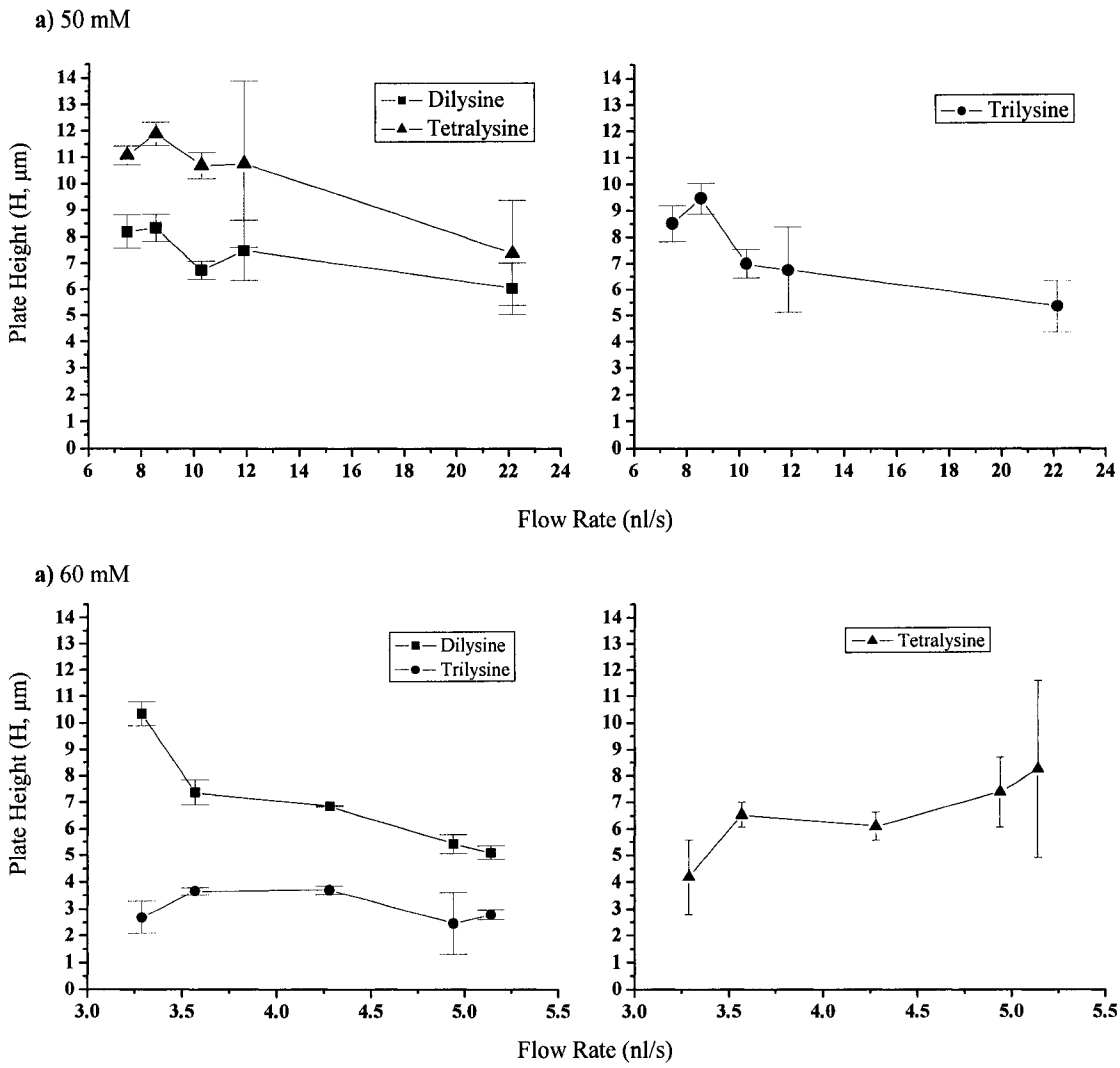

Figure 2.11 van Deemter Plots- In a) 50 mM KH_2PO_4 buffer, pH 7 and b) 60 mM KH2PO4, pH 7. The buffer was 60% in acetonitrile. All peptide concentration at 50 nM. Parameters: a) injection: 10 s at 500 V, separation: from 750 V to 1,500 V; b) injection: 10 s at 500 V, separation: from 650 V to 1,000 V. See text for pushback values.

its limited interactions with the stationary phase, dilysine was less affected by change in ionic strength conditions.

In section 1.3.1, the total plate height equation was defined:

$$H = A + B / \mu + (C_S + C_M) \mu \quad (2.2)$$

where μ is the flow velocity, A is Eddy diffusion, (B / μ) is longitudinal diffusion, μC_S and μC_M are resistance to mass transfer in the solid and mobile phase, respectively. Factors limiting efficiency for a given column can therefore be pinpointed using van Deemter plots. The A term, being flow rate independent, is constant at all flow rates (note that Eddy diffusion is the term whose value is lowered in CEC versus LC due to flat EOF profile). Longitudinal diffusion is prevalent at low flow rates: more time is given to the analyte to diffuse about the center of the moving peak, widening the eluting peak. The C terms take over at high flow rates: analytes are not given enough time to equilibrate with the stationary or mobile phases, creating a concentration imbalance at the front and end of the moving peak which in turn produces bandbroadening.

With this in mind, the van Deemter curve shape for the three peptides at 50 mM (Figure 2.11a) show a constant H value for all three peptides, within error limits; the major source of bandbroadening was therefore Eddy diffusion. For Eddy diffusion-limited separations, better efficiencies can be obtained through the use of smaller diameter beads (see Table 1.1 for further A, B, C_S and C_M definition). At 60 mM buffer concentration (Figure 2.11 b), both trilysine and tetralysine showed constant H values for the flow rate investigated: Eddy diffusion was therefore the major cause of bandbroadening. The dilysine separation showed a decrease in plate height for faster separations, indicating a longitudinal diffusion-limited separation.

Finally, comparing efficiency for this system to previously published work on SCX CEC systems shows the good efficiency of the microdevice presented here. Ye et al. reported separation efficiencies between 240,000 and 460,000 plates/meter for CEC of small charged peptides[31]. Their experiments were run in microcapillaries packed 10 cm long with 5 μm diameter SCX beads under UV detection. These compare well with efficiencies obtained for the two peptides that interacted the most with the phase at 60 mM buffer strength: trilysine at 400,000 plates/meter and tetralysine at 238,000 plates/meter. The calculated value for dilysine was 196,000 plates/meter.

2.4. TWO-COLUMN CEC

2.4.1. MICRODEVICE FABRICATION

The fabrication method for the two-column microdevice used the two mask system described in section 2.3.1 for the single column CEC. The single column mask

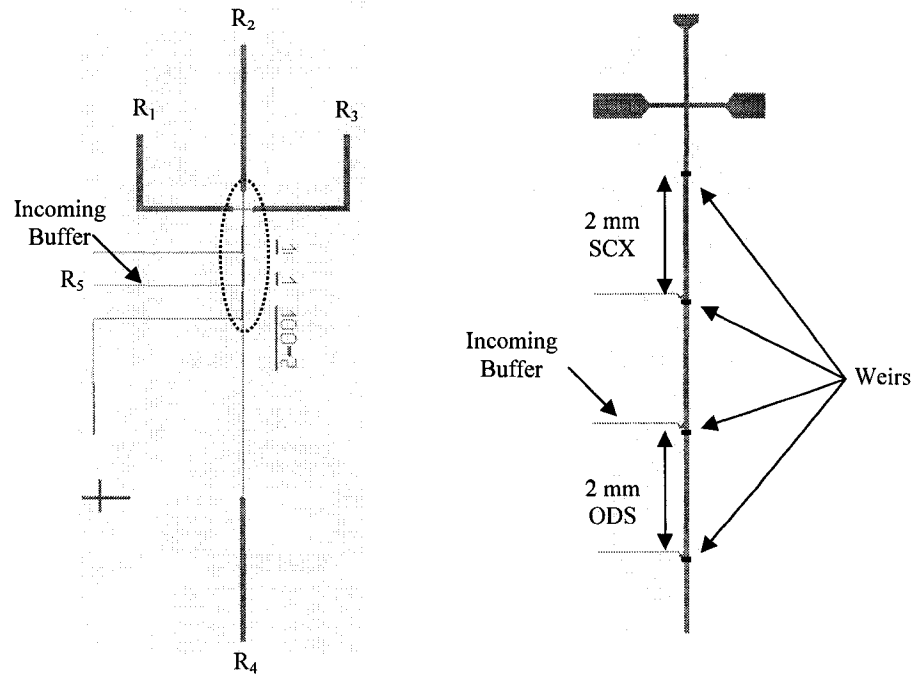

Figure 2.12 Two-Column Microdevice- Grey represents clear on the mask. The microdevice is shown with the two 2 mm bed highlighted by a dotted circle (left), a close-up of the bed region is shown (right). R_1, R_2, R_3 and R_4 as before (Figure 2.1); R_5 represents the ODS-compatible buffer reservoir. Four 40 μm long weirs are shown, for trapping of the first (SCX) and second (ODS) bed.

design was applied three times to the wafer, with a photoresist developing step between each design application. The resulting two-column microdevice is pictured in Figure 2.12. The column closest to the injector was packed with SCX beads, the end column was packed with ODS beads. The middle column was not packed: its side-arm was used to change the buffer content before the ODS column. Mixing at the meeting point of the side-arm and main separation channel would affect bandbroadening of a peak eluting from the SCX column. However, because of the focusing effect of ODS columns on incoming peaks (as discussed in section 2.3.3.2), this bandbroadening by mixing effect on the final peak shape was predicted to be minimal. All other fabrication parameters were as in section 2.3.1. Reservoirs R_1, R_3 and R_4 representing the reservoirs for sample, sample waste and buffer waste, respectively. R_2 and R_5 represent the two buffer reservoirs: R_2 for SCX-compatible buffer (i.e. low acetonitrile content) and R_5 for ODS-compatible buffer (i.e. high acetonitrile content). Note that the side-arm for the two

packed columns contained both beads and polymer material: they did not contribute to buffer flow.

After conditioning the device with, successively, 0.1M NaOH and deionized water, the same packing procedure as described previously in section 2.3.1 was used. ODS beads (5 μm diameter, 100 Å pore size) ~ 3 μg/ml in 1:1 acetonitrile : water were packed first, followed by polymer entrapment (as described in section 2.3.1). This was then followed by SCX bead packing in 1:1 methanol : water and polymer entrapment.

2.4.2. MICRODEVICE OPERATION

Before use, the microdevice was conditioned for 10 minutes with deionized water and 20 minutes with the mobile phase by applying negative pressure at R_4. All samples were diluted in the SCX mobile phase at the mentioned concentration. The detector was positioned in the center of the microchannel either upstream or downstream of column one or two, as mentioned in the text, with the weir just out of the field of view. The voltage configuration for on-chip studies is described next; it describes most studies unless otherwise stated. R_1 contained the analyte (diluted to the mentioned concentration in SCX-compatible running buffer), R_2 and R_3 were filled with the SCX-compatible running buffer solution, while R_4 and R_5 contained the ODS-compatible buffer. Note that all buffer solutions contained 0.005% Tween 20. For analyte injection, R_1 was grounded and R_3 was kept at – 0.5 kV with all other reservoirs left floating. After 10 seconds, separation in the main channel proceeded by applying a negative voltage to R_2 while simultaneously grounding R_4 and R_5. This then drove the SCX-compatible buffer into the SCX-column and ODS-compatible buffer into the ODS column. To avoid sample leakage from the injection side channels, a low negative voltage was applied to R_1 and R_3 during separation (set at ¼ of the voltage applied on the main separation channel).

2.4.3. RESULTS

Initial studies focused on the effect of buffer composition on elution of dilysine. Using 60% 25 mM KH_2PO_4 / 40% acetonitrile buffer at pH 7.0, 50 nM of the peptide (diluted in the running buffer) was injected and the resulting peak observed before and after the SCX column as well as after the ODS bed. The results are shown in Figure 2.13 for a) before SCX, and b) after SCX and ODS (as indicated). Parameters: injection at 0.5 kV for 10 s and separation at 2 kV with – 400 V pushback. Figure 2.13c presents the

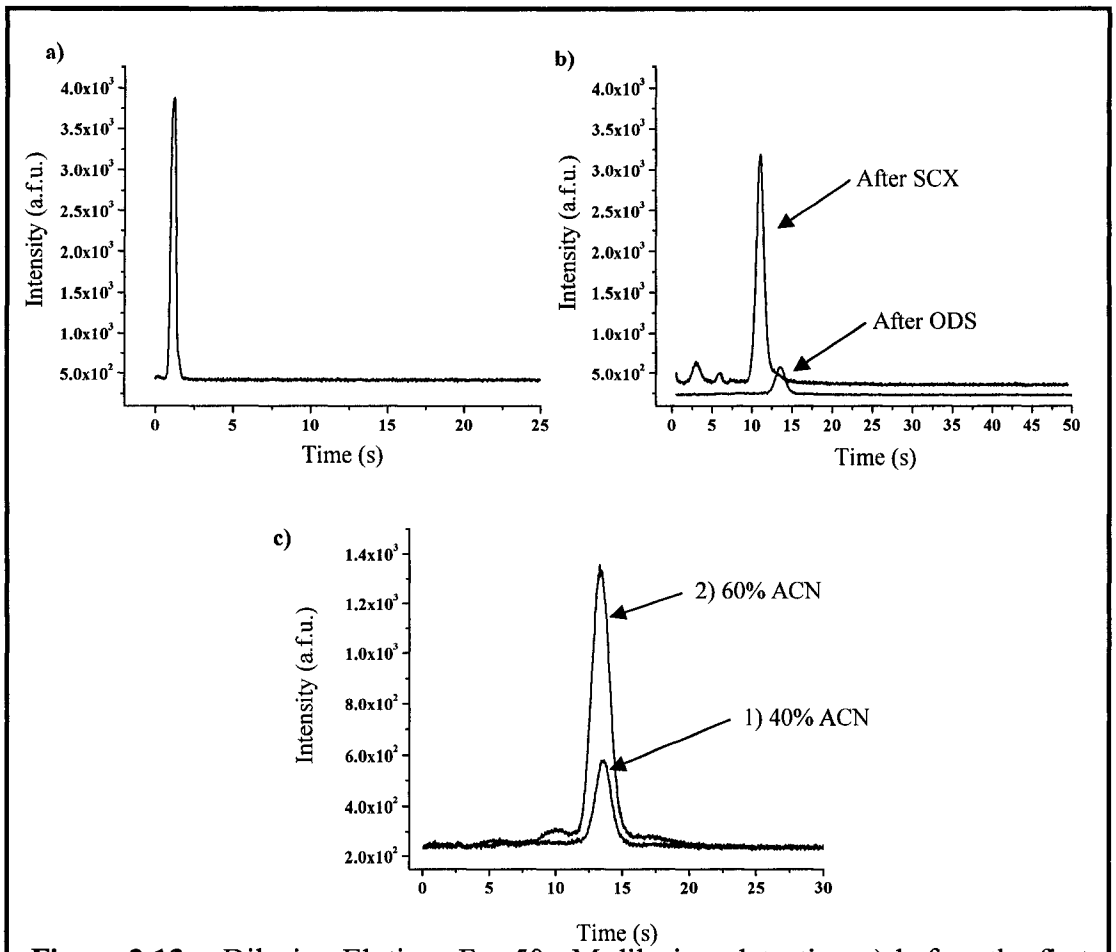

Figure 2.13 Dilysine Elution- For 50 nM dilysine, detection a) before the first weir, b) after the SCX and ODS columns (as indicated). Buffer: 60% 25 mM KH_2PO_4 / 40% acetonitrile at pH 7.0. c) Detection after the ODS column for two different buffer composition in R_5 (as indicated). Buffers: 1- 40% acetonitrile / 60% 25 mM KH_2PO_4 and 2- 60% acetonitrile / 40% 25 mM KH_2PO_4. All other reservoir compositions: 60% 25 mM KH_2PO_4 / 40% acetonitrile. Parameters: injection: 10 s at 0.5 kV, separation: 2 kV with – 400 V pushback.

resulting trace for dilysine elution after ODS bed for two different buffer compositions in reservoir R_5, i.e. in the side-arm leading up to the ODS bed. R_5 buffer content was: 1- 40% acetonitrile / 60% 25 mM KH_2PO_4 and 2- 60% acetonitrile / 40% 25 mM KH_2PO_4. Note that all other reservoir compositions were as before, i.e. 60% 25 mM KH_2PO_4 / 40% acetonitrile buffer. Comparing the peaks for injection (a) and elution after the SCX column (b), the dilysine was recovered within 11 s. However, the peak intensity was greatly reduced for elution after the ODS column (b). It was presumed that the acetonitrile content in the elution buffer (40%) was too low for efficient elution off the

hydrophobic column: the peptide was sorbed at the head of the ODS column. Higher acetonitrile content in reservoir R_5 (60%) resulted in the trace shown in Figure 2.13c. The resulting peak area for dilysine after the SCX column was 3,246 a.f.u.(s). The peak area after the ODS column for 40% acetonitrile was 494 a.f.u.(s) and 1,744 a.f.u.(s) for 60% acetonitrile. The 60% acetonitrile composition was therefore more efficient at displacing the peptide through the ODS bed. However, comparing peak elution times, 11.1 s after the SCX versus 13.4 s after the ODS at 60% acetonitrile, one can conclude that the peptide was not sorbed on the ODS bed; the low peptide recovery could therefore not be explained by high sorption on the hydrophobic bed. The low recovery can be explained by looking back to Figure 2.12 for the microdevice design: the microchannel leading to R_5, used to alter the buffer condition in the main separation microchannel, was open. A weir and packed ODS bed was located just below the meeting point between this open channel and the main separation microchannel. The weir and bed section constituted a region of high resistance to flow: sample eluting from the SCX bed preferentially entered the low resistance microchannel, i.e. the open channel to R_5. From experimental data shown in Figure 2.13c, 60% acetonitrile percent in the open channel minimized loss. Higher acetonitrile content reduced EOF in the side-channel compared to EOF in the separation channel. At this acetonitrile content, the preferred flow for the analyte plug was through the higher EOF microchannel; the sample plug could then partially overcome the bed-induced backpressure and be driven through the separation bed.

The microdevice design was therefore not efficient: adding an open side-channel just above the densely-packed ODS bed resulted in sample loss. The experiments also implied that acetonitrile percent could not freely be tuned to maximize separation efficiency in the reverse-phase system. Finally, the possibility of efficient buffer mixing at the meeting point of the side-channel and main separation channel before reverse-phase separation was doubtful due to the EOF difference between high versus low percent acetonitrile regions. Further evidence of this is seen in Figure 2.13c: the elution time for dilysine after the ODS column under 40% versus 60% acetonitrile in the side-channel was equal (13.6 s versus 13.4 s).

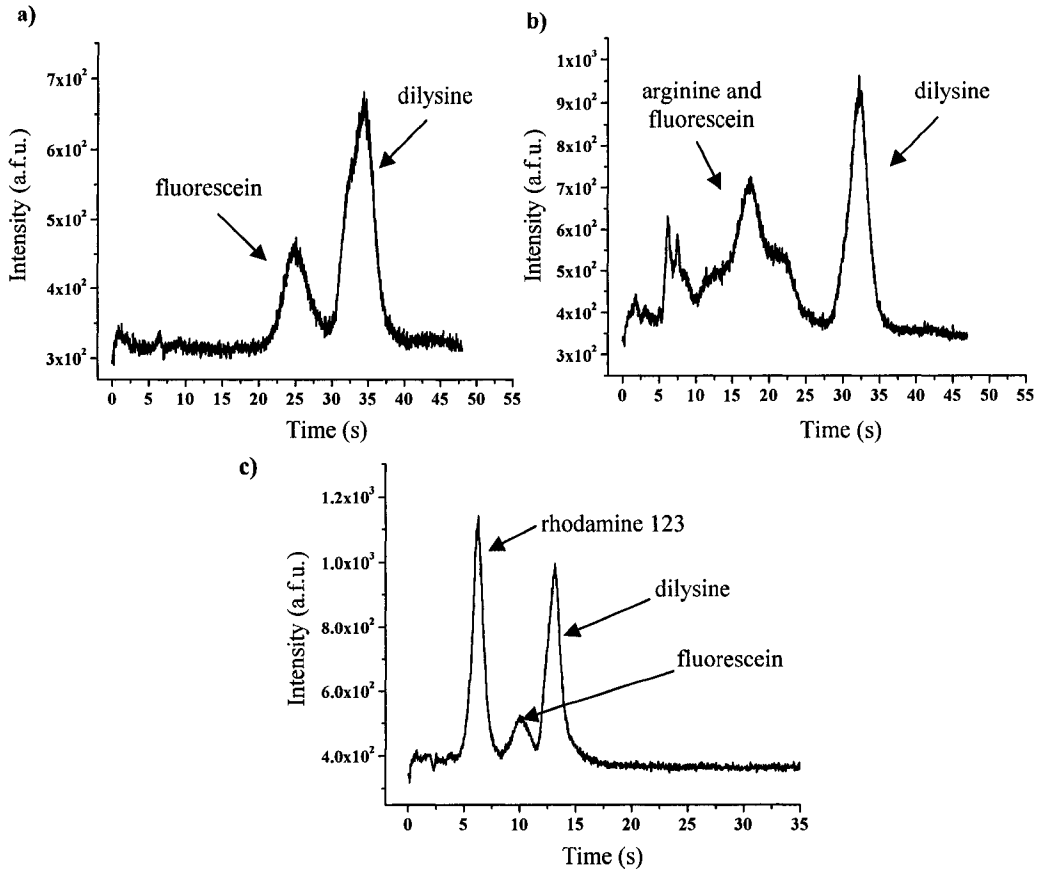

Figure 2.14 Elution on the Two-Column System- Elution after the ODS column for mixtures of a) fluorescein and dilysine, b) fluorescein, dilysine and arginine and c) fluorescein, dilysine and rhodamine 123. All samples were 50 nM. Buffer: 60% 25 mM KH_2PO_4 / 40% acetonitrile at pH 7.0. Parameters: for a) and b) injection: 10 s at 0.5 kV, separation: 1 kV with –250 V pushback. For c) injection: 10 s at 0.5 kV, separation: 2 kV with –400 V pushback.

A second problem, unrelated to microdevice design, was identified. For efficient separations in both dimensions, analysis in the second dimension must be faster than in the first. Peaks that are not separated during the first separation can then be separated in the second, given the right chemistry. Figure 2.14a presents the electrochromatogram resulting after the ODS column for the separation of a mixture of dilysine and fluorescein (both 50 nM, in separation buffer). Parameters: injection at 0.5 kV for 10 s and separation at 1 kV with – 250 V pushback, all buffers at 40% acetonitrile / 60% 25 mM KH_2PO_4. Earlier studies on the SCX single column microdevice showed fluorescein eluting from the SCX column within ~ 3 s in a sharp peak because it did not interact with

the SCX column. Here, fluorescein eluted at 25 s: it therefore interacted with the ODS phase. From the resulting migration time and excessive bandbroadening of the peak, the second separation is slow and inefficient: an analyte co-eluting from the SCX bed with fluorescein would be difficult to separate in the second dimension. Figure 2.14b illustrates this point. A mixture of three components, dilysine, fluorescein and arginine (all 50 nM in separation buffer), were tested, the electrochromatogram presents the elution after the ODS column. Parameters: injection at 0.5 kV for 10 s and separation at 1 kV with – 250 V pushback, all buffers at 40% acetonitrile / 60% 25 mM KH_2PO_4. Electrochromatogram of arginine after the SCX bed resulted in an elution time of 6 s at 1 kV: the sample therefore showed a weak interaction with the SCX bed. Figure 2.14b shows both fluorescein and arginine interacting with the ODS column: the fluorescein peak is seen over a broad baseline shift from the arginine elution. Both addition of 70% acetonitrile in the side arm and higher separation voltage (2.5 kV with – 500 V pushback) did not result in three resolved peaks. Therefore, the slow separation combined with peak broadening contributed to the collapsing of the two peaks and no separation was possible.

The method did work in one instance: Figure 2.14c shows the resulting electrochromatogram, after the ODS bed, for a mixture of fluorescein, rhodamine 123 and dilysine (all 50 nM in buffer). Parameters: injection at 0.5 kV for 10 s and separation at 2 kV with – 400 V pushback, all buffers at 40% acetonitrile / 60% 25 mM KH_2PO_4. The three peaks are resolved, the first peak being rhodamine 123, the second, fluorescein and third, dilysine. The interest in this lies in the reversal in elution order from elution from the SCX versus elution from the ODS. Rhodamine 123, being positively charged, will interact with the SCX phase and therefore elute from it after fluorescein. From the figure, rhodamine 123 interacts weakly with the ODS phase and elutes quickly, whereas fluorescein shows a large interaction, slowing down its elution through the ODS bed: the elution order was reversed.

2.5.CONCLUSION

Bead-based, on-chip strong cation exchange capillary electrochromatography was studied under laser induced fluorescence detection. The resulting column efficiencies on the 2 mm packed bed for the three test peptides studied were: 196,000 plates/meter for dilysine, 400,000 plates/meter for trilysine and 238,000 plates/meter for tetralysine. At

60 mM buffer concentration, van Deemter plot analysis showed that both trilysine and tetralysine were Eddy-diffusion limited. For dilysine, longitudinal diffusion was the limiting factor for efficient separation in the flow rates range probed. The two-column system studied showed the limitation of the geometry proposed in the face of significant EOF mismatches induced by the column packings; the opened side-channel used brought about sample loss and prevented efficient mixing of ODS-compatible buffer at the head of the ODS column.

2.6. REFERENCES

(1) JACOBSON, S. C.; HERGENRODER, R.; KOUTNY, L. B.; RAMSEY, J. M. *ANALYTICAL CHEMISTRY* **1994**, *66*, 2369-2373.

(2) XU, W.; UCHIYAMA, K.; SHIMOSAKA, T.; HOBO, T. *JOURNAL OF CHROMATOGRAPHY A* **2001**, *907*, 279-289.

(3) XU, W.; UCHIYAMA, K.; HOBO, T. *CHROMATOGRAPHIA* **2002**, *23*, 131-138.

(4) OLESCHUK, R. D.; SHULTZ-LOCKYEAR, L. L.; NING, Y.; HARRISON, D. J. *ANALYTICAL CHEMISTRY* **2000**, *72*, 585-590.

(5) JEMERE, A. B.; OLESCHUK, R. D.; OUCHEN, F.; FAJUYIGBE, F.; HARRISON, D. J. *ELECTROPHORESIS* **2002**, *23*, 3537-3544.

(6) JEMERE, A. B.; OLESCHUK, R. D.; HARRISON, D. J. *ELECTROPHORESIS* **2003**, *24*, 3018-3025.

(7) RO, K. W.; CHANG, W.-J.; KIM, H.; KOO, Y.-M.; HAHN, J. H. *ELECTROPHORESIS* **2003**, *24*, 3253-3259.

(8) CERIOTTI, L.; ROOIJ, N.; VERPOORTE, E. M. J. *ANALYTICAL CHEMISTRY* **2002**, *74*, 639-647.

(9) HE, B.; TAIT, N.; REGNIER, F. *ANALYTICAL CHEMISTRY* **1998**, *70*, 3790-3797.

(10) HE, B.; JI, J.; REGNIER, F. *JOURNAL OF CHROMATOGRAPHY A* **1999**, *853*, 257-262.

(11) SLENTZ, B. E.; PENNER, N. A.; LUGOWSKA, E.; REGNIER, F. *ELECTROPHORESIS* **2001**, *22*, 3736-3743.

(12) SLENTZ, B. E.; PENNER, N. A.; REGNIER, F. *JOURNAL OF CHROMATOGRAPHY A* **2002**, *948*, 225-233.

(13) SLENTZ, B. E.; PENNER, N. A.; REGNIER, F. *JOURNAL OF SEPARATION SCIENCE* **2002**, *25*, 1011-1018.

(14) PUMERA, M. *TALANTA* **2005**, *66*, 1048-1062.

(15) NGOLA, S. M.; FINTSCHENKO, Y.; CHOI, W. Y.; SHEPODD, T. J. *ANALYTICAL CHEMISTRY* **2001**, *73*, 849-856.

(16) LAZAR, I. M.; LI, L.; YANG, Y.; KARGER, B. L. *ELECTROPHORESIS* **2003**, *24*, 3655-3662.

(17) BANDILLA, D.; SKINNER, C. D. *JOURNAL OF CHROMATOGRAPHY A* **2004**, *1044*, 113-129.

(18) ERICSON, C.; HOLM, J.; ERICSON, T.; HJERTEN, S. *ANALYTICAL CHEMISTRY* **2000**, *72*, 81-87.

(19) SLENTZ, B. E.; PENNER, N. A.; REGNIER, F. *JOURNAL OF CHROMATOGRAPHY A* **2003**, *984*, 97-107.

(20) GOTTSCHLICH, N.; JACOBSON, S. C.; CULBERTSON, C. T.; RAMSEY, J. M. *ANALYTICAL CHEMISTRY* **2001**, *73*, 2669-2674.

(21) ROCKLIN, R. D.; RAMSEY, R. S.; RAMSEY, J. M. *ANALYTICAL CHEMISTRY* **2000**, *72*, 5244-5249.

(22) RAMSEY, J. D.; JACOBSON, S. C.; CULBERTSON, C. T.; RAMSEY, J. M. *ANALYTICAL CHEMISTRY* **2003**, *75*.

(23) CHEN, X.; WU, H.; MAO, C.; WHITESIDES, G. M. *ANALYTICAL CHEMISTRY* **2002**, *74*, 1772-1778.

(24) WANG, Y.; CHOI, M. H.; HAN, J. *ANALYTICAL CHEMISTRY* **2004**, *76*, 4426-4431.

(25) LI, Y.; BUCH, J. S.; ROSENBERGER, F.; DEVOE, D. L.; LEE, C. S. *ANALYTICAL CHEMISTRY* **2004**, *76*, 742-748.

(26) BUCH, J. S.; LIU, J.; YANG, S.; TSAO, C.-W.; SONG, T.; SIVANESAN, P.; PHALNIKAR, K.; LEE, C. S.; DEVOE, D. L., TOKYO 2006; 1579-1581.

(27) HERR, A. E.; MOLHO, J. I.; DROUVALAKIS, K. A.; MIKKELSEN, J. C.; UTZ, P. J.; SANTIAGO, J. G.; KENNY, T. W. *ANALYTICAL CHEMISTRY* **2003**, *75*, 1180-1187.

(28) SWEEDLER, J. V.; SHEAR, J. B.; FISHMAN, H. A.; ZARE, R. N.; SCHELLER, R. H. *ANALYTICAL CHEMISTRY* **1991**, *63*, 496-502.

(29) SEILER, K.; HARRISON, D. J.; MANZ, A. *ANALYTICAL CHEMISTRY* **1993**, *65*, 1481-1488.

(30) FAN, Z. H.; HARRISON, D. J. *ANALYTICAL CHEMISTRY* **1994**, *66*, 177-184.

(31) YE, M. L.; ZOU, H. F.; LIU, Z.; NI, J. Y. *JOURNAL OF CHROMATOGRAPHY A* **2000**, *869*, 385-394.

CHAPTER 3 DESIGN OF A SILICON-BASED MICROFLUIDICS DEVICE FOR PROTEIN ANALYSIS

3.1.INTRODUCTION

Microfluidic platforms for proteome analysis have been introduced; most focus on separation strategies for protein or peptide analysis[3-6]. Few truly multiplexed microfluidic systems have been reported, i.e. microdevices including sample processing, separation and detection. Regnier presented a multi-column system in polydimethylsiloxane (PDMS) for laser induced fluorescence detection of a protein digest[7]. The microdevice included 1) beads for protein digestion, 2) beads for affinity capture of digested peptides and 3) a micromachined column for capillary electrochromatography (CEC) of eluted peptides. Wang presented a two-bed system for on-chip protein digestion on trypsin beads, peptide pre-concentration on solid phase extraction (SPE) beads, capillary electrophoresis of eluted peptides and electrospray ionization mass spectrometric (ESI MS) detection[8]. Taylor further developed the system: 20 channels, each containing the trypsin and SPE beds, were built on a microdevice[9]. The channels met at the inlet and outlet of the microdevice: the inlet was fitted with a capillary for isoelectric focusing (IEF) of a protein sample and the outlet, with an ESI emitter for on-line ESI MS of eluting peptides. After capillary IEF, proteins would be fractionated into one of the 20 microchannels on the fluidic device, followed by pressure-driven trypsin digestion, SPE of digested peptides and elution of peptides fractions for ESI MS analysis. Since the SPE-to-MS distance increased from channel-to-channel, discrete peptides fractions were expected to elute to the MS, each corresponding to a fractionated protein. However, due to poor bead packing reproducibility, elution to the mass spectrometer was not directly correlated with channel length.

Photolithographic processes for microfabrication are well-known and result in highly uniform microstructures[10]. In an effort to solve the non-uniform flow problem from Talyor's microdevice, this study presents a microfluidic platform with lithographically-defined beds for on-chip protein digestion, peptide preconcentration and ESI MS detection. A flow chart of the device fabrication process is shown on p. 103.

3.2.CHIP DESIGN

Figure 3.1 is a schematic of the proposed microdevice (electrodes not shown); it is based on the one studied by Taylor. To reduce the difficulty in assembling the final platform, two simplifications were introduced. First, the number of channels was

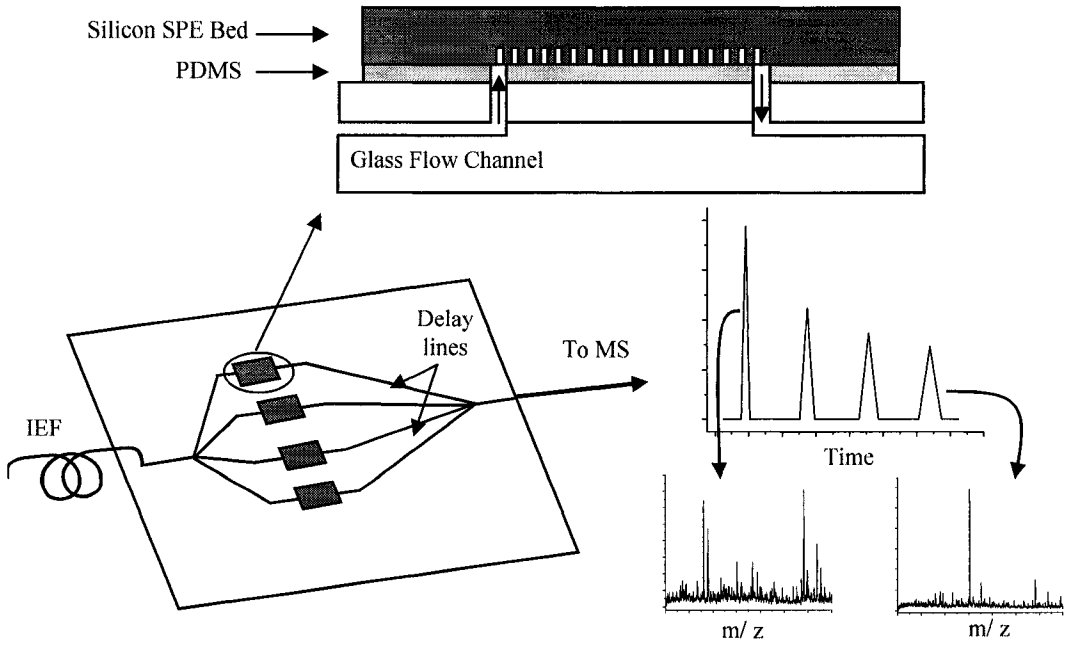

Figure 3.1 Silicon-Based Multiplexed Device for Protein Analysis- The complete platform (bottom left) and side-view of one of the 4 microchannel (top) is depicted (grounding electrodes not shown). Microfabricated silicon make-up the SPE beds, bonded to the glass microchannels through a PDMS layer. Protein fractions are sorbed on the ODS-derivatized silicon bed. Following on-bed trypsin digestion, resulting peptides are released. Delay lines allow for discrete fractions, each corresponding to a fractionated protein, to be analyzed by pressure-driven ESI MS (bottom right).

reduced from 20 to 4. Secondly, each channel contains only one bed, the solid phase extraction (SPE) bed, for trapping of the incoming protein fraction, on-bed digestion and peptide elution.

As shown in Figure 3.1, the beads are replaced by a silicon bed, coated with a C18 phase to act as an SPE bed. The lower glass wafer contains the microchannels for solution flow, the upper glass wafer has drilled access holes for solution flow to the silicon bed, and the polydimethylsiloxane (PDMS) layer acts as "glue" in the system. The silicon beds contain an array of 5 μm square posts etched 10 μm deep, with a separation between them of 1.6 to 1.8 μm, making them porous. Since these posts are defined by well-known lithographic techniques, they are uniform, making the resulting

bed-to-bed porosity uniform. The elution profile will then be controlled by SPE-to-MS microchannel length and sequential elution, dependent upon channel length, will result.

Silicon was chosen for the SPE bed for the following reasons: first, it can be etched anisotropically and therefore high bed porosity (and loading capacity) with efficient mass transport to and from the stationary phase can be obtained. The Regnier group described microstructures in quartz and PDMS[1, 11-14]. Quartz can be etched anisotropically; however, quartz deep dry etching is not a process available at the University of Alberta Nanofab at present, whereas silicon etching is done routinely. Silicon has another advantage over quartz: each Si column can be coated with the C18 phase independently of the rest of the device, restricting protein adsorption to the Si beds. High aspect ratio PDMS microstuctures bend and stick to nearby PDMS structures, making PDMS beds a poor choice. Slentz et al.[12] studied the effect of geometry on CEC separation efficiencies and found that 5.5^2 μm^2 PDMS microstructures must be at most 5.5 μm high and at least 4 μm apart to prevent sticking, producing beds with very low loading capacity and low mass transport to and from the stationary phase.

The following chapter is divided in three main sections: 1- glass processing, 2- silicon processing and 3- glass-to-silicon bonding. In the first section, the following are described: microchannel processing in the lower glass, access hole drilling in the upper glass, bonding the two glass wafers and ESI interface processing. Glass processing was complicated by the need to minimize the dead volume in the chamber connecting the silicon bed with the underlying glass microchannels. For an eluting peak, variance will be directly proportional to V^2, the chamber volume[15]; therefore, to obtain discriminate peak elution in the multichannel device, a 70 μm thick upper glass layer was used. The silicon bed lengths were small compared to glass microchannels length, to avoid electrical breakdown and current passage through the silicon during the experimental process. For silicon processing, as explained in the previous paragraph, beds containing high aspect ratio microstructures separated by a minimal length needed to be fabricated. However, since the lower limit for the mask generator at the University of Alberta's Nanofab was not known, several mask designs were tested for efficient silicon bed photolithography. From these, the final mask design was chosen and used for silicon processing: silicon photolithography, etching and octadecylsilyl (ODS) derivatization are

described. In the last section, several approaches to efficiently bond the processed glass and silicon structures presented in the two previous sections are discussed. Because 70 μm 0211 glass was used as the upper layer, and 0211 does not anodically bond to silicon due to its low sodium content and thermal expansion coefficient, this process could not be used. Initial tests showed that processing un-cured PDMS or glue did not result in a satisfactory microdevice. Two processes resulting in satisfactory microdevices are described: one that reduced chamber dead volume through the used of PDMS having a thickness of less than 20 μm, and the second involving PDMS with thickness larger than 600 μm.

3.2.1. GLASS WAFER

3.2.1.1. MASK DIMENSIONS

Figure 3.2a shows the L-Edit output for the mask used in the glass lithography process (grey indicates clear on the mask). Figure 3.2b is an expanded view of the point of contact of the 4 channels on the multichannel device. Masks were made by the University of Alberta Nanofab on 5 in x 5 in soda lime glass, 0.09 in thick. The mask is divided into two sections, as shown in Figure 3.2a. The upper section contains single channels with 6 mm, 4 mm and 2 mm discontinuities for single channel analysis of 6, 4 and 2 mm silicon column lengths. In the lower section, the multichannel device is shown. All discontinuities are 2 mm in length, the variable region lengths are indicated; they vary, as mentioned before, by 0.5 cm from channel-to-channel. The channel width (60 μm) and depth (20 μm) were in line with those of the devices studied by Taylor, with two modifications shown in Figure 3.2b, in the expanded view of the fractionation region. First, all channel-to-channel angles were 30°, for an even flow distribution. Second, to reduce the dead volume created by the merger of the 4 channels, each was tapered to a 10 μm width. Assuming an average 25 μm etch depth and a 1:1 isotropic etch ratio, a device with 60 μm width throughout will have its 4 channels merged over a 200 μm length. For the tapered device shown, this length is reduced to 100 μm, reducing the dead volume. The lower limit on the tapered width is set by restrictions in photoresist developing during lithography. Developing widths smaller than 10 μm would imply overdeveloping the 60 μm regions.

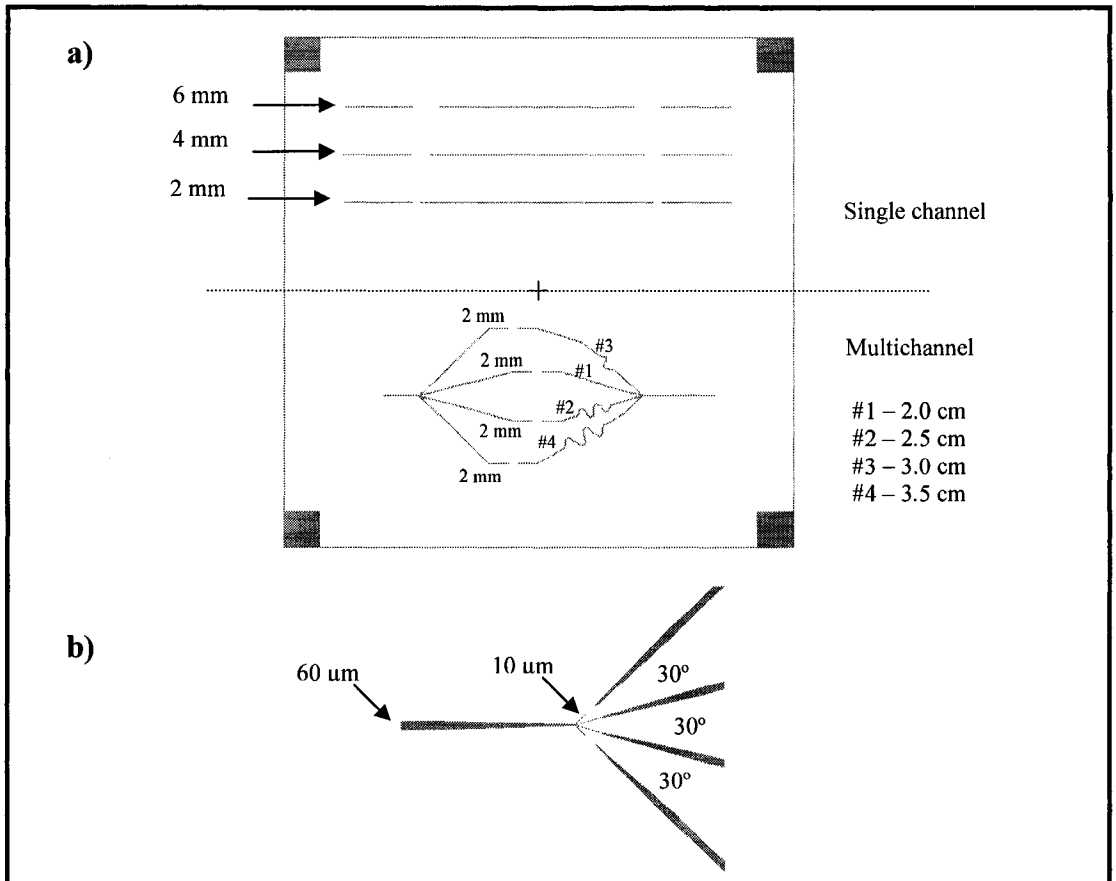

Figure 3.2 Mask Design for Glass Processing- a) Mask design for the complete wafer and b) close-up on the fractionation region of the multichannel device. The wafer contains six single channel devices, for single channel analysis in 2, 4 and 6 mm silicon bed lengths and one multichannel device, consisting of four 2 mm silicon beds. In b) the fractionation region was tapered from 60 μm to 10 μm width, to reduce the dead volume. All channels were kept at 30°, for even flow distribution.

3.2.1.2. LOWER GLASS: MICROFABRICATION

All microfabrication was done at the University of Alberta Nanofab facility and followed standard procedures published in the literature[16]. First, 4 in x 4 in Corning 0211 glass (600 μm thick, Precision Glass and Optics) was cleaned in piranha (H_2SO_4:H_2O_2 at 3:1), thoroughly rinsed with water, dried and loaded into the Lesker, two target, sputtering system (Kurt J. Lesker Company). With the system under vacuum (around 1.5 x 10^{-6} Torr), 30 nm chrome and 150 nm gold were sputtered, successively (parameters: 7

mTorr argon, Cr: 300 W for 3 minutes, Au: 75 W for 18 minutes). Photoresist (HPR 504, OCG Microelectronic Materials) was spin-coated onto the Cr/Au 0211 wafers (Solitec, 500 rpm for 10 s, 4,000 rpm for 40 s). The pieces were oven-baked for 30 minutes at 115 °C and left to re-hydrate at room temperature for 15 minutes. Both the mask and 0211 wafer were loaded onto the mask aligner (ABM Inc.), brought into contact and exposed to UV (λ: 365 nm for 4 seconds). The UV-exposed area of the photoresist was removed by rinsing for 25 seconds with a developer (354 Developer, Electronic Materials L.L.C.). After gold and chrome removal of the exposed areas (Au etching solution: $KI:I_2$ at 4:1, Cr etching solution: from Fujifilm), the glass wafer was immersed in a glass etching solution (H_2O:HF:HNO_3 , 66:20:14). The average target glass depth was 20 μm. To prepare the wafer for bonding to the upper glass wafer, excess photoresist was removed with acetone and the wafer given a piranha wash. Remaining gold and chrome were removed using the gold and chrome etchants.

3.2.1.3. UPPER GLASS: ACCESS HOLES DRILLING

As seen in Figure 3.1, access holes are drilled into the top layer leading to the Si bed. Two things must be considered for the drilling. First, the amount of dead volume must be minimized, minimizing band broadening (i.e. width) of the eluted peaks. Second, the access holes being in close proximity to each other (2 mm in the multichannel device), any excessive chipping at the drilled holes will prevent efficient bonding of the two 0211 glass wafers. This will lead to leakage at the holes or, worst-case scenario, to no bonding in the 2 mm space between the two holes. For these reasons, 70 μm thick Corning 0211 glass (Precision Glass and Optics) was chosen as the upper glass wafer and holes were drilled using 150 μm diameter drill bits (S300 series, TYCOM). Assuming a negligible PDMS thickness, the void volume generated by a 150 μm hole drilled into a 70 μm thick wafer would be:

$$V_{void} = \pi\,(75\ \mu m)^2\,(70\ \mu m) = 1.24 \times 10^6\ \mu m^3 \qquad (3.1)$$

or 1.24 nl added to the elution profile. Assuming a 0.25 μl/min flow rate to the mass spectrometer, this would translate into 0.3 s extra time added to the final elution, a negligible amount. Alignment is obviously crucial when drilling the holes. A sacrificial 600 μm 0211 wafer was processed as outlined in the last section, up to the first Cr/Au etching of the microchannels. The contrast between the clear microchannels that result

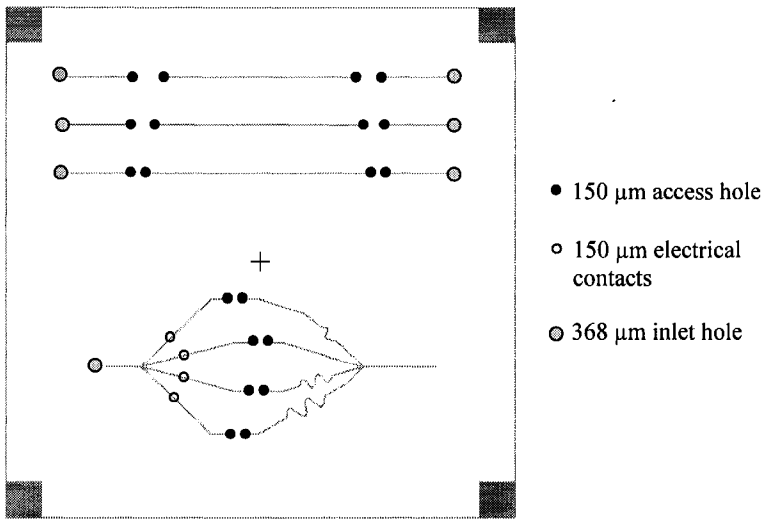

Figure 3.3 Position of the Drilled Holes on the 70 μm Wafer- Drilling for electrode contacts (150 μm diameter), inlet holes (368 μm diameter) and access holes (150 μm diameter).

and the remaining Cr/Au layer on top was used for alignment purposes. The 70 μm glass was then mounted on top of this visual aid using Crystalbond (#509, Aremco Products Inc.). This structure was setup on a XY translation stage at the drilling station (Model 7010, Servo Products Company). A loupe was used to align the drill bit with the microchannels on the visual aid. Once aligned, a drop of water was deposited on the glass wafer and the hole drilled. Figure 3.3 shows the position of the drilled access holes for the entire wafer.

Also shown in Figure 3.3 are inlet and electrical contact holes drilled in the 70 μm glass. A larger diameter drill bit, 368 μm, was used to drill the inlet holes to make coupling with the inlet capillary easier. In preliminary experiments, the inlet hole was drilled on the 600 μm side of the device. In this configuration, the device broke at the inlet because the 70 μm wafer was too thin to sustain the pressure produced in the final system. Inlet holes were therefore moved to the 70 μm glass in future experiments. The holes drilled to act as electrical contact during IEF experiments were 150 μm in diameter. These were positioned at a 1 cm radius around the inlet fractionation section. After the drilling process, the 70 μm glass was removed from the visual aid by heating on a hot

plate, which softens the Crystalbond, and immersed in an acetone bath (20 minutes twice) for partial removal of the Crystalbond.

3.2.1.4. BONDING

Bonding of the 70 and 600 μm glass wafers was complicated by the fragility of the 70 μm glass and the difficulty in aligning the two wafers. A 600 μm thick 0211 support wafer was used to hold the 70 μm glass, taking care of the fragility issue. Further, bonding of the two wafers was done on the ABM mask aligner (usually used for UV exposition during lithography, as mentioned in section 3.2.2.2.). This made alignment much less difficult than bonding by visual inspection, since the mask aligner has a CCD camera and a XY translation stage. The 600 μm wafer (with the microchannels) was mounted on the mask aligner in the mask position, and the 70 μm wafer (with the drilled holes) was mounted as the substrate. Once aligned, the two were brought into contact.

The complete bonding process was as follows: the 600 μm wafer (with the microchannels), the 70 μm wafer and its 600 μm support were first given a piranha wash. After thorough rinsing with water, the first wafer (with the microchannels) was dried, mounted on a ring holder and loaded into a high pressure washer (Micro Automation 2066, settings: 5 rinse cycles, 10 dry cycles). Similarly, the 70 μm glass was dried and mounted on a ring holder, with the support wafer mounted underneath it. The ring holder was then mounted in the high pressure washer, with the same rinse/dry cycle as above. Finally, the two wafers were mounted on the mask aligner, aligned and brought into contact. After this initial cold bonding process, the two wafers were irreversibly bonded in a thermal bonding oven (settings: room temperature to 440 °C at 10 °C/min hold 30 min, 440 °C to 473 °C at 2 °C/min hold 30 min, 473 °C to 592 °C at 2 °C/min hold 6 hours, 592 °C to 473 °C at 4 °C/min hold 30 min).

Initially, processing of the 70 μm wafer was difficult, therefore the very first bonded device consisted of two 600 μm wafers. The drilled access holes were 200 μm in diameter. As expected in section 3.2.1.3, channels with the 2 mm discontinuities did not bond: the closeness of the two 200 μm diameter drilled holes and chipping at their edge prevented efficient bonding. However, the 4 mm and 6 mm devices were bonded and used for single channel analyses.

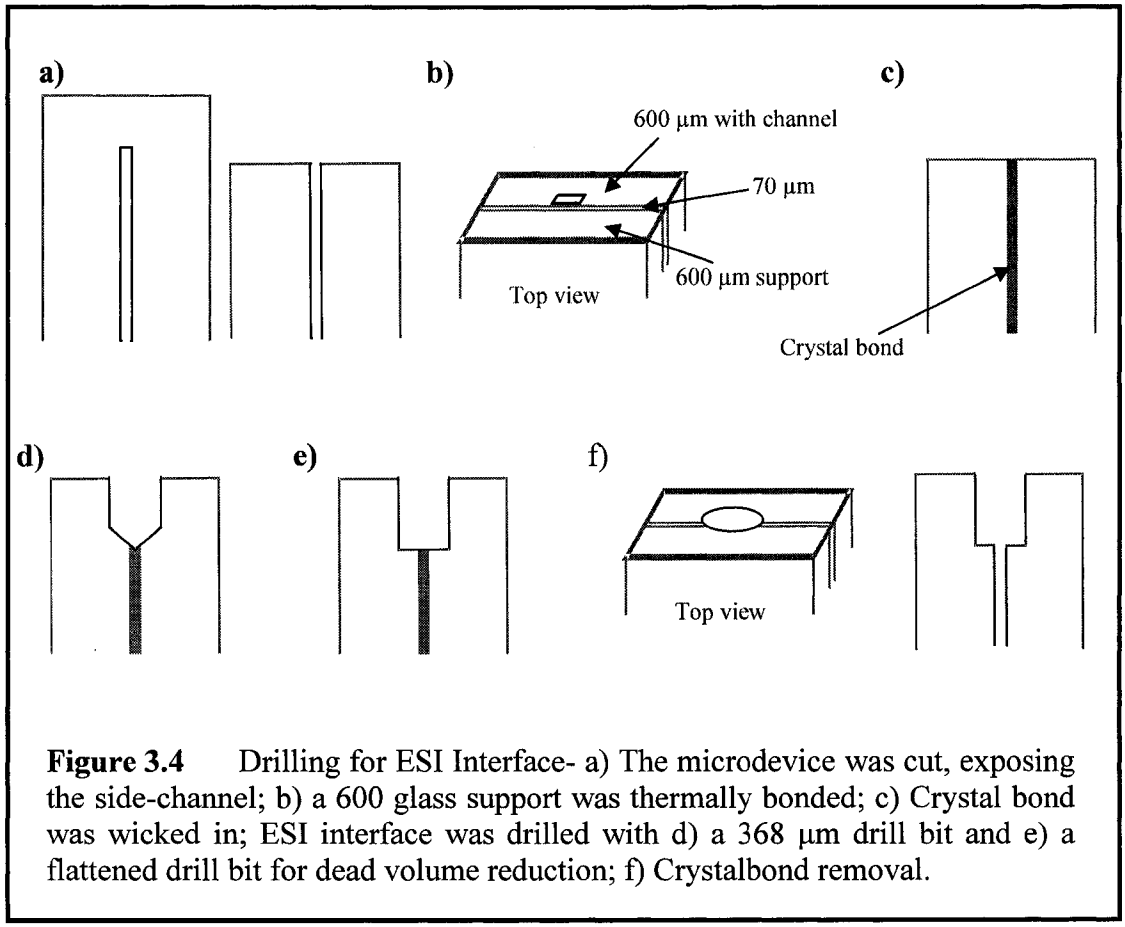

Figure 3.4 Drilling for ESI Interface- a) The microdevice was cut, exposing the side-channel; b) a 600 glass support was thermally bonded; c) Crystal bond was wicked in; ESI interface was drilled with d) a 368 μm drill bit and e) a flattened drill bit for dead volume reduction; f) Crystalbond removal.

3.2.1.5. ESI INTERFACE

Microdevice-to-ESI tip coupling has been described previously[17]. Here a description is given for the thermally-bonded device of the previous section, with reference to Figure 3.4. The fabrication of the ESI tips, made from 365 μm o.d., 50 μm i.d. capillary, is then described.

First, the edge of the chip was cut, exposing the microchannel to which the ESI tip will be connected, as shown in Figure 3.4a. For a 360 μm o.d. capillary to be inserted into the edge of the device, its 50 μm i.d. lined up with the microchannel, the 70 μm thick glass must be reinforced with a thicker glass plate. Therefore, a 600 μm thick 0211 glass piece, approximately one square centimeter in size, was thermally bonded to the edge of the device, on the 70 μm side (Figure 3.4b). For this process, both the device and square piece were given a piranha wash, thoroughly rinsed with water and dried, brought into contact and put in the thermal bonding oven (settings as described in section 3.2.2.4.).

Following this, Crystalbond was inserted into the edge of the device, by heating the device on a hot plate and letting a small drop of Crystalbond be drawn into the microchannel (Figure 3.4c). Upon cooling, the Crystalbond hardens, preventing glass chips produced during drilling from entering the microchannel. The edge of the chip was polished to make visualization of the hole easier, it was then mounted on a XY translation stage at the drilling station. A 368 μm drill bit (#29 series 225, TYCOM) was used for drilling (Figure 3.4d). A dead volume is associated with the triangular shape of the hole drilled. To reduce this volume, a second 368 μm drill bit, its head flattened by manual polishing, was used for the final drilling (Figure 3.4e). The drilled end of the device was kept in water overnight. The Crystalbond was removed by heating the device on a hot plate while applying vacuum to the drilled edge (Figure 3.4f). For complete removal of the Crystalbond, the drilled edge of the device was soaked in acetone for 20 minutes and put in the thermal bonding oven overnight (settings as described in section 3.2.2.4.).

ESI tips were prepared as follows: the polyamide coating was removed from a small middle section of a 15 cm length capillary (360 μm o.d., 50 μm i.d.). The capillary was then loaded into a capillary puller (Micropipette Puller, model P-2000, Sutter Instrument Compagny). Pulling resulted in a diameter around 3 μm (settings: Heat = 260, Velocity = 42, Delay = 30). Tips were loaded into the Lesker two target sputtering system. With the system under vacuum (around 1.5 x 10^{-6} Torr), 30 nm chrome and 150 nm gold were sputtered, successively (as described in section 3.2.2.2). The 3 μm tip was opened to around 10 μm by careful scratching with a syringe needle. Tips were inserted into the ESI interface of the microchip just before being used. Before inserting the tip, it was rinsed with ultrapure water (Millipore Canada) and filtered (0.2 μm, Chromatographic Specialties Inc.). The tip was placed into the drilled edge of the microdevice and secured with epoxy.

3.2.2. SILICON WAFER

A basic surface area calculation was done to gauge the possible dimensions of the silicon SPE bed. Dimensions for the SPE beds in Taylor's device[9] were: 2 mm length, 400 μm wide and 120 μm deep, packed with 60 μm diameter C18 beads. The total bead surface area was calculated to be 5 x 10^6 μm^2. Assuming a silicon bed consisting of an array of 5 μm square posts separated by 1 μm, total width of 400 μm etched 10 μm deep,

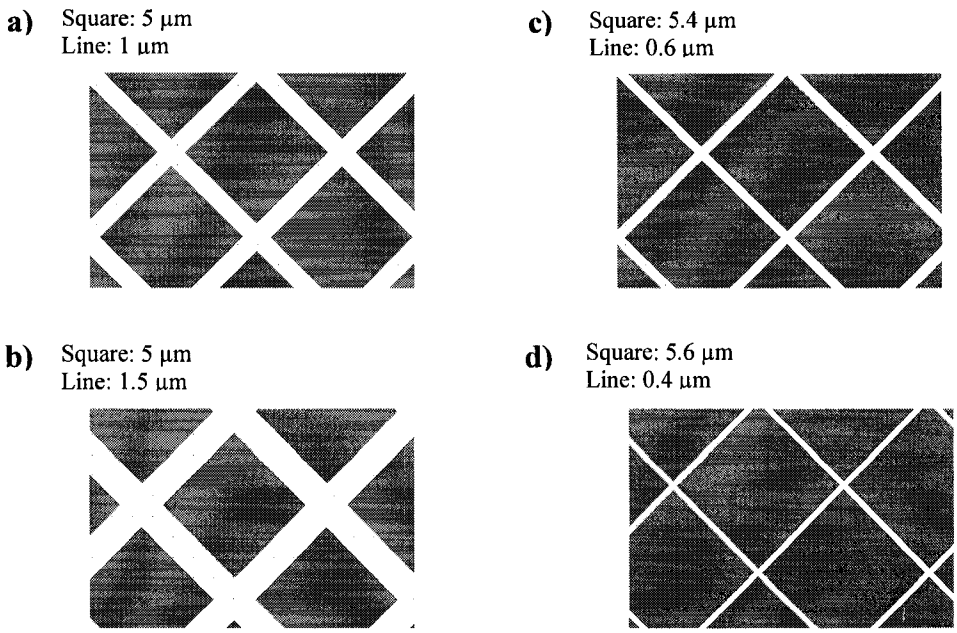

Figure 3.5 L-Edit Output for the Test Mask- Four different square/line size combinations were used to test the lower limit on the mask pattern generator: a) 5 μm square, 1 μm line; b) 5 μm square, 1.5 μm line; c) 5.4 μm square, 0.6 μm line; d) 5.6 μm square, 0.4 μm line. Only test columns a and b could be developed

a 2 mm bed length would correspond to a total surface area of 4.4 x 10^6 μm^2 (only the 5 x 10 μm side walls of the Si columns were included in the surface area calculation). A 2 mm column was then chosen for the multichannel device. There were uncertainties concerning the amount of backpressure the inlet port to the microdevice could sustain. Therefore a short column length, 2 mm in this case, seemed like a wise choice.

3.2.2.1. TEST MASK FOR SILICON WAFER

The mask for the silicon wafer processing was made at the University of Alberta Nanofab facility on 5 in x 5 in soda lime glass, 0.09 in thick, using a DWL 200 Pattern Generator. At the time of making this mask, the lower limit reached by the pattern generator without added optics was not known. Therefore a mask was designed to test this limit. Figure 3.5 presents the L-Edit output for 4 tested columns on a single mask, magnified to show the different sizes (grey indicates chrome on the mask). The target on-mask size for the square was 5 μm and 1 μm for the line. Processing of the mask after the pattern has been written involves developing the exposed photoresist followed by

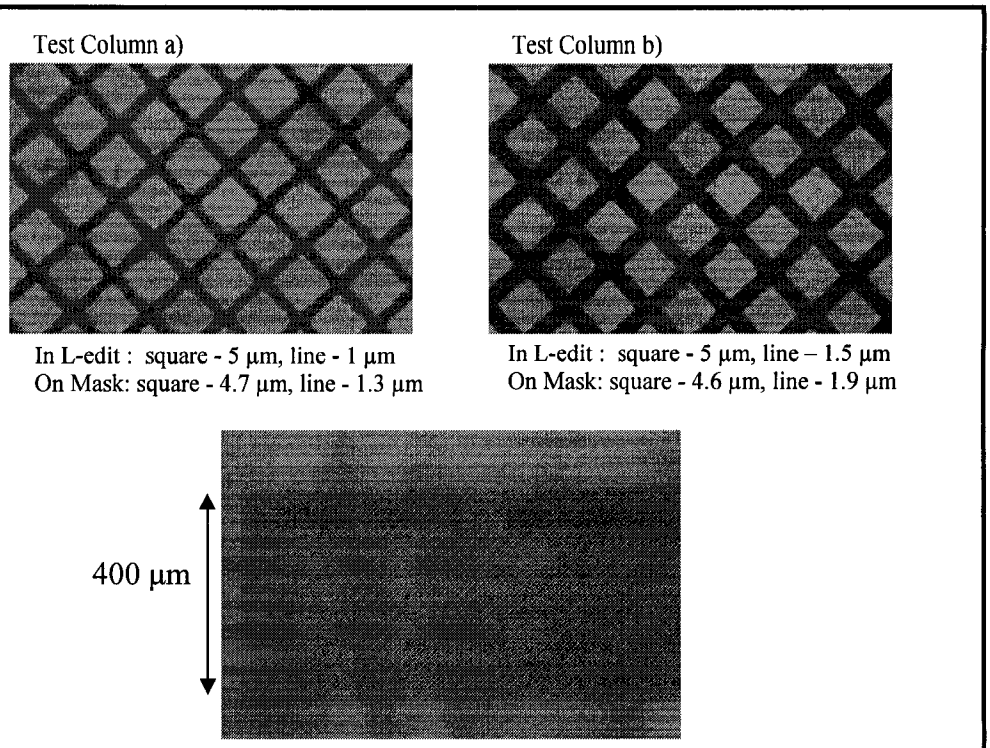

Figure 3.6 Test Column Results on Mask- Test column a (top left) and b (top right), with L-edit and critical dimension (CD) measurements. Long-range homogeneity is shown for the 400 μm wide test column a (bottom). Test column b was slightly over-etched.

chrome etching of the developed areas. According to the Nanofab personnel, these two processes can add as much as 0.7 μm on the developed areas, due to photoresist overdeveloping and chrome over-etching. For example, a clear line designed to be 10 μm in width will most likely be 10.7 μm wide on the finished mask. This was taken into consideration when designing the test mask.

After processing, only test columns a and b could be developed, setting the lower limit on the mask generator to 1 μm. Column b had to be over-developed and its chrome over-etched for column a to be processed correctly. Pictures of the developed columns are shown in Figure 3.6. Also shown are critical dimension (CD) measurements taken for each (CD measurements taken with an inspection microscope, model INM 100, Leica Microsystems). The results shown are for 10 measurements taken randomly on the surface. The bottom picture in Figure 3.6 is an expanded view of test column a, showing the long-range homogeneity that resulted.

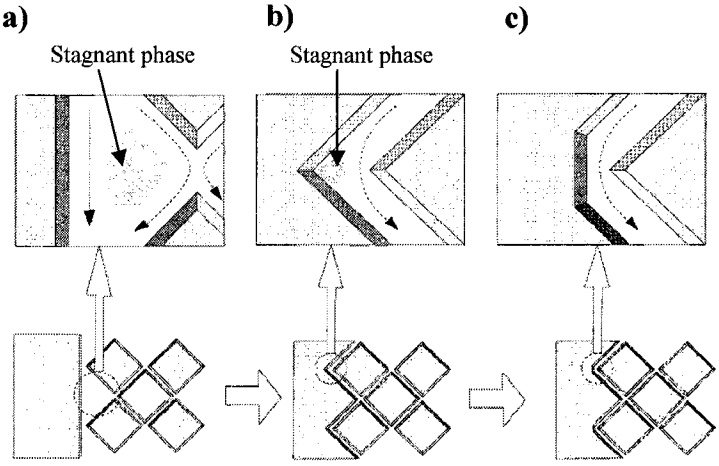

Figure 3.7 Potential "Wall-Effects" in Micromachined Columns- Geometry depicted in a) has high amount of stagnant mobile phase, unswept during chromatography, design b) reduces the problem and c) eliminates it. Adapted from He et al.[1], with permission from authors.

In the case of column a, 0.3 μm was added to the developed lines. During mask processing, the developing and chrome etch times were kept to a strict minimum, resulting in a smaller added line width than originally expected. For column b, 0.4 μm was added, because of the slight over-developing and over-etching mentioned previously. Two other observations were obvious: corners were rounded off and ripples were seen on the edges, showing the limitations of the pattern generator. The L-Edit file was sent to Adtek Photomask for an estimate on the cost for the mask to be done by e-beam lithography, a process that would minimize these two issues. For a critical dimension of 0.1 μm (i.e. the length between the minimum and the maximum of the ripple on the edge is 0.1 μm), the estimate was $2,000, much more expensive than the Nanofab mask processing. It was assumed that the ripple and rounding affect would not be an issue, so long as the column was homogeneous. Dimensions of test column a were then chosen for the mask, described in the following section, to be processed at the Nanofab.

3.2.2.2. MASK FOR SILICON WAFER

Slentz et al.[12] studied column performance as a function of post geometries in lithographically-defined PDMS columns, concluding that those consisting of square-shaped were the most efficient. He et al.[1] discussed the geometry needed to reduce

stagnant mobile phase at the wall of the column; Figure 3.7 was taken from the paper. The geometry shown in Figure 3.7a would have the worst "wall-effect," a large mobile phase volume would be left un-swept during chromatography. In Figure 3.7b, a smaller stagnant mobile phase volume would result between the posts and the chamber wall. No wall-effect would be seen in the geometry shown in Figure 3.7c.

Figure 3.8 presents the L-Edit output for the fabricated mask (grey represents chrome on the mask). Overall, four 2 mm columns, two 4 mm and two 6 mm columns were patterned on one mask. Windows, 500^2 μm^2 in size, were also incorporated as alignment markers during the dicing stage. The first output, Figure 3.8a, is the entire 4 in

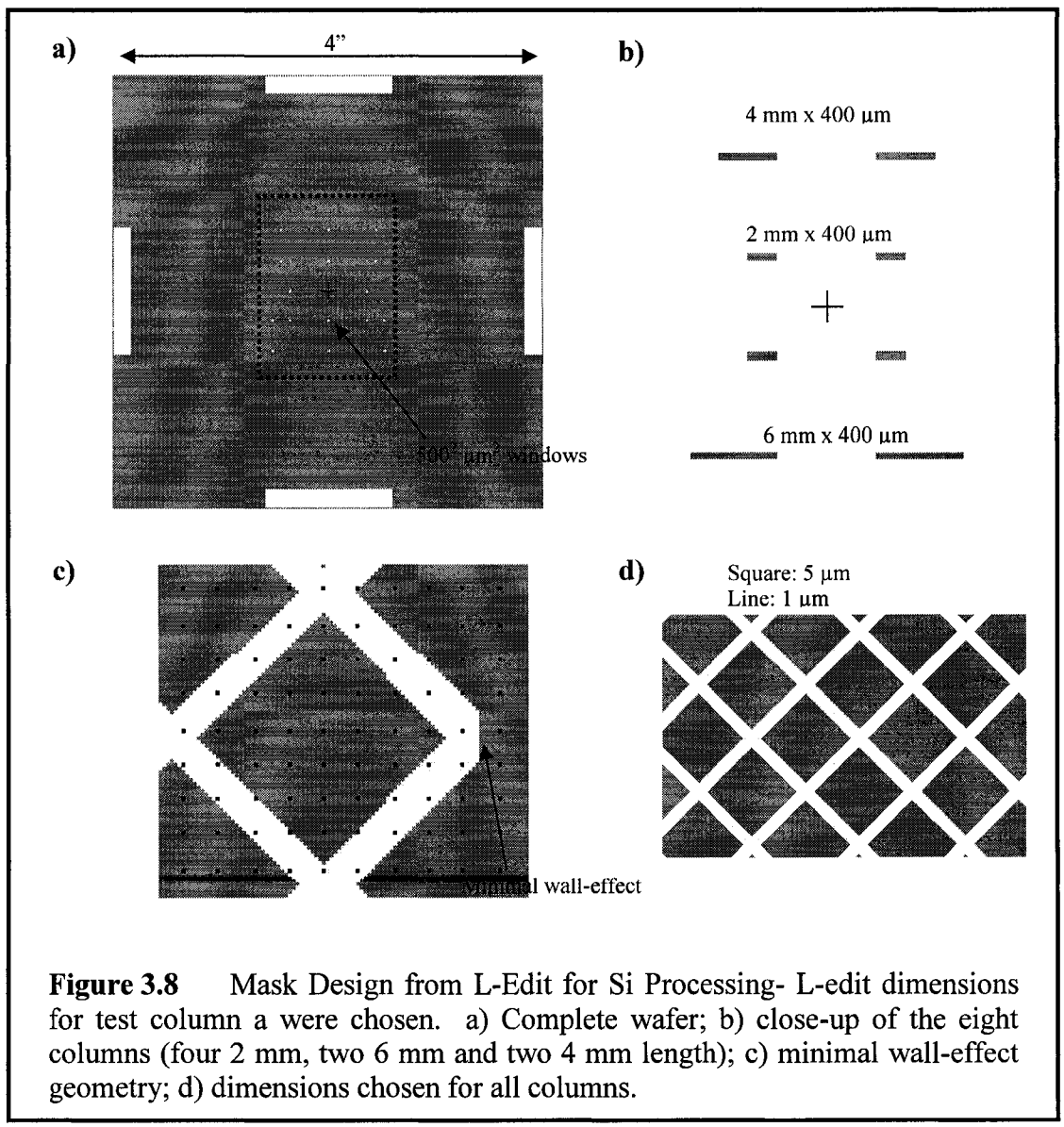

Figure 3.8 Mask Design from L-Edit for Si Processing- L-edit dimensions for test column a were chosen. a) Complete wafer; b) close-up of the eight columns (four 2 mm, two 6 mm and two 4 mm length); c) minimal wall-effect geometry; d) dimensions chosen for all columns.

design; Figure 3.8b is a magnification of the region outlined in Figure 3.8a showing the eight columns on a white background; in Figure 3.8c, the region at the end of one column has been magnified, showing the low wall-effect design discussed above; and Figure 3.8d presents the posts and line widths.

3.2.2.3. SILICON RESULTS

For a small percent exposure of the silicon wafer surface, a generic Bosch process will work reproducibly with little input from the user. However, cryogenic ICP RIE, which produces smooth sidewalls, is more involved and takes much time to develop for one's specific wafer design. The Bosch process was thus chosen as the etching procedure, despite the rough side-walls it generates.

Silicon processing is described below, following well-known lithographic procedures[18]. Silicon wafers (4 in diameter, p-doped/boron, <111>, Silicon Valley Microelectronics Inc.) were cleaned in piranha solution, rinsed thoroughly with water, dried and loaded into a thermal oxidation system (Minibrute Furnace). The tube furnace was kept at 900 °C for 3 hours, steam being fed continuously into it (20 psi nitrogen flow). This wet oxidation process resulted in a 0.3 μm oxide growth. Because photoresist does not adhere well to hydrophilic surfaces such as SiO_2, the wafers were given a treatment with HMDS (hexamethyldisilazane, Y.E.S. Oven). HMDS treatment lasts only a few hours, therefore photoresist coating must be done as soon as possible. Photoresist (HPR 504, OCG Microelectronic Materials) was spin-coated on the silicon wafers (Solitec, 500 rpm for 10 s, 4,000 rpm for 40 s). The pieces were baked for 90 s at 115 °C on a hot plate (Solitec) and left to re-hydrate at room temperature for 15 minutes. Both the mask and silicon wafer were loaded onto a mask aligner (ABM Inc.), brought into contact (contact vacuum at -20 mm Hg) and exposed to UV (λ: 365 nm, exposure time to be discussed on the next page). The UV-exposed area of the photoresist was removed by rinsing with a 50% developer solution (354 Developer, Electronic Materials L.L.C.) in water. Using 100% developer solution resulted in over-developing of the features due to their small sizes. As a result, a diluted developer solution was used. SiO_2 removal of the exposed areas proceeded with a buffered oxide etch (BOE, $HF:(NH_4)HF_2$ at 10:1, J. T. Baker). Silicon etching was done in an Oxford ICP RIE system (model 100, PlasmaLab). A program developed at the Nanofab, NORCADA 0, was used for all Si

Exposure (s) / Developing (s)	Observation
Day 1	
4 / 25	Overdeveloped
3 / 25	Overdeveloped
4 / 35	Overdeveloped
3 / 15	Good
2.5 / 15	Bad Features
2 / 15	Good
Day 2	
3 / 15	Good
3 / 12	Good

Table 3.1 Silicon Processing Observations- For two different days, silicon processing at set exposure and developing times. For such small features (< 2 μm), the day's weather (i.e. humidity and temperature) will affect the final feature size.

Bosch processing; 0.5 μm step size was usually obtained. The target etch depth, measured at the 500^2 μm^2 windows, was 12 μm. The etched wafers were cleaned with acetone to partially remove photoresist. For complete photoresist removal, the wafer was loaded into a MicroEtch RIE system (PlasmaLab) and treated for photoresist ashing (100% O_2 flow, 400 mTorr, 100 W RF, 20 minutes).

Photolithography of features smaller than 3 μm can be difficult because the resulting features will vary wildly for seemingly small changes in processing. In Chapter 1, the fundamental limit to a lithographic process was given:

$$B_{min} = 1.5[\lambda (S + Z/2)]^{1/2} \qquad (3.2)$$

where B_{min} is the minimum line width, λ is the wavelength of exposing light, Z is the photoresist thickness and S, the distance between the mask and the photoresist during exposure. Typically, λ is 365 nm and Z is 1.2 μm. Assuming perfect contact between the

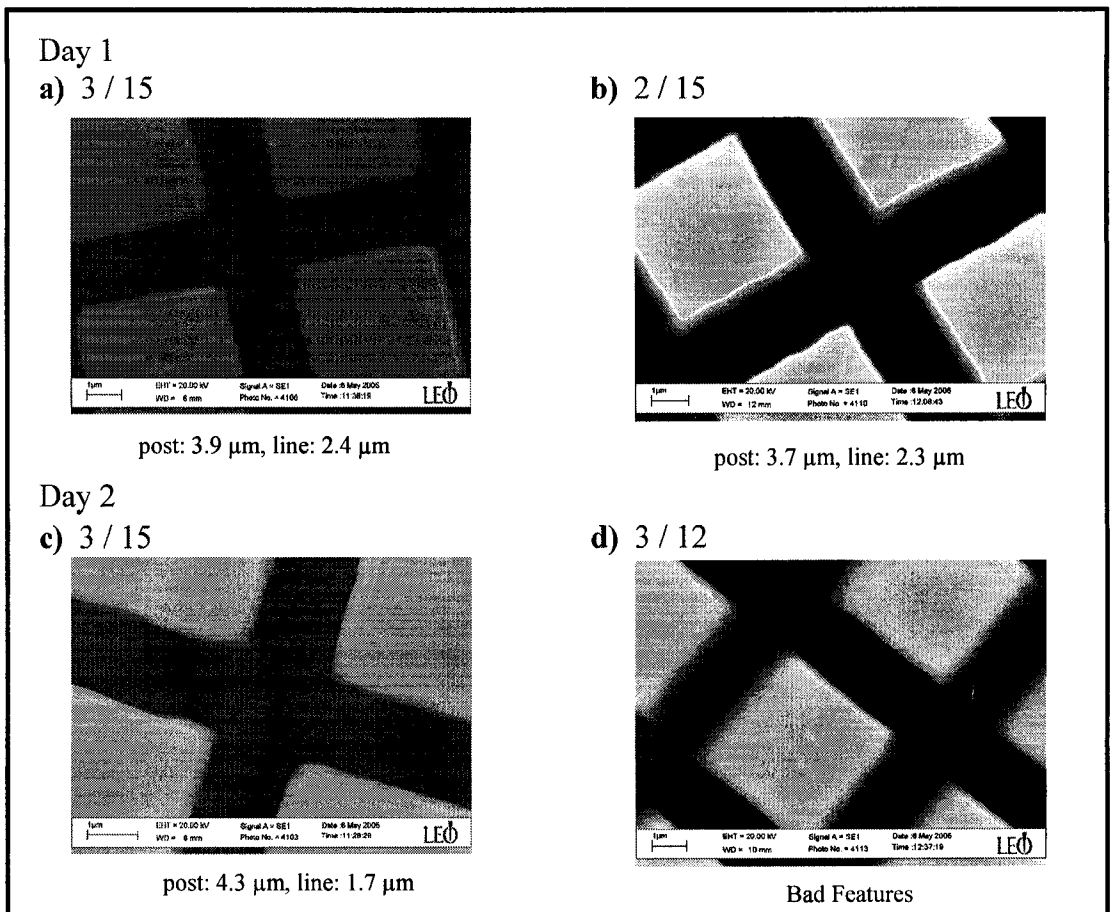

Figure 3.9 SEM Results under Different Processing Conditions- SEM images of four silicon columns after 10 μm etch. Top images were processed on day 1, bottom images on day 2. CD measurements are given for posts and lines. Overdeveloped features resulted for a) 3 s exposure with 15 s developing time and for b) 2 s exposure / 15 s developing. Good features were obtained on the second day, for c) 3 s exposure / 15 s developing.

mask and substrate (i.e. S at 0 μm), the theoretical limit is 0.7 μm. On any given day, λ and Z will be stable. However, a 1 μm impurity on the surface will increase the S value, increasing the theoretical limit to 1.1 μm, a sizable increase considering the small length scale. Therefore, when exposing the silicon wafer to the UV light, two things should be taken into consideration. First, any visible impurities on the wafer will affect the feature size, the number of people in the lithography area must be kept to a strict minimum to reduce contamination. Second, a contact vacuum of at least -20 mm Hg must be applied during exposure to minimize the S value.

UV exposure and developing time lengths also affect the final feature size; different times were then tested to gauge this effect. On day one, 6 different exposure/developing time combinations were processed; two different ones were processed on day two. The results were inspected under the microscope and critical dimension measurements taken using an inspection microscope (model INM 100, Leica Microsystems): initial observations are shown in Table 3.1. Wafers marked "Good" were processed completely as described above (BOE, ICP RIE, PR strip). The final wafers were then completely stripped of their oxide layer with BOE, cut and loaded into the scanning electron microscope (SEM, LEO 1430). Figure 3.9 presents the SEM pictures taken, along with the calculated line and post lengths. Numbers above the pictures represent the exposure/developing times. Figure 3.9d had a defect, either with the actual feature or during SEM analysis, therefore it was not taken into account. From the images shown, exposure times have a minimal effect on the final dimensions. More important are the developing times which, as seen when comparing pictures Figure 3.9a and Figure 3.9c, change from day-to-day due to temperature changes (for example, in hotter weather, faster developing times are observed).

Having a set developing time for silicon wafer processing was therefore not an option. After these tests, whenever processing a silicon wafer, a test wafer was first processed up to the developing stage, its features observed under the microscope and critical dimension measurements taken. If these corresponded to those measured in the case of Figure 3.9c, the same process was applied to the remaining wafers. An easy way to gauge developing times is by monitoring the 500^2 μm^2 windows on the substrate. Those windows were added to the final mask design as alignment markers when dicing the final wafer; during developing they can serve as photoresist development markers. After the 500^2 μm^2 windows have developed, the wafer is left another 2-3 seconds and removed from the developer solution. The typical line dimensions were therefore around 1.7 μm throughout this study. Figure 3.10 shows SEM pictures taken from the result obtained in Figure 3.9c. In Figure 3.10a, one can observe a smoothing of the ripple effect observed along the edges of the square posts on the mask (mask under 100x microscope is shown in Figure 3.10b). The long-range homogeneity of the silicon

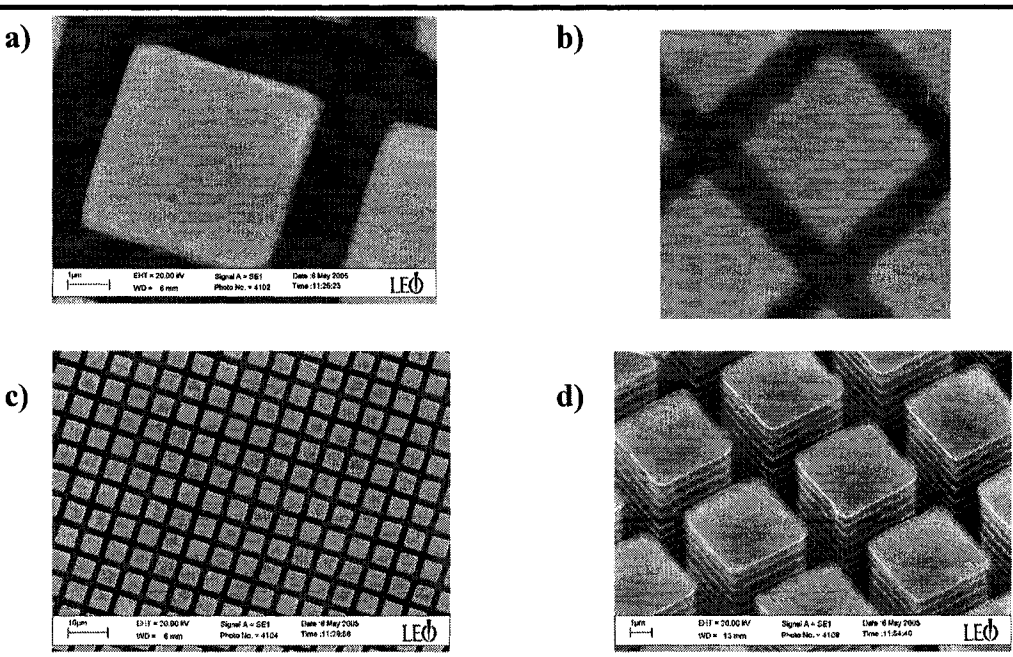

Figure 3.10 Results for One Si Column- a) SEM image of a post on silicon column compared to b) the square on the mask, showing a smoothing of the ripples produced by the pattern generator; c) long-range homogeneity of the silicon column and d) side-view of the silicon posts, showing the effect of Bosch ICP RIE.

column is seen in Figure 3.10c; the effect of Bosch processing on the side of the posts is shown in Figure 3.10d.

3.2.2.4. SURFACE DERIVATIZATION OF SILICON

The surface was derivatized to show hydrophobic behavior using a procedure developed by Walba et al.[19] Surface modification using trichlorosilanes is difficult due to its sensitivity to moisture. Any contact with moisture will greatly degrade the quality of the derivatization, therefore all reagents must be distilled and the reaction done in a glove box under nitrogen flow. Walba described a simpler derivatization procedure of silicon using octadecyltriethoxysilane (OTE), a reagent much less reactive towards water. However, this reagent is also less reactive with the surface than typical trichlorosilanes, a problem alleviated by the use of a catalyst, n-butylamine, during the reaction. The catalyst triggers covalent attachment of the silane to the surface and crosslinking between silanes[19]. The presence of a small amount of water during derivatization was also thought by the authors to produce higher quality surface modification.

Condition	Day 1	Day 2	Day 3
Ambient	102 °	100 °	98 °
N_2	101 °	100 °	88 °
N_2 with water	98 °	90 °	87 °

Table 3.2 Contact Angle Measurements- On three different days, the derivatization reaction was run in ambient and nitrogen atmosphere. For the N_2 experiments, both with and without added water was tested.

The surface derivatization reaction was tested on bare silicon (about 1 cm^2 pieces). Three different tests were run: first, the reaction was conducted under nitrogen atmosphere using a Schlenk tube apparatus; second, under nitrogen atmosphere with added water; third, in ambient atmosphere. The silicon pieces were piranha-cleaned, rinsed with distilled water and thoroughly dried with nitrogen. The derivatization solution was prepared as follows: in a round-bottom flask under nitrogen atmosphere, 35 ml of toluene (a.c.s grade, Fisher Scientific), 1.64 ml of n-octadecyltriethoxysilane (United Chemical Technologies Inc.) and 0.5 ml of n-butylamine (99.5%, Aldrich) were mixed. About 40 ml of toluene was added and mixed. The resulting solution was separated into 3 parts: 20 ml were used in the ambient atmosphere experiment, 20 ml for the nitrogen atmosphere experiment and to the last 20 ml, 30 µl of water were added and the reaction left under nitrogen atmosphere. The cleaned silicon pieces were left to react for 90 minutes, removed, rinsed with toluene, dried with nitrogen and left to cure in a vacuum oven for 24 hours (100 °C, -25 mm Hg). Contact angle measurement results are shown in Table 3.2 for experiments done on three successive days. The measurements were done at the University of Alberta Nanofab using a contact angle measurement system (First Ten Angstroms Inc.). It is clear that the quality of the derivatization reaction degrades from day-to-day, due to degradation of the starting silane through contact with humidity. Although ethoxysilanes are less susceptible to degradation due to humidity than chlorosilanes, they still show reactivity towards moisture. This was simply taken care of by more careful manipulation of the silane under nitrogen flow during transfer for surface modification. The starting silane was therefore kept under nitrogen

atmosphere in a round-bottom flask. From Table 3.2, the addition of water degraded the surface quality, whereas both the reactions under ambient and nitrogen atmosphere showed similar coverage. Walba et al. could routinely obtain contact angles of 105° using the process described above. The results presented in Table 3.2 are in-line with these measurements. The processed silicon wafers described in the last section were cut (13 mm x 7 mm) using a silicon dicing saw (RFK series, Diamond Touch Technology) and derivatized using the ambient atmosphere method.

3.2.3. GLASS-TO-SILICON BONDING

The bonding of silicon pieces to the glass microdevices is described next. Three overall methods were studied: 1- using un-cured glue or PDMS, 2- using half-cured thin PDMS and 3- using cured thick PDMS.

The usual method used for glass-to-silicon permanent bond is anodic bonding. In this process, high sodium content glass such as borofloat or pyrex is used; these have similar thermal expansion coefficient to silicon. The silicon and glass are brought into contact and heated to 300-450 °C, making the sodium ions in the glass matrix mobile. A voltage (-500 V to -1000 V) is applied on the glass, the mobile sodium ions migrate away from the silicon-glass boundary, leaving a depletion layer. This creates a high electric field region which results in a strong silicon-to-glass bond. The device used for this study, for reasons discussed previously, is made with 70 μm 0211 glass, which is not suitable for anodic bonding due to its low sodium content and thermal expansion coefficient. The smallest thickness for borofloat and pyrex glass is 1 mm, too thick for use here. Also, the silicon posts are derivatized with a C18 phase before bonding; the phase would not sustain high temperatures and voltages. Therefore an alternative bonding method was sought, and three issues had to be kept in mind. First, the bonding had to be strong enough to sustain the high pressures produced in the device. Second, the bonding procedure had to be reproducible so that all channels would have the same flow profile. Third, the distance between the silicon bed and the glass wafer had to be minimized, to minimize bandbroadening and elution peak widths.

3.2.3.1. INITIAL TESTS USING GLUE OR PDMS

The first obvious technique was to spin-coat polydimethoxysilane (PDMS, 10:1 ratio of base to curing agent, SYLGARD 184 Silicone Elastomer Kit, Dow Corning

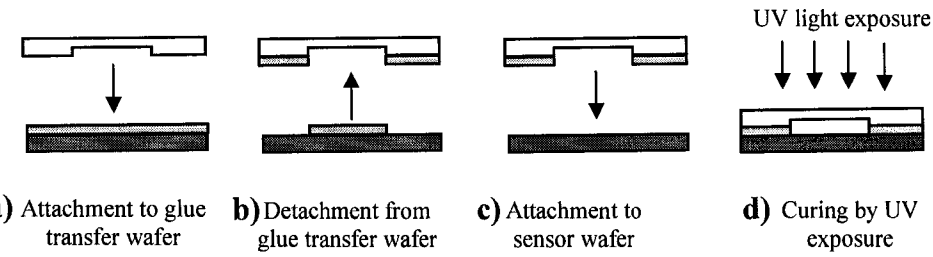

Figure 3.11 Glue Stamping Procedure- a) Glue was spin-coated onto a transfer wafer and brought into contact with microdevice; b) the transfer wafer and microdevice were detached, transferring the glue to the microdevice; c) the microdevice was brought into contact with the device to be bonded to; d) glue was cured by UV exposure.

Corporation) directly onto the bonded device on the 70 μm side; however PDMS was drawn into the channels through the 150 μm access holes. Covering the holes with black tape did not prove successful; PDMS would always find its way into the microchannels. Another technique tested involved stamping glue or PDMS onto the glass wafer, a technique developed by Schlautmann et al[2]. Figure 3.11 shows a cartoon taken from the publication of the process. First, UV curable glue is spin-coated onto a transfer wafer. The device is brought into contact with the transfer wafer and detached (shown in Figure 3.11a and 3.11b). The device is then attached to the bottom glass wafer (called sensor wafer in the cartoon, shown in Figure 3.11c. Finally, the glue cured (shown in Figure 3.11d). The authors could achieve less than 3 μm thick glue and position it with an accuracy of ± 15 μm around the microchannels.

This technique was tested with both UV-curable glue and PDMS. UV-curable glue consisted of a 3.84% weight/volume ratio of a curing agent (dimethoxyphenylacetophenone, DMPA, Aldrich) to a monomer solution (isobornyl acrylate, Aldrich). On a silicon wafer, the glue (or PDMS) was spin-coated (Solitec, 5 s at 500 rpm, 20 s at 4,000 rpm), brought into contact with 0211 glass, detached using a razor blade, attached to a clean silicon wafer and cured. The first observation made was that the cartoon shown in Figure 3.11 is an idealized situation, whereby all the glue transfers onto the device following detachment. This does not happen. The glue (or PDMS) partitions between the transfer wafer and the device, leaving both with glue (or

PDMS) residue that is not equally transferred throughout the device. This resulted, upon final attachment to the clean silicon wafer, in regions that were not bonded to the device. Also, the partitioning was random, which meant that no two wafers were bonded reproducibly. Finally, during pulling of the transfer wafer from the device, the two would shear and glue (or PDMS) would spread. In my hands an accuracy of ± 15 μm could not be achieved.

A third tested technique involved wicking UV-curable glue between clamped 0211 glass and silicon wafers. Figure 3.12a describes the process tested. A test silicon wafer, containing etched microchannels, was brought into contact with a 0211 wafer, the two were clamped, a drop of glue was deposited at their junction and left to wick in-between the two. Once wicked in, the glue was cured. Note that the test silicon wafer contained microchannels that had no relation to the silicon wafer described earlier (with the posts). Here, the silicon microchannels were simply used to test whether the glue could be contained within an area defined by the microchannels (channels were 30 μm wide, etched 60 μm deep).

The glue cured to a thickness of 1 μm and was localized outside the microchannels, as pictured in Figure 3.12a; the 30 μm wide, 60 μm deep silicon microchannel could therefore be used to contain the glue. However, localizing the glue outside the post structure would be problematic when applying this method to the silicon bed device: to contain the glue away from the posts, a micromachined structure would need to be added outside the bed region, adding a flow path outside the post region. Figure 3.12b shows a theoretical layout for a silicon bed device if the glue wicking technique were applied to the silicon bed. The first cartoon presents a top view of the silicon bed, with the inner white square representing the micromachined posts and the outer line, the micromachined trench that would be used to contain the glue, keeping it away from the post region. The side view presents the silicon piece, glued onto the lower glass device containing the microchannels; the trench is shown close to the glass access holes. From the test run in Figure 3.12a, the glue would stop outside the trench region, i.e. the trench would be opened. Although the minimum trench width needed to contain the glue was not tested (only 30 μm width was tested), it would need to be a few micrometers wide to contain the very non-viscous glue, compared to the 1.7 μm post-to-

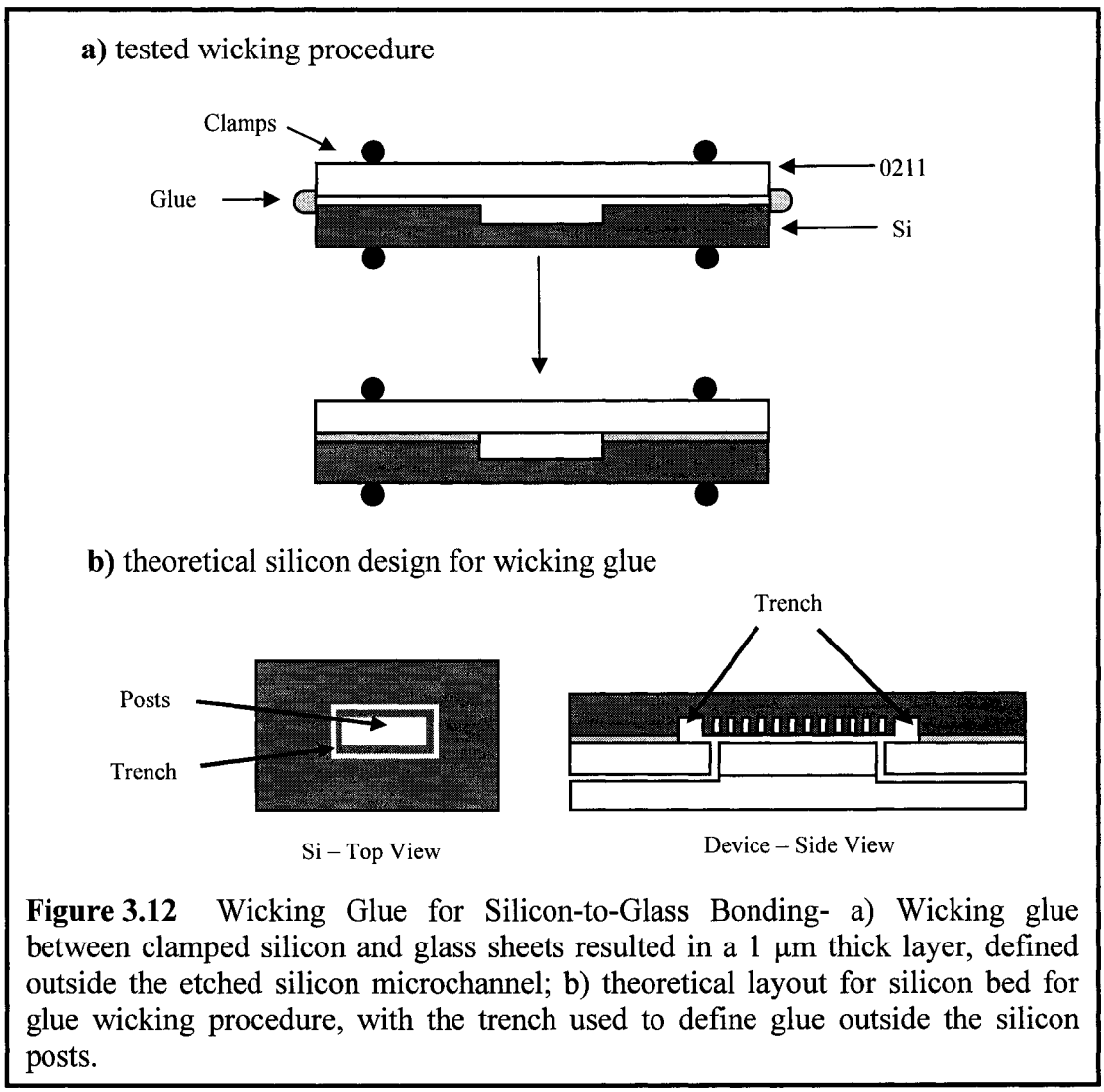

Figure 3.12 Wicking Glue for Silicon-to-Glass Bonding- a) Wicking glue between clamped silicon and glass sheets resulted in a 1 μm thick layer, defined outside the etched silicon microchannel; b) theoretical layout for silicon bed for glue wicking procedure, with the trench used to define glue outside the silicon posts.

post length in the bed structure. Therefore, liquid entering the silicon bed would have two flow paths: through the high flow-resistance post structure or through the low flow-resistance trench. This would mean that a preferential flow path would be added outside the silicon posts: no liquid would then enter the post region.

To get around the trench problem, a different approach was used to wick the PDMS directly onto the glass microdevice. The test is illustrated in Figure 3.13. A blank silicon wafer was cleaned in piranha, thoroughly rinsed with water and dried. The wafer was put into a vacuum chamber along with 1 ml of trichloro(1H,1H,2H,2H-perfluorooctyl)silane ($C_8H_4Cl_3F_{13}Si$, 97%, Aldrich) overnight. The resulting silicon wafer did not adhere to PDMS. The glass device and silicon wafer were clamped

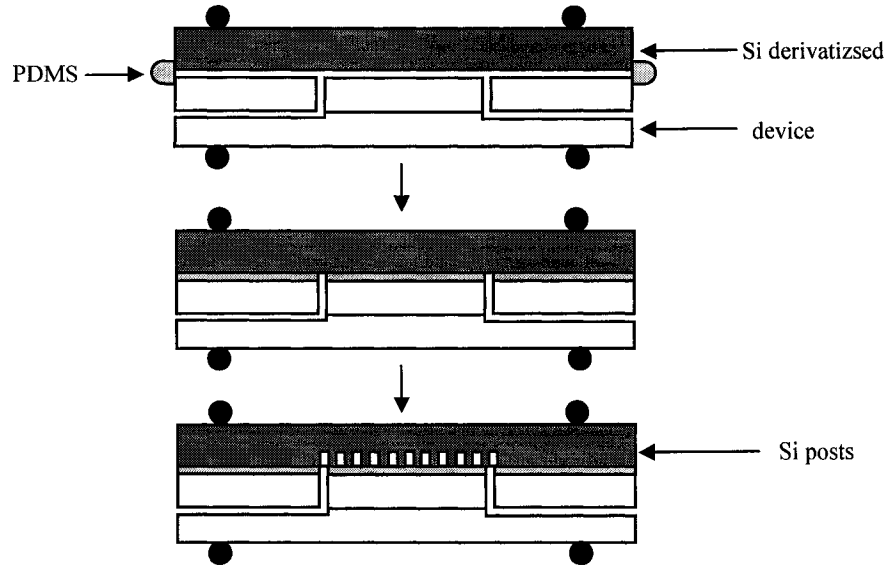

Figure 3.13 Wicking PDMS for Silicon-to-Glass Bonding- Wicking PDMS between clamped silicon and glass microdevice: access holes on the microdevice were used to define PDMS outside the microchannels. Because of chipping at the glass hole, the PDMS could not be contained.

together, a drop of PDMS was deposited at their junction and left to wick in-between the two. Once wicked in, the PDMS was cured, the silicon wafer removed and the silicon piece containing the posts was bonded. The assumption here was that the drilled holes would act as the Si trenches did, stopping the PDMS at the holes' edge without having PDMS sipping in the microchannels.

The PDMS layer produced this way did not cure. The most probable reason for this is that the wicking process produced thin layers that did not contain the required 10:1 monomer-to-curing agent ratio. In addition, PDMS would enter the microchannels rather than stop at the borders (as was the case with etched silicon wafer of Figure 3.12a). Etched silicon wafers have sharp, right-angle borders, whereas the borders produced by drilling in glass are not as well-defined, due to chipping during the drilling process. The PDMS cannot be stopped at the edge and enters the microchannels.

Working with un-cured glue or PDMS did not result in a useful final device. Two processes using pre-cured PDMS were then tested: one involving thin PDMS (< 20 μm),

the other, thick PDMS (> 600 μm). Both methods resulted in well-defined, leak-free silicon-to-glass bonding: microdevices produced by both methods were used for protein sorption and on-bed digestion, as described in Chapter 4.

3.2.3.2. THIN PDMS

The thin PDMS process involved spin-coating PDMS onto a silicon wafer previously derivatized with trichloro(1H,1H,2H,2H-perfluorooctyl)silane. In initial tests, the PDMS was then fully cured, both the glass device and PDMS-on-silicon were given an oxygen plasma treatment with the MicroEtch RIE system (PlasmaLab, 25% O_2 flow, 150 mTorr, 100 W RF, 30 seconds), brought into contact and bonded. At a thickness of about 15 μm, PDMS could not be bonded to the device. The 70 μm glass side of the device was not completely flat after thermal bonding, therefore the PDMS-on-silicon did not contact the glass device completely, leaving large parts with non-bonded PDMS. A different approach was then used, Figure 3.14 describes the process. First, silicon pieces were cut (7 mm x 13 mm) and derivatized with trichloro(1H,1H,2H,2H-perfluorooctyl)silane as before. The device was cleaned with piranha, thoroughly washed with water and dried. PDMS was spin-coated onto the Si pieces (Solitec, 20 s at 500 rpm, 40 s at 4,000 rpm) and oven-baked at 70 °C for 2-3 minutes. This resulted in a PDMS that was half-cured, viscous enough that it would not enter the glass holes upon bonding with the glass device yet liquid enough to adjust to the rough surface of the 70 μm side on the glass device. The PDMS-on-silicon piece was then contacted with the glass device and left overnight at 70 °C. Access holes were then processed in the PDMS using the MicroEtch RIE system.

The University of Alberta Nanofab's Microetch RIE system, used until now for oxygen plasma cleaning of PDMS surfaces, allows for different process gases to be introduced into the chamber. It can therefore be used for dry etching of different substrates, for example silicon. To etch a substrate under dry plasma conditions, the byproducts of the reaction between the process gas and the substrate must be volatile. For example, under SF_6 process gas flow, F radicals are generated by the plasma; upon interaction with a silicon substrate, $SiF_{4(g)}$ is generated, and the substrate etches. Because PDMS consists of a silicon-containing molecular matrix, it was assumed that it could be etched using plasma etching under SF_6 flow. Initial tests were conducted using thick

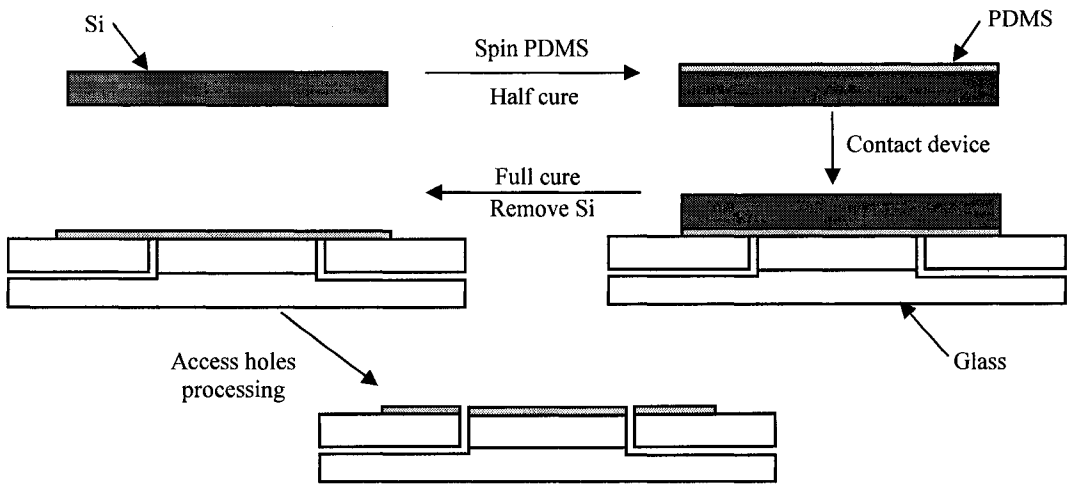

Figure 3.14 PDMS Processing for Silicon-to-Glass Bonding- PDMS was span onto silicon, half-cured and contacted to the microdevice. After full cure of PDMS, the silicon was removed and access holes processed using RIE.

PDMS and blue tape as a mask layer; blue tape leaves minimal amount of residue on the surface. Half the PDMS was masked with the blue tape, the other half was left exposed. Microetch RIE settings: 80% O_2, 20% SF_6, 125 mTorr, 200 W. After exposing the PDMS for 20 minutes, no change in step height was observed between the exposed and unexposed regions of the PDMS. Also, the blue tape did not react well to the exposure: it could not be completely removed from the underlying PDMS. A different mask was then used: a silicon wafer cover with a nitride layer. Again half the PDMS was masked, this time using the nitride-containing Si, and exposed to the O_2-SF_6 plasma for 1 hour. This resulted in a step height of 5.6 μm. However, because the silicon mask layer did not contact the PDMS equally everywhere, the boundary between the etched and masked PDMS was not well-defined. Large parts of the mask were also etched during the process; a different masking method was then needed. Since chrome has a low vapor pressure, it was therefore assumed that it could sustain the conditions in the plasma chamber better than other masks. Chrome was deposited on 70 μm thick 0211 glass using the Lesker two target sputtering system (settings as before, see section 3.2.2.2.). Half the PDMS was masked using the 0211/Cr (0211 side contacted to the PDMS), the other half left exposed. The pressure in the plasma chamber was increased to 400 mTorr

	Depth	Diameter	$D_{isotropic}$	$D_{anisotropic}$
Large area	18 μm	———	———	———
2 mm	13 μm	———	———	———
360 μm	11.8 μm	410 μm	383.6 μm	360 μm
150 μm	10 μm	240 μm	170 μm	150 μm

Table 3.3 PDMS Etch Depths- Actual (Depth and Diameter) and expected ($D_{isotropic}$ and $D_{anisotropic}$) feature size after PDMS RIE etching for 90 minutes using the masking approach described in the text. Four exposed areas were tested.

in an effort to increase the etch rate (settings: 80% O_2, 20% SF_6, 400 mTorr, 200 W, 1 hour). This resulted in a 10.5 μm etch, twice the etch rate as for 125 mTorr pressure. The edges were well-defined, therefore there was good contact between the PDMS and the mask. Although the chrome layer was more transparent, indicating that some had been removed, the major part of it was still present, and the 70 μm glass was left untouched: 0211/Cr was used as the mask layer for all future experiments.

The experiments described before were done on large exposed PDMS area. However, etching within 150 μm exposed area would lower the etch rate, due to restricted access of the process gas to the substrate. The 0211/Cr mask layer was drilled using 3 different drill bit sizes: 2 mm, 350 μm and 150 μm. After cleaning in a cold piranha bath (i.e. less than 40 °C so as to not dislodge the chrome layer), the 0211/Cr was contacted with the PDMS, left in the Microetch RIE for 1½ hour (settings: 80% O_2, 20% SF_6, 400 mTorr, 200 W) , with a 30 minutes cleaning step at half-time. The resulting etch depth and hole diameter are shown in Table 3.3. Also shown are diameters expected for isotropic ($D_{isotropic}$) and anisotropic ($D_{anisotropic}$) etches.

As expected, a smaller etch rate is obtained for smaller hole size. The etched diameter results, however, were unexpected. Under reactive ion etching, one of two mechanisms will direct the etching process. In the first mechanism, a radical formed from the process gas (for example, F radical from SF_6 gas) strikes the substrate surface in all directions, spontaneously forming a volatile byproduct ($SiF_{4(g)}$ in our example). This process produces an isotropic etch. Under the second mechanism, the radical interacts

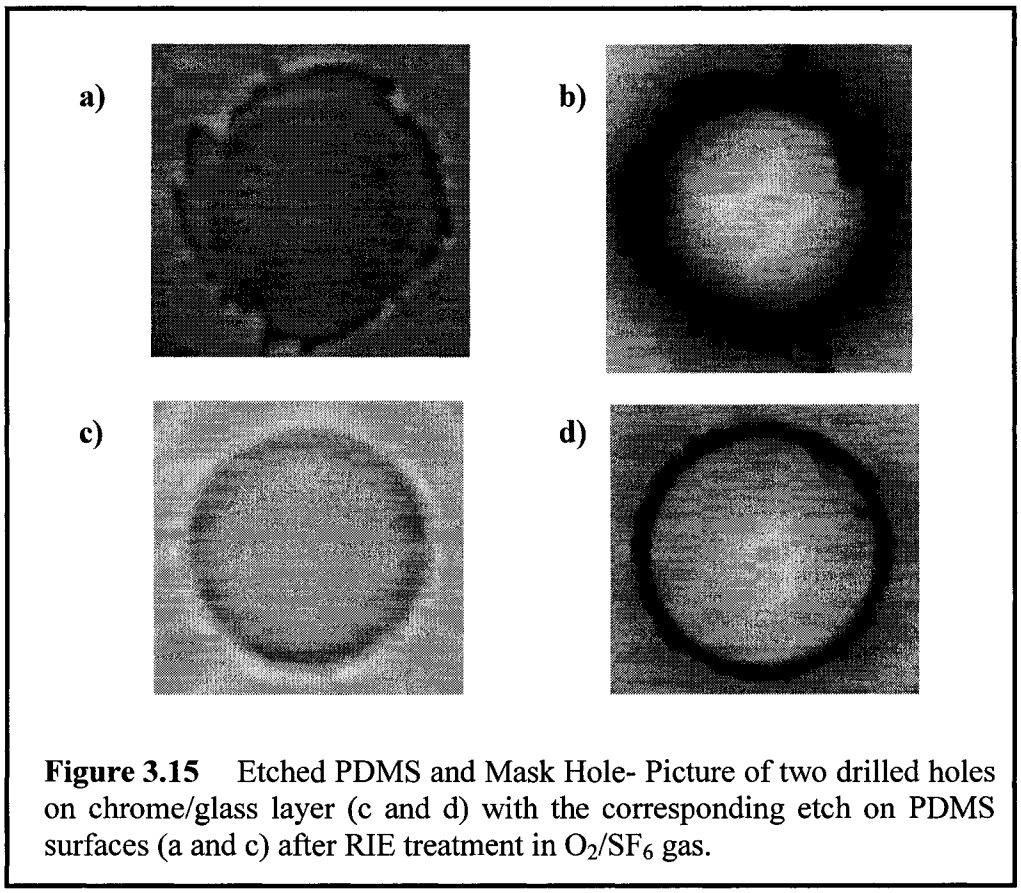

Figure 3.15 Etched PDMS and Mask Hole- Picture of two drilled holes on chrome/glass layer (c and d) with the corresponding etch on PDMS surfaces (a and c) after RIE treatment in O_2/SF_6 gas.

with the substrate without producing the volatile byproduct. An ion striking the substrate perpendicularly will transfer its energy to the surface ion/radical, producing a volatile byproduct and etching the surface anisotropically. From Table 3.3, the etched diameter was larger than both the theoretical diameter under isotropic or anisotropic conditions.

Figure 3.15a presents a picture of the PDMS etched under the above conditions, the drilled 150 μm hole on the 0211/Cr mask is shown in Figure 3.15b. The pattern on the hole is perfectly reproduced on the PDMS. This then explains the discrepancy in hole diameter: the drilled hole itself has a larger diameter due to chipping during the drilling process. A new 150 μm drill bit was used to drill the 0211/Cr mask, the process described above was used again to etch the PDMS with the following etching/chamber cleaning times: 1 hour etch / 30 minutes chamber cleaning / 2 hours etch (settings as before). The resulting PDMS etching is shown in Figure 3.15c, the 0211/Cr hole is shown in 3.15d. A 20 μm etch depth was obtained, with a 205 μm diameter. Since the

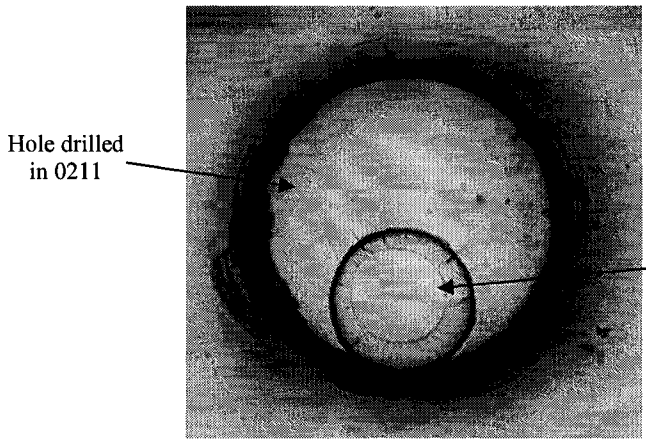

Figure 3.16 Etched PDMS Aligned with 0211 Hole- Hole drilled using the RIE procedure described in the text.

drilled hole diameter was 205 μm, the etching was anisotropic and followed the second mechanism.

The 0211/Cr hole shown in Figure 3.15d was used for the etching of a PDMS hole in a glass/PDMS substrate. PDMS was spun onto a silicon piece, derivatized to prevent PDMS sticking (using trichloro(1H,1H,2H,2H-perfluorooctyl)silane), to a thickness of 12 μm. It was then transferred to a 0211 wafer having a 360 μm hole drilled in it. The 0211/Cr mask was aligned with the 360 μm hole, brought into contact with the PDMS and left in the Microetch RIE for 2 hours. One hour into the etching process, the structure was removed from the chamber and the RIE system was cleaned for 30 minutes. The result is shown in Figure 3.16.

After application of PDMS onto the device, the silicon pieces containing the columns are prepared for bonding to the PDMS. PDMS-to-Si bonding requires an oxygen plasma treatment; because the columns are derivatized with a C18 coating, they need to be protected from the treatment. This is done by depositing blue tape (0.5 mm x 2, 4 or 6 mm) on top of the column section of the silicon piece. Both the silicon piece and device are put in the Microetch RIE system (settings: 25% O_2, 100 W, 150 mTorr, 30 s). Following the treatment, the blue tape is removed from the Si column, a drop of water is deposited on the silicon piece and the device is brought into contact. The drop of water

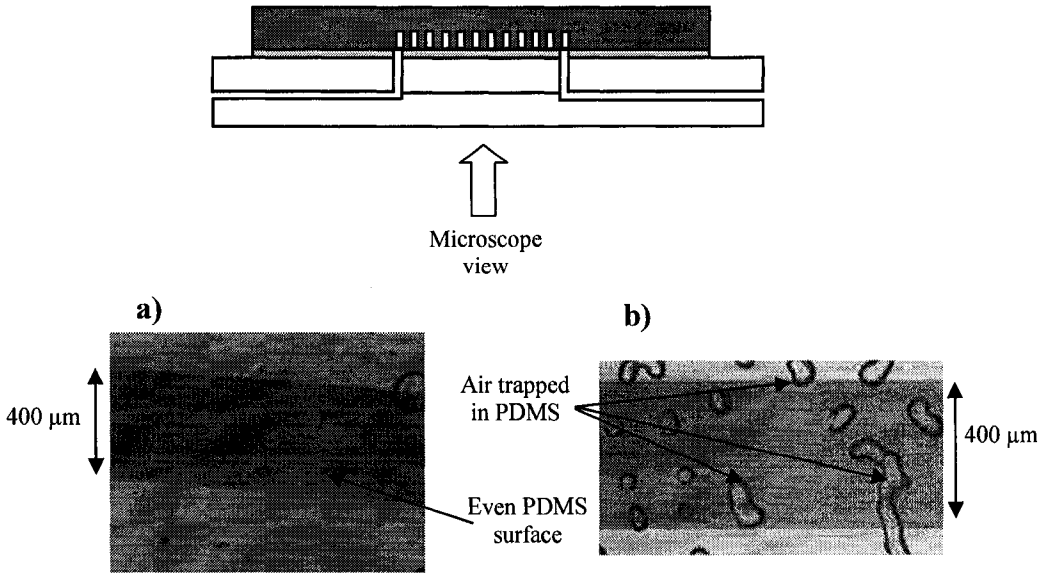

Figure 3.17 Thin PDMS in Single and Multi Channel Devices- a) Depiction of the field of view (top) for images of single-channel silicon microdevice and b) one of the silicon beds on the multichannel device. The single channel resulted in an even surface, whereas air was trapped in the PDMS.

allows for the Si piece to be moved during alignment under the dissection microscope. Once satisfied with the alignment, the structure is left at 70 °C overnight.

The process described for half-cured PDMS works well on single-channel devices. A 1 cm wide device is simply dropped on top of the PDMS-on-Si substrate and left to cure at 70 °C; Figure 3.17a shows a single-channel device under 10x magnification assembled this way. The view for the picture is shown on the cartoon of Figure 3.17. The silicon piece and part of the microfabricated posts region is seen in the field of view. As mentioned in section 3.2.1.4 where glass bonding was discussed, bonding the 70 μm thick drilled glass to the 600 μm thick micromachined glass was not successful initially, therefore two 600 μm thick glass substrates were used. The 6 mm single-channel microdevice that resulted was used for most of the single-channel analyses described in the next chapter. Because of the thickness of the drilled wafer on this microdevice (600 μm), the resulting surface after thermal bonding of the two glass substrates was flat. This then made bonding of half-cured PDMS easy: all regions of the glass surface would make

contact with the half-cured PDMS at the same time and the resulting PDMS surface was even throughout the bed region. However, difficulties arose when using the 4 channel device, built using 70 μm thick drilled glass wafer. After thermal bonding with the micromachined 600 μm wafer, the 70 μm surface that resulted was not flat. Any small debris trapped between the two glass layers would curve the 70 μm surface. When bonding the half-cured PDMS to the 70 μm surface, part of the glass would make contact with the PDMS without contacting the complete surface. Pressure would then need to be applied, which would result in either half-cured PDMS entering the access holes (and therefore entering the underlying glass microchannels) or in large areas of trapped air in the half-cured PDMS upon release of the silicon. Figure 3.17b shows the result on one column of a multichannel device. This, as will be discussed in the following chapter, will have an impact on the flow profile of the 4 channel device.

3.2.3.3. THICK PDMS

Because of the difficulty in processing a bubble-free PDMS layer using the technique described in the last section, a more conventional approach to PDMS processing was tested for the 4 channel device. PDMS was cured, holes punched, both the device and PDMS were treated in an oxygen plasma and brought into contact. The main issue here is the thickness of the PDMS: a thinner PDMS will mean a lower dead volume in the final device and therefore smaller peak widths. However, problems arose when using pre-cured thin PDMS. As mentioned previously, the 70 μm glass side of the device is not completely flat after thermal bonding and thin (around 15 μm) PDMS does not bond to it, therefore no attempt at bonding thin pre-cure PDMS was further attempted here.

Thick PDMS processing is described next: first, three dishes, each containing a 10:1 ratio of PDMS monomer-to-curing agent, were left to cure overnight. The three resulting PDMS layers were brought into contact; the upper and lower PDMS layers (about 200 μm thick each) protected the middle one (over 600 μm thick) from debris during hole punching. The hole puncher, made by the chemistry department's machine shop (tip o.d. at 180 μm, tip i.d. at 100 μm), was loaded onto the drill press and lowered through the PDMS structure. The resulting hole was about 150 μm in diameter (see Figure 3.18c, middle picture). The device and PDMS middle structure were loaded into

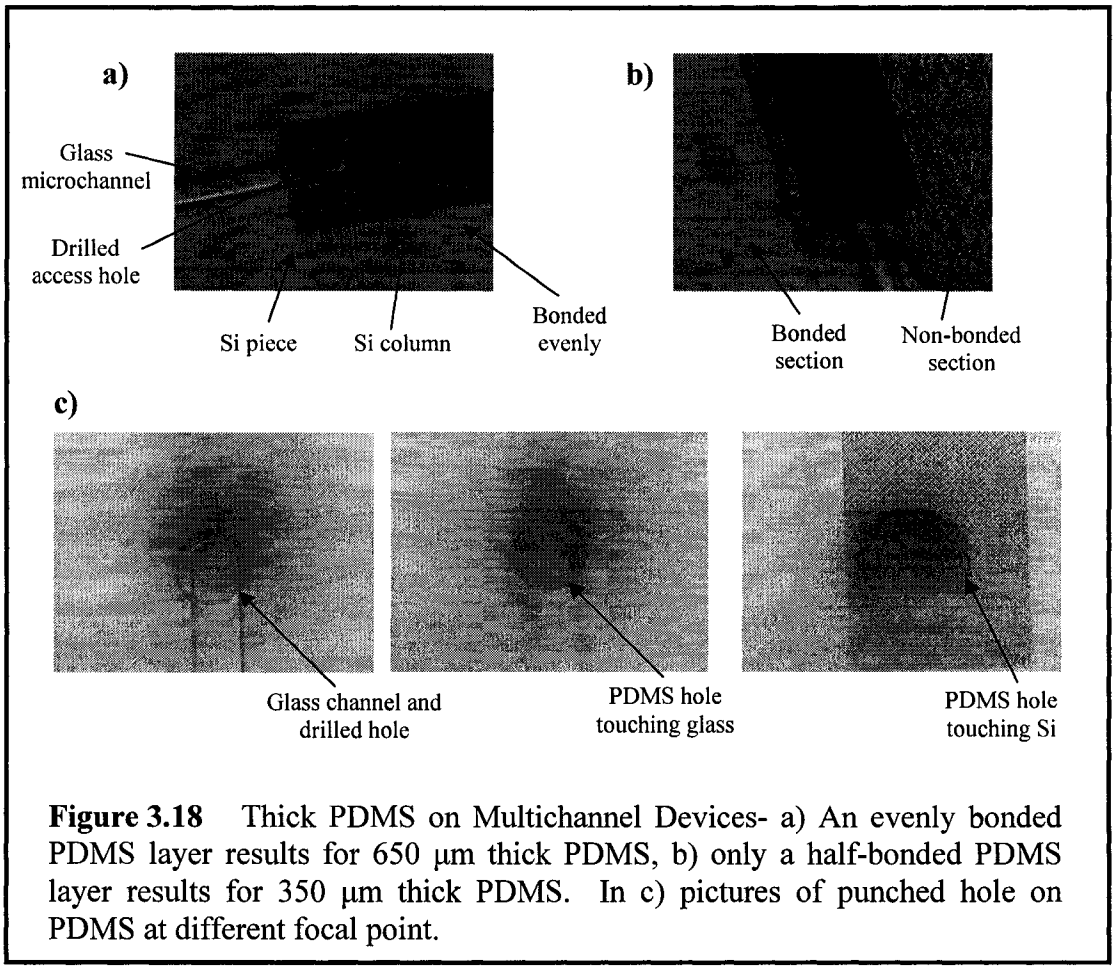

Figure 3.18 Thick PDMS on Multichannel Devices- a) An evenly bonded PDMS layer results for 650 μm thick PDMS, b) only a half-bonded PDMS layer results for 350 μm thick PDMS. In c) pictures of punched hole on PDMS at different focal point.

the Microetch RIE system (settings: 25% O_2, 100 W, 150 mTorr, 30 s), aligned, brought into contact and left at 70 °C for 2 hours. The Si columns were then bonded to the device, using the same procedure as described in section 3.2.4.1.

The effect of PDMS thickness on bonding quality is shown in Figure 3.18. All pictures are from the same view as shown in Figure 3.17. The glass microchannel is seen, leading to the drilled access hole and micromachined silicon column. In the picture presented in Figure 3.18a, good bonding is observed for a 700 μm PDMS thickness. All 4 channels were equally well-bonded. In Figure 3.18b, a device with a 350 μm PDMS structure is shown. As seen in the picture, only half of the PDMS is bonded to the silicon columns. In Figure 3.18c, pictures taken for a third multichannel device is shown, again showing good bonding for a 650 μm PDMS thickness. The sequence presents the device at different imaging depths. The issue with the 350 μm PDMS does not come from the

non-flat regions of the 70 μm glass, as for the thin PDMS; here, the glass-to-PDMS bonding is of good quality. The problem comes from Si-to-PDMS bonding, which would suggest inequalities in the PDMS surface. During PDMS processing, the base and curing agent are mixed together and left to cure overnight at room temperature, time during which the PDMS settles. However, because no mold was used during processing, the PDMS surface is not completely flat. The problem occurred in the 350 μm thick PDMS, no such issue was observed for the thicker PDMS, as shown in Figure 3.18.

3.3.FINAL DEVICE

Micodevices using both the thin (section 3.2.3.1) and thick PDMS (3.2.3.2) bonding approaches were used for ESI MS analysis described in the next chapter. Two final processes were done to the device before usage: first, a NANOPORT (Upchurch Scientific) was attached to the 360 μm entrance hole on the glass device. Second, an ESI tip was inserted into the drilled edge of the microchip. The NANOPORT allows for leak-free coupling of a capillary to the device. The ESI tip was discussed before (section 3.2.2.5). A flowchart of the entire microfabrication process is shown next, followed by device pictures.

Flow Chart of Si-Based Microfluidics Device Processing

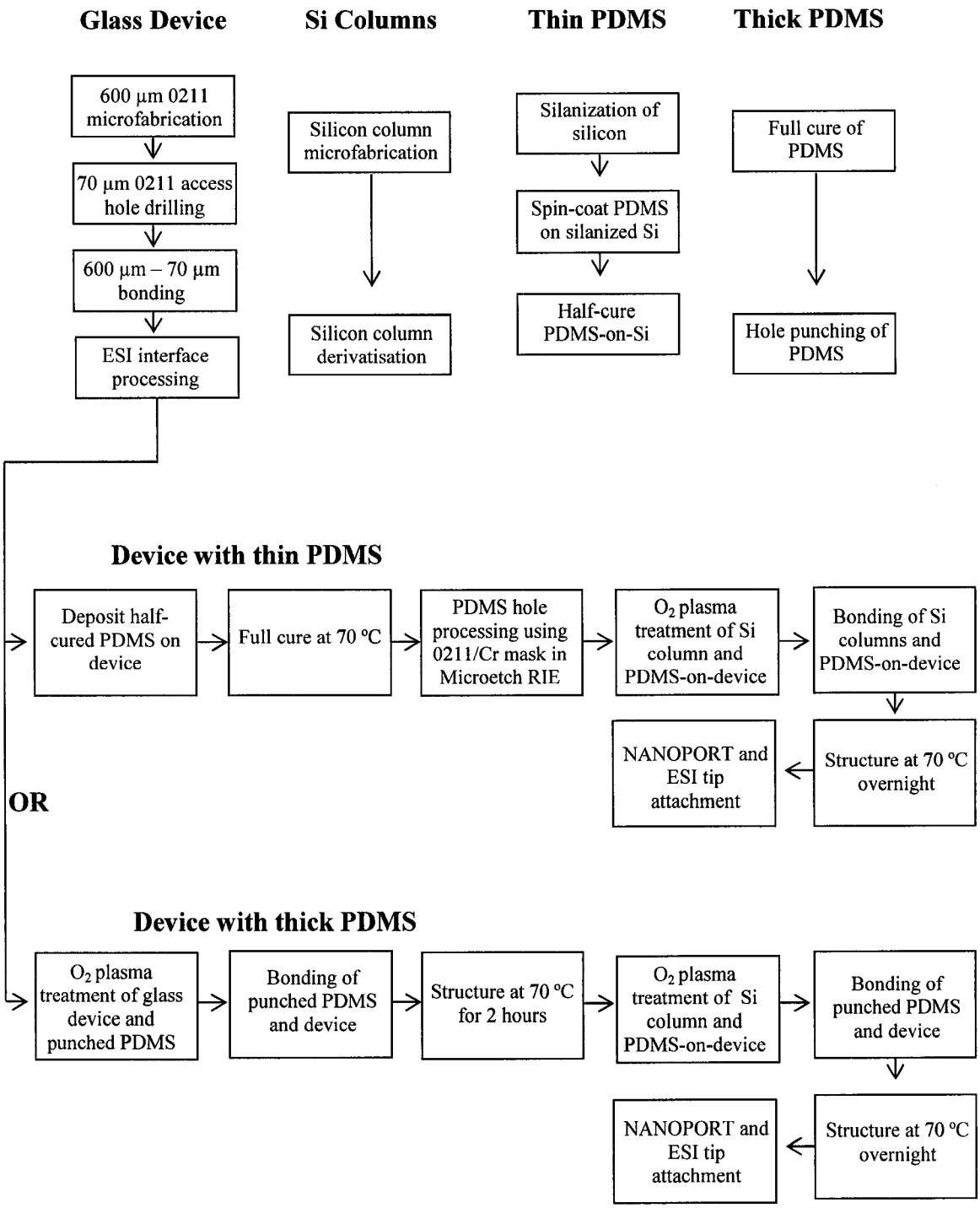

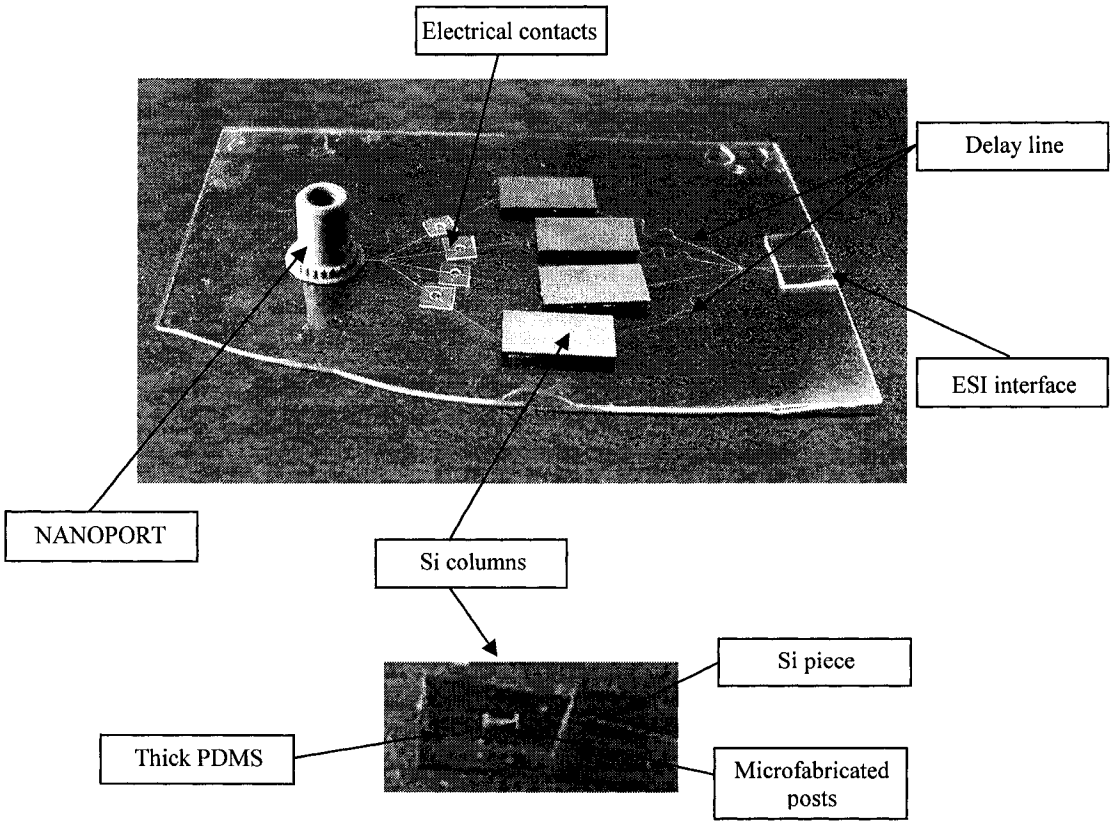

Figure 3.19 Multichannel Device – Picture of the entire device (top) and a close-up of a silicon bed (bottom), bonded using the thick PDMS approach.

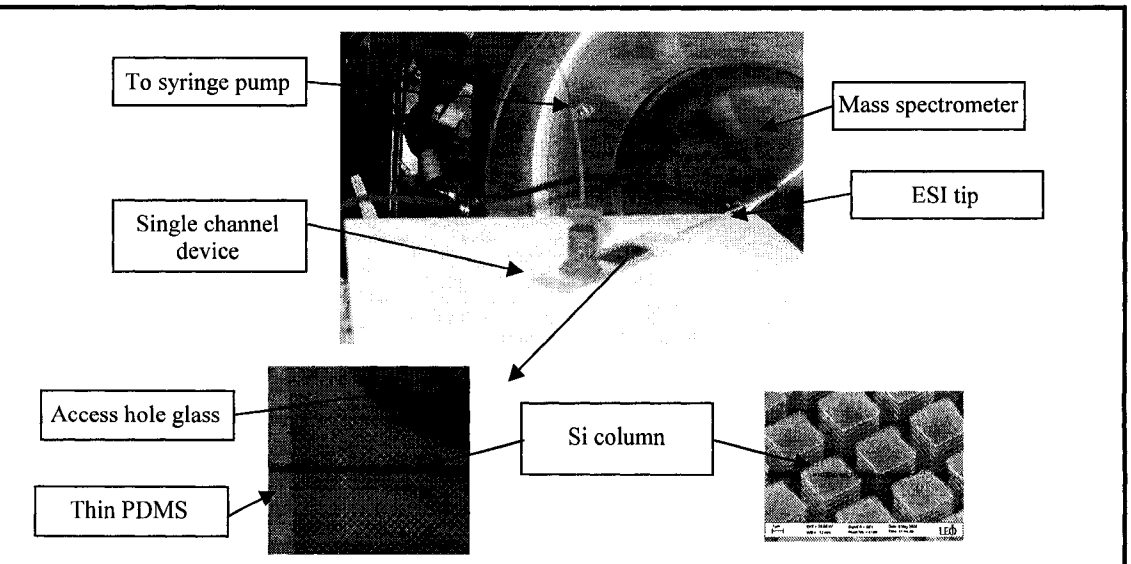

Figure 3.20 Single Channel Device- Picture of the device in front of the MS (top), with a close-up of the silicon column (bottom left) bonded using the thin PDMS procedure, and an SEM image of the silicon pillars (bottom right)

3.4.REFERENCES

(1) HE, B.; TAIT, N.; REGNIER, F. *ANALYTICAL CHEMISTRY* **1998**, *70*, 3790-3797.

(2) SCHLAUTMANN, S.; BESSELINK, G. A. J.; RADHAKRISHNA PRABHU, G.; SCHASFOORT, R. B. M. *JOURNAL OF MICROMECHANICS AND MICROENGINEERING* **1993**, *13*, S81-S84.

(3) FIGEYS, D.; PINTO, D. *ELECTROPHORESIS* **2001**, *22*, 208-216.

(4) LION, N.; REYMOND, F.; GIRAULT, H. H.; ROSSIER, J. S. *CURRENT OPINION IN BIOTECHNOLOGY* **2004**, *15*, 31-37.

(5) LION, N.; ROHNER, T. C.; DAYON, L.; ARNAUD, I. L.; DAMOC, E.; YOUHNOVSKI, N.; WU, Z. Y.; ROUSSEL, C.; JOSSERAND, J.; JENSEN, H.; ROSSIER, J. S.; PRZYBYLSKI, M.; GIRAULT, H. H. *ELECTROPHORESIS* **2003**, *24*, 3533-3562.

(6) FREIRE, S. L. S.; WHEELER, A. R. *LAB ON A CHIP* **2006**, *6*, 1415-1423.

(7) SLENTZ, B. E.; PENNER, N. A.; REGNIER, F. E. *JOURNAL OF CHROMATOGRAPHY A* **2003**, *984*, 97-107.

(8) WANG, C., UNIVERSITY OF ALBERTA, EDMONTON, 2001.

(9) TAYLOR, J., UNIVERSITY OF ALBERTA, EDMONTON, 2004.

(10) WOLF, S. *MICROCHIP MANUFACTURING*; LATTICE PRESS: CALIFORNIA, 2004.

(11) HE, B.; JI, J. Y.; REGNIER, F. E. *JOURNAL OF CHROMATOGRAPHY A* **1999**, *853*, 257-262.

(12) SLENTZ, B. E.; PENNER, N. A.; REGNIER, F. *JOURNAL OF SEPARATION SCIENCE* **2002**, *25*, 1011-1018.

(13) SLENTZ, B. E.; PENNER, N. A.; REGNIER, F. E. *JOURNAL OF CHROMATOGRAPHY A* **2002**, *948*, 225-233.

(14) SLENTZ, B. E.; PENNER, N. A.; LUGOWSKA, E.; REGNIER, F. *ELECTROPHORESIS* **2001**, *22*, 3736-3743.

(15) CANTWELL, F. *CLASS NOTES- ANALYTICAL SEPARATIONS*, 2000.

(16) FAN, Z. H.; HARRISON, D. J. *ANALYTICAL CHEMISTRY* **1994**, *66*, 177-184.

(17) BINGS, N. H.; WANG, C.; SKINNER, C. D.; COLYER, C. L.; THIBAULT, P.; HARRISON, D. J. *ANALYTICAL CHEMISTRY* **1999**, *71*.

(18) SZE, S. M. *SEMICONDUCTOR DEVICES: PHYSICS AND TECHNOLOGY*; JOHN WILEY: NEW YORK, 1985.

(19) WALBA, D. M.; LIBERKO, C. A.; KORBLOVA, E.; FARROW, M.; FURTAK, T. E.; CHOW, B. C.; SCHWARTZ, D. K.; FREEMAN, A. S.; DOUGLAS, K.; WILLIAMS, S. D.; KLITTNICK, A. F.; CLARK, N. A. *LIQUID CRYSTALS* **2004**, *31*, 481-489.

CHAPTER 4 PERFORMANCE OF THE SILICON-BASED MICROFLUIDICS DEVICE

4.1. INTRODUCTION

Protein digestion is an integral part of protein analysis[2, 3]; microfluidic systems for proteome analysis will have to include a digestion module[4]. Microdevices for open-channel[5-7], polymeric[8-10], membrane[11], silicon[12] and bead[13-17] based, on-chip protein digestion have been described. Wang et al. used one- and two-bed systems for on-chip, bead-based protein digestion[16, 17]. Taylor further multiplexed the two-bed system described by Wang; difficulties in efficiently packing the beads led to unpredictable pressure-driven elution to the mass spectrometer[18]. Discussed in the present chapter is the performance of the hybrid silicon-glass microdevice described in Chapter 3. First, the single-channel device is used to test protein sorption on the silicon bed. Second, conditions for efficient on-bed protein digestion in the single-channel device are described. Third, the performance of the multichannel microdevice for systematic elution of cytochrome c and fluorescein, using both laser-induced fluorescence and mass spectrometry detection, is discussed. Finally, on-chip electrical fractionation is studied.

Doucette et al. studied bead-based protein digestion using conventional proteomics techniques[19-21]. Proteins were sorbed onto reverse-phase chromatographic beads placed in a microcentrifuge tube, tryspin solution was added for on-bead digestion and the resulting peptides released using high organic content buffer. The supernatant was then analyzed by MALDI or ESI MS. The authors concluded that equal digestion efficiencies were obtained for 5 and 30 minute digestion times. The described digestion method is therefore much faster than the conventional one, whereby trypsin digestion beads are added to a protein solution (16 hours digestion time). The surface-bound protein digests showed, however, a higher number of missed cleavages. Finally, only minor differences in peptide maps were found for different bead (silica versus polystyrene) and bead surface (C4, C8 or C18) types. This technique was used for protein digestion in the silicon-glass microdevice described in Chapter 3. Silicon beds were derivatized with a C18 coating for initial protein sorption, followed by digestion using trypsin solution and finally, peptide elution for ESI MS analysis.

4.2. MATERIALS AND METHODS

The microdevices were fabricated as described in Chapter 3: the specific fabrication method (i.e. thin versus thick PDMS) will be mentioned at the beginning of each study.

A syringe pump (Harvard Apparatus, PHD 2000) was used for solution flow through the system: a 50 μm i.d., 360 μm o.d. microcapillary (Polymicro Technologies) fitted with a sleeve was coupled to the microdevice through the Nanoport assembly (Upchurch Scientific) and to the syringe (Hamilton) using a coupling assembly (Upchurch Scientific). For mass spectrometric detection, a single quadrupole Sciex API 150EX (Applied Biosystems / MDS Sciex) instrument was used. All experiments were done in the positive ion mode. MS parameters: nebulizer gas = 0, curtain gas = 8, orifice = 35 V, focusing ring = 175 V, entrance quadrupole = -10 V, interquadrupole lens = -11, stubbies = -15 V, first resolving quadrupole = -11, deflector = -250, channel electron multiplier = 2,200 V, ion spray voltage = between 3,200 and 4,000 V. Data acquisition parameters: step size = 0.5 a.m.u., dwell time = 1 ms, pause time = 2 ms. The setup for fluorescence detection was similar to the one presented in Chapter 1 for single point LIF detection (section 1.3.5.) with a few changes made to allow for LIF images of large microdevice areas to be taken. The microchip sat on top of an inverted microscope on an X-Y translation stage. A laser beam (Argon ion laser, 488 nm, operated at 4 mW Model 2214-105L, Uniphase, San Jose, CA) was directed by mirrors to impinge on the area to be imaged from the top of the microdevice. The resulting fluorescence was gathered by the 5x, 0.1 N.A. objective of the inverted microscope, passed through a dichroic mirror (505DRLP, Omega, Brattleboro, VT), focused by a tube lens (f = 200 mm, Newport, PAC064, Irvine, CA) and redirected by a mirror to form an image filtered by an emission filter (530DF 30, Omega). A CCD camera (SONY) placed at the image plane collected the resulting image and the data was recorded using a VCR.

The following chemicals were obtained from Sigma-Aldrich: cytochrome c from horse heart (M.W. = 12,384 g/mol), myoglobin from horse heart (M.W. = 16,951 g/mol), bovine serum albumin (BSA, M.W. = 66,433 g/mol), trypsin from bovine pancreas, dithiothreitol (DTT), iodoacetamide, fluorescein, ammonium bicarbonate (NH_4HCO_3), ammonium hydroxide (NH_4OH). Formic acid (CH_2OH) was from Fluka and LC-MS grade methanol (MeOH) form Riedel-de Haen. Methanol was distilled before use. All aqueous solutions were made in ultrapure water (Millipore) and filtered before use (0.2 μm, Chromatographic Specialties). Protein solutions were prepared in siliconized

microcentrifuge tubes (Rose Scientific). Trypsin-immobilized beads were from Pierce Chemical Company.

Procedure for myoglobin and BSA reduction: 5 μl of 1 mg/ml protein solution was mixed with 10 μl of the digestion buffer and 5 μl of 45 mM DTT. The reaction was allowed to proceed at room temperature for 1 hour. The disulfide bonds were capped by adding 5 μl of iodoacetamide (100 mM) and leaving at room temperature for a further 20 minutes. Protein solutions were then ready for off- or on-chip digestion.

Procedure for off-chip digestion of cytochrome c, BSA and myoglobin: 1 mg of one of the proteins was diluted in the digestion buffer (0.1 M of NH_4HCO_3, pH 8.0). In a separate siliconized vial, 150 μl of trypsin-immobilized beads were washed three times with 500 μl of digestion buffer (beads and supernatant separated by centrifugation at 10 krpm for 5 minutes). The resulting gel containing the trypsin-immobilized beads was suspended in 200 μl of digestion buffer and added to the protein solution. The digestion was allowed to proceed in the dark for 16 hours, with shaking, at room temperature. Beads and digest were separated by centrifugation (three times at 10 krpm for 5 minutes).

4.3. SINGLE CHANNEL STUDY

Before use, microdevices were rinsed with 25% MeOH in H_2O for 30 minutes and the silicon columns observed under a microscope to make sure all parts of the bed were wetted. The mass spectrometer was used as the detector. The results are presented in two ways: either as a total ion chromatogram (TIC) or mass-to-charge ratio (m/z) spectrum. The TIC represents the sum of all intensities in the range of m/z scanned, giving a count per second (c.p.s) versus time plot. Each point in the TIC plot has a m/z spectrum associated with it, representing the m/z intensities at time t, shown as a c.p.s. versus m/z plot.

4.3.1. CYTOCHROME C SORPTION ONTO THE SILICON BED

Initial tests were conducted to ascertain the hydrophobic behavior of the C18-coated silicon bed using cytochrome c. Studies were conducted in 6 mm column lengths using thin PDMS as described in section 3.2.3.1. After rinsing the bed with, successively, water and 50 mM NH_4HCO_3 (pH 8.5), 0.5 mg/ml cytochrome c in 50 mM NH_4HCO_3 (pH 8.5) was flowed into the microdevice. The solution was then switched to 100% 0.1 M formic acid; the resulting TIC spectrum scanned over the range of 550-1,200 a.m.u. is

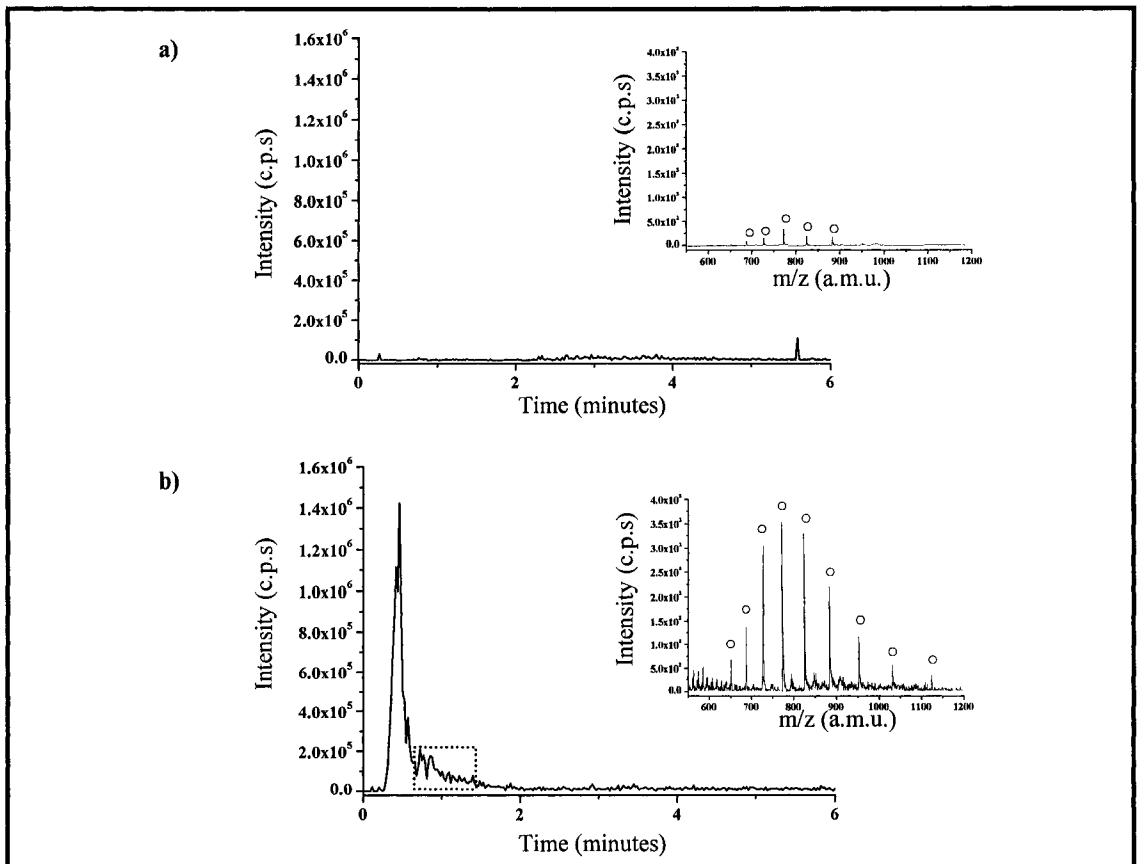

Figure 4.1 Cytochrome C Sorption on the Silicon Bed- a) Cytochrome c (0.5 mg/ml) was sorbed onto the silicon column; TIC spectrum was obtained for elution in 0.1 M formic acid (m/z spectra for 1-6 minutes shown in inset); b) TIC spectrum obtained for elution in 67% MeOH / 33% 0.1 M formic acid (m/z spectra for 1-6 minutes shown in inset). Both elutions at a flow rate of 1 µl/min. Cytochrome c charge states shown in open circles. Lag in elution profile due to microchamber volume shown by the dotted area in TIC spectrum of b).

shown in Figure 4.1a. The m/z spectrum associated with the 0-6 minute region is shown in the inset. The solution was then switched to 67% MeOH / 33% 0.1 M formic acid: the TIC and m/z spectrum for the associated 0-6 minute are shown in Figure 4.1b for an elution flow rate of 1 µl/min. Peaks in the inset m/z spectrum represent the different cytochrome c charge states (identified in open circles, see Table 4.1 of the appendix for charge states and their associated m/z value).

From Figure 4.1, the C18 silicon bed retains cytochrome c under aqueous conditions; only a negligible amount is eluted. At high organic content, the protein partitions between the hydrophobic bed and elution buffer resulting in the elution profile shown in

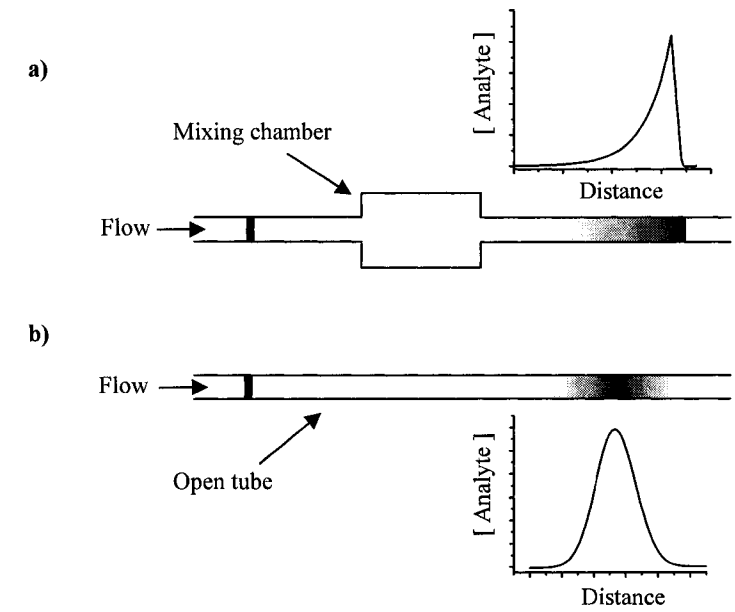

Figure 4.2 Bandbroadening in Microchannel and Microchamber- a) Bandbroadening of an analyte plug entering a microchamber will result in tailing of the peak; b) for an open tube, the bandbroadening results in a Gaussian distribution.

the TIC spectrum of Figure 4.1b. The protein is eluted in one minute with a symmetrical elution profile: the microdevice design is therefore symmetrical, i.e. the PDMS holes are well-defined. The effect of the microchamber (i.e. the hole connecting the silicon bed to the glass microchannel) can be seen as a small lag in the profile (highlighted in the figure by a dotted box), a lag which was more evident at the lower elution flow rate shown in Figure 4.3. Assuming a plug-like elution off the silicon column, two parameters will affect peak bandbroadening. First, the microchamber behaves as a "mixing chamber" which results, for an incoming plug, in an exponential analyte concentration profile shown schematically in Figure 4.2a. Second, the SPE-to-MS microchannel behaves as a non-sorptive open tube, which will distribute the analyte according to a gaussian profile, as shown in Figure 4.2b. These two effects result in the typical tailed elution peak seen in Figures 4.1 and 4.3.

As stated before, this lag in elution profile is more evident in Figure 4.3a for elution at a lower flow rate (0.5 μl/min, note that a different 6 mm microdevice was used here). The experiment was run to show the effect of MeOH content on elution. Cytochrome c (0.12 μg) was run through the column followed by a 50 μl water wash and elution at 1)

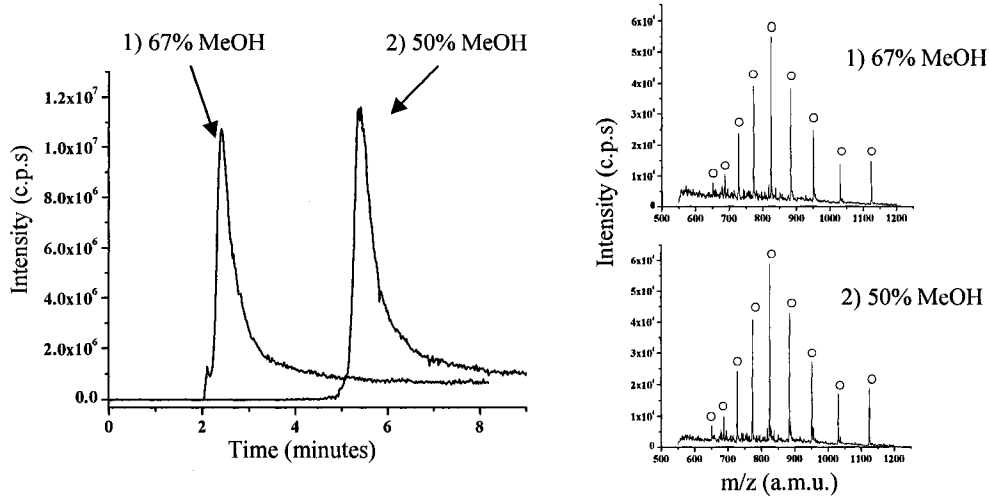

Figure 4.3 Effect of MeOH Percent on Elution Time- TIC for Cytochrome c (0.12 μg) eluted at 0.5 μl/min with 1) 67% MeOH / 33% 0.1 M formic acid and 2) 50% MeOH / 50% 0.1 M formic acid, as indicated (left). Resulting m/z spectra of cytochrome c charge states (right). Cytochrome c charge states shown in open circles.

67% MeOH / 33% 0.1 M formic acid or 2) 50% MeOH / 50% 0.1 M formic acid. From the TICs, a shift to longer elution time for lower organic content was observed, indicating a dependence on methanol percent, in agreement with elution from a reverse-phase surface. The MeOH percent was kept at 67% for all studies, in an effort to keep elution times to a minimum. Also, because of the well-known effects of high organic content on PDMS behavior (swelling and release of non-crosslinked monomers at the surface), higher organic content elution buffers were not used.

The solid phase extraction behavior of the 6 mm bed was tested; results are shown in Figure 4.4. Five different amounts of cytochrome c were loaded onto the column at a flow rate of 1 μl/min: 5 μl or 10 μl of 2.4 x 10^{-3} mg/ml (final load: 0.012 μg and 0.024 μg); 5 μl or 10 μl of 2.4 x 10^{-2} mg/ml (final load: 0.12 μg and 0.24 μg); 5 μl of 2.4 x 10^{-1} mg/ml (final load: 1.2 μg). After each loading, the column was rinsed with 50 μl of water and cytochrome c eluted at 0.5 μl/min with 67% MeOH / 33% 0.1 M formic acid. Figure 4.4a shows the TIC traces for three elutions, as indicated. Figure 4.4b presents peak areas versus protein load for five experiments; bed saturation occurred at 0.24 μg cytochrome c. This translated into a 0.08 μg cytochrome c capacity for a 2 mm bed. In Section 3.2.2, surface area calculations led to the silicon bed dimensions; these

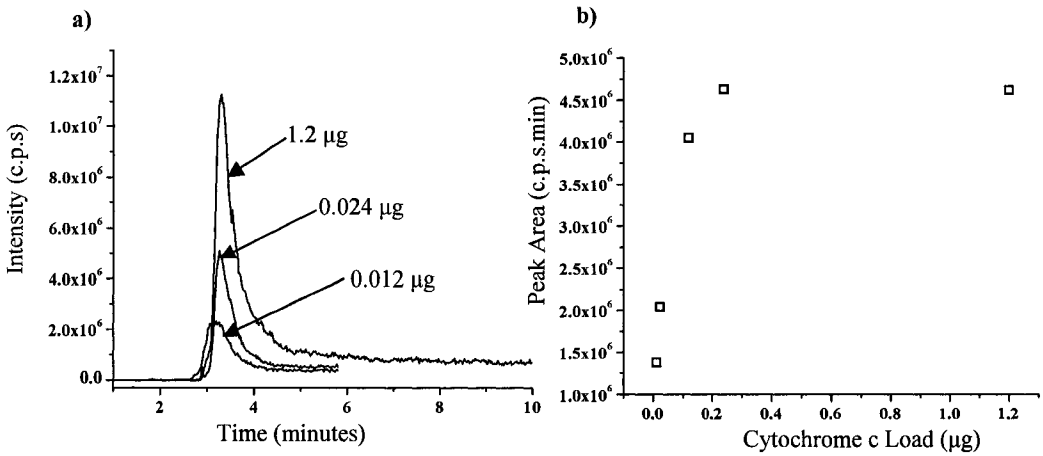

Figure 4.4 Cytochrome c Load- a) TIC for three different cytochrome c loads on a 6 mm column, as indicated; b) peak area versus Cytochrome c Load for five different loads. Cytochrome c was flowed at 1 µl/min: 5 µl and 10 µl of 2.4 x 10^{-3} mg/ml; 5 µl and 10 µl of 2.4 x 10^{-2} mg/ml; 5 µl of 2.4 x 10^{-1} mg/ml. Each loading stage was followed by a water wash (50 µl) and elution at 0.5 µl/min with 67% MeOH / 33% 0.1 M formic acid. Bed saturation occurred at 0.24 µg.

calculations were based on SPE bed dimensions from earlier work on the multiplexed platform (60 µm diameter Oasis HLB Plus beads, packed in 0.4 x 0.125 x 2 mm^3 bed)[18]. From these bed dimensions, the theoretical load according to the manufacturer was 1.8 µg of protein digest: the silicon bed had therefore a lower loading capacity. This was to be expected since the surface area calculations of Section 3.2.2 did not account for pores in the commercial SPE beads. A higher bed capacity can be achieved by simply making the bed longer or by making the silicon bed porous through anodization of the Si bed posts in a HF / ethanol solution[12]. However, the lower bed capacity had a beneficial affect on tryptic peptide elution, as will be seen in section 4.3.2.1: because of the low peptide load, all peptides elute at the same time, in a single peak having a relatively short full width at half maximum. This is contrary to earlier studies, which showed a wide variety of peak widths depending on the tryptic peptide eluting from the commercial SPE bed, making analysis on the multiplexed platform almost impossible[18]. Silicon column dimensions for multichannel analysis were therefore kept as described in Chapter 3.

At the other extreme, 194 fmol cytochrome c was preconcentrated; the resulting TIC is shown in Figure 4.5. Loading of 10 µl of 2.4 x 10^{-4} mg/ml cytochrome c at 1 µl/min was followed by a water wash (50 µl) and elution at 0.5 µl/min with 67% MeOH / 33%

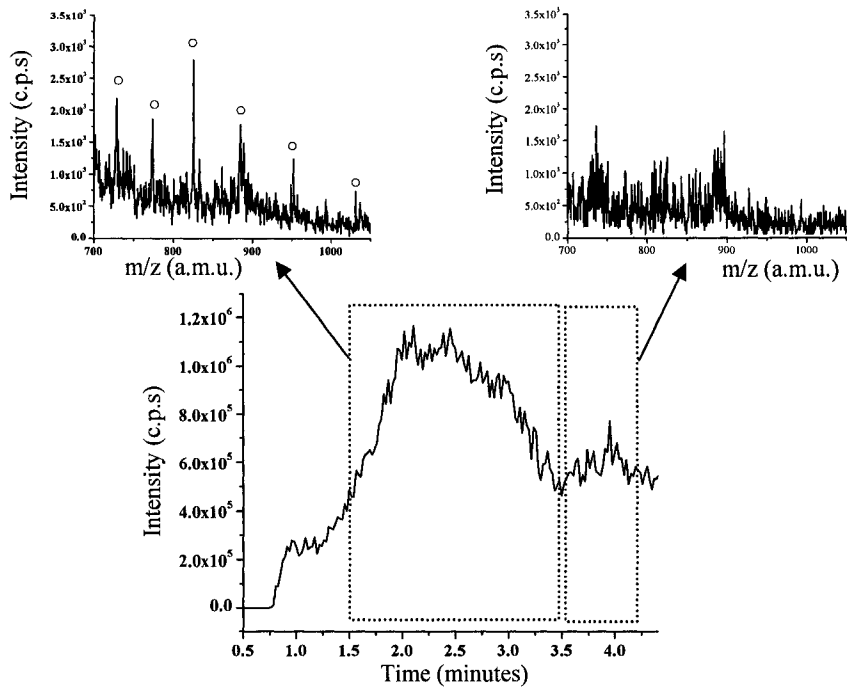

Figure 4.5 Cytochrome c at 194 fmol- Loading of 10 µl of 2.4 x 10^{-4} mg/ml cytochrome c at 1 µl/min was followed by a water wash (50 µl) and elution at 0.5 µl/min with 67% MeOH / 33% 0.1 M formic acid. The m/z spectra for the two indicated time regions are also shown. Cytochrome c charge states shown in open circles.

0.1 M formic acid. The m/z spectra for the two indicated time regions are also shown (note that cytochrome c peaks are marked by an open circle). Cytochrome c charge states can be seen above background in the m/z spectrum for the 1.5-3.5 minutes region; no charged states are obtained in the background region between 3.5-4.5 minutes.

4.3.2. CYTOCHROME C DIGESTION STUDY

The digestion method described by Doucette et al. has its drawback: trypsin peaks will add to the mass spectral background. Because trypsin itself is a protein, it will digest itself (a process called autodigestion) and produce a m/z spectrum. When using the two-bed configuration described by Wang and Taylor, autodigestion is minimized because trypsin is anchored onto the bead surface. Here, trypsin solution is flowed over a protein adsorbed onto the column surface, producing background peaks at elution. Trypsin autodigestion was tested: after conditioning, 10 µl of 0.31 mg/ml trypsin (final load: 3.1 µg, in 50 mM ammonium bicarbonate buffer at pH 8.5) was flowed into the microdevice.

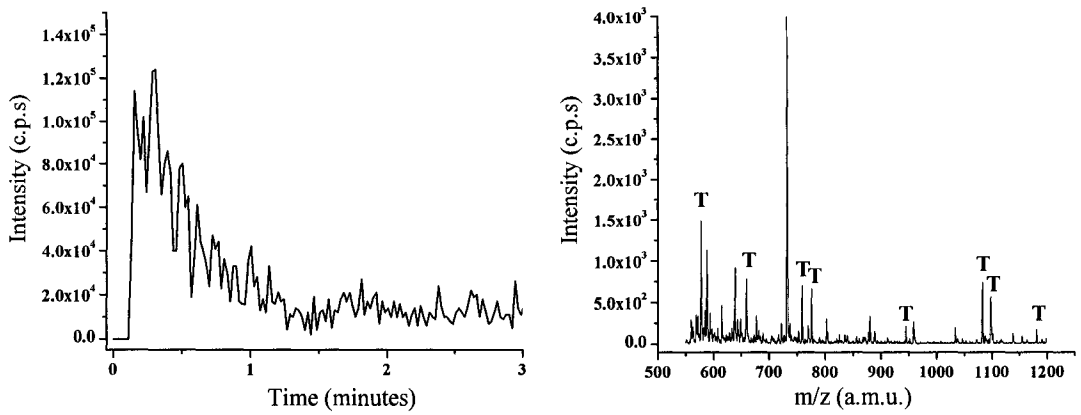

Figure 4.6 Trypsin Autodigestion- TIC (left) and resulting m/z for the first 1.5 minute (right). 10 µl of 0.31 mg/ml trypsin (final load: 3.1 µg, in 50 mM ammonium bicarbonate buffer at pH 8.5) was flowed into the microdevice. Spectrum obtained after a 30 minutes reaction time. Elution conditions: 67% MeOH / 33% 0.1 M formic acid at 0.5 µl/min flow rate. Trypsin autodigestion peaks shown with a **T**.

After a 30 minutes reaction time, the solution was switched to the elution buffer, 67% MeOH / 33% 0.1 M formic acid, and the resulting elution peak obtained at 0.5 µl/min flow rate for the m/z range of 550-1,200 a.m.u. Figure 4.6 presents the TIC (left) and m/z (rigth) spectra obtained. Peaks from trypsin autodigestion are shown with a **T** and are enumerated in Table 4.2 of the Appendix. From the figure, there are peaks unaccounted for, such as the highest-intensity peak at 732.0 a.m.u. (which regularly shows up in all studies). This peak was attributed to non-crosslinked monomer at the PDMS surface desorbing under higher organic percent buffer conditions.

Initial digestion studies focused on three different parameters for maximum on-chip cytochrome c digestion efficiency: trypsin-to-cytochrome c ratio, trypsin flow during digestion and percent organic during digestion. These are described in the following section. Two notes on these initial studies: first, the microdevice used had a leak at the Nanoport which was sealed using epoxy. Because this seal did not conform perfectly to the glass microdevice, a dead volume existed at the entry Nanoport. Therefore, throughout these initial studies, a stagnant pool of cytochrome c was present at the Nanoport, which led to high levels of cytochrome c charge states peaks to be detected upon elution. Second, high elution flow rates were used: as mentioned in section 4.3.1,

the final purpose of this study being the multiplexing of several SPE columns onto one platform, limiting elution peak widths was essential for discriminate peak elution.

4.3.2.1. INITIAL DIGESTION STUDIES

4.3.2.1.1. TRYPSIN–TO–CYTOCHROME C RATIO

The following experimental protocol was used for all experiments discussed in this section: 10 μl of 0.25 mg/ml cytochrome c solution in ammonium bicarbonate buffer (50 mM, pH 8.5) was flowed into the microdevice at 1 μl/min, followed by 50 μl ammonium bicarbonate buffer wash and 10 μl trypsin in the ammonium bicarbonate buffer. After a set digestion time under stop-flow condition, the elution buffer (67% MeOH / 33% 0.1 M formic acid) was then delivered at a flow rate of 1 μl/min and TIC spectra obtained. Mass-to-charge spectra were compared to spectra obtained for off-chip digested cytochrome c.

Initial tests were conducted at low trypsin load to minimize background from autodigestion peaks. The SPE bed was saturated by loading 2.5 μg of cytochrome c; using a 30 minutes digestion time for 0.3 μg, 0.6 μg and 1.9 μg trypsin loads produced only spectra from cytochrome c charge states, indicating no digestion. Cytochrome c charge state peaks were monitored following overnight digestion (15 hours) for two different trypsin-to-cytochrome c ratios. For a 3.7 μg cytochrome c load, 0.31 μg and 3.1 μg trypsin loads were tested. The resulting m/z spectra for the eluted peaks are shown in Figure 4.7 for a) 0.31 μg trypsin after 15 hours digestion and b) 3.1 μg trypsin after 15 hours digestion. Note that cytochrome c charge states are shown by open circles, and cytochrome c digest peaks by full circles (cytochrome c digest peaks are enumerated in Table 4.3 of the Appendix). The remaining peaks were from trypsin autodigestion (not marked in the figure for clarity) and impurities. No cytochrome c charge states were observed at 3.1 μg trypsin load, as opposed to the 0.31 μg load; the higher load was therefore more efficient and resulted in five observed digest peaks, versus four for the lower trypsin load.

As shown in the m/z spectrum of Figure 4.7c following a 30 minute digestion time, initial tests at 1.9 μg trypsin load showed no evidence of digestion for this short digestion time: only cytochrome c charge states resulted. The higher trypsin load was therefore used for all subsequent studies. Figure 4.7d presents the m/z spectrum for a 30

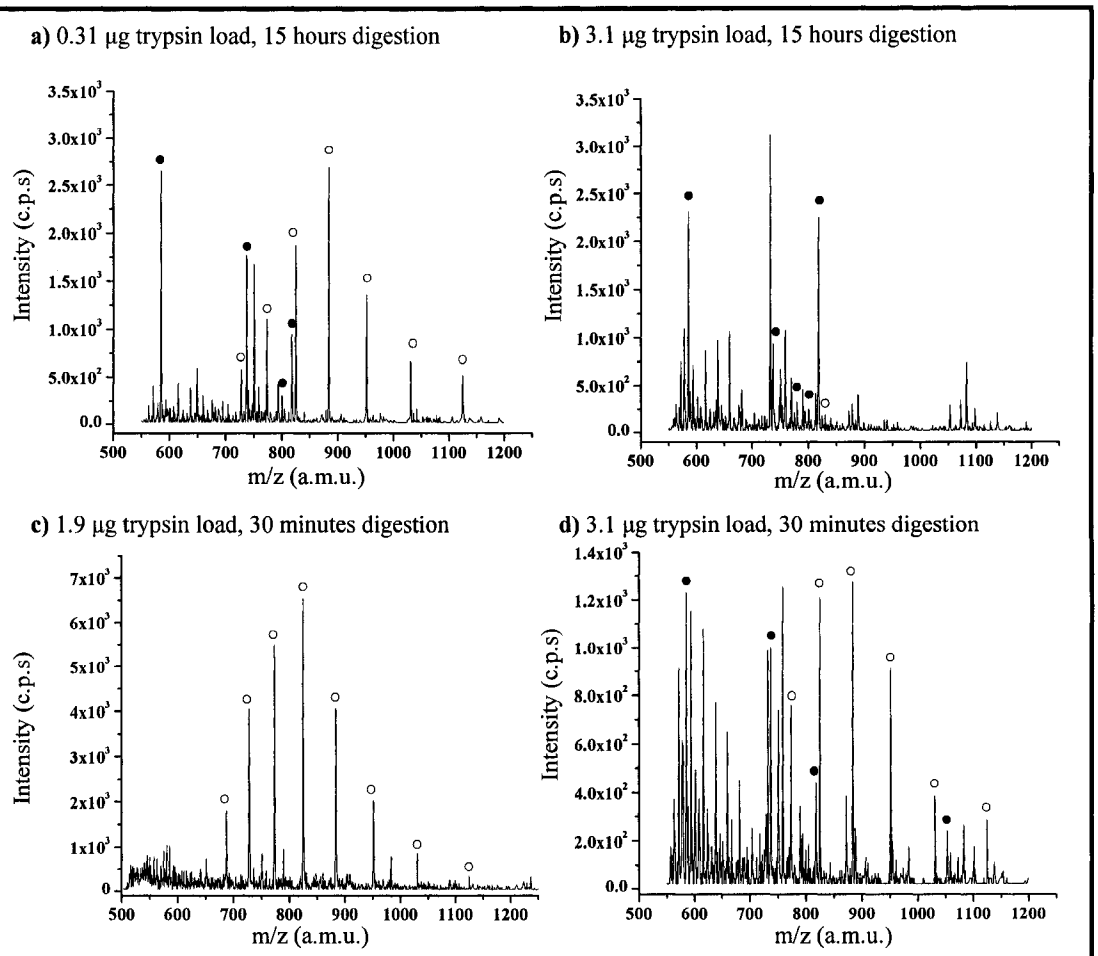

Figure 4.7 Cytochrome c Digest- Cytochrome c (10 µl of 0.25 mg/ml) was flowed at 1 µl/min. Following a 50 µl ammonium bicarbonate buffer wash, 10 µl trypsin in ammonium bicarbonate buffer (50 mM, pH 8.5) was flowed. After digestion under stop-flow conditions, peptides were eluted with 67% MeOH / 33% 0.1 M formic acid at 1 µl/min. m/z spectra for a) 0.31 µg trypsin load, 15 hours digestion; b) 3.1 µg trypsin load, 15 hours digestion; c) 1.9 µg trypsin load, 30 minutes digestion and d) 3.1 µg trypsin load, 30 minutes digestion. Cytochrome c charge states shown in open circles, cytochrome c tryptic peptides shown in full circles.

minutes digestion time using the higher trypsin load (3.1 µg). As seen from Figure 4.7d, only four tryptic digest peaks were observed and cytochrome c peaks were still present after 30 minutes digestion. From Doucette et al.[20], a 30 minute digestion time should result in an efficient digestion of proteins sorbed onto reverse-phase beads; the observed charge states therefore came from elution of cytochrome c trapped in the dead volume at the sealed Nanoport. Further evidence of this leak is seen by comparing Figure 4.7b for

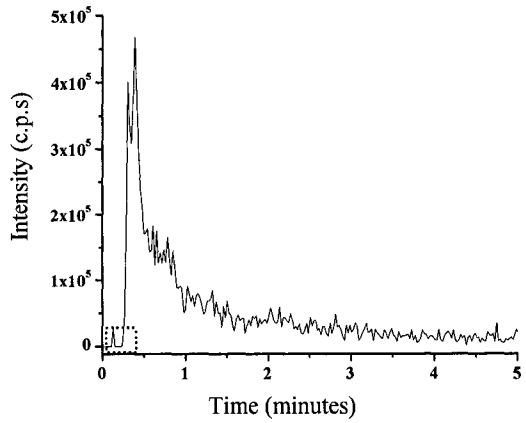

Figure 4.8 Typical TIC Spectrum for Peptide Elution- All digestion parameters as described in Figure 3.7b. Initial ESI stabilization shown by the dotted box.

15 hours digestion and Figure 4.7d for 30 minutes digestion under 3.1 μg tryspin load; under the same trypsin load, the 15 hour digest produced no cytochrome c charge states peaks. Digestion in the stagnant cytochrome c solution at the Nanoport would act as do homogeneous digestion and therefore require longer digestion times; no charge states were therefore observed for the 15 hours digestion. The 30 minutes digest produced both tryptic peaks from the heterogeneous digestion and charge states from the homogeneous digestion. Although the leak at the Nanoport may have skewed the digestion results, the higher trypsin load (3.1 μg) was used for all subsequent studies. Another effect on the m/z spectrum can be seen from the addition of glue to seal the leaking Nanoport in Figure 4.7d: a high number of unidentified peaks were detected, most probably from the leakage of glue by-products under acetonitrile coniditions.

An increase in cytochrome c and trypsin load produced no change in the cytochrome c peptide mass map, only trypsin peaks produced higher intensity values. These results show that 1) the observed tryptic digest peaks did indeed come from the tryptic digest and 2) the column was saturated. Column saturation during the initial cytochrome c loading stage is important to minimize trypsin background: at low cytochrome c loads, unoccupied sites on the SPE bed will be saturated with trypsin, which will in turn be digested by trypsin in solution.

Figure 4.8 is the TIC of a typical tryptic digest elution: all peptides elute within a short timeframe, a result that contrasts with that obtained for the bead-based system studied before[18]. The bead-based system was packed with porous beads, which resulted in high SPE bed capacities. In this system, peptide desorption under high organic content buffer did not result in flash elution: peptides would experience chromatographic behavior in the 2 mm bed and elute at different times, making pressure-driven multiplexed analysis difficult. In the silicon-based system, the low bed capacity (as calculated in section 4.3.1) allowed for flash elution off the column, a pre-requisite for further multiplexing. The high elution flow rate coupled to low silicon bed capacity resulted in small full width at half maximum for the eluted protein digest. However, as shown in Figure 4.7d, only a few peptide peaks were observed, a problem that is discussed next.

4.3.2.1.2. FLOW AND PERCENT ORGANIC DEPENDANCE

In an effort to increase the number of observed tryptic peptide peaks, the influence of both trypsin flow during digestion and percent organic in the buffer was studied. Initially, the presence of residual cytochrome c peaks after a 30 minute digestion (Figure 4.7d) was not attributed to the presence of a dead volume at the Nanoport but rather to inefficient trypsin transport to the sorbed protein under stop-flow digestion condition. To increase trypsin transport, two different flow rates were tested (0.05 µl/min and 0.5 µl/min) during digestion and compared to the stop-flow mode by monitoring the number of observed cytochrome c tryptic digest peaks. No effect was observed on the number or intensity of detected tryptic peptide peaks; the low numbers of observed tryptic digest peaks was therefore not due to low trypsin transport to the sorbed protein. Subsequent digestions were therefore done under stop-flow conditions.

Under 100% aqueous condition, low analyte retention may result in reverse-phase coating collapse of the bonded phase[22]. Conditioning the column with a small amount of organic phase in the conditioning buffer helps to extend the reverse-phase coating into solution and improves phase-to-analyte interaction. Five percent methanol was therefore added to all buffers for on-bed digestion. Comparing 0% to 5% MeOH, three extra tryptic digest peaks are detected; methanol content therefore influenced peptide sorption

onto the reverse-phase coating. All subsequent digestions were conducted in buffer solutions containing 5% MeOH.

4.3.2.1.3. FLOW RATE AT ELUTION

Digestion studies presented so far were done in a microdevice having a dead volume at the Nanoport which led to high numbers of cytochrome c charge states peaks to be detected. Also, since peaks with small full width at half maximum would be needed to obtain discriminated peak elution in the multiplexed device, a high elution flow rate (1 µl/min) was used. Here, a new microdevice was used which showed no sign of leakage (4 mm column built using thin PDMS as described in section 3.2.3.1) and the elution flow rate was slowed down to 0.5 µl/min. The resulting TIC and m/z spectra are shown in Figure 4.9a and Figure 4.9b, respectively. The m/z spectrum was an average of the data obtained for the 3 to 8 minutes interval on the TIC. The slower elution flow rate resulted in a much higher number of detected peptide peaks. Although higher flow rates were preferred for multiplexing purpose, peptide peak detection suffered from it. Two factors can contribute to this: first, at high flow rates the peptides elute rapidly and no stable ESI signal can be obtained before detecting the elution peak. ESI stabilization was achieved at high flow rates under high organic-content buffer conditions: the ESI stabilized upon arrival of the acetonitrile front at the ESI tip. However the high flow rate could translate into a loss in peptide signals as the ESI stabilized between the two buffer systems, i.e. from 100% aqueous to 67% acetonitrile. Comparing TIC signals before the elution peak for the high (Figure 4.8, highlighted by a dotted box) and low (Figure 4.9a, highlighted by a dotted box) flow rates, the difficulty of obtaining a stable ESI signal before peptide elution at high flow rates was a problem. At the higher flow rate (Figure 4.8), no background ESI signal was observed before the elution peak; the ESI therefore did not have time to stabilize before peptide elution. At the lower flow rate (Figure 4.9a), a stable spray was obtained before peptide elution. Second, suppression from cationic species in the elution products could lower the number of detected peptides: in Figure 4.7d, the detection of undigested cytochrome c peaks and unidentified peaks (presumably coming from the leakage of glue by-products under high acetonitrile content) could prevent the detection of cytochrome c digestion products. Because the new microdevice had no dead volume or added glue due to Nanoport leakage, no undigested cytochrome c

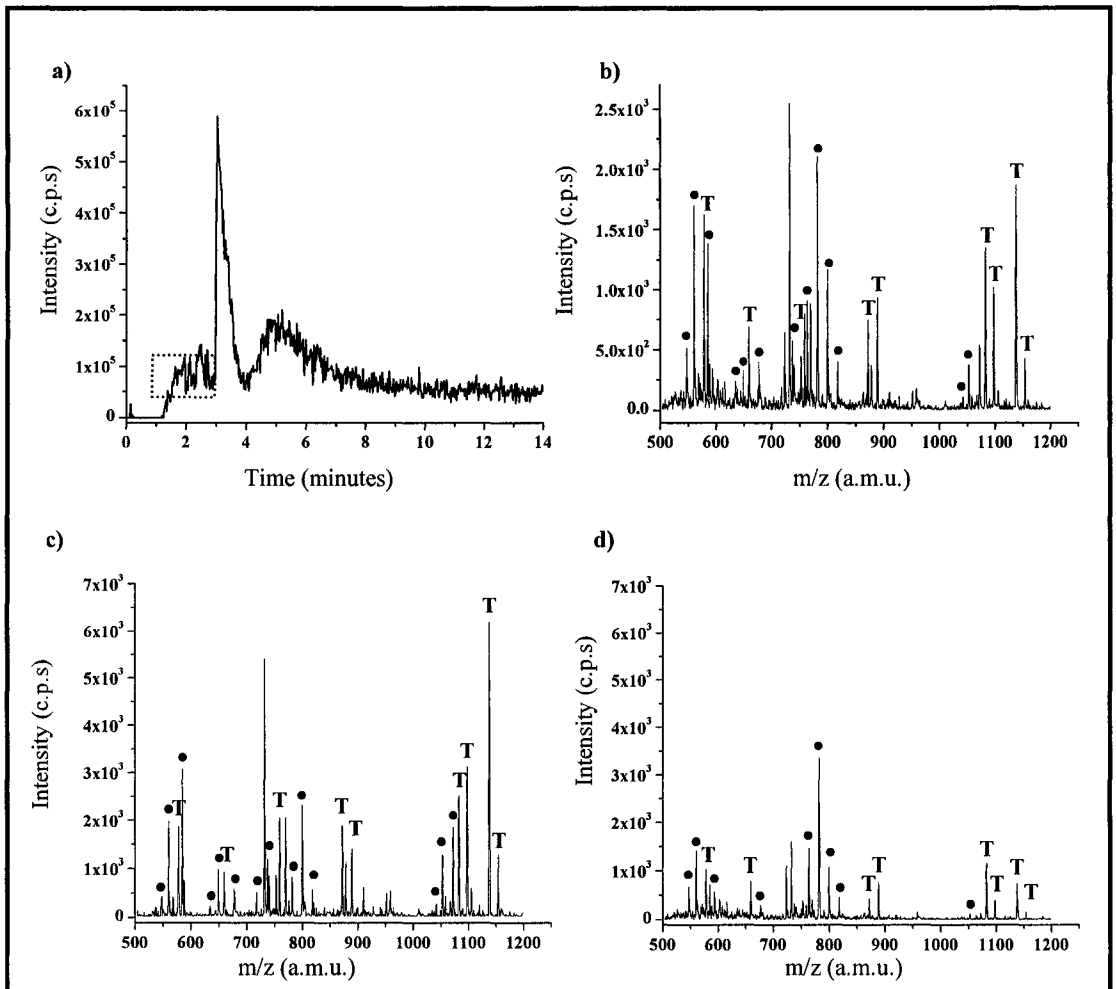

Figure 4.9 Cytochrome c Digest - Flow Rate at Elution- Cytochrome c (10 µl of 0.25 mg/ml) was flowed at 1 µl/min. Following a 50 µl ammonium bicarbonate buffer wash, 10 µl of 0.31 mg/ml trypsin in ammonium bicarbonate buffer (50 mM, pH 8.5) was flowed. After 30 minutes digestion under stop-flow conditions, peptides were eluted with 67% MeOH / 33% 0.1 M formic acid at 0.5 µl/min: a) TIC spectra; b) m/z spectra for 3-8 min region; c) m/z spectra for 3-4 min region; d) m/z spectra for 4-8 min region. Trypsin autodigestion (**T**) and cytochrome c tryptic peptides (full circles). Initial ESI stabilization shown by the dotted box in TIC spectrum.

peaks or peaks due to glue leakage under high acetonitrile conditions were obtained; cytochrome c tryptic peptides could then be readily observed.

Four regions were seen in the TIC of Figure 4.9a: the initial background ESI signal, the first sharp peak, a second broader peak and finally a return to background. Mass-to-charge spectra for the two peak regions are shown in Figure 4.9c for 3-4 minutes

and Figure 4.9d for 4-8 minutes. As shown, peptides eluted throughout the two peak regions, i.e. from 3 to 8 minutes, while trypsin by-products eluted mainly in the initial 3 to 4 minutes, resulting in a two-peak TIC profile.

4.3.3. DIGESTION RESULTS

Following these initial digestion studies, three protein digestions were conducted in 6 mm length column, using thick PDMS (section 3.2.3.2). Cytochrome c, BSA and myoglobin were digested off- and on-chip and analyzed by mass spectrometry. Note that BSA and myoglobin were reduced off-chip prior to trypsin digestion (following the protocol outlined in section 4.2). The protocol for on-bed digestion was derived from the initial studies presented: following bed saturation with the protein of interest (10 µl of 0.37 mg/ml cytochrome c, 20 µl of 0.2 mg/ml BSA or myoglobin, all proteins were diluted in 5% MeOH / 95% ammonium bicarbonate, 50 mM) and a 50 µl ammonium bicarbonate wash (containing 5% MeOH), 10 µl of 0.31 mg/ml trypsin solution (in 5% MeOH / 95% ammonium bicarbonate, 50 mM, pH 8.5) was flowed in the microdevice. Digestion under stop-flow conditions was allowed to proceed for 30 minutes. To reduce the detection of trypsin by-product, which could hamper tryptic peptide detection, the bed was then washed with 50 µl of 5% MeOH / 95% 0.1 M formic acid. For peptide elution, 67% MeOH / 33% 0.1 M formic acid was used at 0.5 µl/min flow rate.

For off-chip digests, two analysis techniques were used: 1) direct infusion through a microcapillary coupled to an ESI tip at 0.5 µl/min; 2) loading into the microdevice, followed by a 5% MeOH / 95% 0.1 M formic acid wash and elution using the elution buffer (67% MeOH / 33% 0.1 M formic acid) at 0.5 µl/min. Conditions for direct infusion: 10 µl tryptic digest diluted in 100 µl elution buffer (67% MeOH / 33% 0.1 M formic acid). Conditions for SPE of off-chip digested proteins: for cytochrome c: 25 µl of digest of tryptic digest diluted 10:1 in 95% ammonium bicarbonate (50 mM, pH 8.5) / 5% MeOH. For myoglobin and BSA: 50 µl of tryptic digest diluted 10:1 in 95% ammonium bicarbonate (50 mM, pH 8.5) / 5% MeOH.

Cytochrome c m/z results for the three studies are presented in Figure 4.10: the observed cytochrome c tryptic peptides are listed in Table 4.3 of the Appendix. In Figure 4.10a, the off-chip digest was flowed directly through the ESI capillary tip. In Figure 4.10b, the off-chip digest was flowed into the microdevice: the tryptic peptides were

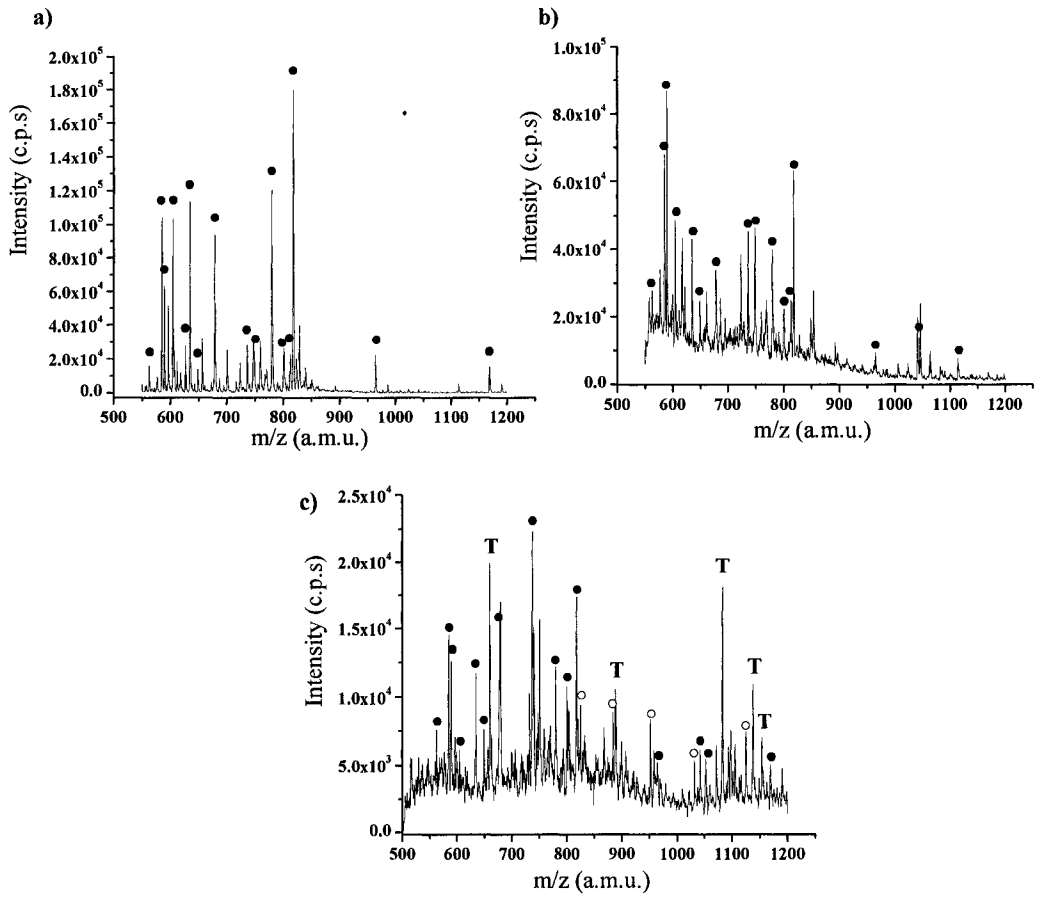

Figure 4.10 Cytochrome c Digest-Final Results- a) Off-chip digest directly infused through an ESI capillary; b) off-chip digest flowed into the microdevice in low MeOH percent buffer for initial peptide trapping, followed by elution at 0.5 µl/min; c) on-chip digestion following the protocol described in the text. Trypsin autodigestion (**T**) and cytochrome c tryptic peptides (full circles).

trapped on the SPE bed. Following a wash with a solution of 5% MeOH / 95% 0.1 M formic acid, the trapped peptides were eluted. In Figure 4.10c, the complete digestion proceeded in the microdevice, following the protocol mentioned above for on-bed digestion. Compared to earlier m/z spectra for a cytochrome c digest (Figure 4.7 and Figure 4.9), higher background signals were observed for the on-chip experiments presented in Figure 4.10b and Figure 4.10c. Previous experiments were done on microdevices with thin PDMS, whereas these were done with thick PDMS structures: the higher background may come from the higher amount of non-crosslinked monomer in the PDMS surface. Comparing the m/z spectra for the background region of the thick

(Figure 4.10c) versus thin (Figure 4.9b) PDMS, a clear background increase resulted in the thick PDMS. Longer conditioning times at the start of the experiments could have lowered these backgrounds, but since the microdevice lifetime was limited, such conditioning was not done. During the course of these studies, the microdevice lifetime was limited by two main factors: clogging at the ESI tip and Nanoport leakage. Clogging at the ESI tip, if not detected fast enough, produced a pressure build up at the silicon bed which resulted in failure of the PDMS-silicon bonding. The microdevice would then leak and could not be used for further studies. The Nanoport was fixed to the glass microdevice using glue provided by the manufacturer (Upchuch Scientific). Large volumes of high organic content buffers will dissolve the glue and eventually lead to leakage at the Nanoport. To wash away the non-crosslinked PDMS monomer, large volumes of high organic content buffers would have to be used: instead of risking a leak at the Nanoport, the microdevice was used without further washing. From Figure 4.10, except for the peptide at 626.5 a.m.u., all peptides detected in Figure 4.10a (for direct infusion of off-chip digest) are recovered in Figure 4.10b (for on-bed SPE of off-chip digest), showing the SPE bed was efficient at sorbing aqueous tryptic peptide solutions. Comparing trypsin by-product detection for experiments with (Figure 4.10c) and without (Figure 4.9b) an extra formic acid wash, a reduction in the number of trypsin autodigestion peaks is accomplished by the washing step. Also, except for a peak at 748.5 a.m.u, all cytochrome c tryptic digest peaks observed for the on-bed SPE of off-chip digest (Figure 4.10b) were recovered during the on-chip analysis (Figure 4.10c); almost all cytochrome c tryptic peptides were recovered after the extra formic acid washing step, showing the good SPE behavior of the bed. The extra formic acid washing step therefore reduced observed trypsin autodigestion peaks while not affecting the protein's tryptic peptides sorption. The final percent coverage for the on-chip digestion of Figure 4.10c was 85%, a clear improvement from early studies shown in Figure 4.7c, where only 4 tryptic peptide fragments were recovered. This result compares well to data published by Craft et al. for on-bead cytochrome c digestion, where a 91% surface coverage was obtained[19].

Results for BSA and myoglobin digestions are shown in Figure 4.11: observed myoglobin and BSA tryptic peptides are listed in Table 4.4 and Table 4.5 of the

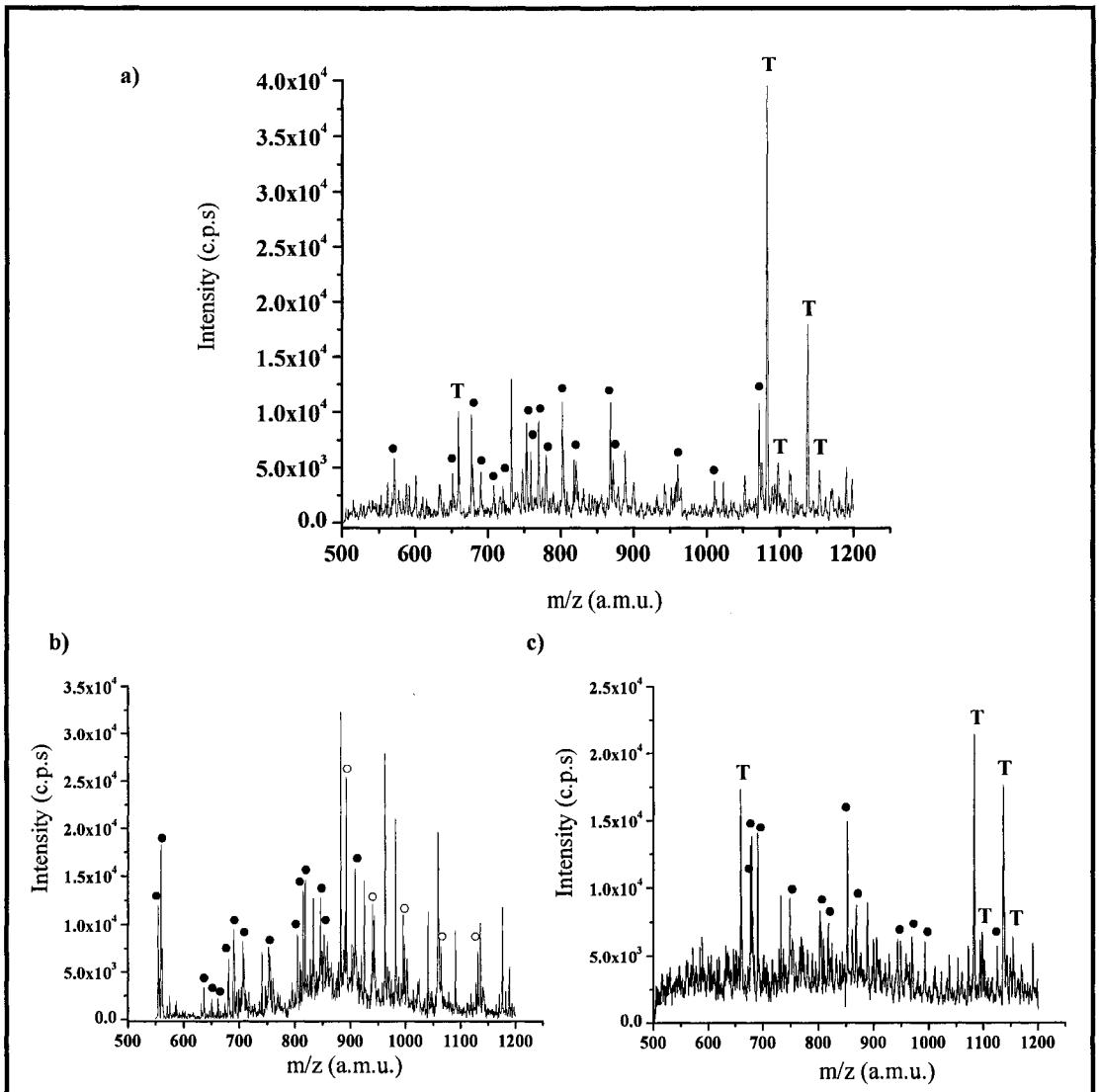

Figure 4.11 Myoglobin and BSA Digests- a) On-chip BSA digest, following the protocol described in the text; b) off-chip myoglobin digest directly infused through an ESI capillary; c) on-chip myoglobin digestion following the protocol described in the text. Trypsin autodigestion (**T**), protein tryptic peptides (full circles) and myoglobin charge states (open circle).

Appendix, respectively. Figure 4.11a presents the on-chip BSA digest; Figure 4.11b presents the result for off-chip myoglobin digest infused directly through the ESI capillary tip; Figure 4.11c presents the on-chip myoglobin digestion results. The BSA results show a lower background than for the myoglobin and cytochrome c on-chip digests. Because BSA was the last protein to be tested, non-crosslinked monomer at the surface of the PDMS had desorbed during previous experiments, which reduced the

background by half. Seventeen peptide peaks were detected, for a total percent coverage of 47%. Craft et al. obtained a 69% BSA coverage for their on-bead work[19]: the lower percentage obtained here may come from the scanning range used during MS detection, 500 a.m.u. to 1,200 a.m.u. Larger peptide fragments could have been detected for an upper m/z value set to 1,700 a.m.u., giving a higher percent coverage. The detection could also have been affected by trypsin autodigestion peaks: BSA tryptic peptides are present in the 1,050-1,200 a.m.u. mass-to-charge ratio range, where four high intensity autodigestion peaks were detected (see Figure 4.11a and 4.11c). These could have prevented the detection of BSA tryptic digest peaks.

Off-chip digestion of myoglobin was initially performed using the same off-chip procedure as cytochrome c (i.e. without off-chip reduction prior to trypsin digestion), mass spectrometric detection of the reaction products resulted in myoglobin charged states, enumerated in Table 4.1 of the Appendix. No detectable digestion had therefore taken place. The protein was then further reduced (using the protocol of section 4.3.2) and the reduced product used for the on-chip digestion of Figure 4.11. Twelve peptide fragments were detected, for a percent coverage for the on-chip digest of 74% (note that myoglobin was not studied by Craft et al.). Comparing m/z spectra for off-chip digest detection through the ESI tip (Figure 4.11b) versus on-chip digest (Figure 4.11c), peptides below 650 a.m.u. were not recovered during the on-chip procedure. Mass-to-charge spectrum from sorption of the off-chip digest onto the silicon SPE bed followed by release in high organic content buffer also resulted in a loss of these peptides: they were therefore not sorbed onto the SPE bed. As mentioned earlier, Doucette et al. concluded that similar percent coverage could be obtained on different bead phase (i.e. C4 versus C18), but noted small differences in the types of peptides recovered from one phase to the other. Although not tested, a different phase may have retained these 5 peptide fragments and increase the overall percent coverage.

4.4. MULTICHANNEL STUDY

The aim of this study was to test the multichannel microdevice for sequential elution of analytes sorbed onto the silicon SPE beds, as discussed in Chapter 3. The picture of a multichannel microdevice is shown again in Figure 4.12: elution first from the shortest SPE-to-MS distance microchannel should be observed (2.0 cm), followed by elution from

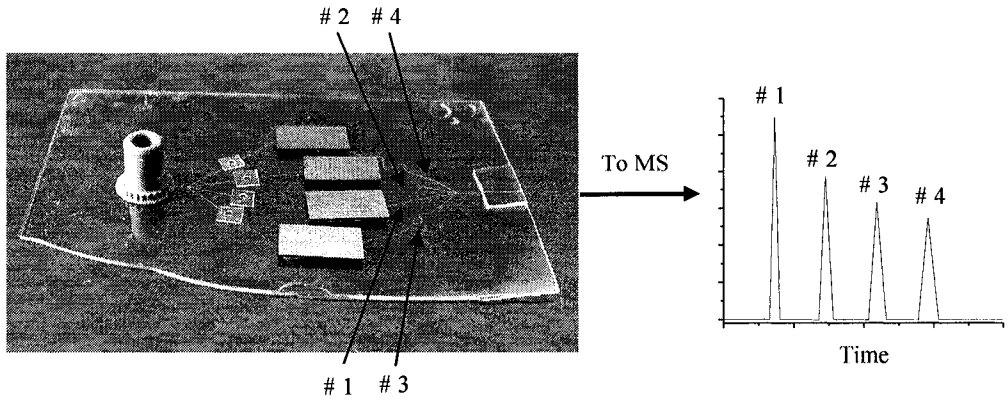

Figure 4.12 Multichannel Microdevice- with a schematic of the expected TIC spectrum upon elution from the silicon SPE beds.

the second (2.5 cm), third (3.0 cm) and finally longest (3.5 cm) SPE-to-MS distance. Microdevices for multichannel studies were prepared as described in Chapter 3, using either the thin PDMS (section 3.2.3.1) or thick PDMS (section 3.2.3.2) protocol, as mentioned in the following subsections. Tests were conducted using two detection methods: ESI MS of cytochrome c and LIF of fluorescein, as described in section 4.2. Before use, microdevices were rinsed with 25% MeOH in H_2O for 30 minutes and the silicon columns observed under a microscope to make sure all parts of the bed were wetted.

4.4.1. THIN PDMS

Four-channel microdevices described in section 3.2.3.1 for thin PDMS were used. Tests were conducted using cytochrome c solutions in water under ESI MS detection. After conditioning, 10 µl of 1.2 x 10^{-2} mg/ml (final load: 0.12 µg) or 10 µl of 1.2 x 10^{-3} mg/ml (final load: 0.012 µg) of cytochrome c was flowed into the microdevice at 1 µl/min, followed by 50 µl water wash and elution using 67% MeOH / 33% 0.1 M formic acid solution at 1 µl/min flow rate. The resulting TIC spectra are shown in Figure 4.13. As seen in Figure 4.13a, a single peak was obtained for the cytochrome c elution (m/z spectrum of the peak showed the usual cytochrome c charged states enumerated in Table 4.1 of the appendix). In an effort to obtain four baseline-resolved peaks, each corresponding to one SPE elution, the cytochrome c load was reduced by a factor of 10 to

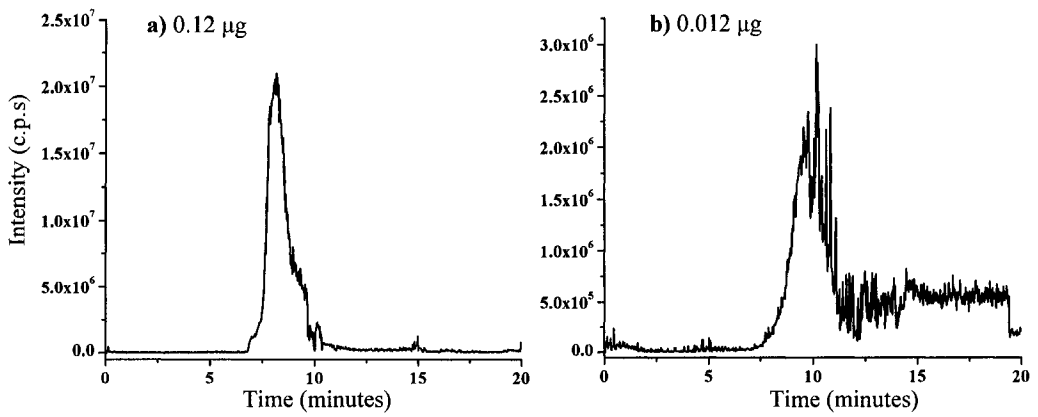

Figure 4.13 TIC Spectra from Multichannel Device-Thin PDMS- Following cytochrome c sorption and water washed, the protein was eluted using 67% MeOH / 33% 0.1 M formic acid solution at 1 µl/min flow rate. Cytochrome c load: a) 0.12 µg, b) 0.012 µg.

decrease the eluting peak widths. As seen in Figure 4.13b, this did not result in four discriminate peaks; neither did elutions at slower flow rates.

ESI MS analysis only assessed the resulting overall elution profile; to gather information about individual microchannel flow behavior, laser-induced fluorescence experiments were conducted. After conditioning the microdevice with water (50 µl), fluorescein in water (100 µM) was continuously flowed into the microdevice (1 µl/min) and the resulting fluorescence was observed at the meeting point of the four microchannels after the SPE beds. The results are shown in the images of Figure 4.14. Figure 4.14a shows the imaged region with a water flow (lights on): the four microchannels met in the center of the image, with microchannels numbered from 1-4, #1 having the shortest SPE-to-MS microchannel distance (2.0 cm), followed by #2 (2.5 cm), #3 (3.0 cm) and #4 (3.5 cm). Figure 4.14b to Figure 4.14e show the LIF results (lights off) for continuous flow of fluorescein, in chronological order. The expected elution order was first from microchannel #1, followed by #2, #3 and finally #4. As seen from Figure 4.14b to Figure 4.14e, this was not the case: elution from #3 was seen first, followed by #1 and finally, coelution of microchannels #2 and #4.

Pictures of the four silicon SPE beds under 20x microscope objective are shown in Figure 4.15. From the pictures, large air bubbles were trapped in the thin PDMS

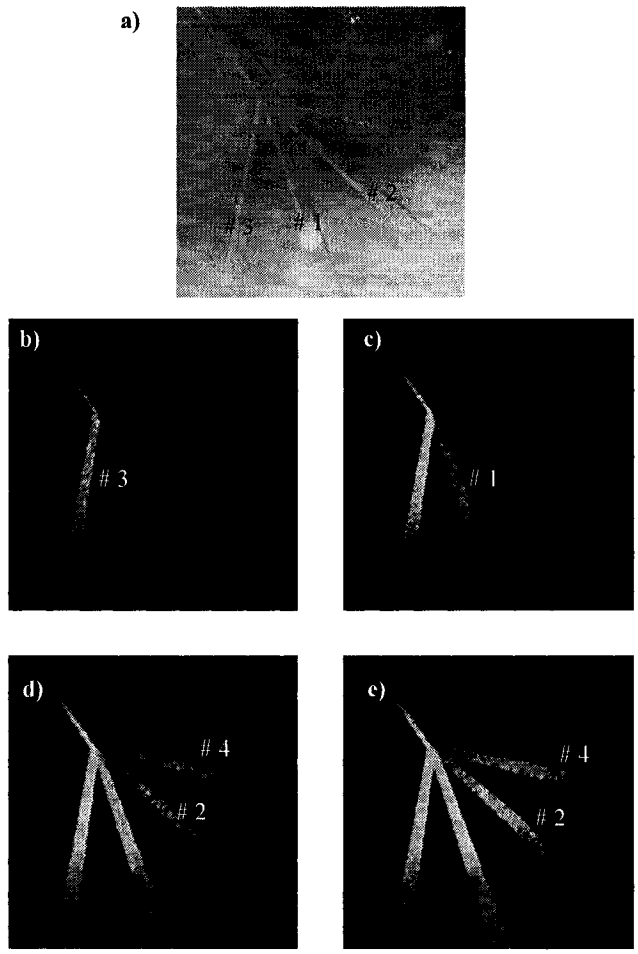

Figure 4.14 Fluorescence Image from Multichannel Device- Using thin PDMS. a) Image of the observed region, just before the ESI tip; b) to e) observed fluorescein breakthrough in chronological order, from b to e. Fluorescein was 100 μM in water, continuously flowed into the microdevice at 1 μl/min flow rate.

structure; the source of these was discussed in Chapter 3 (section 3.2.3.1). In the case of column #3, the area covered by the trapped air was large enough to allow the fluorescein solution to travel from one end of the silicon column to the other through the air pockets above the silicon pillars, rather than through them. The lower resistance to flow then allowed column #3 to elute first. The area covered by the trapped air on column #1 was less extensive than in column #3 and did not interconnect; in this case the bubbles acted as extra dead volume delaying fluorescein elution. Column #4 did not contain any flaw and column #2, a small area containing trapped air. From the picture of column #2, another source of extra dead volume was seen: a flaw in the PDMS hole, highlighted in

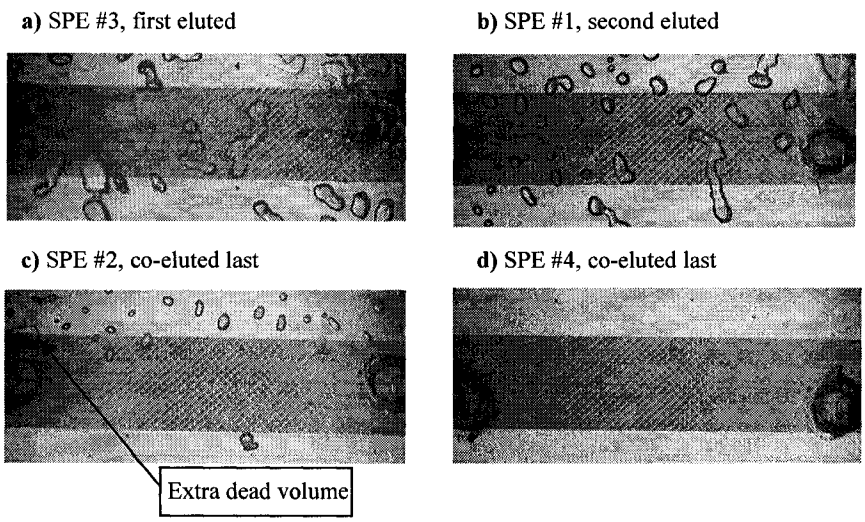

Figure 4.15 Pictures of the Four Silicon SPE under 20x- bonded to the glass microdevice using the thin PDMS technique

the picture by the arrow, further delaying fluorescein elution. Columns #2 and #4 therefore co-eluted. It was clear that great care must be taken in building the microdevice: what seemed a small imperfection, as was the case with column #2, led to a discrepancy in the microdevice flow profile. As discussed in Chapter 3, several attempts at making a microdevice without trapped air in all four columns failed; devices prepared with pre-cured thick PDMS were then tested.

4.4.2. THICK PDMS

Four-channel microdevices described in section 3.2.3.2 for thick PDMS were used. Tests were conducted using cytochrome c solutions in water under ESI MS detection. After conditioning, cytochrome c in water was flowed into the microdevice, followed by a 50 µl water wash and elution using 67% MeOH / 33% 0.1 M formic acid solution. The resulting TIC spectra are shown in Figure 4.16: a) 0.16 µg cytochrome c was injected and eluted at 0.1 µl/min, b) 0.08 µg cytochrome c was injected and eluted at 1 µl/min. Three elution peaks can be seen overlapping in Figure 4.16a due to their broad full width at half maximum. Faster elution of a smaller cytochrome c amount resulted in a single peak, as shown in Figure 4.16b.

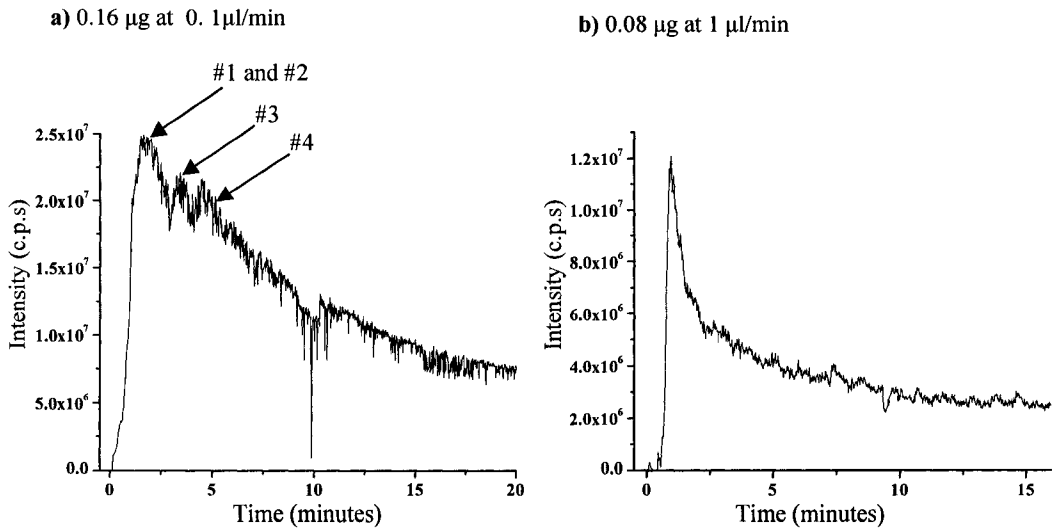

Figure 4.16 TIC Spectra from Multichannel Device-Thick PDMS- Following cytochrome c sorption and water washed, the protein was eluted using 67% MeOH / 33% 0.1 M formic acid solution. Cytochrome c load and elution flow rate: a) 0.16 µg at 0.1 µl/min, b) 0.08 µg at 1 µl/min.

LIF images of fluorescein were again used to monitor flow through the microdevice: results are shown in Figure 4.17, in chronological order from Figure 4.17a to Figure 4.17d. After conditioning the microdevice with water (50 µl), fluorescein in water (100 µM) was continuously flowed into the microdevice (1 µl/min) and the resulting fluorescence was observed at the meeting point of the four microchannels after the SPE beds. From LIF images of Figure 4.17, the actual elution profile fits the expected one, i.e. from microchannel #1 having the smallest SPE-to-MS distance, to microchannel #2, #3 and finally #4, having the longest SPE-to-MS distance. This result was reproduced on two different microdevices, showing the validity of the thick PDMS processing technique. This did not, however, translate into four baseline-resolved peaks in the TIC spectrum of Figure 4.16. As mentioned in Chapter 3, the distance between the silicon bed and glass microchannel must be minimized to reduce dead volume during elution, and therefore reduce the width of eluting peaks. The thick PDMS, at 650 µm thickness, proved to be too thick for discriminating peak elution on this microdevice geometry. Considering the results of the LIF experiments, one can assign microchannel

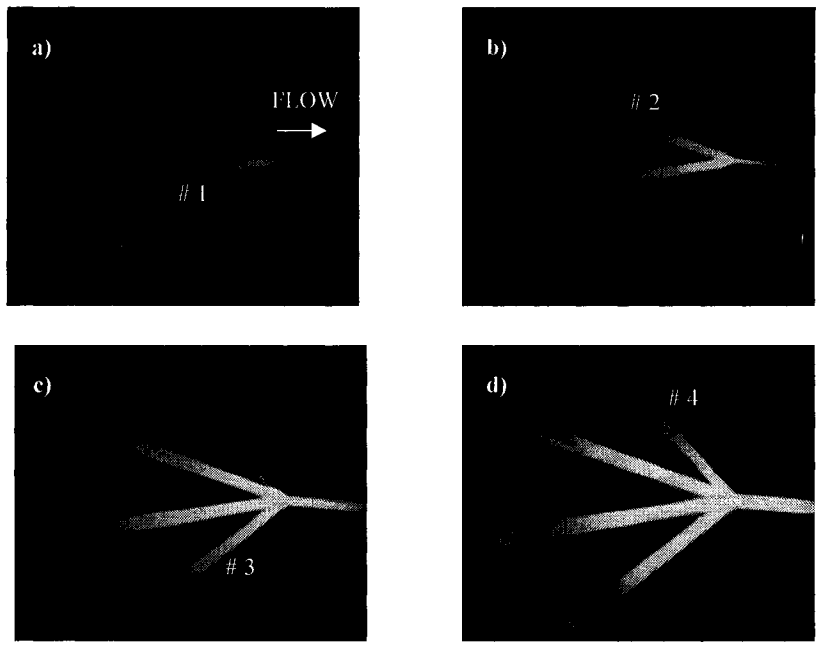

Figure 4.17 Fluorescence Image from Multichannel Device- Using thick PDMS. Observed region same as for Figure 3.14. Observed fluorescein breakthrough in chronological order, from a to d. Fluorescein was 100 μM in water, continuously flowed into the microdevice at 1 μl/min flow rate

elution numbers to the three peaks of Figure 4.16a: the first peak from microchannel #1 and #2, second peak from microchannel #3 and finally third peak for microchannel #4. The faster elution from Figure 4.16b did not solve the problem, a single peak with a large amount of tailing resulted.

The effect of having a microchamber on elution peak shape was discussed in section 4.3, and illustrated in Figure 4.2. The probable cause of tailing peaks is the presence of an expanding dead volume acting as a mixing chamber on the eluting peak. From Figure 4.16b, the tailing was significant in thick PDMS. For a 2 mm length silicon column consisting of square posts, each post having 4.3 μm side lengths, etched 10 μm deep and separated by a 1.7 μm length, the total bed elution volume is 2.2×10^{-12} m^3. The volume of the thick PDMS microchamber is 1.3×10^{-11} m^3, six times the total elution volume: the major contribution to bandbroadening in the thick PDMS device was mixing in the SPE-to-microchannel microchamber section, an effect that did not allow for baseline-resolved peak elution using this microdevice geometry.

4.4.3. THEORETICAL ELUTION

To pinpoint the different bandbroadening processes at work in the microdevice, as well as to assess whether anything can be done to obtain discriminated elution in thick PDMS structures, theoretical elution profiles of cytochrome c eluted through the multiplexed device are discussed here. Assuming plug-like elution from the SPE bed and no flow disturbance at the chip-to-ESI tip connection, peak widths will be a function of analyte dispersion in two regions: first in the PDMS-glass hole connecting the silicon column and glass microchannels (referred to as a "chamber") and second in the variable-length microchannels leading up to the mass spectrometer. Dispersion in the chamber ($\sigma^2_{chamber}$) was discussed in section 4.3.1. In the second case, treating the microchannels as non-sorptive open tubes, analyte dispersion will be affected by longitudinal dispersion (σ^2_{ld}, bandbroadening due to the random movement of individual components about the center of the moving peak) and trans-column resistance to mass transfer in the mobile phase (σ^2_m, bandbroadening arising from the parabolic flow profile in the tube). Both were discussed in Chapter 1, section 1.3. The total peak variance will therefore be:

$$\sigma^2_{total} = \sigma^2_{chamber} + \sigma^2_{ld} + \sigma^2_m \qquad (4.1)$$

Each variance contribution, in time units, as a function of microdevice dimensions and elution flow rate is:

$$\sigma^2_{ld} = 2DA^3L/F^3 \qquad (4.2)$$

$$\sigma^2_m = 0.055(d^2AL)/(DF) \qquad (4.3)$$

$$\sigma^2_{chamber} = V^2/F^2 \qquad (4.4)$$

where D is the diffusion coefficient of the analyte, F is the elution volume flow rate, V is the chamber volume, A, d and L are the microchannel cross-sectional area, depth and length, respectively. Note that σ^2_m was modified from the traditional equation to account for the geometry of the etched microchannels, approximated for calculating σ^2_m as a rectangular channel of 20 μm depth and 100 μm width[23].

For an isotropically etched microchannel, the cross-sectional area can be calculated as:

$$A = wd + 0.5\pi d^2 \qquad (4.5)$$

where w is the width of the microchannel as defined on the lithographic mask. In this case, d = 20 μm and w = 60 μm, giving a cross-sectional area of 1,828.3 μm^2. Variance

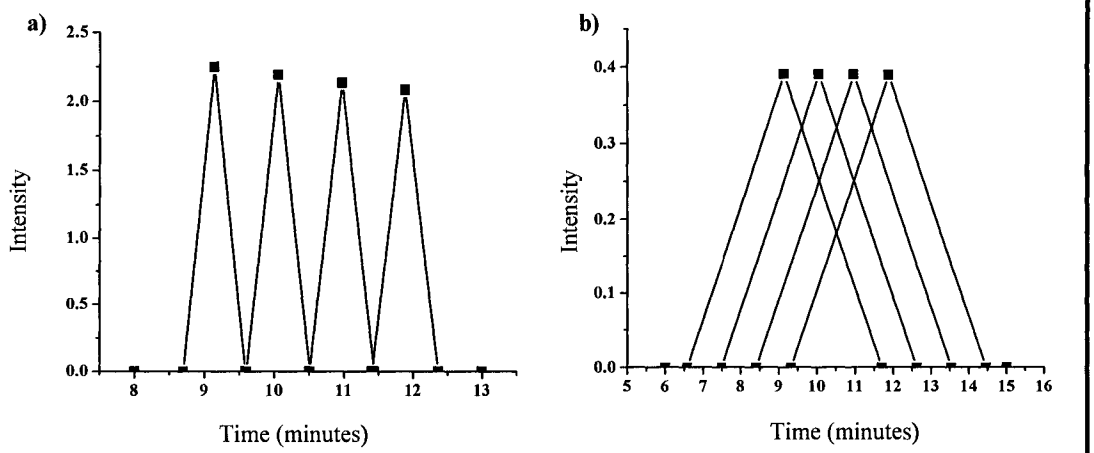

Figure 4.18 Theoretical Elution Profiles- for microdevices built using a) thin PDMS and b) thick PDMS. All theoretical parameters are shown in the Appendix, for thin PDMS: Table 3.6 and thick PDMS: Table 3.7.

contribution in each microchannel of length L_1 to L_4 is calculated in the appendix for thin (Table 4.6) and thick (Table 4.7) PDMS microdevices. All parameters used are enumerated in Table 4.8 of the Appendix. Note that 3.0 cm were added to each microchannel length L to account for the ESI tip length (the chamber thickness length was negligible and was therefore not added to the total length). Also, the volume of the chamber in the thin PDMS was calculated using a radius of 75 μm and thickness of 85 μm (i.e. 70 μm for the 0211 glass plus 15 μm for the PDMS); for the thick PDMS, the thickness was 720 μm (i.e. 70 μm for the 0211 glass plus 650 μm for the PDMS).

To produce a graph of a theoretical elution profile (Intensity versus Time), one can approximate each eluting peak as a triangle of set area A_t with base equal to 4σ; the resulting height (H_t) for each peak can then be calculated as $A_t/(2\sigma)$. The apex of the triangle representing these peaks is set at elution time t, equal to the channel volume over elution flow rate:

$$t = A*L/F \qquad (4.6)$$

The intensity will drop to zero at $t \pm 2\sigma$ around the eluted peak. These parameters (σ, t and H_t) are also shown in Table 4.6 and 4.7 for a set A_t value of 1.

Figure 4.18 shows the theoretical elution profiles generated for a) thin and b) thick PDMS microdevices at a flow rate of 0.04 μl/min. From these, elution from a thin PDMS chamber would result in baseline resolution whereas a thick chamber would not.

Figure 4.18b shows the four elution profiles intersecting just below the elution peaks due to their broad full width at half maximum, much like the experimental cytochrome c elution obtained in Figure 4.16a. From the calculated values (Table 4.6 for thin and Table 4.7 for thick), variance contribution from longitudinal diffusion in the SPE-to-MS microchannels is negligible in both microdevices ($\sigma^2_{ld} \approx 10^{-3}$ min^2). The two main variance contributors in the thin PDMS microdevice are σ^2_m and $\sigma^2_{chamber}$, both having about equal values (at $\approx 10^{-2}$ min^2). In the thick PDMS microdevice, both σ^2_{ld} ($\approx 10^{-3}$ min^2) and σ^2_m ($\approx 10^{-2}$ min^2) are negligible compared to the main bandbroadening contributor, $\sigma^2_{chamber}$, at a value of 1.6 min^2. As expected, chamber volume is a large contributor to peak bandbroadening.

From equation 4.4, for a fixed chamber volume V, $\sigma^2_{chamber}$ can be reduced by increasing the flow rate F of the elution. However, from experimental data presented in Figure 4.16b for cytochrome c elution in thick PDMS microdevices, high flow rates did not produce discriminated peaks. Theoretical elution using thick PDMS parameters supported this: discriminated peak elution was not possible at higher flow rates. Values for variance contributions in each microchannel at 0.4 μl/min flow rate are presented in Table 4.9 of the Appendix. From these values, the chamber still accounts for most of the bandbroadening though its value has decreased 100 fold ($\sigma^2_{chamber} = 1.6 \times 10^{-2}$ min^2 at 0.4 μl/min versus $\sigma^2_{chamber} = 1.6$ min^2 at 0.04 μl/min). However, since elution time t is proportional to 1/F, as is $\sigma_{chamber}$ and therefore σ_{total}, the result on the elution profile is unchanged, resulting in overlapping peaks. At the other extreme, further decrease in flow rate in the theoretical calculation increased the bandbroadening contribution from the chamber; no discriminate elution resulted.

Setting σ^2_{total} equal to $\sigma^2_{chamber}$, a reasonable assumption provided the values calculated so far in thick PDMS chambers, and keeping V and F constant, only the elution time t can be changed to obtain discriminated elution in thick PDMS microdevices. From equation 4.6, both the microchannel cross-sectional area A and SPE-to-MS lengths L could be changed. To reduce flow disturbance at the ESI tip, A was set at the value presented in Table 4.8 of the Appendix, changing this value would introduce a new source of bandbroadening coming from disturbance at the ESI tip. Therefore, only the difference in SPE-to-MS lengths can be changed. In the microdevice studied so far,

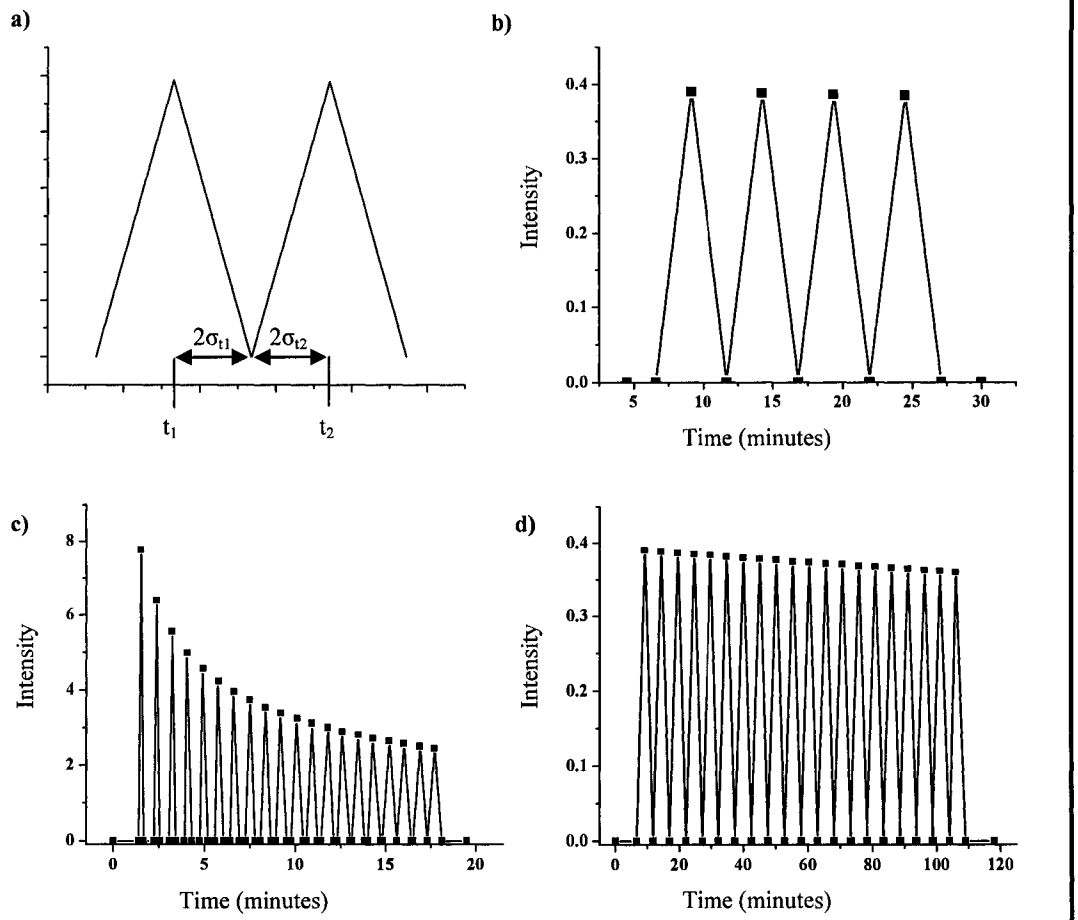

Figure 4.19 Theoretical Elution Profiles- a) Definition of parameters in equation 4.7; b) effect of longer delay lines on theoretical elution in thick PDMS: channel-to-channel line delay was increased to 2.8 cm. For a 20-channel microdevice with 2.8 cm delay line lengths, theoretical elution in c) thin PDMS and d) thick PDMS.

the delay length from one microchannel to the next was set to 0.5 cm; longer channel-to-channel delay lengths will produce discriminated elution profiles in the thick PDMS microdevice. The length of this delay line is calculated next.

Figure 4.19a presents the elution profile of two adjacent peaks, eluting at time $t_1 \pm 2\sigma_{t1}$ and $t_2 \pm 2\sigma_{t2}$. For baseline resolution:

$$t_2 - t_1 = 2(\sigma_{t1} + \sigma_{t2}) \quad (4.7)$$

Since the chamber is the main source of bandbroadening, both peak widths are equal, i.e. $\sigma_{t1} = \sigma_{t2}$ (see equation 4.4). Also, using equation 4.6 for the definition of t:

$$A/F*(L_2-L_1) = 4\sigma_t = 4*(V/F) \quad (4.8)$$

Solving for L_2-L_1:

$$\Delta L = 4*(V/A) \quad (4.9)$$

giving a ΔL value of 2.8 cm. A theoretical elution profile was generated using this value: L_1 was set at 5 cm, L_2 = 7.8 cm, L_3 = 10.6 cm and L_4 = 13.4 cm. The resulting elution parameters are shown in Table 4.10 of the Appendix and the profile in Figure 4.19b. From these, baseline resolution is obtained: longer channel-to-channel delay lengths could therefore result in discriminated peak elution in thick PDMS microdevices. The main drawback of this simple solution is the long elution times needed for discriminate elution. The bead-based multiplexed device developed by Taylor had 20 microchannels; Figure 4.19 present the theoretical elution profiles of cytochrome c for microdevices with 20 silicon beds built using c) thin PDMS and d) thick PDMS. Both theoretical profiles were developed using the new delay lines lengths (L_1 = 5 cm, L_2 = 7.8 cm up to L_{20} = 58.2 cm, note that 3 cm were added to account for the ESI tip length). Because the thin PDMS produces less bandbroadening, higher flow rates can be used and still obtain baseline resolution for later-eluting peaks: elution from all 20 microchannels would occur in less than 20 minutes. On the other hand, for the thick PDMS layer, faster flow rates result in overlapping of later eluting peaks; for all peaks to be baseline-resolved, an elution time of about 2 hours would be needed. Finally, another obvious problem would be the difficulty of fitting 20 microchannels, with lengths ranging from 2 cm to 55.2 cm (without the ESI tip length), on a four inches glass wafer. Finally, the theoretical bandbroadening analysis for thick PDMS microdevices is an optimistic estimate of the elution profile: the eluting peak shape would present severe tailing due to the presence of the mixing chamber, as shown schematically in Figure 4.2. The true peak shape will show both a gaussian and exponential distribution, resulting in a broader peak than the simple triangular shape used in the theoretical analysis.

4.4.4. ELECTICAL FRACTIONATION

As discussed in Chapter 3, the entire platform would work in five steps: first, isoelectric focusing of a protein sample in the microcapillary connected to the Nanoport; second, electrical fractionation of the separated protein fractions into the microchannels on the device; third, protein fraction sorption on the silicon SPE bed; fourth, trypsin

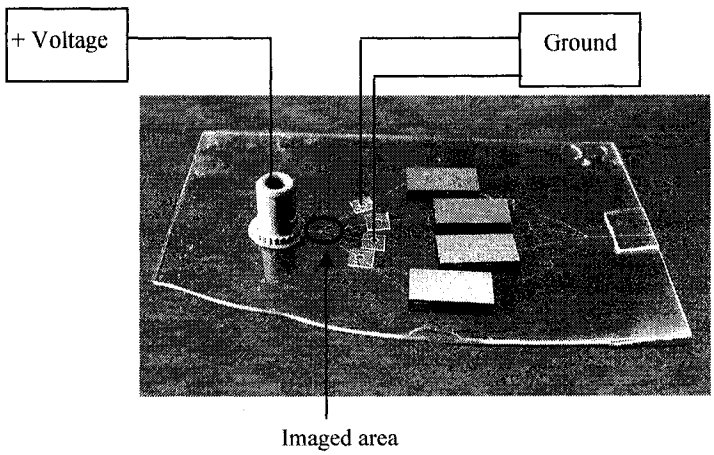

Figure 4.20 Electrical Fractionation Scheme- Voltage was applied sequentially between the inlet Nanoport and buffer-filled PDMS reservoirs using a house-built relay box.

digestion and; fifth, elution for final ESI MS analysis. Work presented up to now has focused on protein sorption and digestion on SPE beds as well as systematic elution from multichannel microdevices. Earlier work on the 20-channel platform had shown the limitations of the electrical fractionation scheme[18]: the area where the 20 microchannels met resulted in a large dead volume where incoming sample would diffuse before making their way into the microchannel. The mixing produced in this region would have an adverse effect on separation efficiency, negating the high resolution of the solution-phase capillary electrophoresis separation. The fractionation region for the present work has a smaller area due to 1) the presence of only four microchannels and 2) the tapering of the microchannels at their meeting points (as discussed in section 3.2.1.1.). The following discusses the testing of this geometry for electrical fractionation using LIF detection of fluorescein.

Figure 4.20 presents the experimental set-up. Note that holes were drilled on the 0211 glass, aligned with the microchannel structures and PDMS reservoirs added for electrical fractionation work (see section 3.2.1.3.). LIF detection system was discussed in section 4.2; the imaged area is shown in Figure 4.20. In-house written LabVIEW programs (National Instruments, Austin, TX) were used for computer control of the voltage at the inlet Nanoport. The computer-controlled power supply and relay

arrangement have been described previously[24]. Sequential grounding at the PDMS reservoirs was applied via a house-built relay box equipped with a timer control[18]. After setting the appropriate time on the relay box, the grounding sequence was initiated. The first channel would then be grounded for the time set on the relay box while all other channels were left floating. After the set time, the second channel would be grounded for the second set amount of time with all other channels left floating, etc. For wall conditioning, the microdevice was washed with 0.1 M NaOH, followed by distilled, filtered water and 50 mM ammonium bicarbonate buffer (pH 8.5) for 10 minutes each, successively. To protect the C18 phase on the silicon columns from the NaOH solution, the microdevice was first filled with water, the conditioning solutions were then introduced into the PDMS wells and vacuum was applied at the Nanoport. Fluorescein, 100 mM in 50 mM ammonium bicarbonate buffer, was then introduced at the Nanoport and voltage applied. Note that liquid levels in the Nanoport and PDMS reservoirs had to be equal to prevent siphoning, which is detrimental to the fractionation process. A 0.5 kV voltage was applied at the Nanoport while simultaneously starting the sequential grounding on the relay box for a 1 minute period on microchannels #2 and #3, sequentially.

The results are presented in Figure 4.21 for a) the first and b) the second minute. The images show that fractionation is possible but the dead volume problem remains, although less severe than previously. The microchannel width was tapered on the mask from 60 μm to 10 μm in the fractionation region. This translates, after a 20 μm isotropic etching of the glass microchannels, to a final taper from 100 μm to 50 μm. From Figure 4.21, this still significantly hinders the fractionation process. The reason for a taper down to 10 μm was explained in section 3.2.1.2.: photolithography of 60 μm widths and, for example, 5 μm widths would result in severe overdeveloping of the larger region. A possible solution would then be to use a two-mask process: the first mask would define the 60 μm areas with a taper to 10 μm and the second mask would define the inlet fractionation region, from 10 μm down to 3 μm (note that photolithography of 3 μm features is easily feasible). To further reduce the amount of dead volume, the depth of the first mask could be reduced from 20 μm to 10 μm. However, this would only reduce the problem without circumventing it entirely. Wang[25] produced a microdevice for

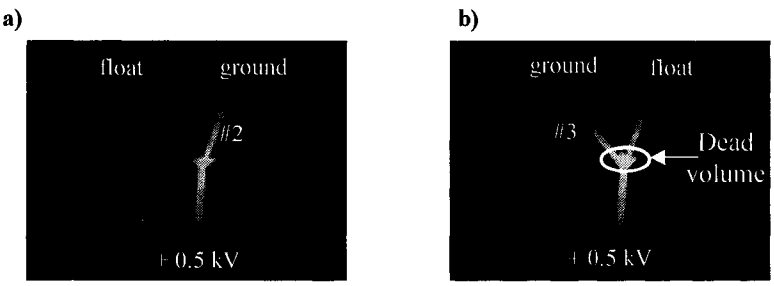

Figure 4.21 Fluorescence Image – Electrical Fractionation- Fluorescein (100 mM in 50 mM ammonium bicarbonate buffer, pH 8.5) was driven sequentially by CE in microchannels #2 and #3. Applied voltage: 0.5 kV for a) the first minute and b) the second minute.

diffusion-free electrical fractionation. In this work, the incoming analyte is surrounded by a voltage-controlled sheath buffer flow, allowing for sharp, well-defined analyte plugs to be distributed sequentially into microchannels.

4.5.CONCLUSION

The single channel glass microdevice with silicon SPE bed was successfully used for protein sorption and digestion under ESI MS detection. Cytochrome c load on the 6 mm ODS-derivatized silicon bed was calculated at 0.24 μg. For cytochrome c digest, 85% coverage was obtained; 74% and 47% were obtained for myoglobin and BSA digests, respectively. The two approaches described in Chapter 3 for efficient bonding of the glass microdevice to the silicon SPE bed were used and tested for multichannel ESI MS discriminated peak detection of cytochrome c under pressure-driven flow. For microdevices built using the thin (< 20 μm) PDMS structure, defects in the PDMS layer resulted in non-sequential elution to the MS. For microdevices built using the thick (> 600 μm) PDMS structures, sequential elution resulted, as demonstrated by laser-induced fluorescence imaging of fluorescein flow through the microdevice. Under ESI MS detection, however, the bandbroadening introduced by the large dead volume at the PDMS layer prevented baseline-resolved peak detection. Theoretical calculations demonstrated that, for baseline-resolved peak detection under ESI MS in the thick PDMS structure, the channel-to-channel difference in SPE-to-MS length must be longer than 2.8 cm. Finally, electrical fractionation study showed that although tapered microchannels

reduced dead volume in the fractionation region, the dead volume was still significant. This would then translate into mixing of incoming protein fractions: tapering of the microchannels did not efficiently address the problem of mixing in the fractionation region.

4.6.REFERENCES

(1) CLARK, S. M.; KONERMANN, L. *JOURNAL OF THE AMERICAN SOCIETY FOR MASS SPECTROMETRY* **2003**, *14*, 430-441.

(2) RABILLOUD, T. *PROTEOMICS* **2002**, *2*, 3-10.

(3) ANDERSON, N. L.; ANDERSON, N. G. *MOLECULAR & CELLULAR PROTEOMICS* **2002**, *1*, 845-867.

(4) FREIRE, S. L. S.; WHEELER, A. R. *LAB ON A CHIP* **2006**, *6*, 1415-1423.

(5) GOTTSCHLICH, N.; CULBERTSON, C. T.; MCKNIGHT, T. E.; JACOBSON, S. C.; RAMSEY, J. M. *JOURNAL OF CHROMATOGRAPHY B* **2000**, *745*, 243-249.

(6) LIU, Y.; LU, H. J.; ZHONG, W.; SONG, P. Y.; KONG, J. L.; YANG, P. Y.; GIRAULT, H. H.; LIU, B. H. *ANALYTICAL CHEMISTRY* **2006**, *78*, 801-808.

(7) HUANG, Y.; SHAN, W.; LIU, B. H.; LIU, Y.; ZHANG, Y. H.; ZHAO, Y.; LU, H. J.; TANG, Y.; YANG, P. Y. *LAB ON A CHIP* **2006**, *6*, 534-539.

(8) PETERSON, D. S.; ROHR, T.; SVEC, F.; FRECHET, J. M. J. *ANALYTICAL CHEMISTRY* **2002**, *74*, 4081-4088.

(9) SAKAI-KATO, K.; KATO, M.; TOYO'OKA, T. *ANALYTICAL CHEMISTRY* **2003**, *75*, 388-393.

(10) PETERSON, D. S.; ROHR, T.; SVEC, F.; FRECHET, J. M. J. *ANALYTICAL CHEMISTRY* **2003**, *75*, 5328-5335.

(11) GAO, J.; XU, J. D.; LOCASCIO, L. E.; LEE, C. S. *ANALYTICAL CHEMISTRY* **2001**, *73*, 2648-2655.

(12) EKSTROM, S.; ONNERFJORD, P.; NILSSON, J.; BENGTSSON, M.; LAURELL, T.; MARKO-VARGA, G. *ANALYTICAL CHEMISTRY* **2000**, *72*, 286-293.

(13) JIN, L. J.; FERRANCE, J.; SANDERS, J. C.; LANDERS, J. P. *LAB ON A CHIP* **2003**, *3*, 11-18.

(14) SLOVAKOVA, M.; MINC, N.; BILKOVA, Z.; SMADJA, C.; FAIGLE, W.; FUTTERER, C.; TAVERNA, M.; VIOVY, J. L. *LAB ON A CHIP* **2005**, *5*, 935-942.

(15) YUE, G. E.; ROPER, M. G.; BALCHUNAS, C.; PULSIPHER, A.; COON, J. J.; SHABANOWITZ, J.; HUNT, D. F.; LANDERS, J. P.; FERRANCE, J. P. *ANALYTICA CHIMICA ACTA* **2006**, *564*, 116-122.

(16) WANG, C.; OLESCHUK, R.; OUCHEN, F.; LI, J. J.; THIBAULT, P.; HARRISON, D. J. *RAPID COMMUNICATIONS IN MASS SPECTROMETRY* **2000**, *14*, 1377-1383.

(17) WANG, C., UNIVERSITY OF ALBERTA, EDMONTON, 2001.

(18) TAYLOR, J., UNIVERSITY OF ALBERTA, EDMONTON, 2004.

(19) CRAFT, D.; DOUCETTE, A.; LI, L. *JOURNAL OF PROTEOME RESEARCH* **2002**, *1*, 537-547.

(20) DOUCETTE, A.; CRAFT, D.; LI, L. *ANALYTICAL CHEMISTRY* **2000**, *72*, 3355-3362.

(21) DOUCETTE, A.; CRAFT, D.; LI, L. *JOURNAL OF THE AMERICAN SOCIETY FOR MASS SPECTROMETRY* **2003**, *14*, 203-214.

(22) PRZYBYCIEL, M.; MAJOR, R. E. **2002**, *20*, 516-523.

(23) DUTTA, D.; LEIGHTON, D. T. *ANALYTICAL CHEMISTRY* **2001**, *73*, 504-513.

(24) SEILER, K.; HARRISON, D. J.; MANZ, A. *ANALYTICAL CHEMISTRY* **1993**, *65*, 1481-1488.

(25) WANG, Z., UNVERSITY OF ALBERTA, EDMONTON, 2007.

4.7.APPENDIX

1- Myoglobin and Cytochrome c Charge States

Cytochrome c and myoglobin charge states and their corresponding m/z values are presented in Table 4.1. Mass-to-charge values were derived by dividing the protein's molecular weight, 12,358 g/mol for cyochrome c and 16,951 g/mol for myoglobin, by the corresponding charge state and adding 1 to represent $[M + nH]^{+n}$.

Cytochrome c		Myoglobin	
Charge State (n)	Mass-to-Charge (m/z)	Charge State (n)	Mass-to-Charge (m/z)
+ 11	1,124.5	+ 15	1,131.0
+ 12	1,031.0	+ 16	1,060.5
+ 13	951.5	+ 17	998.0
+ 14	883.5	+ 18	942.5
+ 15	825.0	+ 19	893.0
+ 16	773.5	+ 20	848.5
+ 17	728.0	+ 21	808.0
+ 18	687.5		
+ 19	651.0		

Table 4.1 Observed Cytochrome c and Myoglobin Charge States

2- Trypsin Tryptic Peptides

Observed trypsin tryptic peptides are shown in Table 4.2. The list was compiled using ExPASY (http://ca.expasy.org/) and Protein Prospector (http://prospector.ucsf.edu/) databases with the following parameters: trypsin digest, 3 missed cleavages, peptide N-terminus = hydrogen, peptide C-terminus = free acid, modifications considered = oxidation of methionine and protein N-terminus acetylated, cysteine unmodified. Peptides m/z values are listed based on monoisotropic masses of the form $[M + nH]^{+n}$.

m/z	Missed Cleavages	Position	Modification
577.5^{+2}	0	126-136	
659.5	0	44-49	
759.0^{+3}	0	70-89	
775.0^{+3}	1	187-208	
944.0^{+5}	3	90-136	
1082.5^{+2}	0	50-69	
1097.5^{+2}	0	150-170	
1137.5^{+2}	0	70-89	
1154.0	0	126-136	
1181.0^{+3}	2	137-170	

Table 4.2 Observed Trypsin Tryptic Peptides

3- Cytochrome c Tryptic Peptides

Observed cytochrome c tryptic digest peptides are shown in Table 4.3. The list was compiled using ExPASY (http://ca.expasy.org/) and Protein Prospector (http://prospector.ucsf.edu/) databases with the following parameters: trypsin digest, 3 missed cleavages, peptide N-terminus = hydrogen, peptide C-terminus = free acid, modifications considered = oxidation of methionine and protein N-terminus acetylated, cysteine unmodified. Peptides m/z values are listed based on monoisotropic masses of the form $[M + nH]^{+n}$.

m/z	Missed Cleavages	Position	Modification
562.5	1	100-104	
547.5	0	1-5	
559.5^{+3}	2	23-38	
585.0^{+2}	0	28-38	
589.5	0	1-5	acetylated
604.5	0	56-60	1 Met-Ox
626.5^{+3}	2	9-25	
634.5	0	9-13	
649.0^{+2}	1	28-39	
678.5	0	74-79	
717.5^{+2}	1	26-38	
736.0^{+2}	0	40-53	
737.0^{+3}	2	56-73	
748.5^{+2}	0	61-72	

Table 4.3 Observed Cytochrome c Tryptic Peptides

m/z	Missed Cleavages	Position	Modification
763.5^{+2}	2	14-27	
779.5	0	80-86	
781.5^{+2}	2	26-39	
800.0^{+2}	1	39-53	
812.5^{+2}	1	61-73	
817.5^{+2}	1	9-22	
964.5	0	92-99	
1041.5^{+2}	1	56-72	
1052.0	1	56-72	1 Met-Ox
1113.5^{+2}	2	56-73	
1168.5	0	28-38	1 Met-Ox

Table 4.3 continued Observed Cytochrome c Tryptic Peptides

4- BSA and Myoglobin Tryptic Peptides

Observed myoglobin and BSA tryptic digest peptides are shown in Table 4.4 and 4.5, respectively. The list was compiled using ExPASY (http://ca.expasy.org/) and Protein Prospector (http://prospector.ucsf.edu/) databases with the following parameters: trypsin digest, 3 missed cleavages, peptide N-terminus = hydrogen, peptide C-terminus = free acid, modifications considered = oxidation of methionine and protein N-terminus acetylated, cysteine modified by carbamidomethylation. Peptides m/z values are listed based on monoisotropic masses of the form $[M + nH]^{+n}$.

m/z	Missed Cleavages	Position	Modification
554.5^{+4}	1	32-45	
559.0^{+4}	1	119-139	
636.5^{+2}	0	32-42	
650.5	0	148-153	
662.5	0	57-62	
680.5^{+2}	1	134-145	

Table 4.4 Observed Myoglobin Tryptic Peptides

m/z	Missed Cleavages	Position	Modification
690.0^{+2}	0	64-77	
707.0^{+3}	0	80-98	
748.5^{+3}	0	134-139	
752.0^{+2}	0	119-133	
804.0^{+2}	0	17-31	
814.0^{+4}	2	14-45	
818.5^{+2}	2	64-79	
852.0^{+4}	1	1-31	
847.0^{+4}	1	103-133	1 Met-Ox
908.5^{+2}	0	1-16	
928.0^{+2}	0	80-96	
943.5^{+2}	0	103-118	
949.0^{+3}	2	119-145	
969.5^{+2}	2	32-47	
992.0^{+2}	1	79-96	
1125.0^{+2}	1	119-139	1 Met-Ox

Table 4.4 continued Observed Myoglobin Tryptic Peptides

m/z	Missed Cleavages	Position	Modification
572.0^{+2}	1	524-533	
652.0^{+4}	1	445-465	
659.0	0	94-98	
677.0^{+3}	2	397-413	
690.5	1	13-41	
708.5^{+2}	0	545-556	1 Met-Ox
720.5^{+2}	1	336-347	
753.5^{+4}	1	286-312	
759.0	0	174-180	
770.0^{+2}	1	459-471	
780.0^{+4}	2	160-185	
802.5^{+5}	2	42-76	
818.5	0	119-133	
780.0^{+3}	1	538-544	
869.0^{+3}	1	445-465	
872.0^{+3}	2	240-261	
960.5	1	186-194	
1010.5^{+2}	1	115-131	
1072.5	0	286-294	

Table 4.5 Observed BSA Tryptic Peptides

5- Theoretical Elution Parameters

The following tables show the calculated parameters for the theoretical elution profile analysis presented in section 4.4.3.

$F = 1 \times 10^{-11}$ m^3/min	L_1	L_2	L_3	L_4
σ^2_{Id} (min^2)	5.9×10^{-3}	6.4×10^{-3}	7.0×10^{-3}	7.6×10^{-3}
σ^2_{m} (min^2)	2.1×10^{-2}	2.3×10^{-2}	2.5×10^{-2}	2.7×10^{-2}
$\sigma^2_{chamber}$ (min^2)	2.2×10^{-2}	2.2×10^{-2}	2.2×10^{-2}	2.2×10^{-2}
σ^2_{total} (min^2)	4.9×10^{-2}	5.2×10^{-2}	5.5×10^{-2}	5.7×10^{-2}
σ_{total} (min)	2.2×10^{-1}	2.3×10^{-1}	2.3×10^{-1}	2.4×10^{-1}
t (min)	9.1	10.1	11.0	11.9
H_t	2.2	2.2	2.1	2.1

Table 4.6 Elution Parameters for Thin PDMS Microdevices

$F = 1 \times 10^{-11}$ m^3/min	L_1	L_2	L_3	L_4
σ^2_{Id} (min^2)	5.9×10^{-3}	6.4×10^{-3}	7.0×10^{-3}	7.6×10^{-3}
σ^2_{m} (min^2)	2.1×10^{-2}	2.3×10^{-2}	2.5×10^{-2}	2.7×10^{-2}
$\sigma^2_{chamber}$ (min^2)	1.6×10^{0}	1.6×10^{0}	1.6×10^{0}	1.6×10^{0}
σ^2_{total} (min^2)	1.6×10^{0}	1.6×10^{0}	1.6×10^{0}	1.6×10^{0}
σ_{total} (min)	1.3×10^{0}	1.3×10^{0}	1.3×10^{0}	1.3×10^{0}
t (min)	9.1	10.1	11.0	11.9
H_t	0.39	0.39	0.39	0.39

Table 4.7 Elution Parameters for Thick PDMS Microdevices

A	1.8×10^{-9} m^2	L_1	0.050 m
d	20×10^{-6} m	L_2	0.055 m
$D_{cyt\ c}$[1]	9.6×10^{-9} m^2/min	L_3	0.060 m
F	1.0×10^{-11} m^3/min	L_4	0.065 m
V_{thin}	1.5×10^{-12} m^3	V_{thick}	1.3×10^{-11} m^3

Table 4.8 Parameters Used in the Theoretical Elution Calculations

$F = 1 \times 10^{-10}$ m^3/min	L_1	L_2	L_3	L_4
σ^2_{ld} (min^2)	5.9×10^{-6}	6.4×10^{-6}	7.0×10^{-6}	7.6×10^{-6}
σ^2_{m} (min^2)	2.1×10^{-3}	2.3×10^{-3}	2.5×10^{-3}	2.7×10^{-3}
$\sigma^2_{chamber}$ (min^2)	1.6×10^{-2}	1.6×10^{-2}	1.6×10^{-2}	1.6×10^{-2}
σ^2_{total} (min^2)	1.8×10^{-2}	1.8×10^{-2}	1.9×10^{-2}	1.9×10^{-2}
σ_{total} (min)	1.4×10^{-1}	1.4×10^{-1}	1.4×10^{-1}	1.4×10^{-1}
t (min)	9.1×10^{-1}	1.0×10^{0}	1.1×10^{0}	1.2×10^{0}
H_t	3.7	3.7	3.7	3.6

Table 4.9 Elution Parameters for Thick PDMS-High Flow Rate

$F = 1 \times 10^{-11}$ m^3/min	L_1	L_2	L_3	L_4
σ^2_{ld} (min^2)	5.9×10^{-3}	9.2×10^{-3}	1.2×10^{2}	1.6×10^{-2}
σ^2_{m} (min^2)	2.1×10^{-2}	3.3×10^{-2}	4.4×10^{-2}	5.6×10^{-2}
$\sigma^2_{chamber}$ (min^2)	1.6×10^{0}	1.6×10^{0}	1.6×10^{0}	1.6×10^{0}
σ^2_{total} (min^2)	1.6×10^{0}	1.6×10^{0}	1.7×10^{0}	1.7×10^{0}
σ_{total} (min)	1.3×10^{0}	1.3×10^{0}	1.3×10^{0}	1.3×10^{0}
t (min)	9.1	14.3	19.4	24.5
H_t	0.39	0.39	0.39	0.38

Table 4.10 Elution Parameters for Thick PDMS-Long Delay Lines- L_1 at 5 cm, L_2 at 7.8 cm, L_3 at 10.6 cm, L_4 at 13.4 cm.

CHAPTER 5 CONCLUSION

5.1.INTRODUCTION

The following summarizes the research presented in this thesis and proposes improvements for on-chip analyses based on the two microsystems studied: first for capillary electrochromatography and second for multiplexed protein analysis.

5.2.SCX CEC AND TWO-COLUMN ELECTROCHROMATOGRAHY

The column characterization presented in Chapter 2 for strong cation exchange capillary electrochromatography of peptides demonstrated that fast, high efficiency separations could be obtained on-chip. In the two-column system, the short separation window did not produce the high column peak capacities needed for efficient two-dimensional separations. A microdevice with longer columns could lead to a larger separation window and, provided that the column bandbroadening due to the added length is minimal, higher column peak capacities. However, Jemere et al. concluded that longer columns (to 5 mm) could not be efficiently packed using the two weir approach[2]; in-situ polymerized monoliths would need to be used. Issues with sample loss in the downstream side-arm, used to introduce the solvent change needed to go from cation exchange to reverse-phase electrochromatography, also made clear that this microdevice design was not optimal for efficient sequential two-dimensional separation.

A different approach to the two-column system would then need to be used, one mimicking the Shotgun Proteomics approach described in Chapter 1 (p.24). Using the same two-bed system (SCX followed by ODS), the sample would first be sorbed at the head of the SCX column under low ionic strength conditions. Addition of higher ionic strength buffer would displace part of the sorbed analyte: the eluted fraction would be sorbed onto the ODS bed. Addition of high acetonitrile-containing buffer would then displace the sorbed fraction through the second column for ODS CEC of the analyte fraction. The entire process would be repeated for higher ionic strength buffer, etc. until all analytes sorbed on the SCX bed have eluted. Although this approach has been used successfully in the analysis of digested protein samples using a liquid chromatography approach[3], the system would be difficult to establish under capillary electrochromatographic conditions. While an external pump drives the sample in liquid chromatographic experiments, electroosmotic flow (EOF) drives separations in CEC. As discussed previously, the type of buffer used during a CEC experiment will affect EOF

velocity: a decrease in EOF velocity will be observed for low pH, high ionic strength and addition of organic in the buffer solution, while EOF higher velocities will result for high pH, low ionic strength and low organic percent in the buffer solution. Therefore, establishing a system that would efficiently displace sorbed fractions through each bed, with all the buffer necessities implied (different ionic strength buffer for SCX displacement and different acetonitrile content for ODS displacement), while keeping the EOF needed for efficient separation efficiencies would be difficult.

5.3. SINGLE AND MULTI CHANNEL SILICON-GLASS MICRODEVICE

The multichannel approach to protein analysis discussed in Chapter 3 and 4 faces several hurdles before being functional in its entirety. The entire platform would work in five steps: first, isoelectric focusing of a protein sample in the microcapillary connected to the Nanoport; second, electrical fractionation of the separated protein fractions into the microchannels on the device; third, protein fraction sorption on the silicon SPE bed; fourth, trypsin digestion and; fifth, elution for final ESI MS analysis. Single-channel analysis has shown the efficiency of the silicon-based system for protein sorption, digestion and ESI MS analysis. A novel PDMS processing technique, involving reactive ion etching, was developed. Multichannel microdevices built using the thin PDMS (< 20 μm) approach showed the importance of bed-to-bed uniformity for sequential elution under pressure-driven flow. The use of thick PDMS (> 600 μm) in the multichannel microdevice resulted in systematic elution of FITC under laser induced fluorescence imaging. However, because of the large bandbroadening introduced by the thick PDMS layer, longer SPE-to-MS lengths would be needed to obatin baseline-resoved peak elution under ESI MS analysis. Theoretical bandbroadening analysis showed that the SPE-to-MS delay lines would need to differ by 2.8 cm from one channel to the next for baseline resolution of the four peaks. While this problem can be easily resolved in the four-channel microdevice described, a 20 channel system would lead to long elution times and difficulty in fitting all microchannels (from 2 cm to 55.2 cm in length) onto a single glass wafer.

The electrical fractionation of fluorescein into each microchannel was also demonstrated. The implication of having a large dead volume in the fractionation region

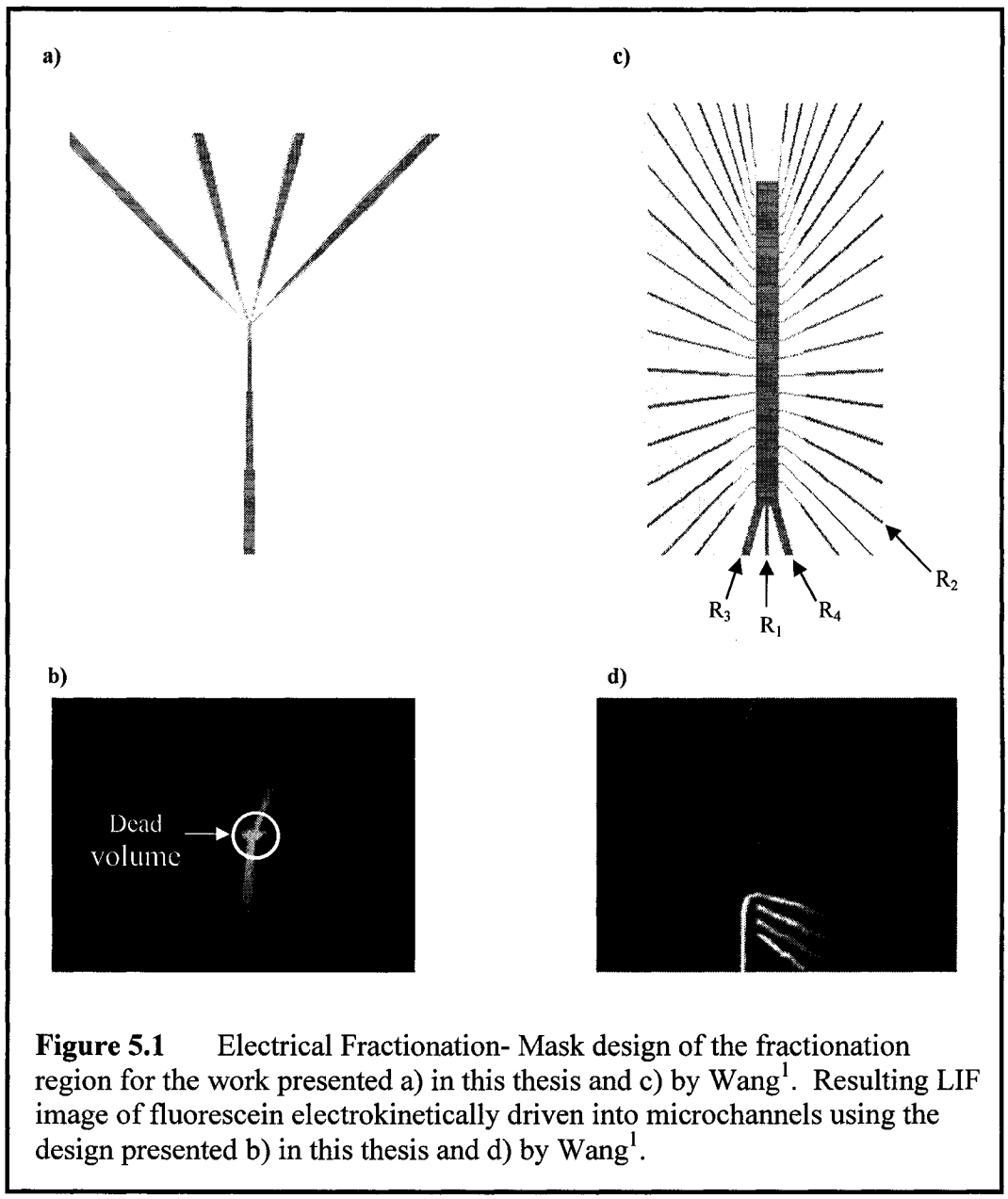

Figure 5.1 Electrical Fractionation- Mask design of the fractionation region for the work presented a) in this thesis and c) by Wang[1]. Resulting LIF image of fluorescein electrokinetically driven into microchannels using the design presented b) in this thesis and d) by Wang[1].

(i.e. at the meeting point of the four microchannels) was discussed in section 4.4.4: the high efficiency obtained during the solution-phase capillary IEF separation would be lost during the voltage-driven transfer to the microdevice due to bandbroadening in the fractionation region. Figure 5.1a presents a close-up of the fractionation region for the microdevice presented in Chapter 3; the resulting electrical fractionation of fluorescein is shown in Figure 5.1b. Diffusion in the fractionation region is evident and would be more pronounced as more microchannels are added to the system. One possible solution to this

problem was discussed in Chapter 4: using a two-mask process for the glass fabrication, the fractionation region dead volume could be reduced. The first mask would define the main microchannels (60 μm width, 20 μm deep) and the second mask, the entry fractionation region (tapered to 3 μm width, 10 μm deep). However, this would only reduce the problem without completely resolving it.

Wang presented a solution to the fractionation problem; the device is shown in Figure 5.1c with the resulting electrical fractionation of fluorescein in Figure 5.1d[1]. Reservoir R_1 contains the analyte, while R_3 and R_4 contain buffer solution. Microchannels along the main channel are the fractionation microchannels where the analyte is to be delivered. Applying a voltage across reservoirs R_1 and R_2, the analyte travels down the main channel; a voltage is also applied to reservoirs R_3 and R_4, moving the buffer solution toward the main channel. The buffer solution, upon meeting the main channel, pinches the analyte, surrounding it with sheath buffer which prevents the analyte from diffusing outwards. This then allows for a very sharp, well-defined analyte plug to be delivered into the microchannel, as shown in Figure 5.1d. Switching the voltage to another microchannel location, sequential delivery was achieved for fluorescein in 36 glass microchannels. However, the geometry of the microdevice would not allow for subsequent pressure-driven flow: calculations show that only the first three rows of microchannels would be pressure driven, while solution in the remaining microchannels would be stagnant. Therefore, protein digestion and further ESI MS analysis would have to be done in CE mode, which presents in itself quite a challenge.

It would then seem that efficient on-chip IEF and subsequent pressure-driven protein analysis are not compatible. Presented next is a possible microsystem that would solve the problems described in the multiplexed system, both the long SPE-to-MS lengths necessary for baseline resolution of neighboring peaks and the inefficient voltage-driven fractionation. The system, for use in MALDI MS protein analysis, is shown in Figure 3.2. Wang's fractionation device would be made in PDMS and used as a protein fraction delivery system (Figure 5.2, bottom left). This fractionation device would be reversibly bonded to a silicon plate having porous microstructures (Figure 5.2 bottom right for the silicon plate, Figure 5.2 top for a side-view of the two systems reversibly bonded together); Chapter 4 has shown the efficiency of porous silicon microstructures for

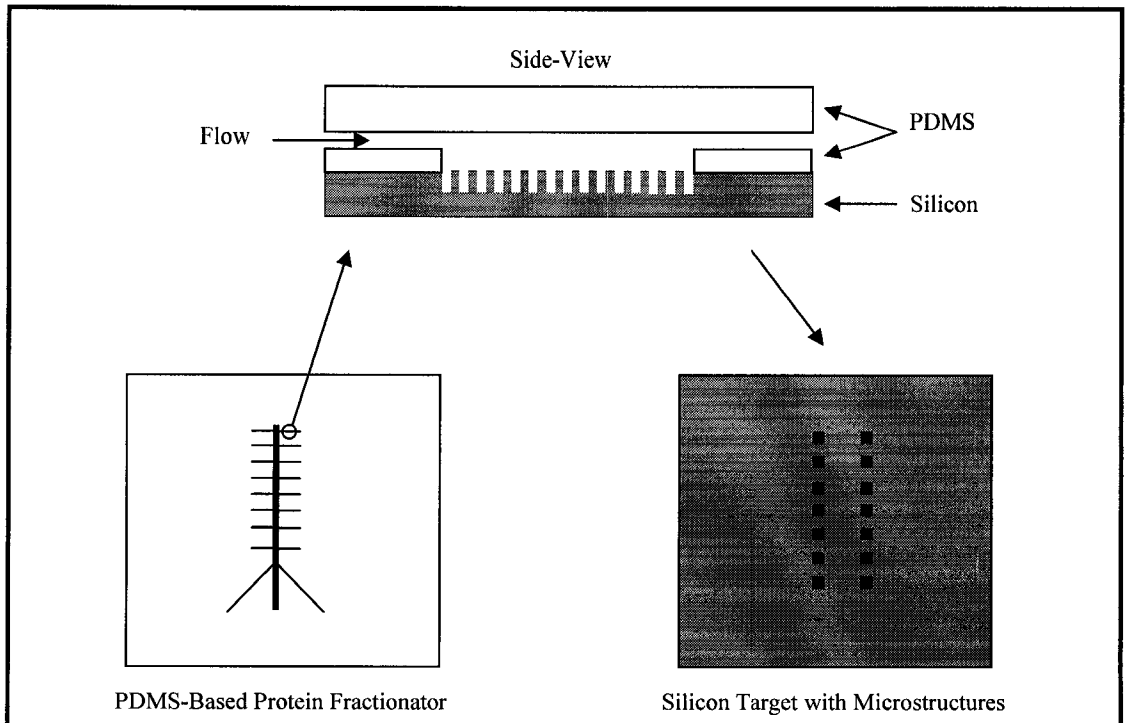

Figure 5.2 Multiplexed Device for MALDI MS Protein Analysis- Depiction of the proposed device with a top view of the PDMS fractionator (bottom left), a side-view of one the fractionation channel (top) and a top view of the silicon target (bottom right).

protein sorption and on-bed digestion. Electrical fractionation in the PDMS structure would deliver protein fractions onto the porous silicon, where proteins would be sorbed. Following fractionation, the PDMS would be peeled away from the silicon structure. Protein fractions would then be washed, digested and the matrix applied before MALDI MS analysis with the silicon wafer, having the porous microstructures, acting as the MALDI target. Laurell et al. have studied the use of microstructure-containing silicon as MALDI target[4-7] and showed low detection limits in porous silicon; in their studies, proteins were delivered through a droplet-dispensing unit. In the system proposed in Figure 5.2, both the high fractionation efficiency afforded by the PDMS fractionation system and the possibility of a high number of sorption sites for incoming fractions on the silicon target could produce a truly multiplexed microsystem for protein analysis. To avoid electrical breakdown at the silicon beds, low voltages would need to be used during the initial fractionation process.

5.4.REFERENCES

(1) WANG, Z., UNVERSITY OF ALBERTA, EDMONTON, 2007.

(2) JEMERE, A. B.; OLESCHUK, R. D.; HARRISON, D. J. *ELECTROPHORESIS* **2003**, *24*, 3018-3025.

(3) LINK, A. J.; ENG, J. K.; SCHIELTZ, D. M.; CARMACK, E.; MIZE, G. J.; MORRIS, D. R.; GARVIC, B. M.; YATES, J. R. *NATURE BIOTECHNOLOGY* **1999**, *17*, 676-689.

(4) ERICSSON, D.; EKSTROM, S.; NILSSON, J.; BERGQUIST, J.; MARKO-VARGA, G.; LAURELL, T. *PROTEOMICS* **2001**, *1*, 1072-1081.

(5) FINNSKOG, D.; JARAS, K.; RESSINE, A.; MALM, J.; MARKO-VARGA, G.; LILJA, H.; LAURELL, T. *ELECTROPHORESIS* **2006**, *27*, 1093-1103.

(6) FINNSKOG, D.; RESSINE, A.; LAURELL, T.; MARKO-VARGA, G. *JOURNAL OF PROTEOME RESEARCH* **2004**, *3*, 988-994.

(7) RESSINE, A.; EKSTROM, S.; MARKO-VARGA, G.; LAURELL, T. *ANALYTICAL CHEMISTRY* **2003**, *75*, 6968-6974.